Cape Peninsula
University of Technology

CubeSat Mission Design for Characterising the Dual Auroral Radar Network (SuperDARN) Field-of-view

By

F. Sagouo Minko

Thesis submitted in fulfilment of the requirements for the degree

Master of Technology: Electrical Engineering

In the Faculty of Engineering

at the Cape Peninsula University of Technology

Supervisor: Prof. Robert R Van Zyl

Co-supervisor: Dr L. Magnus, Mr D.F. Visser

Bellville

2013-03-04

DECLARATION

I, Flavien Sagouo Minko, declare that the contents of this thesis represent my own unaided work, and that the thesis has not previously been submitted for academic examination towards any qualification. Furthermore, it represents my own opinions and not necessarily those of the Cape Peninsula University of Technology.

Signed **Date**

ABSTRACT

The French South African Institute of Technology (F'SATI) at the Cape Peninsula University of Technology (CPUT) began a program in Satellite Systems Engineering in 2009 and is developing its first satellites. The satellites are based on the CubeSat standard, which defines one unit (1U) as a cube with a maximum weight of 1 kg and volume of 1dm^3, and can be scaled up to three units (3U) for increased functionality. ZACUBE-1, a 1U CubeSat that is being developed, will be launched into a sun synchronous orbit in 2013. The main payload of the 1U CubeSat under development is a space weather experiment (beacon transmitter). The beacon transmitter is a scientific payload, which is being developed in collaboration with SANSA Space Science (SANSA SS) in Hermanus, South Africa. The beacon signal will be used to characterise the space weather radar antenna array at the South African National Antarctic Expedition (SANAE IV) base in Antarctica. The SANAE IV radar forms part of the SuperDARN (Dual Auroral Radar Network) project. This phased array antenna network comprises 16 radiating elements, with a 3^o beam width that can be steered in 16 different directions to span the azimuth sector. These antennas are spread over both the northern and southern hemispheres. They operate in the HF band between 8 to 20 MHz and are used to primarily monitor the convection of the Earth's magnetic field by monitoring coherent scatter from it. Orbital analyses were conducted to determine how the choice of the orbit affects the coverage of the array's field-of-view. Propagation analyses were conducted to investigate how space weather variations affect HF signal propagation. The beacon signal will be used as an active target source and will enable the determination of the phase response of the array, thereby determining the direction-of-arrival of the signal. This will allow the experimental verification of the antenna's beam pattern. The beacon signal prototype board was developed by using an RFID transceiver that operates in the HF band, capable of delivering up to 200 mW. Position determination of the satellite will be done by using two line elements (TLE) data. Experimental data will be available once ZACUBE-1 is in orbit; therefore, the work presented here documents a feasibility study and design of the experiment that will be conducted once the satellite is in orbit.

ACKNOWLEDGEMENTS

- Above all, I thank God for being with me from the beginning and allowing me to complete this research. I pray that He continues to watch over me.
- I thank my brother, Jacques Totowa, for all his support, motivation and encouragement.
- I thank my mother, Tangoue Pondoume Cecile, for raising me to become the person that I am today.
- Prof Robert Van Zyl, for allowing me to be part of this group; for his exceptional leadership; and for all the moral and financial support that he has offered me.
- Dr Lindsay Magnus, for his patience and understanding, and for helping me break through every time that I was unable to progress.
- Mr Francois Visser, who always creates time for us no matter how busy he may be; thank you.
- All gratitude to Mr Christopher Wills, Mr Jason Witkowsky and Dr Marco Adonis, for introducing me to F'SATI, and for continuously providing me with their support whenever I needed it.
- Cindy Engel and Ian van Zyl, thank you for ensuring our comfort and for all the work done for F'SATI students.
- Dr Pierre Cilliers, your contributions are appreciated, especially your inputs on space related phenomena.
- Dr Michael R. Owen, from the Northern Lights Software Association, for granting a free NOVA license to the institution and for helping me find my way around the software.
- Khotso Patsa for assisting with FEKO every time I needed help, and Mathieu Sibanda for proof reading my thesis.
- Lastly, I acknowledge the assistance and support of my friends especially Amabo Achoh Daniel and Leopold Lilie N. and all my class mates and everyone who has directly or indirectly contributed towards the completion of this research.

The financial assistance of the French South African Institute of Technology and NRF towards this research is acknowledged. Opinions expressed in this thesis and the conclusions arrived at are those of the author, and should not necessarily be attributed to the French South African Institute of Technology and the NRF.

Table of Contents

List of Figures

List of Tables

List of Appendices

Glossary of Terms

ATC	Air Traffic control
BER	Bit Error Rate
BFSK	Binary Frequency-Shift Keying
Bps	Bits per second
COTS	Commercial-Off-The-Shelf
DPSK	Differential Phase-Shift Keying
EPS	Electrical Power Subsystem
EMF	Electromagnetic Field
F’SATI	French South African Institute of Technology
FEC	Forward Error Correction
f_oF_2	Ionospheric Critical Frequency
FOV	Field-of-View
FSK	Frequency-Shift Keying
GEO	Geostationary Orbit
HF	High Frequency
H_mF_2	The maximum height of the F2 layer
IRI	International Reference Ionosphere
LEO	Low Earth Orbit
MEO	Medium Earth Orbit
Ne	Electron Density
RADAR	Radio Detection and Ranging
RF	Radio Frequency
SS	Space Science
SANSA	South African National Space Agency
SANAE IV	South Africa National Antarctica Expedition

SuperDARN	Dual Auroral Radar Network
TEC	Total Electron Content
TT&C	Telemetry, Tracking and Command
TTFD	Twin Terminated Folded Dipole
UHF	Ultra High Frequency
VHF	Very High Frequency
ZACUBE	South African CubeSat mission series

Chapter 1 Introduction

1.1 General introduction

The French South African Institute of Technology (F'SATI) was officially launched at the Cape Peninsula University of Technology (CPUT) on 28 February 2008 by French President Nicolas Sarkozy. A year later a postgraduate programme in satellite systems engineering was launched in response to one of the "Grand Challenges", as identified by the Department of Science and Technology (DST), namely space science. Thus, F'SATI has established a program where students develop their skills by working on Nano-satellites such as CubeSats, which in turn develop human capacity in South Africa for the national space industry (Visser, n.d.).

The CubeSat standard was developed by students at Stanford University and at California Polytechnic (Puig-Suari, 2001). This was proposed as small educational, low cost and faster space missions (Heidt, Puig-Suari, Moore, Nakasuka, & Twiggs, 2000). At its most fundamental level, CubeSats can be defined as discrete scalable cuboids, which weigh about 1 kg and measure 100 mm each side (Toorian, Blundell, Puig Suari, & Twiggs, 2005). This is commonly referred to as a 1U (unit), but more Cubes may be combined to increase the functionality, as shown in the Pumpkin Inc. Structure, presented in Figure 1.1.

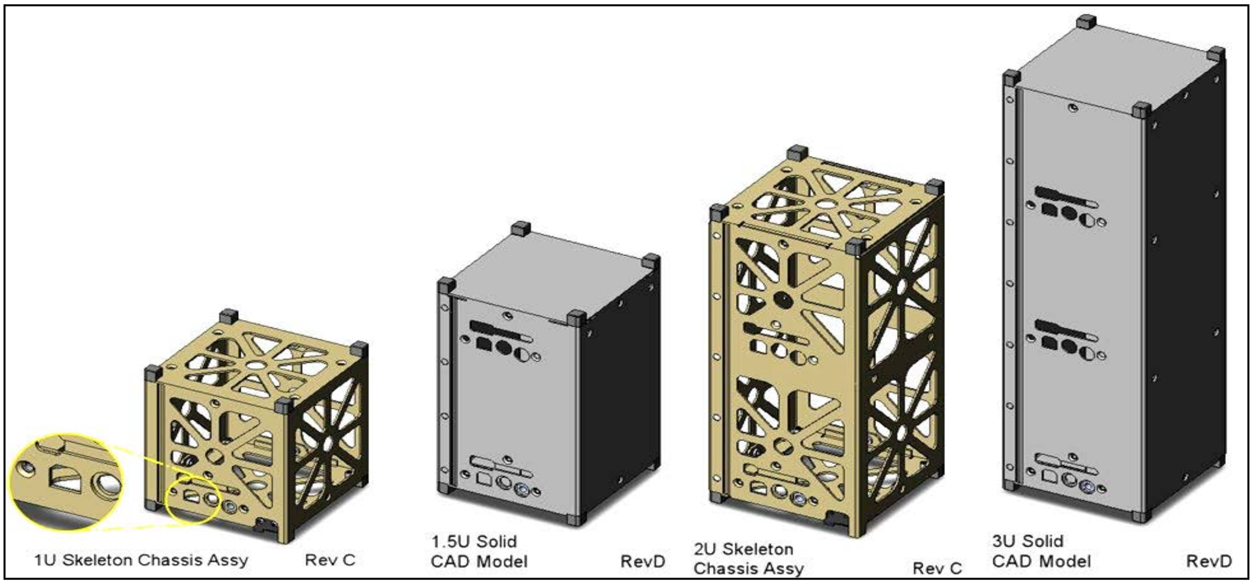

Figure 1.1: Standard CubeSat structures (Adapted from Pumpkin, (n.d.))

Having subsystems similar to those of larger satellites, CubeSats can achieve similar goals. However, since the size (in terms of dimensions) is the main constraint, subsystems should be miniaturised to be accommodated in the dedicated structure. Common use of commercial-off-the-shelf (COTS) components reduces mission development costs significantly. This is the primary objective of CubeSats (the design of a space exploration mission at low cost) (Chang, Kang, Moon & Lee, 2006).

Satellites are launched into various orbits. Commonly used orbits are the Low Earth Orbit (LEO), Medium Earth Orbit (MEO) and the Geostationary Earth Orbit (GEO) (Ipolito 2008:25-29). Because of the planned short operational life of CubeSat missions, many of these are launched into LEO to accelerate the end-of-life process of de-orbiting through atmospheric friction.

There are currently two CubeSats under development by F'SATI postgraduate students. The first CubeSat is a 3U CubeSat (ZACUBE-2 presented Figure 1.2(a)), which will carry two payloads; the first payload being an **imager** for low resolution Earth observation purposes, while the second payload is a **High Frequency (HF) beacon transmitter** for scientific experiments. The scientific payload is being developed in collaboration with SANSA Space Science (SANSA SS)[1] with the purpose of characterising the field-of-view (FOV) of the SuperDARN radar antenna arrays, of which implementation are located in both the Northern and Southern Hemispheres. The second CubeSat is a 1U CubeSat (ZACUBE-1 which is presented in Figure 1.2(b)) that was introduced as a fast-track satellite mission with its main objective being the involvement of students in the complete life-cycle of a satellite mission from concept to launch.

The mission objective of the HF beacon is to serve as an initial study towards the characterisation of the SuperDARN. The ZACUBE-1 payload is also an HF beacon transmitter that will be used to characterise the beam pattern of an HF antenna array at SANSA SS in Hermanus, and for verifying HF propagation ray-tracing simulations conducted by SANSA. It is envisaged that the SuperDARN antenna array at SANAE IV will also be characterised as part of the experiment if feasible within the expected life time of ZACUBE-1

---

[1] The SANSA Space Science was previously known as the Hermanus Magnetic Observatory (HMO) and is based in Hermanus.

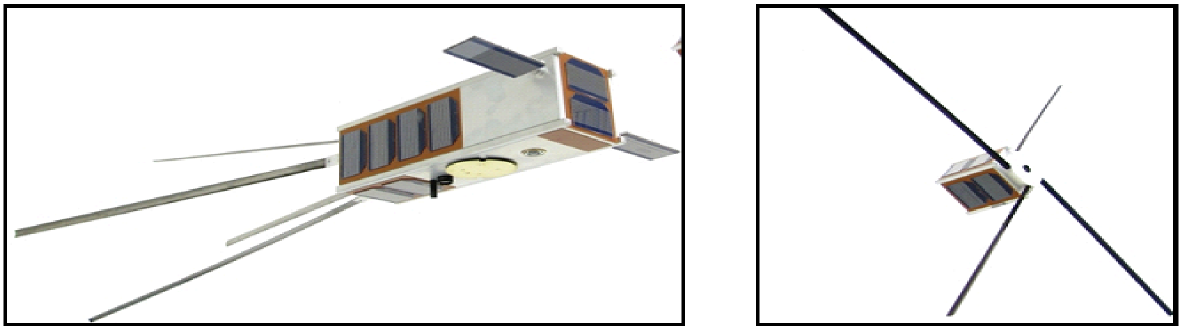
(a) (b)

Figure 1.2: Nano-satellites under development by F'SATI students: a) 3U CubeSats for Earth observation (ZACUBE-2), b) 1U CubeSat for space weather polar experiment (ZACUBE-1)

1.2 Background to the research

South Africa maintains a research base in the Antarctic, namely the South African National Antarctic Expedition (SANAE IV) base. Several instruments deployed at SANAE IV support of an international effort to study space weather phenomena. Among other instruments, South Africa maintains an array of high frequency (HF) antennas, which is part of the Dual Auroral Radar Network (SuperDARN). This network is used to study the polar ionospheric motion, primarily caused by magnetospheric convection. The HF radar antenna array at SANAE IV is a large 16-element array, which pans a wide FOV. The array directs the beam into the polar ionosphere with the purpose of observing ionospheric motion across the polar cap. These measurements are used to infer solar wind coupling with the magnetosphere.

To improve the value of measurements from the SuperDARN antenna array, it is necessary to characterise it. The characterising of large antennas, such as the SuperDARN antenna array at SANAE IV (Figure 2.3), is a challenge owing to the following reasons:

- Far-field measurement requires a large testing range;
- Large antenna arrays cannot be accommodated in closed test facilities; and
- Outdoor characterisation is dependent on the weather, which is generally harsh in the Polar Regions.

The challenges outlined above can be met with a satellite in LEO; it was proposed that a satellite could be used to characterise the HF antenna array at the SANAE IV base. A CubeSat carrying an on-board HF beacon transmitter, which acts as an active signal source, will allow the characterisation of the antenna beam pattern. A satellite beacon is a fixed-frequency, low-power signal, which is transmitted from a satellite.

Once the satellite is launched into orbit and the beacon transmitter is operating, the beacon signal will travel through the beam of the antenna array as the satellite crosses the array's FOV. By measuring the received signal power on the ground as a function of time and elevation, the antenna radiation pattern may then be measured. In addition, the elevation and directions of arrival of signals will also be measured by means of the secondary array. By correlating the measured direction of arrival with ray-tracing simulations, information about the electron content distribution of the ionosphere can also be obtained.

1.3 Statement of the research problem

The aim of this project is to design a scientific CubeSat mission that will be used to study the feasibility of SuperDARN elevation angle and radiation pattern characterisation, using a HF beacon signal as an active signal source placed in LEO satellite.

1.4 Research questions

The following questions outline the study's research objectives:

- What orbital parameters will best suit this polar Space weather mission?
- Does a 1U CubeSat provide a feasible platform for this Space weather mission?
- Can a low cost beacon be developed that satisfies the mission requirements?
- How will the beacon signal help to determine the phase response of the antenna arrays?
- Will the HF beacon signal traverse the ionosphere when the satellite passes over the target receiver?

1.5 Research objectives

The research aims to fulfil the following objectives:

- To analyse and define orbital parameters to suit the required polar mission;
- To determine the permissible LUF for the satellite HF beacon and
- To develop an HF beacon transmitter that will be used as an active signal source placed in LEO.

1.6 Research methodology

A framework, which serves as guide towards the defined objectives, is shown in Figure 1.3. It illustrates the sequence of events from top to bottom.

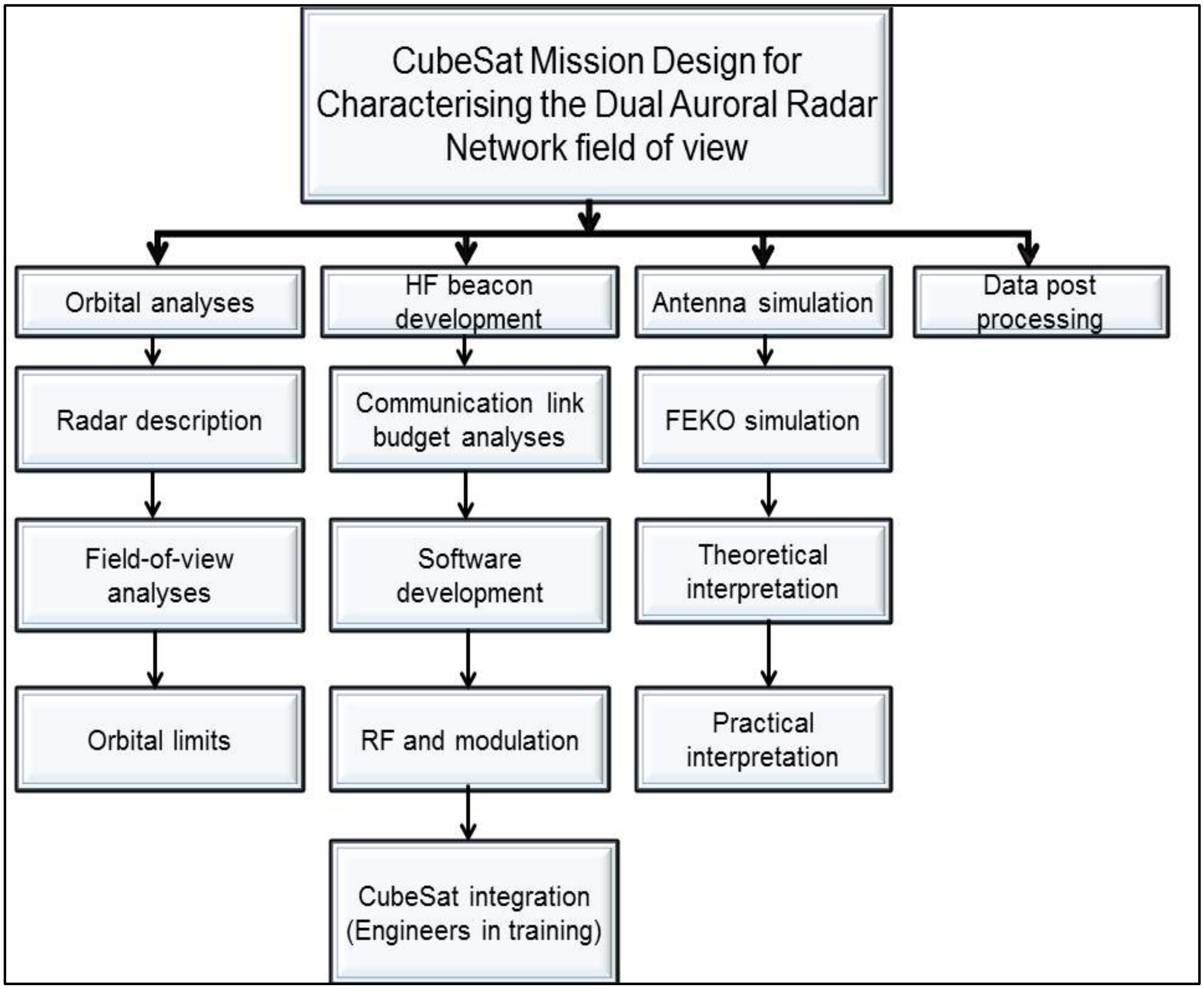

Figure 1.3: Research framework

1.7 Delineation of the research

This research mainly focuses on the design of an experiment to characterise SuperDARN antennas, by using CubeSats.

Factors listed below are not part of the research scope:

- HF frequency transmitter development (a COTS system used).
- Implementation of a flight model beacon for launch.

- Post launch research is not included, as the launch itself is only planned for 2013.
- Data post processing is excluded from this study as it will be the topic of subsequent research.

1.8 Research outcomes

- An HF antenna and receiver, to be incorporated into the ground station at CPUT.
- Electromagnetic simulation of the SANAE IV HF antenna carried out to assess the feasibility of the experiment.
- Orbital analyses are to be conducted and basic orbital elements are to be utilised for FOV analyses.
- FOV analyses are to be done to determine suitable orbits based on selected inclinations, as well as the coverage obtained from these inclinations.
- A propagation analysis is to be conducted in which the lowest usable frequency (LUF) is determined for various seasons.
- A fully functional beacon transmitter that operates at 14.01 MHz with a maximum output power of 100 mW is to be developed.

1.9 Significance of the research

This research will improve the value of the interpretation of data from HF space weather radar systems. This plays an important role in maintaining South Africa's strength in the geosciences, and physical sciences providing the world with more accurate space weather models, which may improve predictions.

The use of a CubeSat as a solution to the research problem helps to develop human capacity in satellite systems engineering through an affordable tool. Thus, skills and knowledge, which are acquired after successfully completing this project, will benefit the engineering and scientific industry.

1.10 Synopsis of the chapters

Chapter 1 gives an introduction and background to the research study, the origin of CubeSats, and a brief description of CubeSats under development by F'SATI students. It also highlights the research methodology, the significance of the research, and stipulates the delineation of the research.

Chapter 2 introduces the concept of space weather and presents how the present research relates to it. An overview of satellites is provided, in which different satellite categories are discussed. Furthermore, the theory behind RF ionospheric propagation, and how it affects HF signals are discussed, followed by the derivation of link budget equations.

Chapter 3 presents the mission analysis, as it applies to this mission, and describes the mission architecture of the conceptualised mission. The orbital parameters and the payload link budget are computed, while ground station specifications and launch vehicle (LV) requirements are defined.

Chapter 4 presents results for the FOV analyses, the evaluation of LUF and the antenna simulation results. The chapter also presents the developed beacon prototype module and describes how the Morse code was generated.

Chapter 5 presents a discussion of results obtained in previous chapters.

Chapter 6 presents the conclusion to the research.

Chapter 2 Technical Review

2.1. Introduction

Space weather prediction is regarded as a science, as it deals with space physics phenomena. Presently, many space weather predictions are obtained from space-borne platforms which give the state of the Earth's upper atmosphere (ionosphere). The ionosphere has a direct impact on radio frequency signals. The behaviour of the ionosphere at high latitude is the subject of the SuperDARN's studies. The mission designed here is to improve the usefulness of the SuperDARN's data. However, prior to the mission design, it is important to discuss certain topics, which are pertinent to this research, namely,

- Space weather;
- Ionospheric propagation;
- Satellite orbits; and
- Field of view

2.2. Introduction to space weather

Space weather is the variation of conditions in the Sun-Earth's environment, as a result of the Sun's and Earth's activities (Koskinen *et al.*, 2001). These conditions are likely to influence the performance of space-borne platforms, ground-based technologies, and in certain extremes, endanger human's lives. SANSA Space Science (SS) is one of the South African governmental organisations, that conducts most of its research in studying space weather effects in Southern Africa, as well as at SANAE IV on the Antarctic continent.

2.2.1 SANAP

The Department of Environmental Affairs, through the South African National Antarctic Program, maintains a research base at SANAE IV. This site was selected because it is an unpolluted environment; therefore, the outcomes of the research conducted in this environment are accurate. As a result, the research outcomes obtained in such an environment can be compared with those obtained in environments that have undergone human transformations, in order to better understand the origin of climate change. In addition, referring to Figure 2.1, the Earth's magnetic fields lines are almost vertical to the Earth at the magnetic poles. This provides an opened gate to space weather components such as cosmic rays, solar winds, light dust, plasmas and many more. These space weather components are related to numerous space weather effects either observed or felt on Earth. Various countries work in collaboration on the Antarctic continent to study these space weather components to better understand their effects, including their contribution to climate change. The SuperDARN plays a significant role in the above studies.

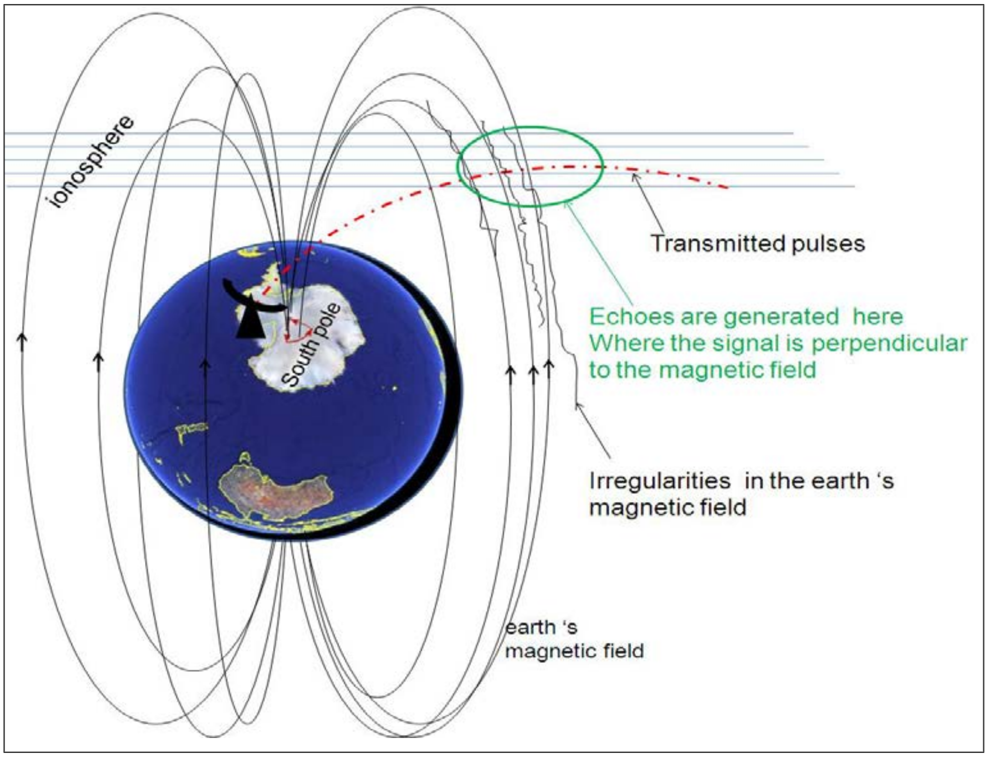

Figure 2.1: **Plasma irregularity measurements by the SuperDARN**

2.2.2 SuperDARN

The SuperDARN is a global network of pulsed radar antenna arrays. Its main objective is to continuously provide a global-scale observation of high latitude ionospheric motion (Hughes, Bristow, Greenwald, & Barnes, 2002). These radars are located in both the northern and southern hemispheres, forming two groups. The northern hemisphere group comprises of eighteen radars, and the southern hemisphere of seven, including the one at the SANAE IV base.

2.2.2.1 Principles of operation

The SuperDARN operates from 8-20 MHz which overlaps the 14 MHz amateur band, and it is used to study space weather phenomena by measuring the signal that is backscattered by field aligned plasma irregularities in the E and F regions of the ionosphere. These field-aligned irregularities tend to align along the Earth's magnetic field lines in their occurrence (Figure 2.2). The radar transmitter module transmits multiple short pulses unequally to distinguish the returning echoes from different altitudes (Bryson, Bristow & Parris, n.d.). These echoes are due to the presence of plasma irregularities, aligned with the Earth's magnetic field lines (Andre & Dudok de Wit, 2003).

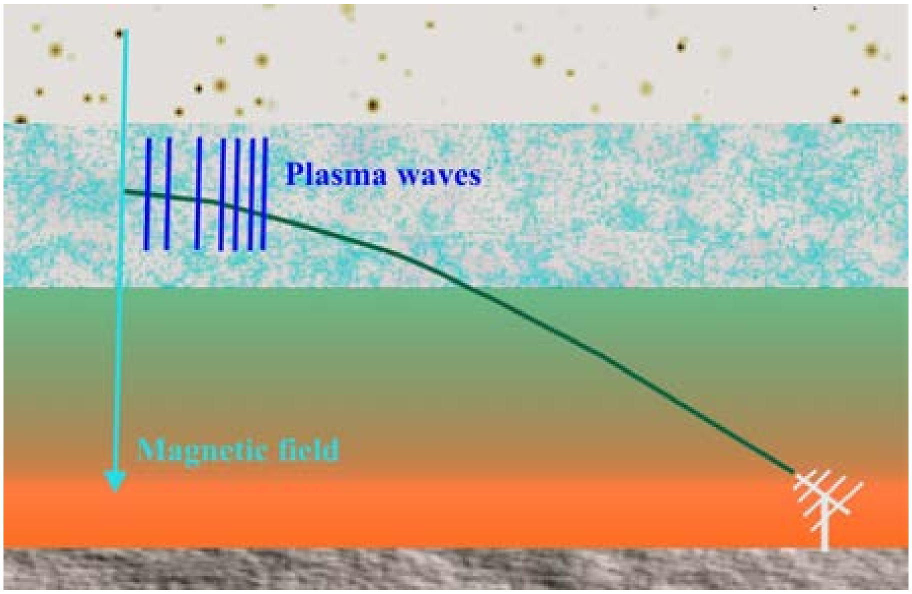

Figure 2.2: HF ionospheric propagation

The line-of-sight Doppler velocity, spectral power density and the spectral width of the returned echoes are derived using the radars' auto-correlation functions (ACF). Since the Doppler velocity obtained characterises the trajectory of plasma velocity in the direction of the radar, when data from two radars are mapped (Figure 2.3), the combined plasma velocities (the small blue and yellow arrows) are obtained. In this way, the velocity vector for the travelling plasma irregularities is also obtained (the red arrow) (Bryson *at al*., n.d.). This is the primary reason why each radar field of view within the SuperDARN overlaps with those of other radars to monitor ionospheric behaviour over the polar caps.

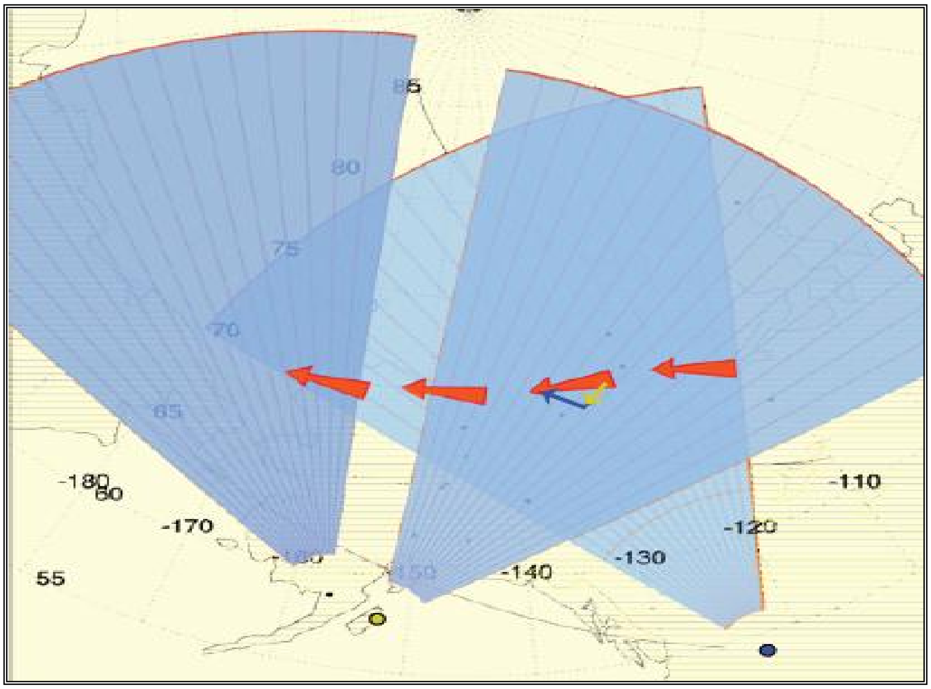

Figure 2.3: Convection mapping of multiple radars allows the determination of the direction of flow of plasma (from Bryson *et al*., (n.d.))

2.2.2.2 Previous approaches to characterisation

There have been some attempts to characterise the elevation resolution and beam patterns of these antennas, but there is no report on successful SuperDARN far field measurements for this purpose. However, there are some documented failed attempts. The failures may be attributed to either human error or improper measurement procedures, as will be discussed.

Sterne (2010:97-101) describes the measurement method of the [2]Saskatoon SuperDARN by using an aeroplane. It is noted that the approach could have been successful, however, for some unexpected problems (the airplane had a dedicated flight path, which may not have been in the trajectory of the radar beam), this approach was unsuccessful. In addition, the laptop battery that was used for logging the position of the earoplane only lasted for a few hours.

At SANAE IV, a [3]helicopter was used for near field measurements of the SANAE IV SuperDARN, where the outcome was indeterminate for unknown reasons. Another problem that was faced with the helicopter approach was that helicopters have limited altitude when they fly. This altitude does not meet the requirements for far field measurements. Hence, the beam

---

[2] Saskatoon is one of the SuperDARN bases located in Canada (52.16°N, 106.53°W).

[3] During the data post-processing, the helicopter path did not correlate with the defined flight path.

pattern of the antenna array could not be measured, in either near field or for far fields of the array.

2.2.2.3 Overview

RADAR is the acronym for Radio Detection and Ranging. Its purpose is to determine the location of a target by bouncing electromagnetic fields (EMF) off that target. This helps to determine and describe parameters such as the range, echo and Doppler shift between the radar and the targeted object.

- *The range* is determined by measuring the time delay between transmission of an electromagnetic signal and the reception of the echo.
- *The echo power* is the power of the received signal at the time of an echo.
- *The Doppler shift* is the difference in frequency between the transmitted signal and the received signal, if the target is in motion relative to the transmit/receive module.

2.2.3 Interferometer

The HF radar at SANAE IV consists of a main and a back array, which together form an interferometer array. The main array (Figure 2.4) consists of 16 elements, and it has transmitting and receiving capabilities, while the back array (Figure 2.5) consists of four elements and it is set to only receive signals. Both the main and the back antenna arrays have the same design topology. The antenna topology consists of twin terminated folded dipole (TTFD) antenna elements, which are suspended on a 16 m mast and supported by guy wires. Five horizontal wires behind the main array serve as reflectors (see Appendix B (b)). The TTFD antennas are designed to withstand polar storms by providing less surface area to the wind. This interferometer array was built in 2009 as the replacement of the log periodic dipole antennas (LPD) array that was blown over by a storm in 2008 (Keith, 2009).

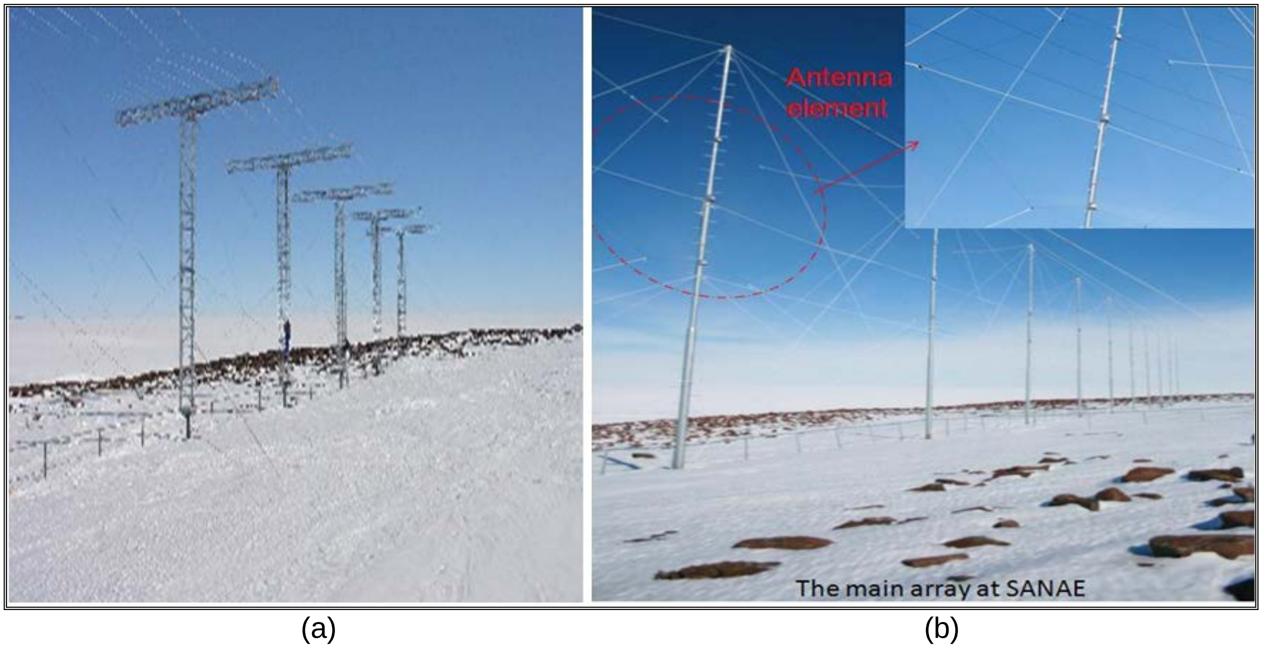

(a) (b)

Figure 2.4: **The main antenna array at SANAE IV: a) LPD replaced by, b) the TTFD**

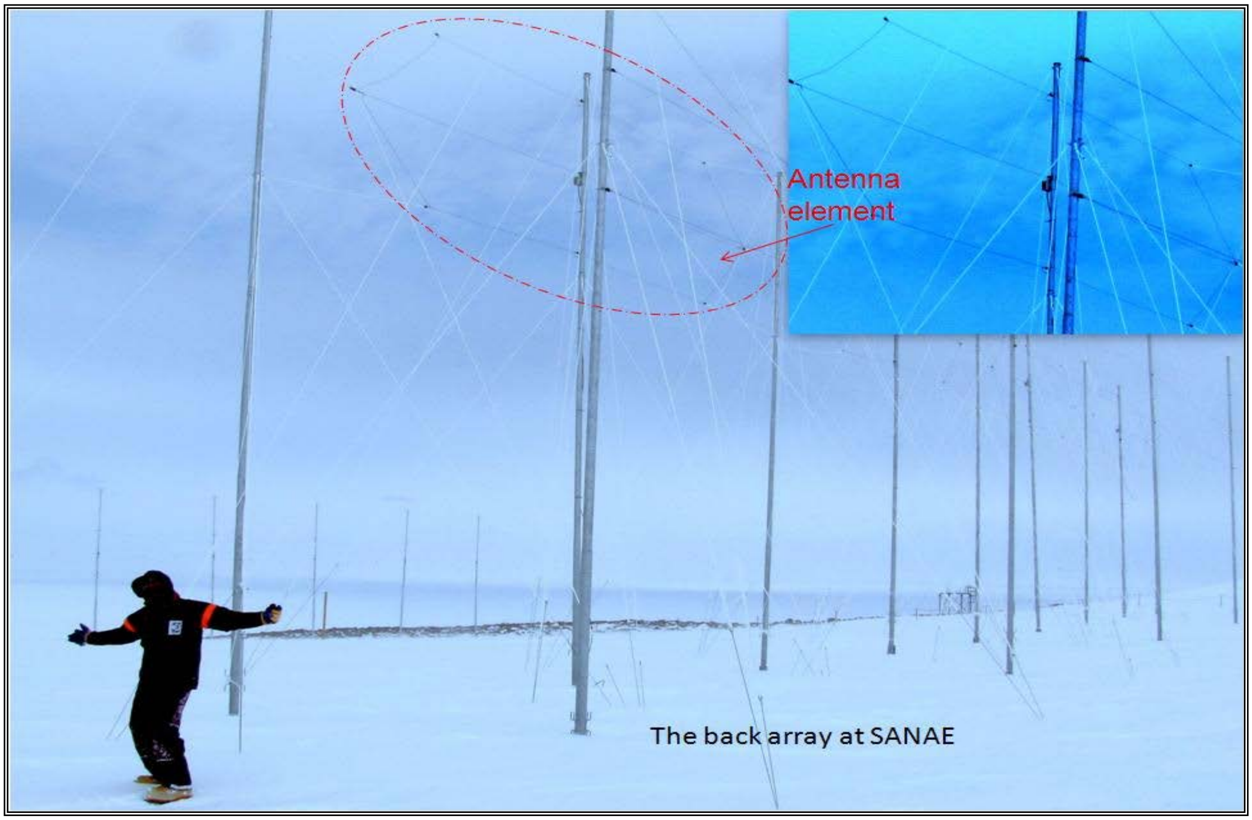

Figure 2.5: **Back array at SANAE IV with the author standing in front of it**

The TTFD was selected because of its structural design (Figure 2.4 (b)), and fewer wires make it more resilient to windy arctic conditions, as compared to the previous LPD design, which had more structures (Figure 2.4(a)). The present antenna element was initially designed with two 100 Ω loads as terminations; but because of the mismatch between the 50 Ω transmission lines and the antennas, the terminations were bypassed, as shown in Figure 2.6. It was discovered while testing the array that, by shorting the termination, the antenna is better matched to the transmission lines.

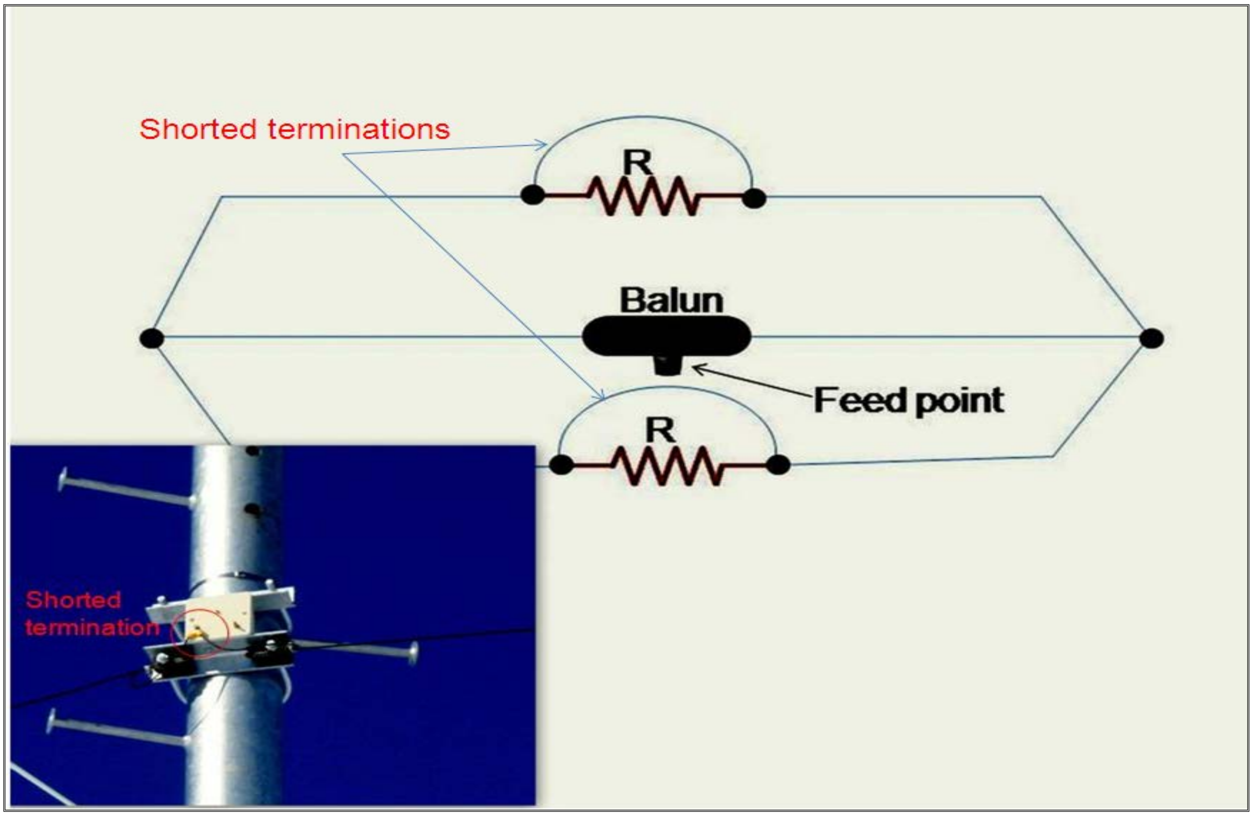

Figure 2.6: TTFD antenna element, showing the damping resistors shorted out

2.2.4 Satellite mission design

A satellite's application defines its type (Anil & Varsha, 2007), while its weight defines its mass category. Although the satellite mass does not influence much the shape and size of an orbit (Louis & Ippolito, 2008:20), it plays an important role in the selection of a launch vehicle (LV). Costs and functionalities are directly related to the satellite mass (Evans, 1999:249). Common types of satellites, with reference to their functionalities, include:

- *Communication satellites:* These are satellites which are used for radio, telephone and television transmission.
- *Weather forecasting satellites*: These satellites provide scientific data for short and long-term space weather prediction.
- *Remote sensing satellites*: Remote sensing satellites provide information about the state of the Earth through observation.
- *Scientific satellites:* These satellites form part of a space based platform that has access to near and far space, and provide data to the ground based platform for space research purposes.
- *Military satellites:* These satellites provide most of the services previously stated, including early warning and navigation.

The classification of satellites according to weight is:

- Large satellite (1,000kg);
- Medium size satellite (500-1,000kg);
- Minisatellite (100-500kg);
- Microsatellite (10-100kg);
- Nanosatellite (1-10kg);
- Picosatellite (0.1-1kg); and
- Femtosatellite (<0.1kg) (Gao *et al.*, 2008).

CubeSats fall under the nanosatellite category. CubeSats are known to be low cost space mission platforms, since most of the subsystems are available as COTS. This satellite platform is a suitable platform to train students at university level on satellite technologies and related applications, as this was the objective of its development by Robert Twiggs and Jordi Puig Suari (Toorian *et al.*, 2005). CubeSat mission design procedures follow the same principles as that of bigger satellites once concepts are identified:

2.2.5 Mission objectives

The mission objectives are regarded as what the mission needs to achieve. The mission objectives are not always scientific (there are also political or military objectives). The mission objectives are identified as scientific when all the stakeholders share the same scientific ideas. The scientific objectives of the ZACUBE missions are listed below:

- The primary objective of ZACUBE-2 is to characterise the elevation angle algorithm of the SuperDARN antenna arrays, and to provide means for measuring their beam patterns; particularly the antenna at SANAE IV.
- ZACUBE-1, in turn, is designed to study how feasible the primary objective is, therefore, ZACUBE-1 serves as proof of concept (POC) towards the characterisation of the SuperDARN arrays.
- The ZACUBE-1 will also be used to characterise the ionospheric refraction over SANAE IV and compare it with the International Reference Ionosphere (IRI) algorithms (Doreen Ahaba). The IRI2007/2011 are ionospheric models which are used by scientists at SANSA SS. for tracing RF signals through the ionosphere.

2.2.6 Preliminary mission requirements and constraints

The preliminary requirements of this mission are related to the payload control system, power system, communication system and launch vehicle.

2.2.6.1 ZACUBE-1 requirements

The preliminary requirements are outlined below, and they characterise a set of parameters that are needed in order to achieve the objectives.

- ***Payload requirements***
    - The mission requires an HF beacon transmitter payload.
    - This transmitter should operate at a constant and low RF power at the carrier frequency.
    - The transmitter development does not require the module to process any data; thus, less complex solutions are investigated.
    - The orbital selection should allow for coverage at low and high latitude.

- ***Attitude Determination and Control Subsystem (ADCS) requirements***

  The ADCS subsystem is a two-axis stabilisation system that is required to put the satellite in a spin to deploy the HF antenna.

- ***Power requirement***

The solar panel should have maximum access to the sun when the satellite is not in the eclipse to charge the batteries while power is supplied to other subsystems. In order to save battery power, the transmitter should be turned on only when transmission is required. The transmitter should remain on during the entire overpass period.

- ***Communication requirements***

There is a need for UHF and VHF communication subsystems for telemetry and for the control of the satellite.

2.2.6.2 Mission constraints

The mission requirements and constraints of ZACUBE-1 are listed in Table 2.1.

Table 2.1: ZACUBE-1 preliminary requirements and constraints[4]

Functional requirements		
Performance	Beacon transmitter	20 dBm at 14.099 MHz, Morse code
	Stabilisation	Spin-stabilised
Orbit	Type	Circular, elliptic
	Height	600 km nominal
	Inclination (optional)	98° polar
	Coverage	Hermanus, South Africa (HF beacon)
		Cape Town, South Africa (TT&C)
		SANAE, Antarctica (HF beacon)
Operational requirements		
Duration	In-orbit lifetime	1 to 2 years
Data transmission	HF beacon	Over SuperDARN antennas including Hermanus
	TT&C	Over supporting ground stations
Constraints		
Cost	Development, human resources, launch	< R4 million
Schedule	Development time	< 2 years
	Mission start date	January 2011
	Launch window	2nd quarter 2013
Dimensions	Size	1 unit CubeSat form factor
	Weight	<1.2 kg

---

[4] A detail specifications is given in Table 3.5.

Regulatory	ITU frequency registration	145.86/437.345 MHz VHF/UHF 14.099 MHz HF
	Licensing	License obtained from South Africa Council for Space Affairs

From Table 2.1, the mission flow diagram was generated. This flow chart presents the evolution of the ZACUBE-1 from the mission definition to the launch campaign. It can be noted from Figure 2.7 that there were still undefined parameters (inclination, launch site) up to this stage. This is because the inclination of piggyback payloads is dictated by primary LV's payload. Thus, this can only be communicated once the LV has been identified. However, we considered the entire range of inclinations in order to conduct the coverage analyses.

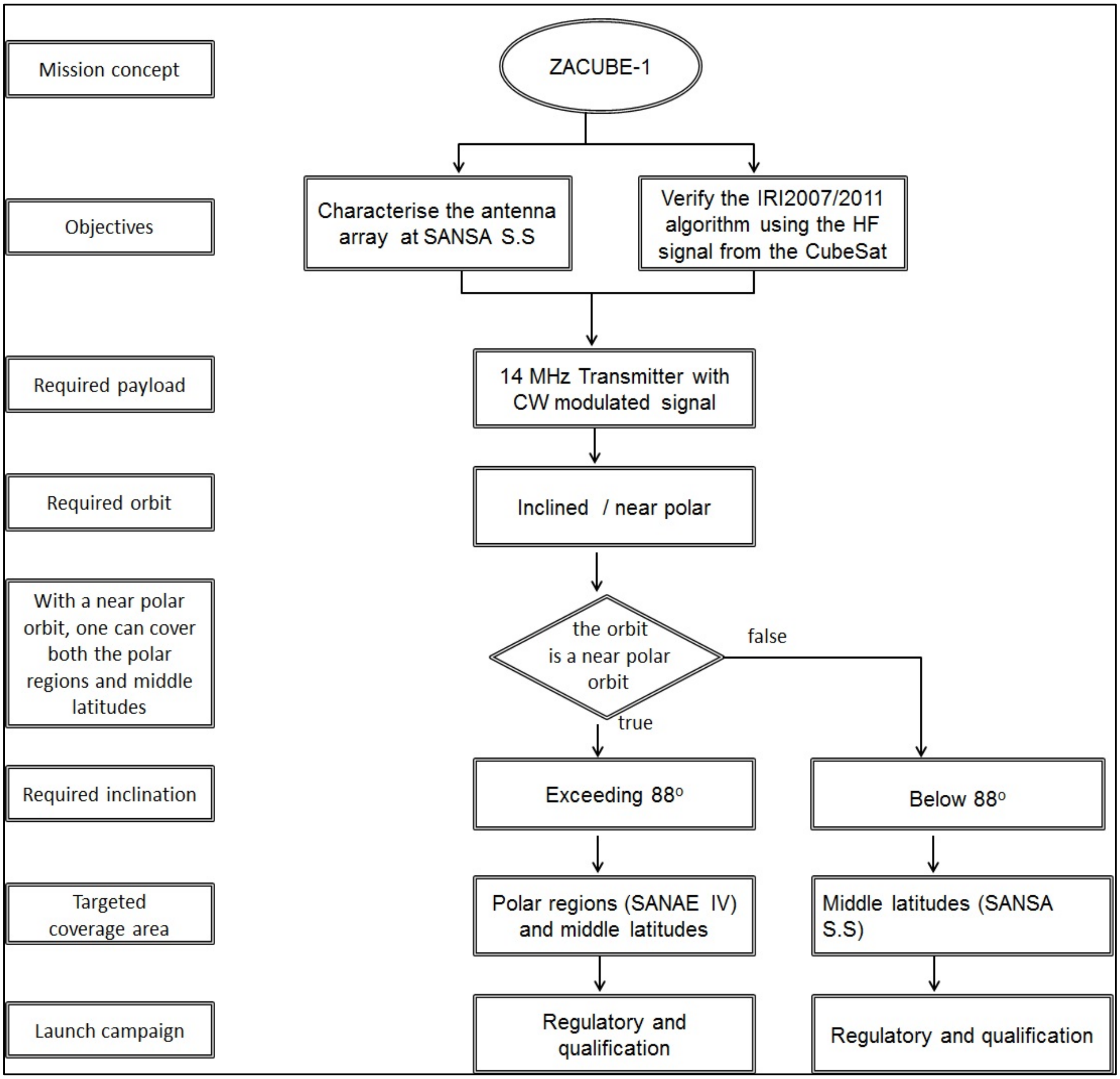

Figure 2.7: ZACUBE-1 mission flow-diagram

2.2.7 Space mission components

The components that form part of a space mission includes the ground segment, the space segment, and the targeted object (the SuperDARN in this case). Space mission components are elaborated in the following sections.

2.2.7.1 Space segment

Two major components constitute the space segment, namely:

- *The orbiting satellite:* the satellite carries one or more instruments designed to achieve the defined objectives.
- *The ground station:* this unit is often referred to as the tracking, telemetry, command and monitoring (TTC&M) subsystem. This segment provides the control to the satellite; it acquires telemetry and sends the tele-commands to the satellite. A tracking antenna provides a communication link for TT&C, and allows data download from the satellite. In this way, the satellite performance is monitored.

Important spacecraft subsystems are listed below:

- *The attitude determination and control subsystem (ADCS)*: the spacecraft will be spin-stabilised owing to volume constraints. Spin stabilisation is based on the concept of nutation frequency, where a small torque is applied to the spacecraft to allow its slow movement, much like a gyroscope with certain angular rate (James & Wiley, 2008:379 380).

- *The TT&C*: is part of the communication subsystem. The operation of this subsystem should be autonomous, as the payload antenna requires pointing owing to its narrow beam width and tracking impedance matching mechanism. This requires the antenna to point in the direction of the radar. There will be one way communication for the main payload and two-way coherent communication for the control of the satellite, which is required for the secondary payload data downlink.

- *Command and data handling (C&DH) subsystem*: this unit allows management of the bus command data by receiving the payload and bus data.

- *The electrical power subsystem* (EPS): The EPS regulates the generated electrical power according to levels that are required by each subsystem. In addition, power will be controlled to prevent various anomalies, such as over-current or over-voltage from occurring during the mission lifetime.

- *The structure and mechanics:* are done to accommodate all subsystems including the deployment mechanism for the antenna’s payload.

2.2.7.2 Spacecraft bus architecture

Four different bus architectures can be implemented when designing a spacecraft bus. Selection of the bus architecture, which forms part of the spacecraft computer specifications, is dependent on the mission complexity and requirements (Jane, Hosken, & Pollock, 1999:652-655). Some spacecraft bus architectures will offer better reliability in comparison to others. The different types of spacecraft bus architectures are:

- Centralised architecture;
- Ring architecture;
- Bus architecture (federated); and
- Bus architecture (distributed) (Jane *et al*., 1999:652-655).

In centralised bus architectures, all data paths share a common point, while in the ring architecture, data flows in a circular pattern which is similar to series networking. This architecture is thought as less reliable with respect to the previous architecture, because failure of one module may compromise the functioning of the entire mission. However, it reduces the current's surge at a single point. The bus architecture (federated) is a tree type of configuration in which each device is connected to its own data point; in this way, a processor facilitates communication between each module. This configuration allows subsystems to be interchanged without compromising communication among the others. The last bus configuration is the bus architecture (distributed), which may be referred to as a scalable architecture. Different processors execute the mission, and a failure of one subsystem may not completely alter the mission's functionalities. These architectures are shown in Figure 2.8.

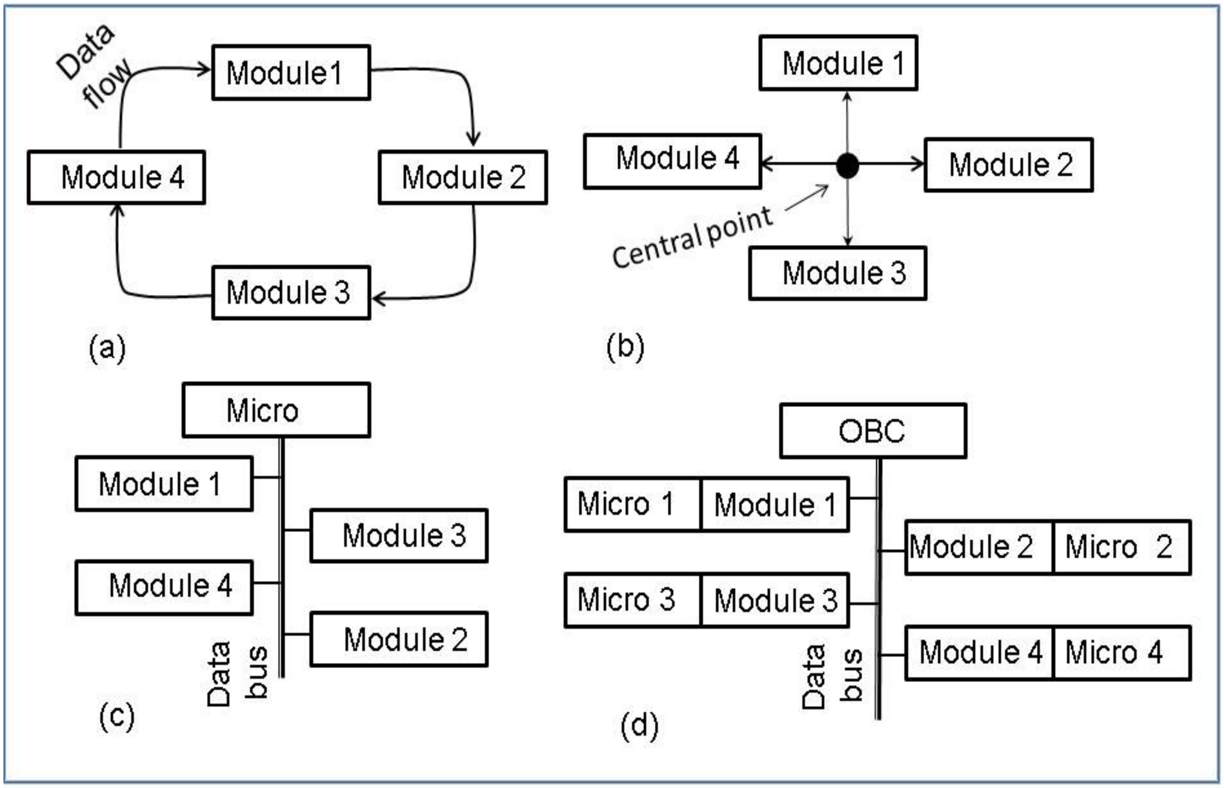

Figure 2.8: CubeSat bus architectures: (a) ring architecture, (b) centralised architecture, (c) bus architecture (federated), (d) bus architecture (distributed)

2.2.7.3 Launch system

There are a few physical considerations before launching a satellite, in general, and CubeSats, in particular. These considerations can be thought of as launch operator requirements. Some of these considerations are:

- The number of satellites to be accommodated within an LV ;
- The satellite's weight and dimensions;
- The required orbit; and
- The mission timeline.

The selection of an LV should be in line with the mission's objectives, and hence, there are a number of things to consider. For instance, the LV performance in terms of capacity to carry; compatibility (whether it can accommodate the spacecraft); its availability (determined by the launch window); and the costs (Loftus & Teixeira, 2008:721-725).

The LV contractors will request a set of tests that should be conducted before accepting the spacecraft. This allows for minimising the risk of one spacecraft's failure to affect other spacecraft in the LV. This risk is significant when the number of piggyback payloads is high. If an LV has not yet been identified, the required set of tests may be conducted according to the CubeSat design specifications manual Rev 12, or the GSFC-STD-7000, which is the NASA reference manual (Riki, 2009). Some of the required tests are:

- The *random vibration test*: this test is done to ensure that all the subsystems are well mounted together and can withstand the vibration conditions during launch. This test is conducted according the above GSFC-STD-7000 reference, or according to the LV specifications.
- The *thermal cycle test* is conducted to insure that the electronics of the satellite will withstand temperature variations in space. This test is followed by the thermal vacuum test.
- The *thermal vacuum test*: this test is conducted to ensure that the selected components can operate in a vacuum under predicted or known temperature conditions. The test is done with certain degrees of margin to accommodate the components' temperature tolerance.
- The *visual inspection test*: this test involves checking the satellite size (length, width, height), and the satellite mass (1330 g for 1 U and 4000 g for 3 U). It also involves checking whether the following items are present: the "remove before flight" pin, the deployment switches, the separation springs and the rails.
- The *design qualification test*: this test should show that the satellite's functionality will not be degraded by encountered space conditions.
- The *proto-flight test* and the *acceptance test* are also conducted according to the above NASA reference document, and after both these tests, the satellite should not be modified or disassembled. Should this happen, the satellite should be retested.

2.2.7.4 *Ground segment*

The ground segment consists of all transmitting and receiving Earth stations around the world (Anil & Varsha, 2007:304). It allows the tracking of the satellite, establishes the communication link using a tracking antenna, and establishes a link between the CPUT ground station and the radio amateur network by means of the GENSO network.

2.3 Ionospheric propagation

Before discussing propagation of electromagnetic waves through the ionosphere, one should first define what the ionosphere is.

2.3.1 The ionosphere

The sun is the most active body in the solar system. As it continuously emits extreme UV into space, it creates ionisation of atmospheric gases in the region within the Earth's atmosphere ranging from 50 km to about 600 km (Frederick *et al.*, 2002:3). The region of the Earth's atmosphere where this process takes place is called the ionosphere.

The Earth's atmosphere is subdivided into four regions where RF communication is mostly affected. These regions are known as the D, E, F1 and F2 layers (see Figure 2.9). The electron density of the ionosphere is reduced at night as the D and E layers disappear and the F layer is reduced to a single layer (Bourdillon, 2008).

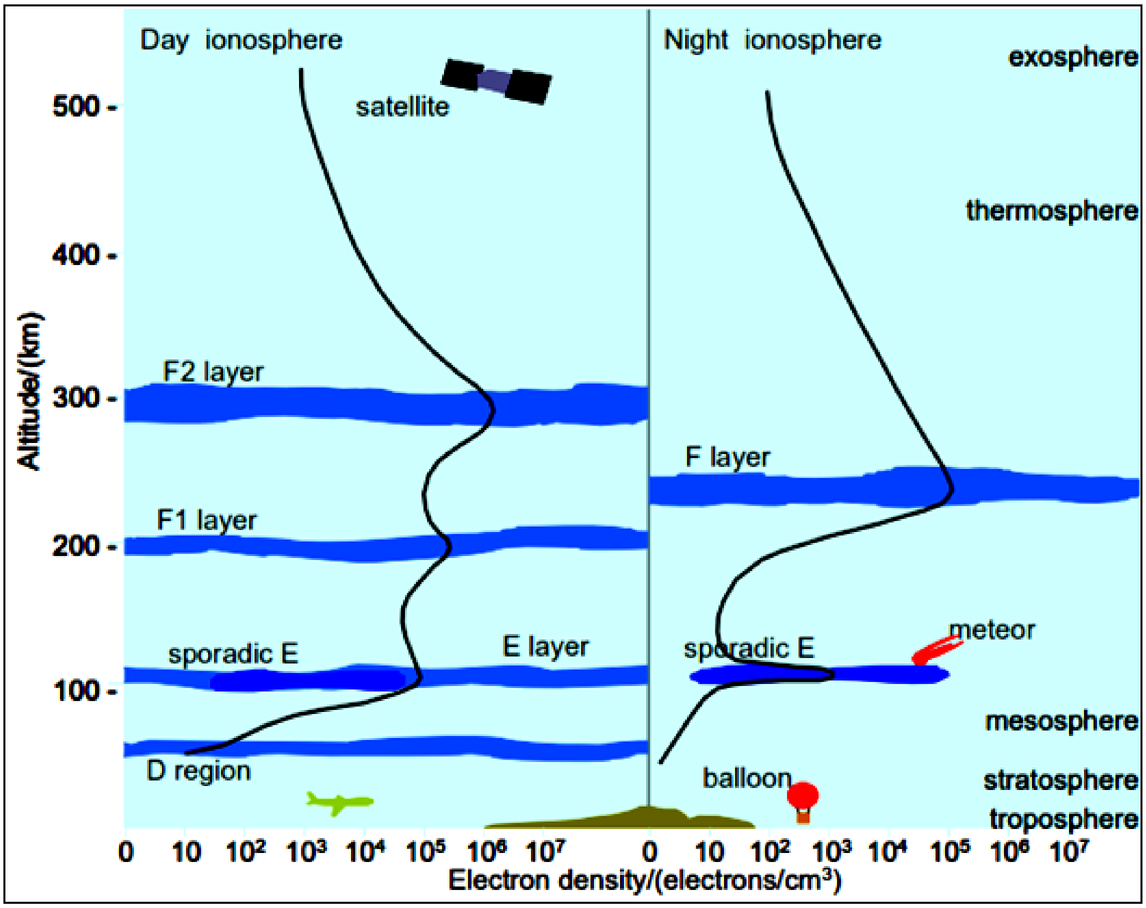

Figure 2.9: Regions of the Earth's atmosphere (Adapted from Australian Goverment, n.d:2)

The ionosphere acts as a screen to radio frequencies. Depending on their frequencies, terrestrial RF signals will be reflected at various altitudes and some will escape the region and propagate in space (Figure 2.10(a)). Seybold (2005) explains that signal frequencies that traverse the ionosphere without being refracted are called maximum usable frequencies (MUF), while the minimum frequencies that are required for propagation in these regions, with a minimum amount of absorption, are known as lower usable frequencies (LUF). For RF signals to traverse the F2 layer, it should be higher than the frequency of oscillating electrons in the F2 layer, which is known as f_oF_2. If the RF signal frequency is lower than the f_oF_2, the corresponding signal will be reflected back to Earth, for vertical incidence.

The refraction index, which determines which RF signals are reflected, depends on the concentration of electrons in the F region (Belehaki *et al.*, 2009). The electron density, therefore, constitutes the primary parameter in ionospheric propagation, and can be measured with an Ionosonde (shown in Figure 2.10(b)), or estimated by using models, such as the IRI (Bilitza & Reinisch, 2008).

The Ionosonde is a scientific instrument that is used to conduct ionospheric research; mainly the measurements of electron density in the F layer by measuring the strength and the delay of the returned signal frequencies (Australian Goverment, n.d.). Figure 2.11 presents a photograph of the Ionosonde at Hermanus, which consists of four cross loop receiving antennas (one of which is presented at the bottom right of the figure), the 30 m HF transmitting antenna (left of the figure), and a transmitter and a receiver module.

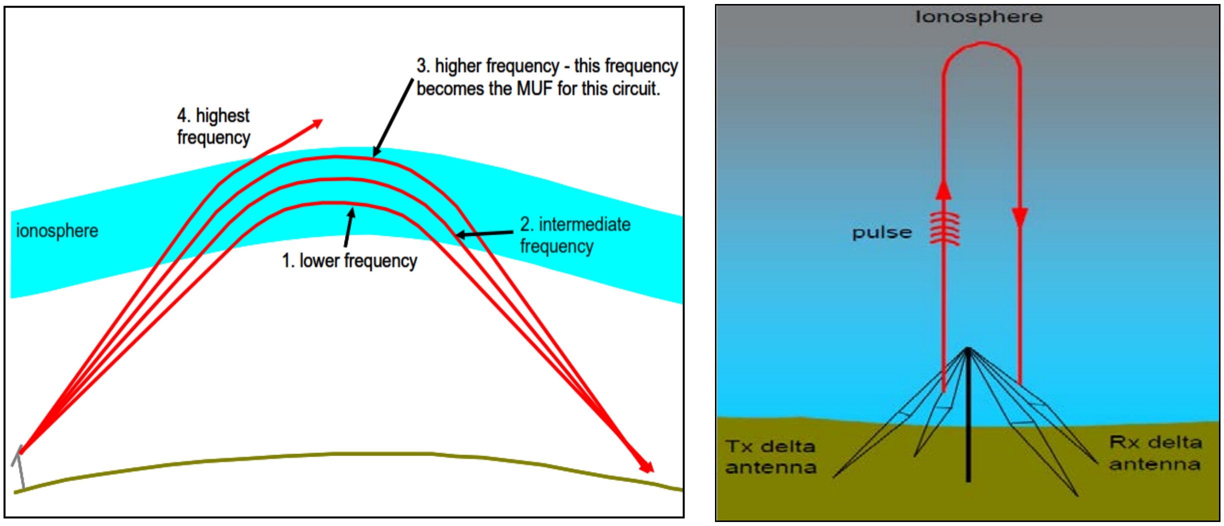

(a) (b)

Figure 2.10: Effect of the ionosphere on HF signal: (a) signals are reflected at various altitudes, (b) multiple pulses are transmitted for ionospheric measurements (Adapted from Australian Government, (n.d.)).

The ionosonde transmits short electromagnetic pulses vertically at different frequencies (0.1 MHz-30 MHz), as shown by Figure 2.10(b), and are reflected at various levels of the ionosphere. Echoes are received from the lower region to the layer below the upper region. The time delay between the transmitted signal and the received echoes provides a means of determining the of a particular electron density of the ionosphere. The frequency of the pulse, determines the electron density at which signal is reflected.

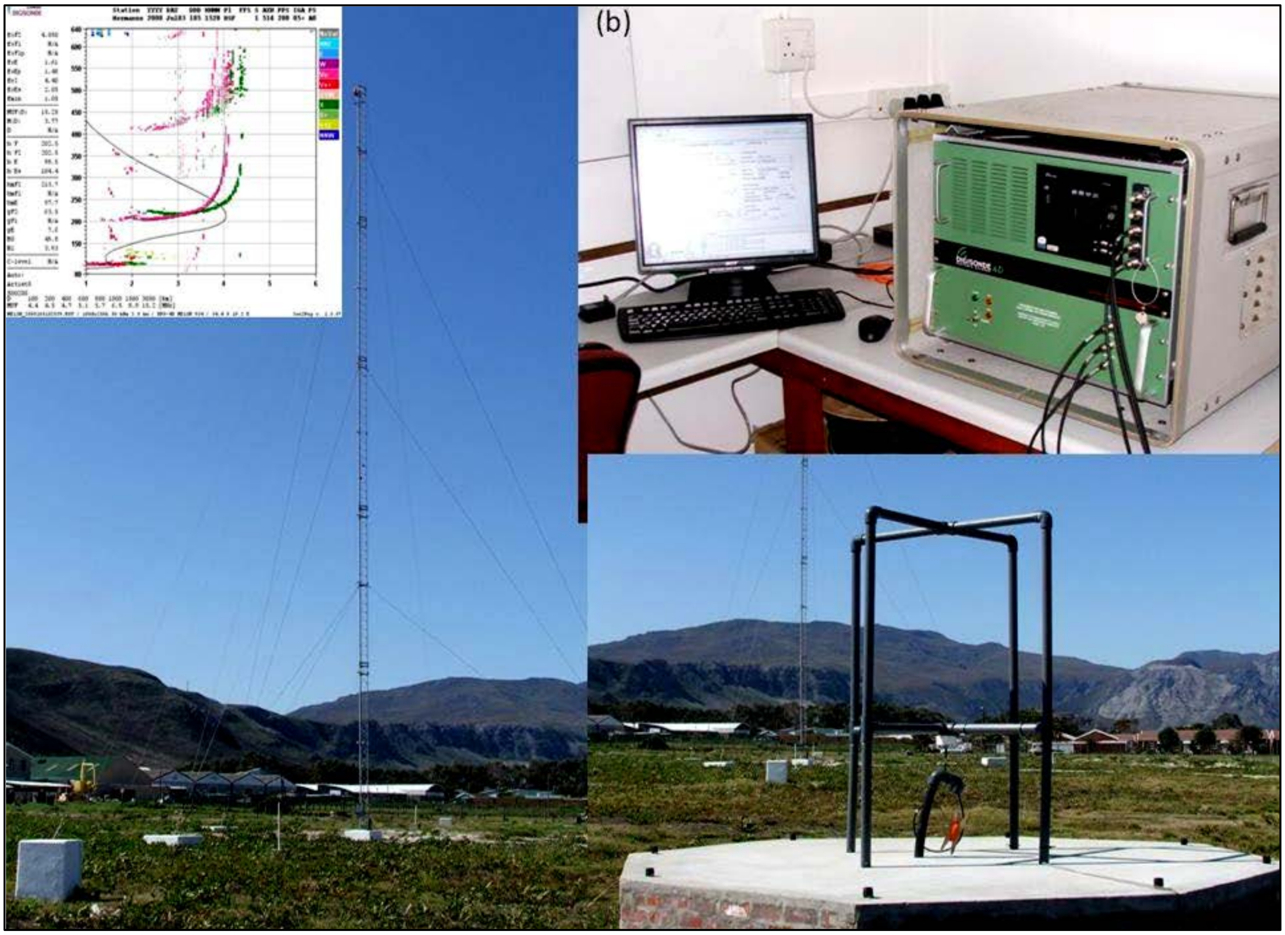

(a) (c)

Figure 2.11: Ionosonde at SANSA Space Science in Hermanus (Adapted from McKinnell, 2008)

2.3.2 Lowest usable frequency (LUF)

Sizun (2003) describes the LUF as being the lowest signal frequency that is received by an HF receiver at a particular time, producing an EMF with acceptable amplitude (Figure 2.10(a)). This perception is valid for ground-to-ground communication only. In the context of the transionospheric HF radio propagation, the LUF is however the lowest frequency that will traverse the ionosphere when the signal is transmitted form the satellite. Radio waves with a frequency lower than the LUF will be reflected from the topside of the ionosphere. For terrestrial (ground-to-ground) HF radio propagation, there is a maximum useful frequency (MUF) which is the highest frequency that would still be reflected from the bottom side of the ionosphere. Radio signal with the frequency above the terrestrial MUF will penetrate the ionosphere and propagate into space. Hence, the LUF for transionospheric radio propagation is equal to the MUF for terrestrial ground-to-ground radio propagation.

For vertical incidence, the MUF is equal to the f_oF_2, the ionospheric critical frequency, for all incidence angle of ψ at the reflection point; hence, relationship between the MUF and the LUF is given by:

$$MUF \text{ (ground-to -ground)} = \frac{f_oF_2}{\cos(\psi)} = LUF \text{ (transionospheric)}$$

For vertical incidence $\psi=0$, and the corresponding elevation angle is $\varepsilon=90°$. For all other elevation angles, ψ is related to ε by equation 2.5.

The evaluation of the LUF may be done by various methods, one of which is the use of the IRI models, which provides a good approximation of the LUF in relation to the altitude and incident angles with which signals reach the ionosphere (Krasheninnikov & Egorov, 2010:268-275). Using peak electron densities over a particular site, one can estimate the LUF during particular times of the day. In addition, this can be verified using empirical models, which provide the 3D electron profile along any trajectory.

Satellite mission designers perform propagation analyses to estimate how the signal will be affected by the ionosphere. These analyses allow not only predicting whether communication between the transmitter and the receiver will indeed take place, and whether this is efficient. If one considers the HF band, not all signal frequencies will traverse the ionosphere. For example, considering communication between the satellite and the ground station, the effect of the ionosphere on the signal is similar to when communicating from the ground station to the satellite. The angle of incidence plays a major role to ionospheric propagation, as it defines the distance that the signal travels in the F region between the satellite and a particular ground station. For instance, the signal reaching the ionosphere at $\psi_i = 90°$ will have the shortest propagation path, compared to the signal reaching the region at $\psi_i = 30°$.

The ionosonde one of the principal means for measuring the bottom side profile of the ionosphere, while the top may only obtained using empirical models (Reinisch & Huang, 2001).

ZACUBE-1 mission will validate the accuracy of these empirical models, since the IRI model will be used to trace the ray from the satellite to ground.

The ionospheric critical frequency (f_oF_2) can be computed from equation 2.1. The critical frequency is a function of the electron density N_e in the ionosphere. The higher the UV flux from the sun, the higher this value becomes. Figure 2.12 illustrates the geometry of terrestrial ionospheric propagation by assuming a spherical Earth where ψ is the signal incident angle at the point of impact with extrapolated reflection point in the ionosphere, and ε the elevation from the launch point on the ground.

Due the reciprocity of transionospheric ray propagation, a signal that traverse the ionosphere follows the same path whether it goes from ground to satellite, or satellite to ground, at the any given satellite location.

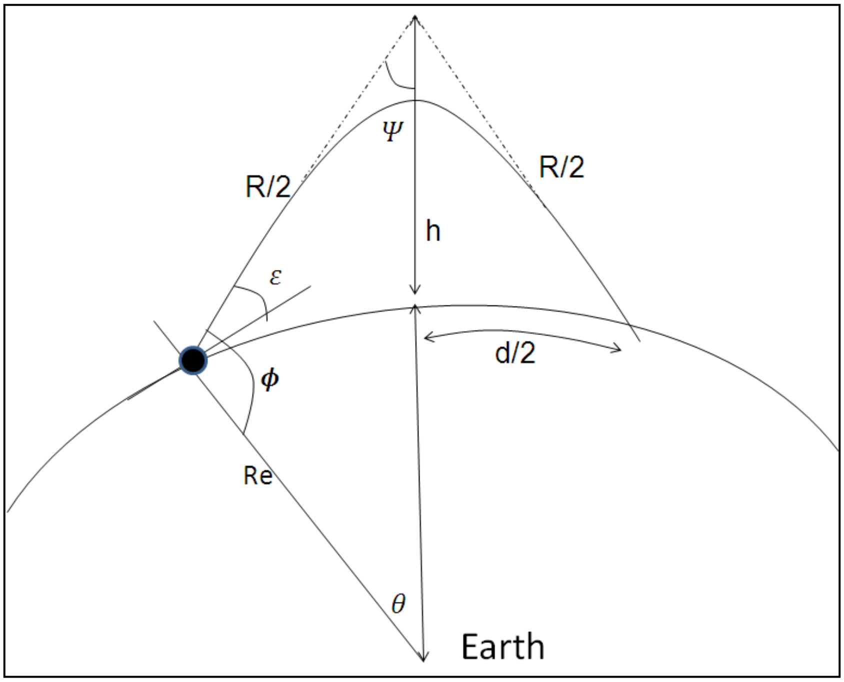

Figure 2.12: Idealised Ionospheric propagation geometry for surface to surface communication using reflection from the ionosphere

Considering ground-to-ground propagation, we define by:

- Ψ the incidence angle of RF signal at the point contact to the ionosphere,
- ε the elevation angle from which signal is launched,
- θ the Earth central angle,
- R_e the Earth radius,

- h the ionospheric reflection height and
- R, the slanted range.

The maximum electron density in the F_2 layer (N_mF_2) is obtained from the ionosonde measurements. It is related to the f_oF_2 peak (the frequency above which a vertically incident signal penetrates the ionosphere and below which it is reflected from it). The relationship between N_mF_2 and f_oF_2 is given in Equation 2.1. It follows that, knowing the N_mF_2; the f_oF_2 can be deduced (Equation 2.2). However, a single parameter such as the f_oF_2 is not sufficient for ray tracing. Therefore, we limited this analysis to the determination of LUF using peak electron densities (N_mF_2), which constitutes the parameter of our interest, as determined from the IRI model.

$$N_mF_2(\mathrm{m}^3) = \frac{1}{80.6}\left(f_oF_2\right)^2 (\mathrm{Hz}), \qquad 2.1$$

From which the critical frequency is

$$f_oF_2 = \left(9\sqrt{N_\mathrm{m}F_2}\right). \qquad 2.2$$

where $N_\mathrm{m}F_2$ is the peak electron density in the ionosphere at a specific location. From the above expressions, the LUF for transionospheric propagation can be computed as

$$LUF = \frac{f_oF_2}{\cos(\psi)}, \qquad 2.3$$

By the sine rule;

$$\frac{\sin\psi}{R_e} = \frac{\sin\Phi}{R_e + h} = \frac{\sin(90° + \varepsilon)}{R_e + h} = \frac{\cos\varepsilon}{R_e + h} \qquad 2.4$$

Hence:

$$\psi = \sin^{-1}\left(\frac{\mathrm{R_e}}{\mathrm{R_e + h}}\cos(\varepsilon)\right) \qquad 2.5$$

2.3.3 Satellite link budget

A link analysis takes into account all communication parameters, and can thus be defined as an account of all the gains and losses in a transmission system. Figure 2.13 illustrates a typical communication system; where T_x and R_x represent the transmitter and the receiver, respectively. The distance between the two modules is *r.*

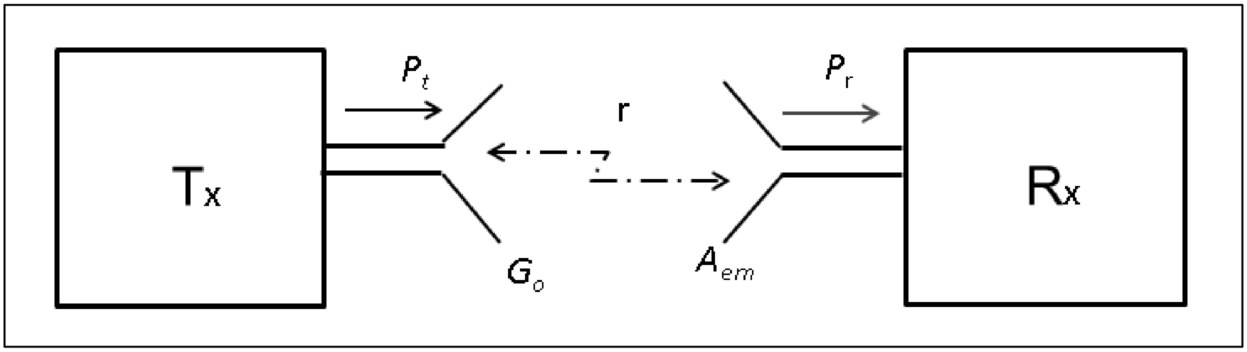

Figure 2.13: Schematic description of the communication system

The Friis transmission equation below gives a general form of the link budget equation, where the reflection coefficients and efficiencies are all accounted for (Balanis, 2005:95):

$$P_r = e_{cdr} e_{cdt} \left(1 - |\Gamma_t|^2\right)\left(1 - |\Gamma_r|^2\right)\left[\frac{\lambda}{(4\pi R)}\right]^2 D_r D_t P_t \cos^2\theta \qquad 2.6$$

where:

- P_r is power received at by the receiving antenna;
- P_t is the power delivered by the transmit antenna;
- D_r is the directivity of the receiving antenna;
- D_t is the directivity of the transmit antenna;
- e_{cdr} is the receiver's efficiency;
- e_{cdt} is the transmitter's efficiency;
- θ is the polarisation angle difference between the transmitter and the receiver antennas;;
- Γ_r is the reflection coefficient of the receiver; and
- Γ_t is the transmitter's reflection coefficient.

Assuming that the antennas are both impedance matched (the satellite antenna matched to the transmitter and the ground station's antenna to the receiver), their reflection coefficients are unity, Equation 2.6 reduces to Equation 2.7:

$$P_r = \frac{e_{cdr} e_{cdt} \lambda^2 D_r D_t P_t}{(4\pi R)^2} \cos^2\theta . \qquad 2.7$$

If we assume a match between the polarisation of the impinging wave and that of the antenna, we get the power ratio of equation 2.8, where the antennas' gains G are related to their directivity D and efficiency by $G = eD$,

$$\frac{P_\mathrm{r}}{P_\mathrm{t}} = G_\mathrm{r} G_\mathrm{t} \left(\frac{\lambda}{4\pi R} \right)^2 \frac{1}{extra\_loss} . \qquad 2.8$$

Equation 2.8 can be converted to decibel units, where P_{loss} takes into account all the losses in the communication system. According to Louis & Ippolito (2008:53), considering the effective isotropic radiated power (EIRP), which characterises the figure of merit of the transmitter, the required received power then becomes:

$$P_{\mathrm{r(dB)}} = EIRP + G_{\mathrm{r(dB)}} - L_{FS(dB)} - extra\_loss \ . \qquad 2.9$$

with $EIRP_{\mathrm{dB}} = P_{\mathrm{t(dB)}} + G_{\mathrm{t(dB)}}$ and $L_{FS(dB)}$ is the free space loss.

2.4 Satellite orbits

Orbital analyses are fundamental to any satellite mission. The determination of the orbital elements is, therefore, a primary step to any hardware development. In this document, the geocentric equatorial coordinate system was used as reference coordinate system to determine the orbital parameters. This coordinate system is aligned with the Earth's axis of rotation and the equator; in which the z-axis points to the north and the x-y plane forms the equatorial plane, as shown in Figure 2.14 (Montenbruck & Eberhard, 2001:25).

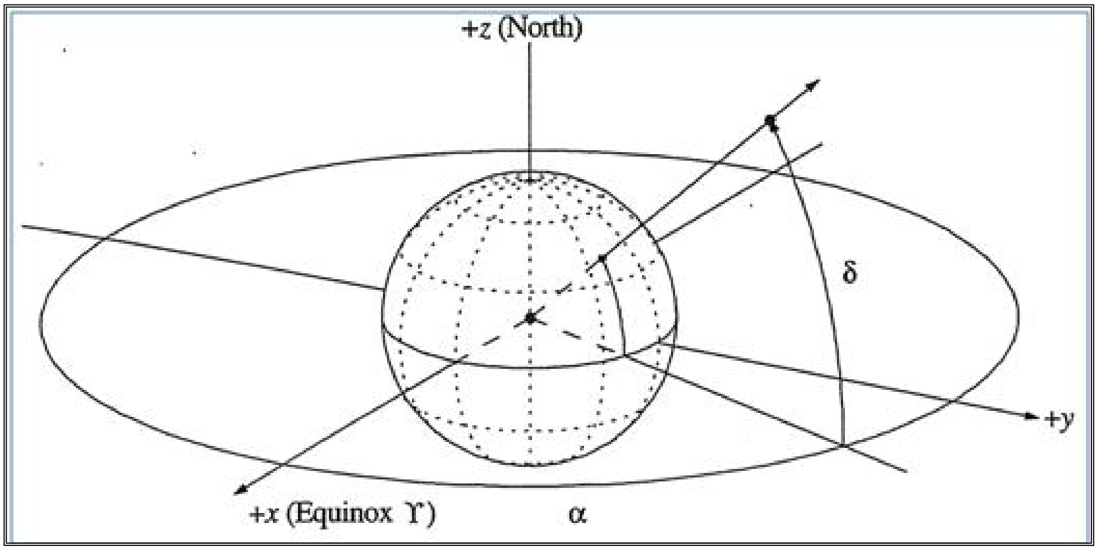

Figure 2.14: Equatorial co-ordinate systems (Adapted from Montenbruck & Eberhard, 2001)

2.4.1 Kepler's laws

It is necessary to acknowledge the work of some scientists whose research has led to findings that have been useful to space science. Johannes Kepler discovered the law of orbital motion, based on observations of the night sky and by using foundations laid by many others, including Tycho Brahe (Van Helden, 2005). Kepler's work was useful to Isaac Newton by assisting in the formulation of the universal law of gravity (Anniina, 2000). Kepler formulated three laws, which form the foundations of astronomy; these are known as Kepler's laws. These laws are briefly stated below (Capderou, 2004).

Kepler's first law states that the orbits are all ellipses and the Sun is at one focus (Figure 2.15(a)). The elliptical orbit follows from the initial conditions. Using the conservation of mechanical energy, the semi-major axis can be found. This defines how elliptic an orbit is.

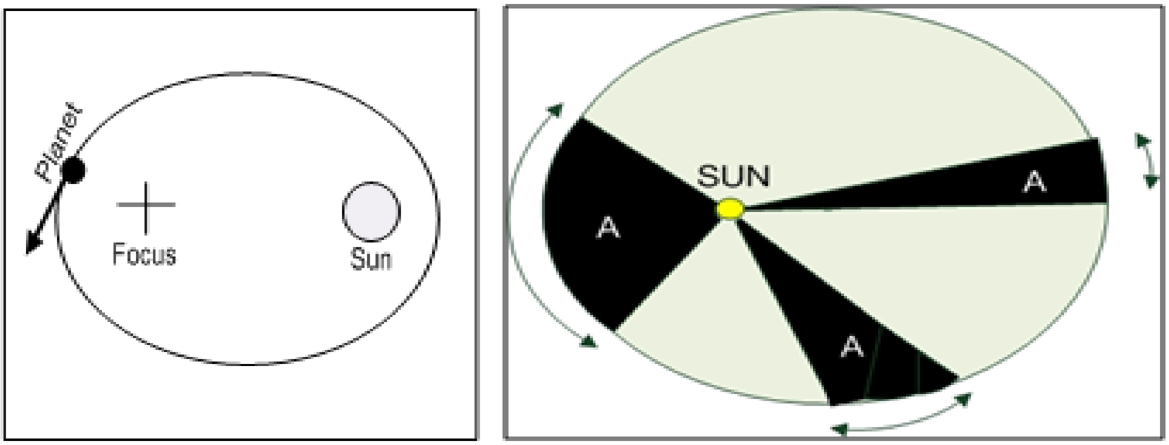

(a) (b)

Figure 2.15: Graphical representation of Kepler's laws: (a) first law, (b) second law

Kepler's second law states that the line joining the Earth to the Sun sweeps out equal areas in equal times as the Earth travels around the ellipse (Figure 2.15(b)). The same concept is applied to any two-body problem. When a satellite is far away from the Earth (at the apogee point), it seems to travel at a reduced velocity, compared to when it is close to the Earth (at the perigee). Thus, a satellite will orbit faster at the perigee than when it is at the apogee (Louis & Ippolito, 2008:27-28).

Kepler's third law states that the square of the orbital period (*P*) of a planet is directly proportional to the cube of half the ellipse major axis. However, the determination of *P* of any moving satellite is possible by combining Kepler's second and third law, while the orbital eccentricity can be found and the perigee distance can be determined by using the conservation of angular momentum (Ravindran, 2009:1-3).

2.4.2 Types of satellite orbits

Orbits are classified according to their altitudes, inclinations and eccentricities. The following sections describe these classifications.

2.4.2.1 Altitude of the orbit

Orbits can be classified according to their distances from the Earth. In such classification, we have:

- *LEO satellites*: These are satellites whose altitudes are less than 1000 km above the Earth's surface. Satellites in this orbit will take about 100 minutes to revolve around the Earth completely, with shorter overpass times. These satellites experience low radio propagation delay because of less distance travelled by the signal. Less propagation losses due to path is required so that less power is required from the communication subsystem. Many remote sensing and weather satellites are launched into LEO.

- *MEO satellites*: These are satellites that orbit the Earth between 1000 km and 20 000 km. They have an orbital period *P* of about 12 hours, longer overpass times and their transmission propagation delays are much greater than for LEO satellites.

- *GEO satellites*: Geostationary satellites are those whose altitude is about 36 000 km. The orbital motion of geostationary satellites are prograde (a satellite with prograde motion rotates in the same direction as the Earth), while their *P* is the same as the Earth's. Consequently, these satellites seem to be stationary when their orbital plane is equatorial and circular. This orbit is suitable for large communication satellites, as the Earth station will always be in view of the spacecraft (Anil & Varsha, 2007:61-66).

2.4.2.2 Inclination of the orbit

The satellite inclination, in contrast to the altitude, is the parameter that determines the orientation of an orbital plane. Depending on the inclination, an orbit can either be inclined, polar or equatorial.

An orbit is said to be inclined when the orbital plane is between 0^o and180^o, while polar and near polar orbits also fall in this category. Satellites in polar or near polar orbits will always pass over the poles or near the poles, respectively. A satellite occupying an inclination of 0° is said to be in a non-inclined orbit, which is commonly known as equatorial orbit (Antonio, 2001).

2.4.2.3 Eccentricity of the orbit

The eccentricity is the orbital parameter that determines the geometry of an orbit. An orbit can be circular, elliptical, parabolic or hyperbolic. An orbit is said to be circular if its eccentricity is 0. It is said to be elliptical if its eccentricity is less than unity. An orbit is parabolic if its eccentricity is equal to unity, while it is hyperbolic if its eccentricity is greater than unity (Louis & Ippolito, 2008). All orbital geometries are derived from conic sections. Figure 2.16 shows the relation between various orbital geometries.

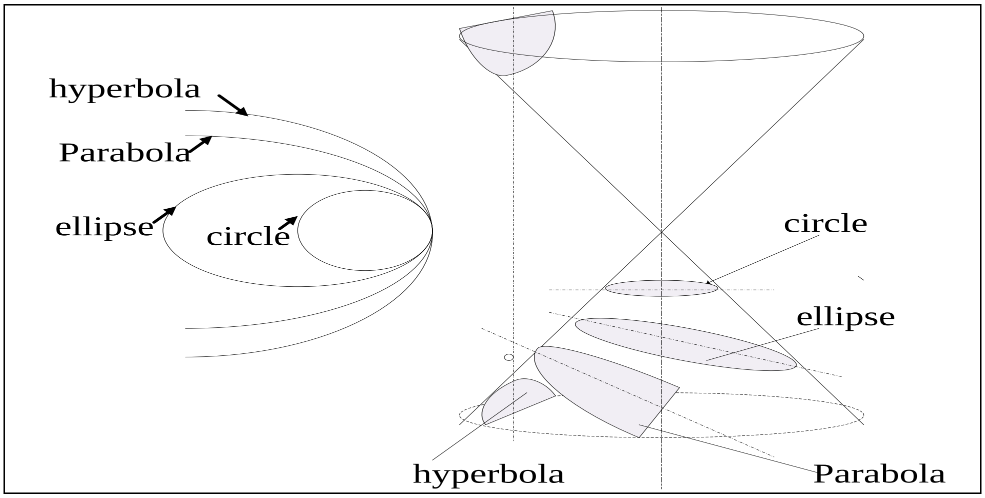

Figure 2.16: The geometry from which orbits are derived (Jane *et al.*, 1999)

2.4.2.4 Sun-synchronous orbit

Sun-synchronous orbits (SSOs) are near polar orbits with inclinations between 96° and 102° (Boain, 2004). It is a special case of inclined orbits in which the orbital plane is fixed around the node of axis (ascending node and descending node). Thus, the satellite rotation is synchronised with that of the Earth. This orbit if preferred for scientific purposes, as it has characteristics that may suit scientific missions. These characteristics are:

- Global coverage in all latitudes;
- Same sunlight conditions throughout mission's life time; and
- Same revisited time every day.

2.5 Field-of-view analyses

The FOV of a satellite is the area that is visible to the satellite at any given time. The height above the Earth's surface plays an important role in the analyses of the spacecraft's field-of-view, as it defines the variation of the coverage angle (Anil & Varsha, 2007:115). As a result, the coverage area increases as the satellite elevation increases at a given altitude. The radar FOV, however, is the area that can be scanned by the radar at any given time.

2.6 Summary

This chapter presented a review of literature and some technical aspects of missions. Orbital parameters were introduced, including the various orbital classifications. The SuperDARN was discussed with a particular focus on the SANAE IV antenna array. A study of ionospheric propagation that entails the understanding of the ionosphere, and parameters that affect the propagation of HF signals through it, was conducted. Finally, various parameters that play an important role in determining the link between two communication systems were described. The following chapter considers specific aspects of the mission's design and analyses relevant to ZACUBE-1.

3.1 Introduction

The ZACUBE-1 mission concept is depicted in Figure 3.1. The types of radio links between the ground stations and satellite are illustrated. The mission architecture was developed from this concept.

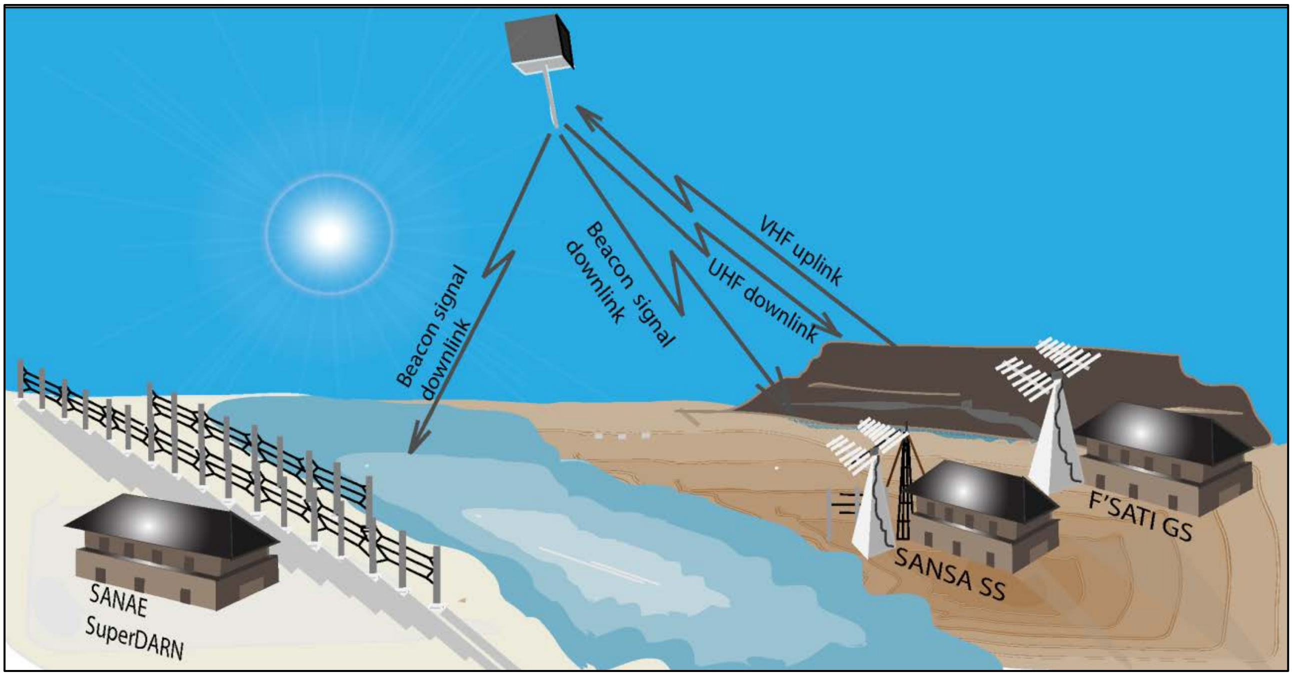

Figure 3.1: Representation of the mission concept

3.2 Mission architecture

The components of the mission architecture are listed and described below:

- The space segment;
- The ground segment;
- The mission target (SANAE Antenna array, SANSA antennas and the ionosphere); and
- The launch system.

Figure 3.2 depicts these components. The target in this case is the radar itself.

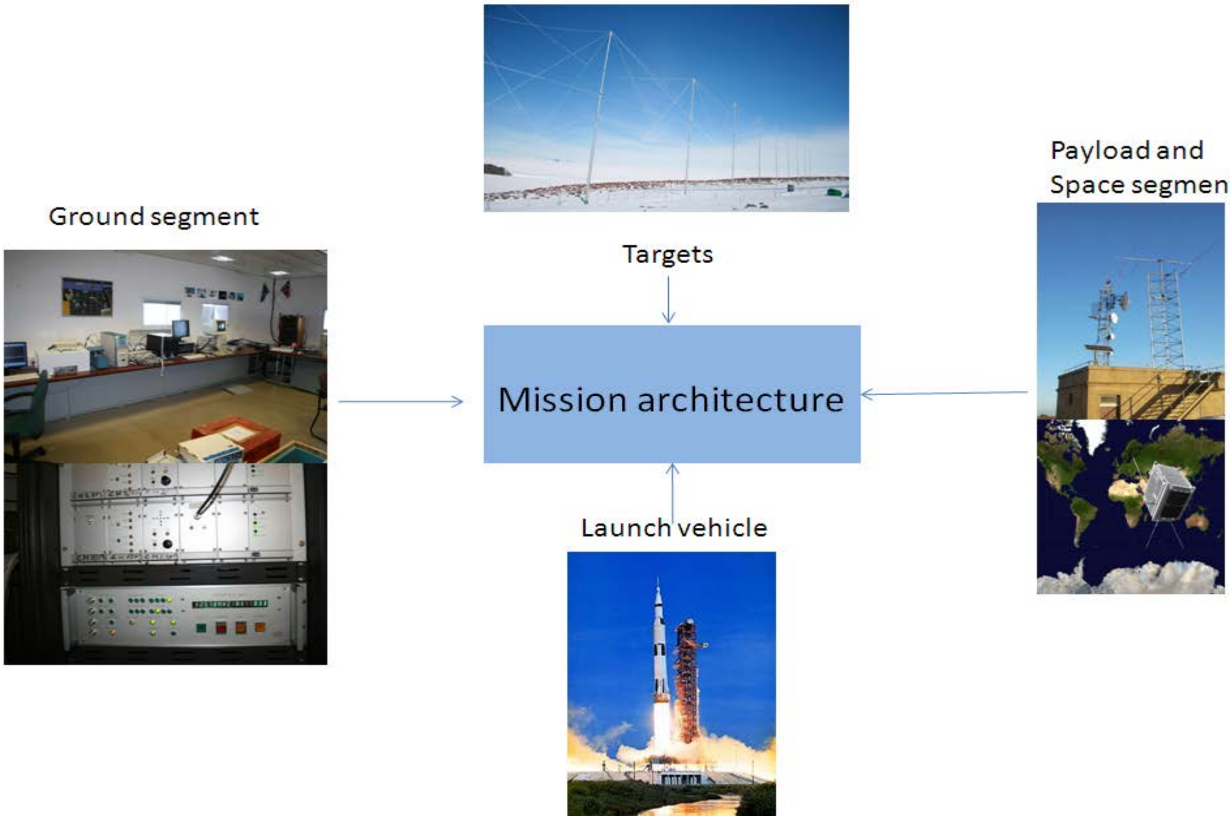

Figure 3.2: ZACUBE-1 mission architecture

3.2.1 Space segment

The satellite is equipped with UHF and VHF radios for the uplink and downlink, respectively. The UHF operates at 437.345 MHz, while the VHF operates at 145.86 MHz. The payload in turn operates at 14.099 MHz. Facilities were installed at CPUT to track the satellite and to upload the commands via UHF/VHF

3.2.1.1 Orbital design

The preliminary orbital parameters were determined to evaluate the feasibility of the space mission in various perspectives. In this section, the orbital parameters that were used to propagation the orbits are described. These parameters were useful for the satellite coverage analyses. Equation 3.1 gives the inclination i of the orbital plane from a given launch latitude (Anil & Varsha, 2007:44):

$$i = \cos^{-1}(\sin A_z . \cos l). \qquad \mathbf{3.1}$$

Where l is the latitude at the injection point, and A_z is the angle between the projected satellite's velocity vector on the equatorial plane and local North. It is observed from the above equation that the inclination depends primarily on the launch latitude, which is determined by a selected LV. Few parameters were thus assumed prior to this analysis; firstly, the orbit geometry was assumed to be circular, thus the eccentricity is zero. Secondly, a range of inclinations was selected as shown in Table 3.1.

Table 3.1: Initial orbital parameters

Altitude	Inclinations	Eccentricity (circular orbit)
600km	60°-102°	0

The semi-major axis can be determined from Equation 3.2. However, with the eccentricity being zero, the semi-major axis is equal to the orbital radius (Maral, Bousquet & Sun, 2009):

$$r = a\,(1 - e.\cos E). \qquad 3.2$$

Where:

- E is the eccentric anomaly of the orbit;
- e is the eccentricity of the ellipse;
- r is the orbital radius; and
- a is the semi-major axis.

E is the angular quantity that defines the position of a moving body along the ellipse. The period P of a satellite can be found (if the semi-major axis, a, is known) by using Equation 3.3 (Maral *et al.*, 2009:19-26), (Anil & Varsha, 2007:38), (Ippolito, 2008:21).

$$P = \left[\sqrt{\frac{4\pi^2 a^3}{\mu}}\right] \times \frac{1}{60} = 96.53\,\text{min}. \qquad 3.3$$

with

$$\mu = (M + m)\,G. \qquad 3.4$$

Where:

- μ is the Kepler's constant = 3.986004×10^{14} (km^3/s^2) with m neglected if $m<<M$;
- M is the Earth's mass (5.9742x10^{24} kg);
- a is the semi major axis of the orbit (6971.14km)
- m is the satellite mass (1 kg); and
- g is the Earth's gravitational constant (9.78 m s^{-2}).

Equation 3.5 shows the relationship between the eccentricity, e, and the semi-major axis,

$$c = ae \;\therefore \mathrm{c} = 0 \tag{3.5}$$

where c represents the distance from the focal point to the centre of the ellipse. The apogee distance pd and the perigee pd distance can both be calculated by using Equation 3.6 and Equation 3.7, respectively (Anil & Varsha, 2007:40):

$$pd = a - c, \tag{3.6}$$

$$ad = a + c. \tag{3.7}$$

Note that for a circular orbit, both the apogee and perigee distances are equal to the semi-major axis. The semi-major axis is related to the Earth's radius, R_e, and height above the ground of the satellite, H:

$$a = (R_e + H). \tag{3.8}$$

The mean motion, or the average angular velocity n, is determined with Equation 3.9. This quantity represents the number of satellite orbits per one Earth's revolution. The orbital mean motion allows one to determine the overall number of satellite orbits per day. If this quantity is expressed in rad/s, Equation 3.10 gives the equivalent in orbits/day (Capderou, 2004:14):

$$n \;\; (rad/s) = \sqrt{\frac{\mu}{a^3}}. \tag{3.9}$$

$$n = \frac{\tau}{P} = \frac{86400}{96.53 \times 60} = 14.917 \text{ orbits/day.} \tag{3.10}$$

Where τ is one earth revolution (24 h = 86400 s).

A total of 5400 orbits per year is therefore expected. The satellite velocity v is obtained as follows (Capderou, 2004:13):

$$v(\text{km/s}) = \frac{1}{1000}\sqrt{\frac{\mu}{a}} = \frac{1}{1000}\sqrt{3.986004 \times \frac{10^{14}}{6971000.14}} = 7.561 \text{ km/s.} \qquad 3.11$$

Table 3.2 presents a relationship between different orbital altitudes and the orbital parameters for a LEO circular orbit.

Table 3.2: Relationships between various LEO parameters

LEO circular orbit parameters			
Orbital altitude [km]	**Velocity [km/s]**	**Period [min]**	**Mean motion [orbits/day]**
200	7.78	88.45	16.27
300	7.72	90.48	15.91
400	7.66	92.52	15.56
500	7.61	94.58	15.22
600	7.55	96.65	14.89
700	7.50	98.73	14.58
800	7.45	100.83	14.28
900	7.40	102.94	13.98
1000	7.35	105.07	13.70
1100	7.30	107.22	13.43
1200	7.25	109.38	13.16
1300	7.20	111.55	12.90
1400	7.16	113.73	12.66
1500	7.11	115.93	12.42

The velocity of the satellite, as seen by an observer on the ground, can be computed once the satellite period is known. This parameter is often referred to as the satellite ground track velocity and is given by Equation 3.12:

$$v_g(\text{km/s}) = \frac{2\pi}{60} \times \frac{R_e}{P}, \qquad 3.12$$

$$v_g = 6.912 \text{ km/s}.$$

The coverage radius is calculated from Equation 3.13:

$$R_c = \left(\frac{\lambda}{360}\right) 2\pi R_e, \qquad 3.13$$

With,

$$\lambda\,(\text{deg}) = \cos^{-1}\left(\frac{R_e}{R_e + H}\right). \tag{3.14}$$

Where H is the orbital height

This gives

$$R_c = 2662.693\ \text{km}.$$

The total overpass time, OP, is the time that the satellite is visible by the ground station. This may be deduced from Equation 3.3 and Equation 3.13:

$$OP = P\frac{R_c}{\pi R_e} = 12.842\ \text{min}. \tag{3.15}$$

The summary of the preliminary orbital parameters are presented in Table 3.3. These parameters may be correlated with those found in Table 3.2 for the same altitude.

Table 3.3: The satellite motion in orbit

Altitude	Semi-major axis	Eccentricity	Period	Orbital mean motion	Satellite velocity	Ground track velocity	Overpass time
600km	6971.14km	0	96.53min	14.917 orbits/day	7. 561km/s	6.912km/s	12.842min

Considering the above altitude, the satellite is subjected to different forces that could place it out of orbit. Some of these are the atmospheric drag and solar radiation. Since ZACUBE-1 does not have means for orbital correction, an analysis was done to verify how long the satellite will take before it deorbits. The model used for the orbital propagation and the perturbation analysis was a two-body propagator. Table 3.4 presents parameters used for the evaluation of the ZACUBE-1 decay process. This analysis was done in satellite tool kits (STK) and the drag coefficient and the solar radiation coefficient are computed as a function of the satellite side area, which is exposed to these forces at any given time.

Table 3.4: Satellite decay parameters

Solar radiation coefficient	Drag coefficient	Satellite mass	Area of each side
1	2.2	1.3 kg	100 cm^2

It is evident that from Figure 3.3 that the orbital altitude gradually decays until the orbital eccentricity becomes unstable (the apogee altitude becomes different from the perigee's), leading to it falling into the atmosphere after about 25 years.

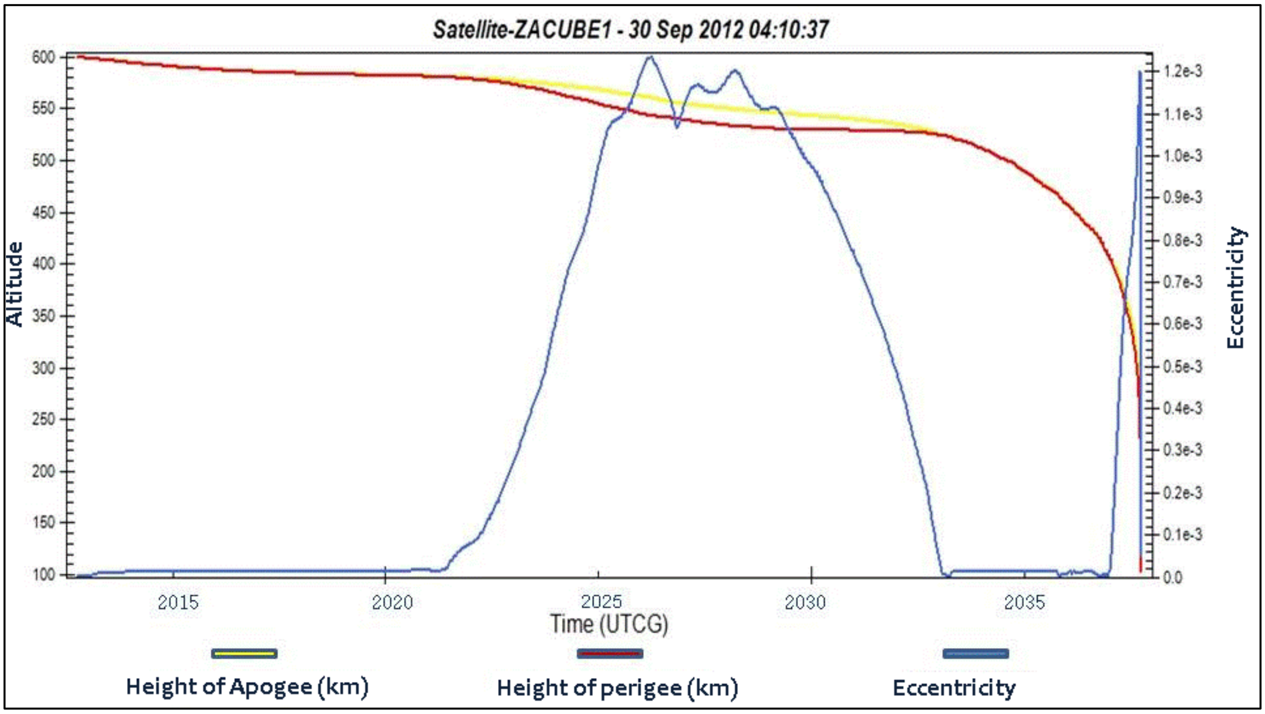

Figure 3.3: ZACUBE-1 orbital decay analysis

3.2.1.2 Satellite bus

Figure 3.4 shows the spacecraft's bus architecture. The architecture that was adopted for the mission was a distributed bus architecture, owing to its advantages elaborated on in Section 2.2.7.2. ZACUBE-1 features the following subsystems:

- The ADCS comprises a magnetometer and gyroscope sensors.
- The radio beacon having a novel antenna deployment mechanism.
- An EPS Clyde Space with Li-Po 1.25Ah batteries. The batteries are 28% efficient and capable of delivering 1 (one) W.
- The VHF/UHF communication having 9600 baud GMSK and 1200 baud AFSK, dual tone multiple frequency (DTMF) modem.
- The OBC is a Pumpkin product with an MSP430 micro-controller.

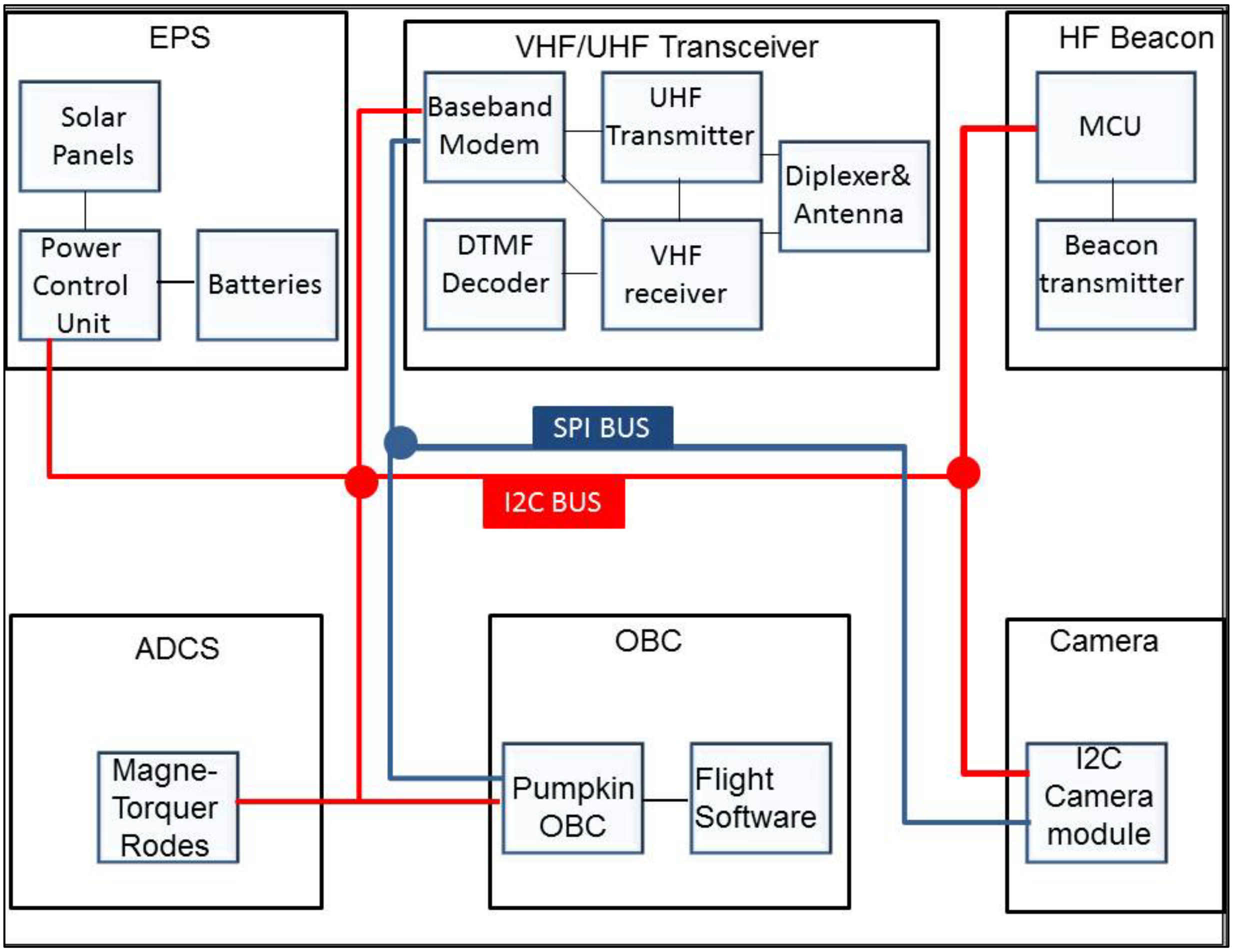

Figure 3.4: Distributed bus architecture of ZACUBE-1

3.2.1.3 Payload

The payloads on F'SATI CubeSats comprise a scientific payload and an imager payload. The scientific payload is the HF beacon. Figure 3.5(a) presents the spacecraft structure and the configuration of different elements on the spacecraft that are numbered as follows:

(1) The CubeSat height with solar panel on each sides;
(2) The CubeSat length and width, yielding a total volume of 1350 cm^3, which is enough to accommodate the electrical power subsystem, the on-board computer, the camera and the beacon transmitter subsystem;
(3) VHF/UHF antennas used for telemetry and tele-commands;
(4) HF Beacon transmitter antenna;
(5) Camera.

The complete satellite (flight model) is depicted in Figure 3.5(b), showing deployable antenna, the remove before flight pin and camera.

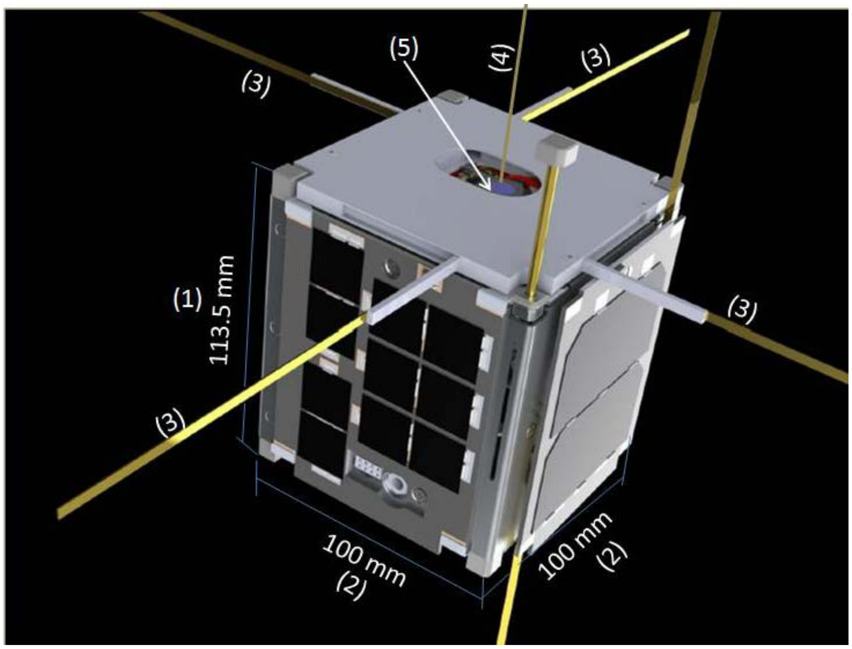

(a)

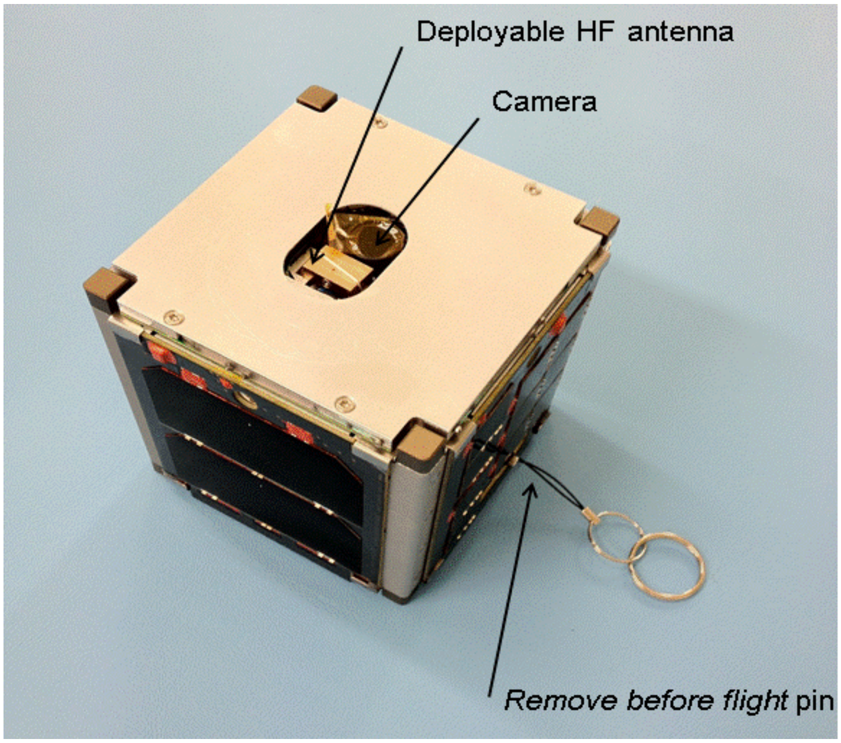

(b)

Figure 3.5: ZACUBE-1 satellite: a) structure and antenna configuration, b) flight model

Table 3.5 presents the HF beacon transmitter and the receiving antenna array parameters obtained from the ZACUBE-1 chief engineer, from which the communication link margin was computed.

Table 3.5: Beacon transmitter and receiver antenna parameters

Parameter	**Value**
Orbit height, H [km]	600
Beacon frequency, f [MHz]	14.099
Satellite transmit power, P_t [mW]	100
Transmit gain at boresight [dB]	0
Feedline and antenna mismatch loss [dB]	2
Antenna gain uncertainty loss [dB]	1
Polarisation loss [dB]	3
Diverse loss [dB]	0.5
Modulation	BPSK
Spectral efficiency [bits/s/Hz]	0.50
E_b/N_o desired [dB]	13.5
Transmission rate, R_b [bit/s]	60
Receiver antenna noise temperature, T_{ant} [K]	3×10^5
Receiver noise figure, NF [dB] worst case	17
GS R_X antenna gain, G_r [dBi]	0
Elevation angle, ε [°]	0

The transmit path loss can be computed from the given specifications by using Equation 3.16 (Louis & Ippolito, 2008:58).

$$L_{\mathrm{FS(dB)}} = 32.5 + 20\log_{10} f + 20\log_{10} R. \qquad 3.16$$

where *f* is the transmit frequency in MHz and *R* is the path length in km. Considering the worst case scenario when the satellite appears at the horizon (the elevation is zero), it follows that the slant range is given by Equation 3.17 in which, *a*, is the semi-major axis and R_e the Earth radius:

$$R = R_e\sqrt{\left(\left(\frac{a}{R_e}\right)^2 - \cos^2\varepsilon\right)} - \sin\varepsilon, \qquad 3.17$$

$$= 6371.14\sqrt{\left(\left(\frac{6971.14}{6371.14}\right)^2 - \cos 0^\circ\right)} - \sin 0^\circ = 2830.8599\ \text{km}.$$

From Equation 3.16 and 3.17 the worst case free space loss at ε=0° elevation is

$$L_{\text{FS(dB)}} = 32.5\text{dB} + 22.98\text{dB} + 69\text{dB} = 124.46\ \text{dB}.$$

Using Equation 2.8, the available signal (see Figure 2.13) power is given as:

$$P_{\text{r\_available(dBm)}} = 20 + 0 + 0 - 124.46 - 6.5 = -110.96\ \ \text{dBm}.$$

Where the extra loss of 6.5 dB is accounted for the polarisation loss, mismatch loss, the antenna uncertainty and diverse loss (see Table 3.5).

Before one can determine the quality of the receiver (figure of merit *M*), it is important to first determine how much the beacon signal will be affected by noise. It is known that the major noise contributor in HF band is the atmospheric noise (ITU, 2007). Using the radio noise graph of Figure 3.6, the antenna noise temperature is 2.9×10^5 K at 14 MHz.

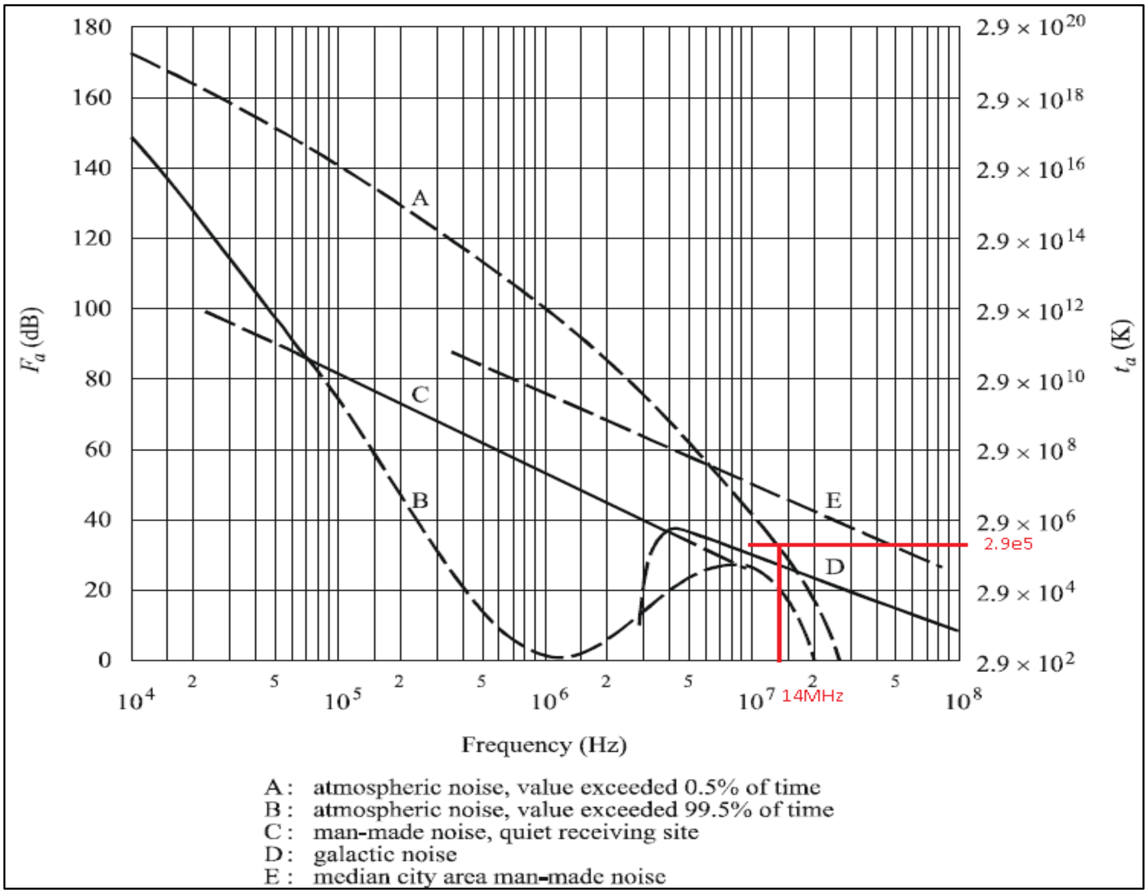

Figure 3.6: ITU antenna noise consideration (ITU, 2007:5)

The antenna's noise temperature is taken to be 3×10^5 K worst case, from which the system noise temperature is computed using Equation 3.18:

$$T_{sys} = T_e + T_{ant} = 290\left(10^{\left(\frac{NF}{10}\right)} - 1\right) + T_{ant}\,. \tag{3.18}$$

which gives

$$T_{sys} = 290\left(10^{\left(\frac{17}{10}\right)} - 1\right) + 2.9 \times 10^5 = 304244.42\text{K} = 54.83 + 30 = 84.83 \text{ dBmK.}$$

It follows that the figure of merit M is

$$M = G_r - T_{sys} = 14 - 54.83 + 30 = -24.83 \text{ dBm.} \tag{3.19}$$

The receiver's system noise power is

$$N_{\text{sys(dB)}} = 10\log_{10}\left(KT_{\text{sys}}\left(\frac{R_{\text{b}}}{spec\_eff}\times 1000\right)\right)+30, \qquad 3.20$$

$$N_{\text{sys(dBm)}} = -10\log_{10}\left(1.38\times 10^{-23}\times 314244.42\times\left(\frac{60^{-3}}{0.5}\times 1000\right)\right)+30 = -122.83\,\text{dBm}.$$

Considering the spectral efficiency (*spec_eff*) and transmission data rate, the receiver's noise bandwidth is

$$B_{\text{noise}} = \frac{R_b\times 1000}{spec\_eff} = \frac{60\times 10^{-6}\times 1000}{0.5} = 20.79\,\text{dBHz}. \qquad 3.21$$

From the above calculated values, the available signal to noise ratio (SNR) may now be computed. It is evident from Equation 3.22 that the system noise is a dominant factor in the entire communication system, due to high antenna noise temperature:

$$SNR = P_{\text{r\_available}} - \text{N}_{\text{noise}} = -110.96 + 22.83 = 11.87\,\text{dB}. \qquad 3.22$$

In order to evaluate the communication link margin, the *energy-per-bit to noise* E_b/N_o needs to be evaluated. This parameter is considered in digital communication as the best way to compare digital and analogue modulation techniques, with respect to their transmission data rate R_b. For HF beacon, the E_b/N_o is calculated as:

$$(E_b/N_o)_{dB} = SNR + B_{\text{noise}} - R_{\text{b}}. \qquad 3.23$$

which gives

$$(E_b/N_o)_{dB} = 1187 + 20.79 - 17.78 = 14.88\ \text{dB}.$$

Assuming a Bit Error Probability (BEP) of 10^{-7}, the desired signal power is evaluated using $E_b/N_o = 13.5\,\text{dB}$, from which the required communication link margin (Equation 3.25) is obtained:

$$P_{\text{r\_desired}} = N_{\text{noise}} + \frac{E_b}{N_o}_{\text{desired}} + \frac{R_b}{B_{\text{noise}}} + 30. \qquad 3.24$$

$$P_{\text{r\_desired}} = -122.83 + 12 - 12.21 - 20.79 + 30 = -112.33\ \text{dBm}.$$

The communication link margin is given by:

$$\text{Link margin} = P_{\text{r\_available}} - P_{\text{r\_desired}} \quad , \tag{3.25}$$

$$\text{Link margin} = -110.96 + 112.33 = 1.37\ \text{dB}.$$

The positive link margin implies that the mission is theoretically feasible on the communication aspect. Since at 0° elevation the communication link is about 1.37 dB, as the satellite rises above the horizon, the slant range reduces, thereby improving the communication link. The slant range is minimum once the satellite reaches 90° elevation giving a maximum link margin.

3.2.1.4 TT&C ground station

The ground station comprises the VHF/UHF antennas and an HF antenna. The software used for controlling the VHF/UHF antenna rotators and the radio is SatPC32 (Eichmann, 2012). The Terminal Node Controller (TNC) used the multimode Radio Amateur software MixW (MixW, (n.d.)). The ground station is also equipped with HF antenna ground support equipment to receive the payload data. The satellite tracking software will be provided to ZACUBE-1 mission operators at SANSA SS and to radar operators at SANAE IV once the satellite is in orbit.

The HF antenna at CPUT is designed to receive the satellite HF beacon, and to enable communication with the radio amateur community. As part of the ground station, the HF antenna is built on the VHF/UHF antenna mast, located on top of the Electrical Engineering building at CPUT Belliville. The selected configuration is an inverted-V dipole. The normal dipole antenna requires more than merely one support to hold the elements. The inverted-V only requires one support, at the apex and at the antenna ends just above the ground. These advantages make the antenna design simpler.

Given the resonant frequency of the antenna (14.099 MHz), the antenna's physical length was computed:

$$L_{\text{ant}}\ (\text{m}) = \frac{c}{4.f\ (\text{MHz})} = 5.32\ \text{m}. \tag{3.26}$$

Where:

- L_{ant} represents the physical length of one antenna element, considering the configuration in Figure 3.7;
- f is the resonant frequency of the antenna,

The total length of the antenna is thus 10.64 m, where each arm length (λ/4) is 5.32 m. Figure 3.7 below shows the antenna configuration.

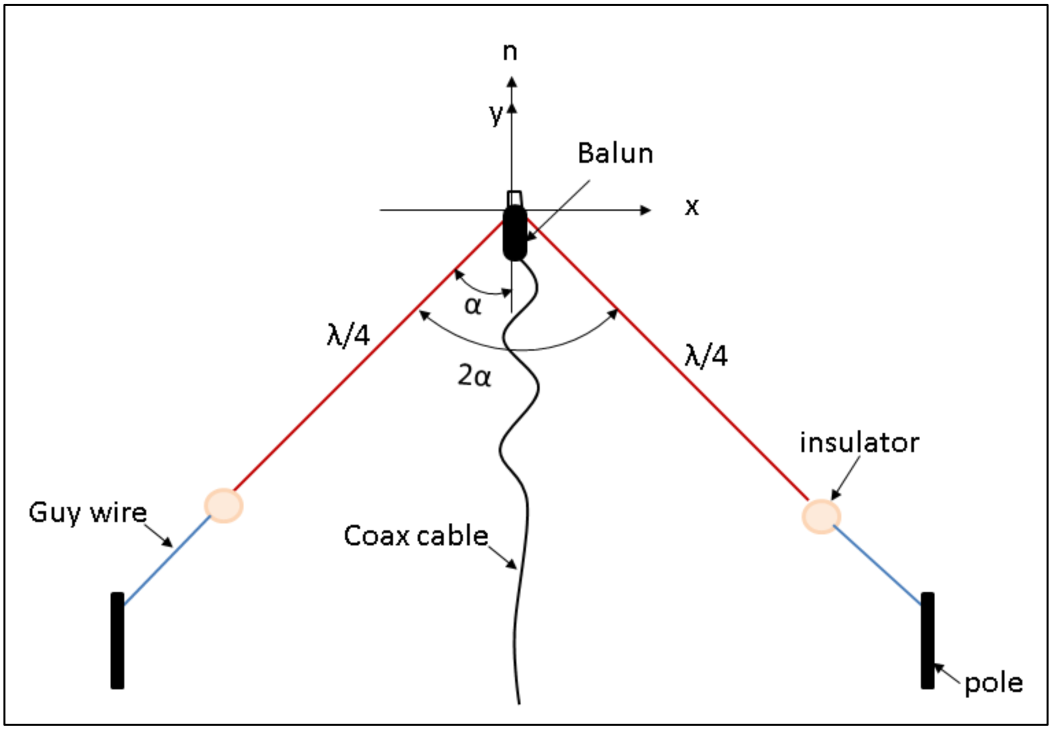

Figure 3.7: Inverted-V dipole representation

3.2.2 Ground segment

The ground segment includes the HF radar arrays at Hermanus and SANAE IV. The latter has been discussed in detail in Section 2.2.2.

3.2.2.1 HF radar array at SANAE IV

Data from ZACUBE satellites will be beneficial on a global scale, thus any of the bases within the SuperDARN that could receive the signal would be able to perform the same measurement as for the SANAE IV radar. The antenna array at SANAE IV is located 72.6667°S, 2.8500°W. It has the following specifications:

- Frequency 8 MHz-20 MHz, 12.5 MHz during normal operation of mode;
- Gain = 20 dBi;
- Maximum transmit power 9600 W; and
- Half power beam width (HPBW) = 3°.

3.2.2.2 HF radar array at SANSA SS in Hermanus

A new antenna array is being developed at SANSA SS, located 34.4204°S, 19.2438°E. This array is built to supplement the TTFD. The array is a seven element L-shape antenna array for finding the direction of the satellite signal. This direction finder (DF) array is being developed because, with the TTFD alone, one cannot determine the elevation angle of the satellite's incoming signal. The array elements are made of crossed square loop antennas whose sides are 1 m long. The implementation of the HF radar array is still under process and does not form part of this research study.

3.2.3 Launch system

The launch facilities comprise of the LV, port operator; assembly and command vehicle, ship or train for spacecraft transportation; launch platform; payload processing; and the launch control centre. The LV selection should be in line with the mission's objectives. Thus, when selecting an LV, a few criteria should be considered, namely the LV's performance in terms of carrying capacity, compatibility (whether it can accommodate the spacecraft), its availability (determined by the launch window), the cost (primary payload or secondary payload) and how reliable the system is (Loftus & Teixeira, 2008:721-725). Some launcher candidates were identified, and missions that were deployed by these launchers are given in Table 3.6. This list is not exhaustive. Conversely, Table 3.7 is a list of a few launch sites; this list is also not exhaustive.

Table 3.6: CubeSat launch vehicles history

Launch Vehicle	Satellite name	Organisation	Launch date	Operational (yes/no)
Delta	AubieSat-1	Auburn University	28/10/2011	Yes
	RAX-2	University of Michigan	28/10/2011	Yes
	Explorer 1	MSUSSEL[5]	28/10/2011	Yes
	MCubed	University of Michigan	28/10/2011	Yes
Dnepr	CP3	California Polytechnic University	17/04/2007	No
	CAPE-1	University of Louisiana	17/04/2007	No
	CP4	California Polytechnic University	17/04/2007	No
Cosmos	CubeSat XI-V	University of Tokyo	27/10/2005	Yes
JAXA M-V	HITSat	Hokkaido Institute of Technology	22/09/2006	No
	Cute-1.7	Tokyo Institute of Technology Matunaga	21/02/2006	No

---

[5] Montana State University Space Science and Engineering Laboratory

Minotaur	RAX	University of Michigan & SRI international	20/11/2010	No
	O/OREOS	NASA Ames & Santa Clara University	20/11/2010	Yes
	NanoSail-D2	NASA & Santa Clara University	20/11/2010	No
	GeneSat-1	N/A	17/04/2006	Yes
PSLV	JUGNU	IIT Kanpur	12/10/2009	Yes
	SwissCube	Ecole Polytechnique Fédéral De Lausanne	23/10/2009	Yes
	ITUpSAT1	Istanbul Teknik Universitesi	23/10/2009	Yes
	UWE-2	University Wurzburg	23/10/2009	Yes
	BEESAT	Technishe Universitat Berlin	23/10/2009	Yes
	Cute-1.7+APD II	Tokyo Institute of Technology	28/04/2008	Yes
	SEEDS II	Nihon University	28/04/2008	Yes
	COMPASS-1	Aachen University of Applies Science	28/04/2008	Yes
Rockot	CanX-1	University of Toronto, SFL	30/06/2003	No
	DTUSat	Technical University of Denmark	30/06/2003	No
	AAU CubeSat	Aalborg University	30/06/2003	No
STS-127	Aggiesat-2	AggieSat Lab at Texas A&M University	30/07/2009	No
	PARADIGM	The University of Texas at Austin	30/07/2009	No

(cubesat, 2013)

Table 3.7: Satellite launch sites

Launch site	Country	latitude	Longitude
Israeli Launch complex	Israel	31.31°N	34.27°E
Plesetsk,	Russia	62.48°N	40.1°E
Baikonur, Cosmodrome	Russia	45.965°N	63.305°E
Sriharikota	India	13°43'22"N	80°9'55"E
Cape Canaveral	USA	28° 24' 21 N,	80° 36' 17 W
Kagoshima	Japan	31.6°N	130.55°E
Korou Launch center	France	5.56°N	52.46°W

The selected LV contractor must meet the mission requirements, which are:

- Final orbit – LEO circular;
- Inclination – 98°;
- Altitude vs. mass – 600 km vs. 1 kg;
- Capable to carry multi-payload;
- Compatible with CubeSats;
- Injection accuracy; and

- Reliability.

Only a few rocket launchers that meet these requirements were identified, according to Table 3.7. These rockets are: Dnepr, Cosmos, Epsilon (from ISAS), PSLV, and Rockot. This list is not exhaustive and requires a more detailed survey.

3.3 Summary

The ZACUBE-1 CubeSat is used as proof-of-concept towards the characterisation of the SuperDARN. The mission architecture and respective ground stations, were presented. Orbital parameters were determined, including the design of the HF payload. The required link margin of the receiver's system was calculated, giving a positive link margin. Finally, a survey of LVs was conducted. From this survey, few LVs and launch sites were identified. In view of these, ZACUBE-1 will be launched from Dombarosky in Russia (Yasny Cosmodrom) by a Dnepr launch vehicle, primarily due to its availability. ZACUBE-1 will be launched alongside 13 other nanosatellites from different countries with a local time of ascending node equal to 10:30 hours. ZACUBE-1 and other nanosatellites are secondary payloads on this launcher, having two main payloads: DubaiSat-2 (<300 kg) and STSat-3 (≈150 kg).

Chapter 4 ZACUBE-1 space weather experiment design and simulation

4.1 Introduction

Chapter 3 introduced the method for orbital design, and presented relevant formulae. This chapter relates the expected orbital inclination to the radar field-of-view. The method for generating the continuous wave (CW) beacon, using an RFID chip, is also presented. Using available space weather data, the variation of the LUF as a function of seasons, location, elevations and time is analysed. Finally, an analyses of the performance of the antenna array at SANAE as well as the on-board deployment HF antenna are also conducted.

4.2 Field-of-view analysis

The NOVA satellite software developed by the Northern Lights Software Association (NLSA, 2011) was used as orbital propagator. The software does not provide options for advanced modelling; thus, the system cannot be modelled in three dimensions. However, one can create a virtual satellite by entering the required orbital elements and the geographic coordinates of ground the station. This was done by entering the coordinates of each operational SuperDARN antenna into the software, and by setting the antenna field of view boundaries (azimuth and the elevation range).

The software outputs a script file that includes three satellite elevations:

- The acquired elevations, which are the elevations when the satellite enters the radar beam;
- The maximum elevations, which are the maximum elevations reached by the satellite in the current orbit; and
- The lost elevations, which are elevations when the satellite exits the radar beam.

From the above sets of elevations, the most important parameter for this analysis is the maximum elevation. The maximum elevation describes how long the GS sees the satellite signal. The acquired and lost elevations describe which way the satellite travels relative to the antenna. Histograms were generated in order to analyse the variation of elevations as a function of the satellite passes. These elevations represent the predicted elevations for a chosen inclination, as seen from SANAE IV and SANSA SS. The software also gives the option of viewing the propagated orbits from three different maps, namely the global map, the rectangular map and the radar map. The global map (Figure 4.2(a)) and the radar map (Figure 4.2(b)) are the most appropriate maps for this analysis. The global map provides details of how the inclinations affect the coverage, while the radar map shows the satellite paths through the radar's field-of-view. These two maps were used to determine the mission's feasibility from the FOV perspective.

Firstly, we considered the two orbital elements that mostly affect the satellite's coverage (the elevation and the altitude) (Anil & Varsha, 2007:115). These parameters impact the communication link as well. At low elevation, for example, the RF signal takes a longer path to propagate through the Earth's atmosphere as compared to high elevation angles. Thus, the signal is more subjected to fading at low elevations than at high elevations, and is season dependant.

The coverage area increases as the altitude increases. At high altitude, for instance a geostationary orbit, the coverage area is about half the Earth's surface area, while in LEO the coverage varies between 1.5% to 7% of the Earth's surface area (Anil & Varsha, 2007:111).

Equation 4.1 gives the relationship between the satellite elevation, the altitude and the angle of coverage, while Equation 4.2 defines the covered area (Anil & Varsha, 2007:110-111). For two different orbits (LEO at 600km and GSO at 35786km), a plot of coverage was generated in order to compare coverage variation between these two orbits. This is presented in Figure 4.1

$$2\alpha = 2\sin^{-1}\left(\left(\frac{R_e}{H+R_e}\right)\cos\varepsilon\right), \qquad 4.1$$

which gives:

$$2\alpha = 2\sin^{-1}\left(\frac{R_e}{H+R_e}\right).$$

When the satellite is at the horizon because the elevation $\varepsilon = 0^{o}$

$$A_C = 2\pi R_e^2\left(\frac{1}{R_e} - \frac{1}{R_e}\sin\alpha^{\circ}\right). \qquad 4.2$$

Where:

A_C = the covered area (m^2),

2α = the coverage angle (deg),

ε = the satellite elevation angle (deg),

R_e = Earth's radius (m),

H = height of the satellite above the Earth's surface.

From Figure 4.1 the legend represents altitudes from LEO to GEO. For each altitude, the covered radius and the covered area is computed. It is evident that a satellite in GEO covers large areas, irrespective of its elevation, but this does not apply to a satellite in LEO. Considering an elevation angle of 10°, the satellite in GEO covers about 10 times surface area than the one in LEO. Although there is enough coverage for a satellite at high altitude, it will require more transmit power to satisfy the requirements of the communication link. To satisfy the mission objectives, we should consider inclinations that will lead to maximum coverage for the selected altitude. This analysis is conducted in the following sections.

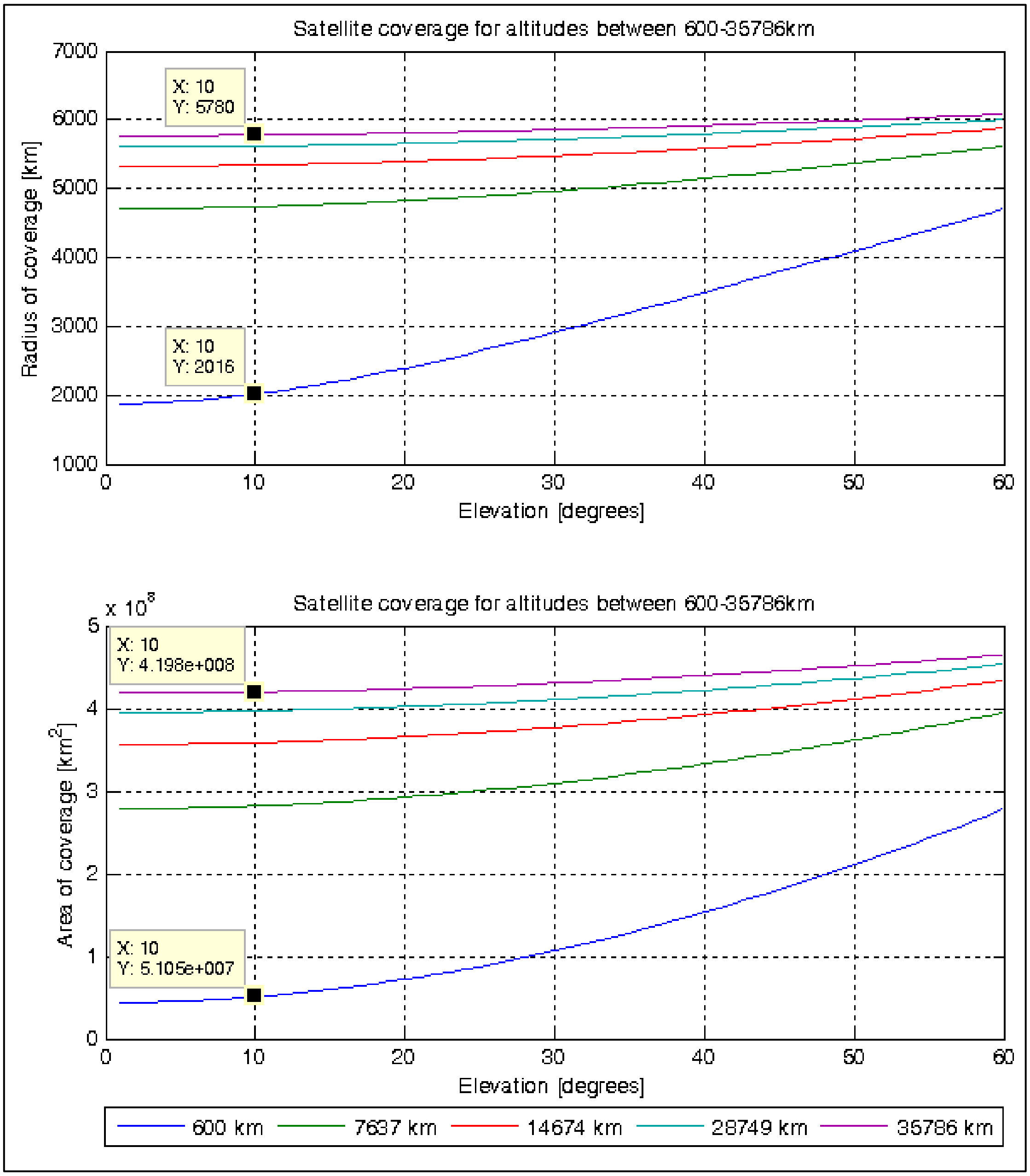

Figure 4.1: The relationship between satellite elevation and the coverage area

4.2.1 Inclination versus coverage for SANAE IV HF antenna

Six different inclination angles are considered in this research to provide a comprehensive idea of what launch opportunities one may seek, once the coverage is known. The selection of the inclination also helps to determine the elevation at which a signal will be received by the antennas. Satellite visibility, based on the inclination criteria, is also considered in more detail. The term ‘blind spot’ in this document refers to the area/zone over which there is no coverage. These areas are located at both poles and they result from a tilt of the orbital plane from the polar axes. The areas are larger for low inclinations and lead to a reduction of the coverage. Before detailing the coverage analyses, we should first define a few concepts that are key to the following sections.

The SANAE IV HF antenna array is situated at 71.68° S 2.85° W, while the antenna's main lobe points in 173.2° azimuth with 52° beam width. Taking the SANAE IV coordinates as the origin of the map with the beam pointing southward, radar maps (Figure 4.2(b)) are obtained in which the different colour lines represent the satellite orbits. The centre of the radar map represents the zenith, and the outer contour represents the horizon. The radar map assumes that the radar detects objects in 360° azimuth. The above assumption is not valid for the SuperDARN, as the detection range is only 52°; therefore, the contour in red on the radar map delimits the FOV. Overpasses enclosed within this FOV should theoretically be visible by the radar. This may not be true practically as obstacles in direct line-of-sight between the satellite and the antenna under test have not been taken into account. An overpass crossing the radar beam between the two crosses (X) on the outer arc in Figure 4.2(b) is considered to be above 3 dB beam width (at maximum power), and it is assumed to be at low power otherwise. The yellow lines on the global map (Figure 4.2(a)) represent the satellite ground tracks, while the south-north white line shows the type of orbit (circular in this case), and also defines in which direction the spacecraft moves relative to Earth (retrograde in this case). The shaded area is the satellite's access point (applicable for satellites that carry radio instruments).

4.2.1.1 Coverage at 90° inclination

By definition, polar orbiting satellites have an inclination equal to 90°. Only satellites that orbit at this inclination will fully achieve global coverage, as stated by Anil and Varsha (2007:114-115). The satellite will always pass over the pole caps (Figure 4.2(a)) and at the same rate if the orbit is circular. This orbit is ideal for polar experimental missions; however, as stated previously in section 2.1, the choice of orbital inclination depends on the selected launch, and not on the mission designer. Therefore, analyses have to be conducted for various inclination angles, to verify whether the satellite will serve its purpose in different orbits. Thus, it is clearly noted that polar orbiting satellites do not experience an orbital tilt (Figure 4.2).

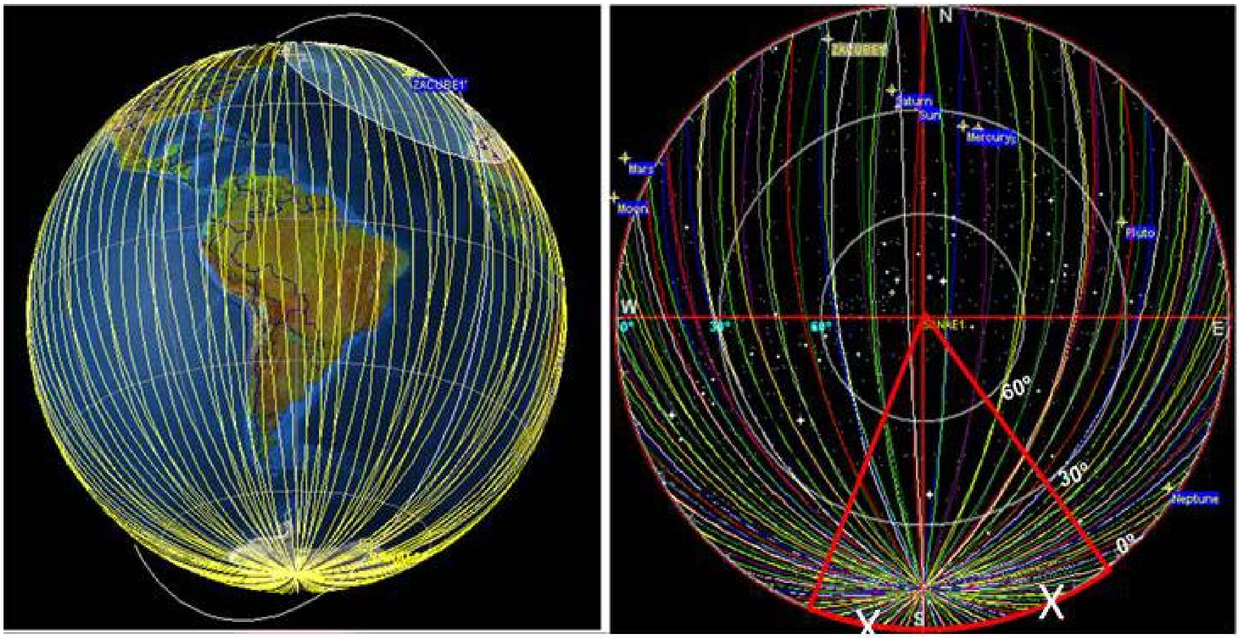

(a) (b)

Figure 4.2: The coverage of a polar orbiting satellite: (a) using a global map, (b) using a radar map with antenna beam pattern pointing south

4.2.1.2 Coverage at 60° inclinations

With 90° inclination, it is shown that the satellite covers the entire Earth; this concept of global coverage becomes impossible if the satellite orbit does not cross at the poles. Figure 4.3 is an illustration of such a case with 60° inclination. The radar map in Figure 4.3(b) presents the effect of low inclination in more detail, as we note that none of the passes intersect the antenna radiation pattern. For example, referring to Figure 4.3(a) for inclinations below 80°, the satellite misses most of the FOV of the radars that are located in Antarctica, and the antenna under test at SANAE IV is invisible to any of the passes at 60° inclination.

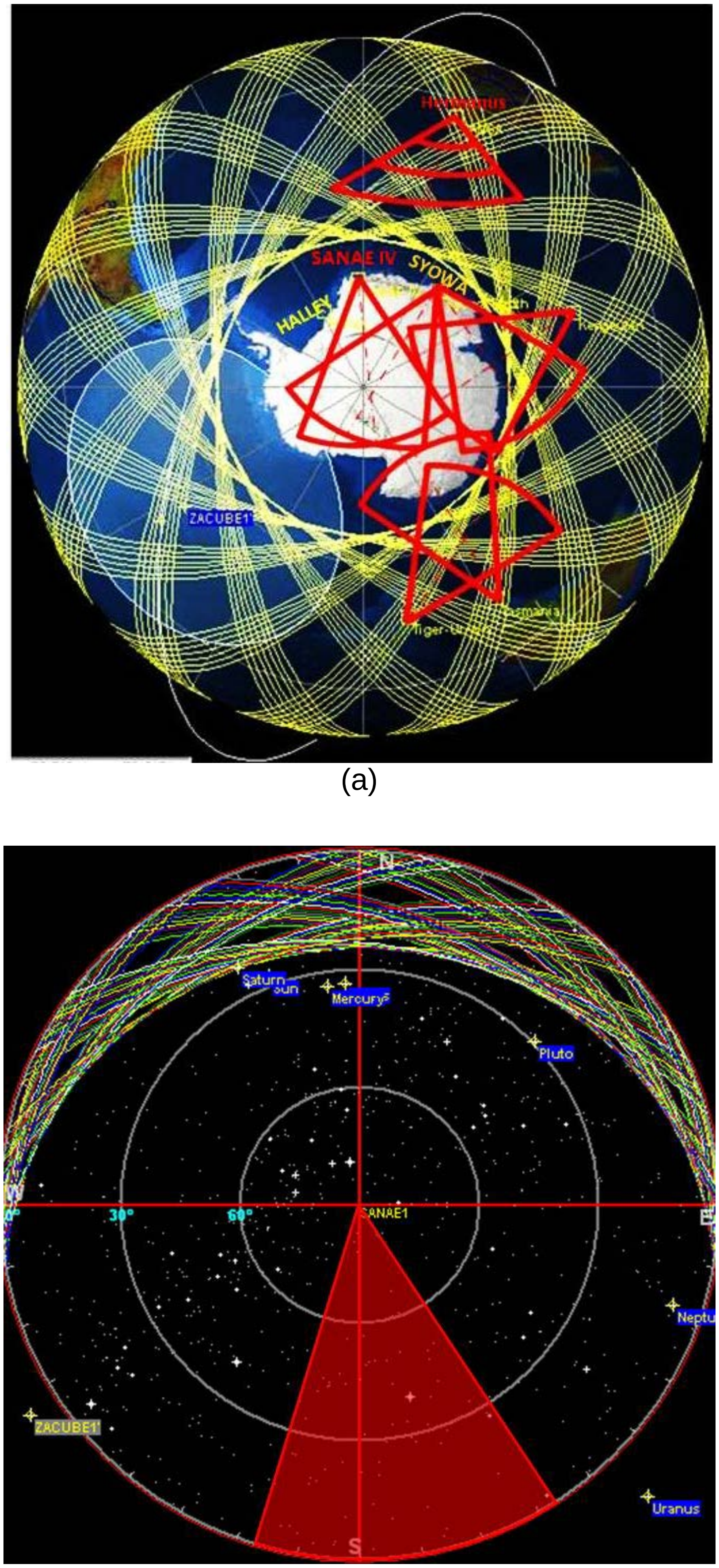

(a)

(b)

Figure 4.3: The coverage of a satellite having 60° inclination: (a) seen from a global map, (b) as seen from a radar map

4.2.1.3 Coverage from inclinations exceeding 80°

From 80° inclination the satellite is partially visible at SANAE IV, but all the overpasses have short durations owing to the blind spot, which is still present (see Figure 4.4). There are no significant overpasses because they all appear at low elevations. This can be noted from Figure 4.4(b) as all visible passes cut the radar beam on the edges. Considering the azimuthal range of the radar, these passes are identified as low elevation passes that may not suffice for measuring the far field radiation pattern of the antenna.

Having investigated the coverage for inclination angles smaller than 90°, the next is to investigate the coverage for inclinations exceeding 90°.

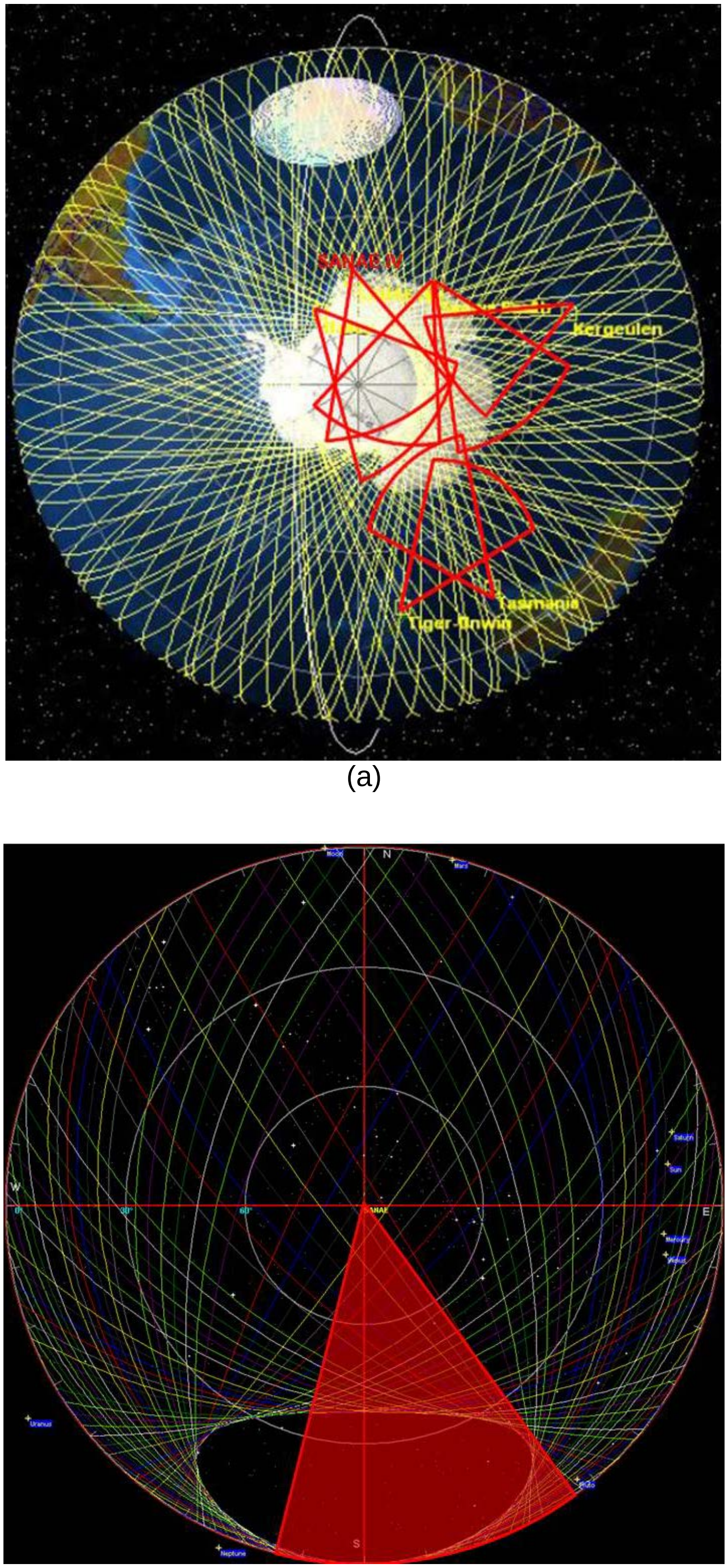

(a)

(b)

Figure 4.4: Coverage of a satellite with an 80° inclination

4.2.1.4 Coverage at 98°inclination

At 98° inclination, the satellite is visible at SANAE IV up to certain degrees of elevation, since Figure 4.5 demonstrates that the blind spot reduces significantly for SSO. It is, therefore, important to determine up to what degree of elevation the satellite will be visible. This information is useful for the link budget calculation, as the distance from the horizon to receiving antenna is inversely proportional to satellite elevation. The lower the elevation angle, the longer the propagation path.

A histogram was plotted with data that was retrieved from the satellite tracking software. A mission operation lifetime estimation of 1 year is assumed. Since it is been shown that a polar or a near polar orbiting satellite will always pass by or near by the pole, most of the above daily orbits will cut the radar beam. These daily overpasses vary between 0° and 26° elevation angles with many occurrences from 24° to 26° (see Figure 4.6 (a)). The access duration was also analysed for a minimum period of a month in order to correlate calculated parameters with simulated data. Results from Figure 4.6(b) show a good correlation between simulated values and calculated ones. It also presents the percentage of coverage giving a maximum overpass time of about 13 min.

The satellite elevations should be accounted for in the calculation of the link budget. Therefore, it is necessary that the link analysis be done using the lowest elevation. Note that only two (2) of the 14 daily overpasses will be over South Africa (one ascending and one descending) with 12hr between overpasses.

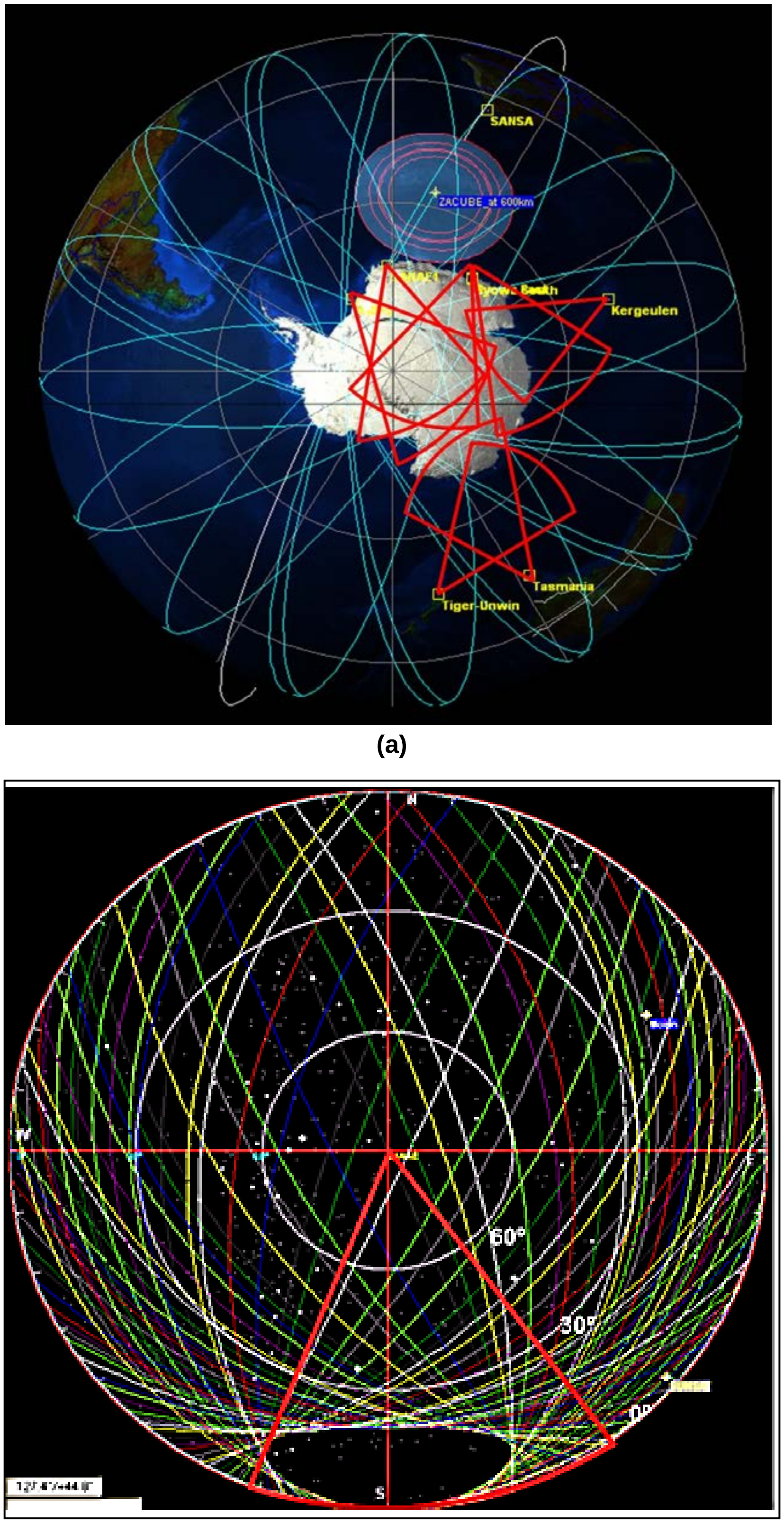

(a)

(b)

Figure 4.5: The coverage of the satellite over SANAE IV at 98° inclination: (a) from global map, (b) using radar view

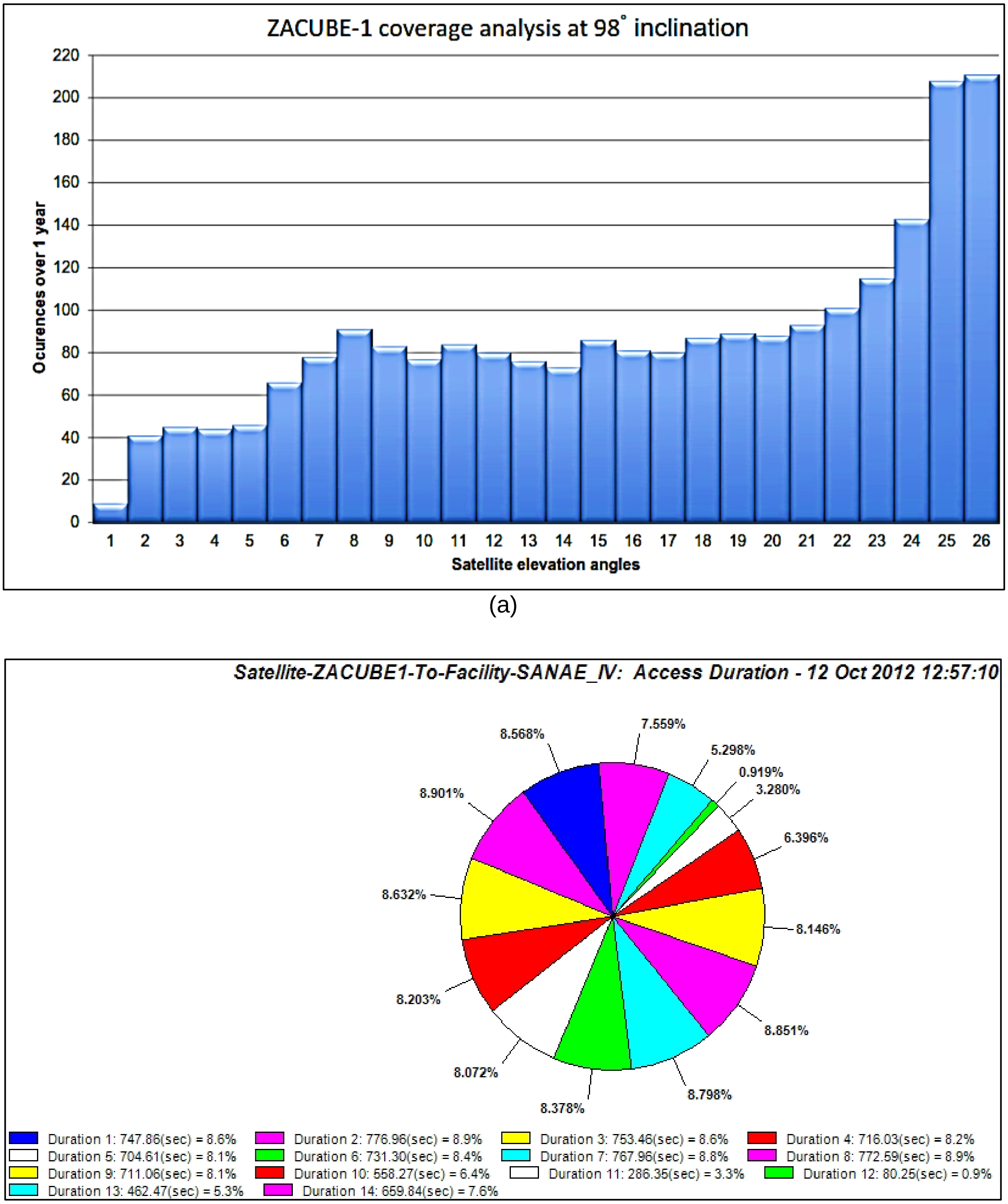

(a)

(b)

Figure 4.6: Coverage history at 98° inclination from SANAE IV perspective: (a) histogram of satellite overpasses, (b) access duration history

Table 4.1 below provides a summary of the coverage analysis as applicable to ZACUBE-1. From this analysis, one can observe that 98° inclination is a suitable orbital inclination for polar experiments. (90° would be most suitable from visibility consideration all over).

Table 4.1: Coverage analysis for six different inclination angles

Inclinations of the orbital plane	Elevation angle observed at SANAE IV	Visibility of ZACUBE-1 observed at SANAE IV
65°	Below horizon	Not visible
70°	Below horizon	Not visible
80°	Extremely low	Partially Visible
90°	0°- 90°	Visible
98°	0°- 30°	Visible

4.2.2 Field-of-view from Hermanus perspective

A replica of the SANAE IV antenna array was constructed at SANSA SS and will be used to determine the feasibility of the mission. In other words, ZACUBE-1 will be used to determine if it is indeed possible to characterise an antenna from space. Future missions will then use whatever is learned from the 1U results to characterise the SANAE IV antenna array, and others. The location of the SANSA SS base in the middle latitudes is ideal, since it allows for flexibility in the selection of launch, as certain orbital constraints will be less significant. If we consider inclination angles from 65° up to 98°, it can be seen from Figure 4.7(b) that there are many significant overpasses which one can use to measure the beam pattern of this antenna element, regardless of the significance of the blind spot shown in Figure 4.7(a).

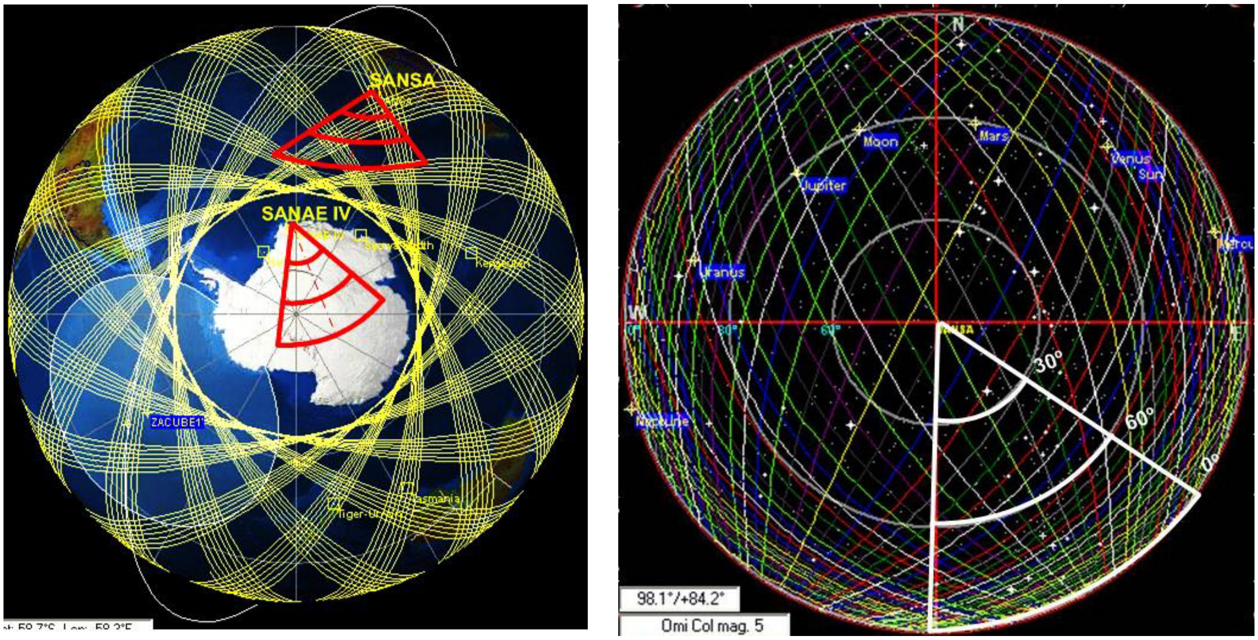

(a) (b)

Figure 4.7: Satellite coverage of SANSA SS in Hermanus at 65° inclination

Figure 4.8(a) presents a histogram of satellite overpasses with an orbital inclination of 65°, as seen from the middle latitudes. One can observe that there are overpasses up to 90° elevation; and because the antenna under test is only one element the beam pattern is much broader. One useful overpass can suffice to characterise this element. Such an overpass will fully cut through the beam of the antenna element. Understanding the behaviour of this single element will give valuable input towards the measurement of the beam pattern of the antenna array at SANAE IV.

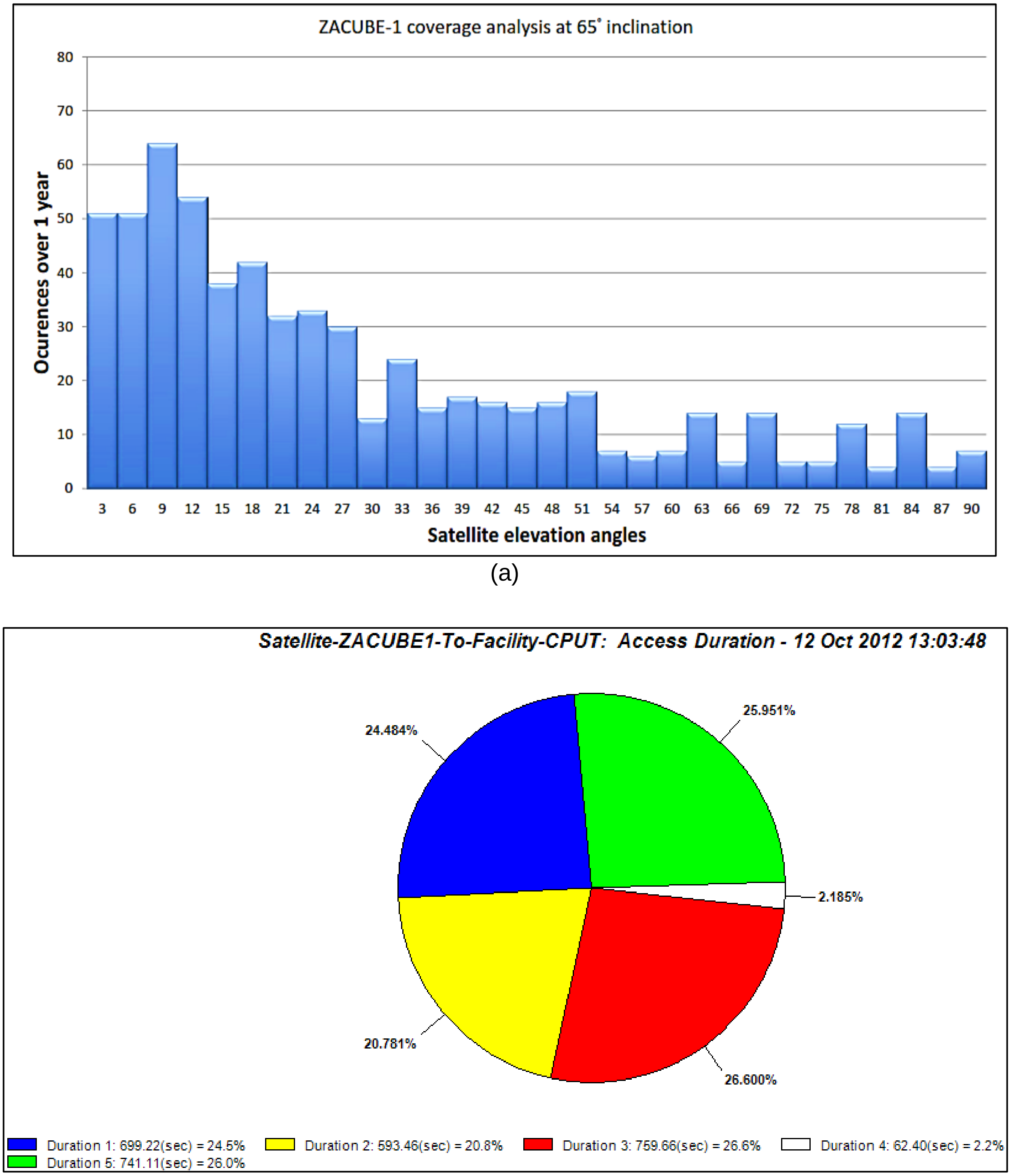

(a)

(b)

Figure 4.8: Satellite visibility of SANSA SS in Hermanus at 65° inclination: (a) histogram of satellite overpasses, (b) access duration history

Form the above observations, the characterisation of the TTFD at SANSA SS does not require the satellite to be in a sun-synchronous orbit. However, it will be suitable if the satellite is in a sun-synchronous orbit, because this will lead to numerous useful overhead passes over Hermanus. The other useful aspect of this orbit is that all overpasses pass over the poles, and Hermanus being in close proximity to the South Pole. It is possible as seen from Figure 4.8(b) to have four useful overpasses a day with about 11 min duration, which traverses both Hermanus and SANAE IV.

4.3 Evaluation of LUF

Based on Equations 2.3 and 2.4 an algorithm was developed in MATLAB for computing the LUF for given N_mF_2. For this evaluation, ionospheric data from Hermanus and Sondrostrom were used. Based on ionospheric measurements, whilst the LUF at SANAE IV derived using the IRI model due to the nonexistence of the ionosonde at SANAE IV. Two of the stated stations are located at high latitude (SANAE IV, 72.66°S, 2.85°W and Sandrostrom 66.98°N, 50.94°W) and the other station (Hermanus 34.4204°S, 19.2438°E). These three stations were selected as the satellites in polar orbit will always cross these regions. SuperDARN antenna arrays are located at SANAE IV and Hankasalmi (62.3°N, 26.6°E). The reason for selecting the Hermanus station was due to the presence of the an ionsonde at SANSA in Hermanus, which would provide relevant data about the electron density over Hermanus for ray tracing of the HF beacon to a receiver at Hermanus. In addition, the TTFD at SANSA in Hermanus will also be characterised by means of the HF beacon signal. Therefore, it is important to know if the HF radar antenna in Hermanus will receive the satellite signal.

The f_oF_2 values for each location and corresponding seasons were obtained from the ionospheric data server; National Oceanic and Atmospheric Administration (NOAA)[6]. This data was used to calculate the electron density and the corresponding LUF using Equation 2.1 through to Equation 2.5, from Section 2.3.2. This was done to investigate how space weather influences the mission. In order to verify whether the HF signals at 14 MHz would penetrate the ionosphere, data for the following hours from selected days were used: 00:00, 06:00, 12:00 and 18:00 UT. Besides these periods, daily peaks are also displayed on graphs in Figure 4.9 through to Figure 4.20. The objective of this analysis is to verify using models of the ionosphere at selected times, the range of LUF for which the mission would be feasible for both summer and winter. This mission would be possible only if, for a certain range of elevations, there are LUF values that are below the beacon frequency for a reasonable number of hours per day.

---

[6] http://www.swpc.noaa.gov/ftpdir/lists/iono_month/

Table 4.2: Peak electron density and foF2 values for SANAE IV station obtained from the IRI model (Bilitza, 2001)

SANAE IV			
Date	**Time[7] (UT)**	**N_mF_2 ($\times 10^{11}$el/m^3)**	**f_oF_2 (MHz)**
2010/01/01	00:00	2.78	4.75
	06:00	3.41	5.26
	08:00	3.76	5.52
	12:00	3.03	4.96
	18:00	2.69	4.67
2010/06/01	00:00	0.426	1.86
	06:00	0.434	1.88
	12:00	1.594	3.59
	18:00	0.468	1.95

Table 4.2 provides N_mF_2 (peak electron density values) as obtained from the IRI2007 model, and the corresponding values of the critical frequency for vertical incidence, f_oF_2, at SANAE IV at selected dates. The resultant LUF for a range of elevation angles is depicted in Figure 4.10 and Figure 4.12. These plots represent the hourly profile for the selected days including the daily peak.

These LUF are based on the assumption that the ionosphere is spherically symmetric, i.e. that the f_oF_2 does not change with latitude along the ray path. In practice, the elevation angle does not go down to zero due to the refraction of the satellite-to-ground signals by the ionosphere (see Figure 4.18). Hence the approximate analysis of the LUF using Equation 2.5 is only valid between the lowest elevation angle for transionospheric waves, and vertical incidence (corresponding to 90° elevation, or satellite directly above the receiver). The following plots are obtained using the assumed maximum ionospheric height h_mF_2 =325 km. All the plots in Figure 4.9 through to Figure 4.20 will have the same scale to facilitate comparison of these plots and comparison with the corresponding plots for Hermanus station.

---

[7] SANAE IV being close to the 0° longitude meridian, Universal Time (UT) is almost the same as Local Time (LT).

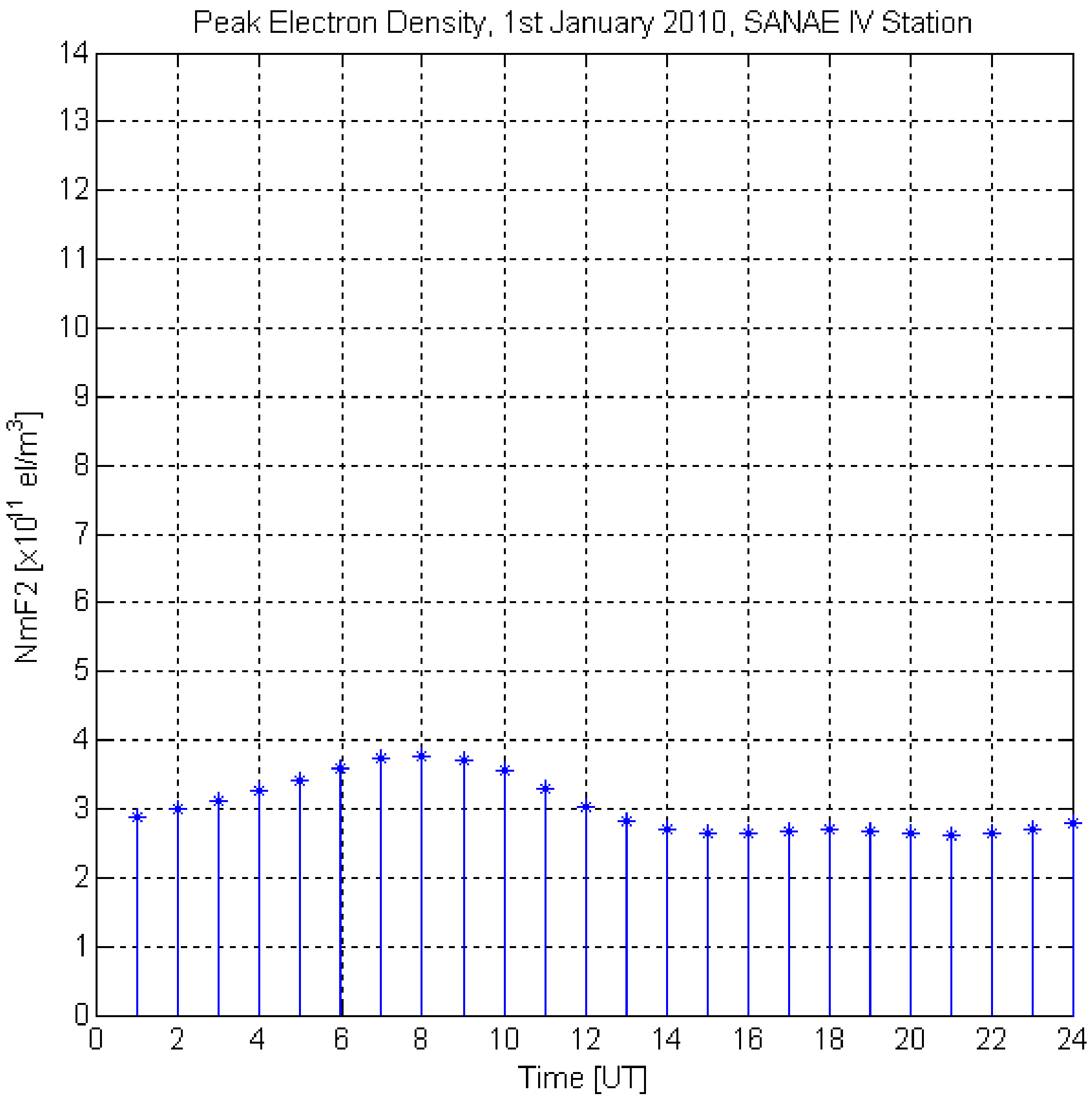

Figure 4.9: Peak electron density N_mF_2 vs. UT time derived from IRI model at SANAE IV on 1 January 2010

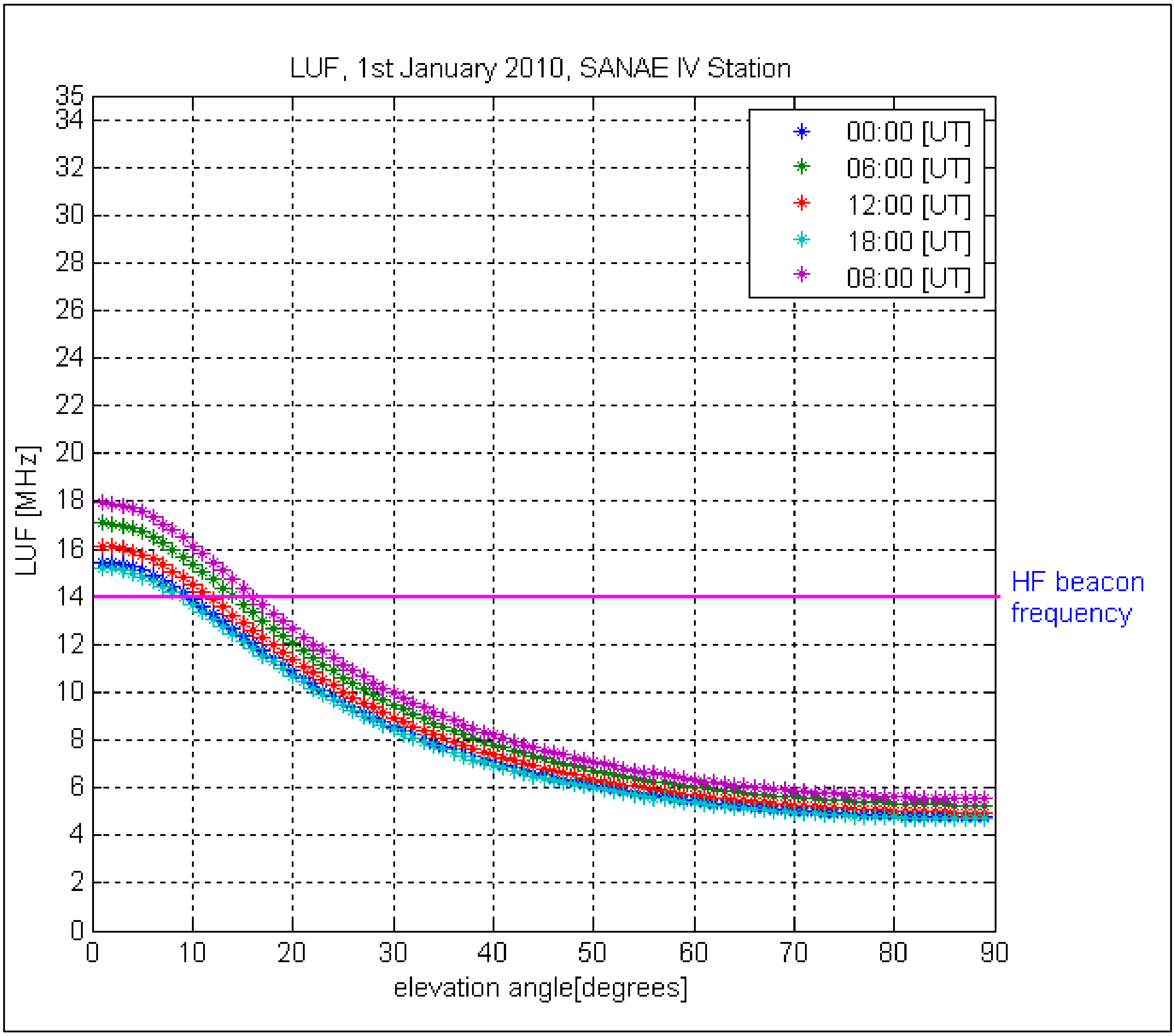

Figure 4.10: Calculated LUF profiles at SANAE IV from the derived N_mF_2 for 01 January 2010

By considering the 14 MHz as the frequency threshold, it is observe from the above figure that signals below 15° elevation would not have traverse the ionosphere on the 01 January 2010. For vertical incident waves, this reveals that the LUF is equal to the ionospheric critical frequency f_oF_2. It is therefore vital that the satellite appears at SANAE IV above 15° elevation if one expects the antennas to receive the HF beacon signal.

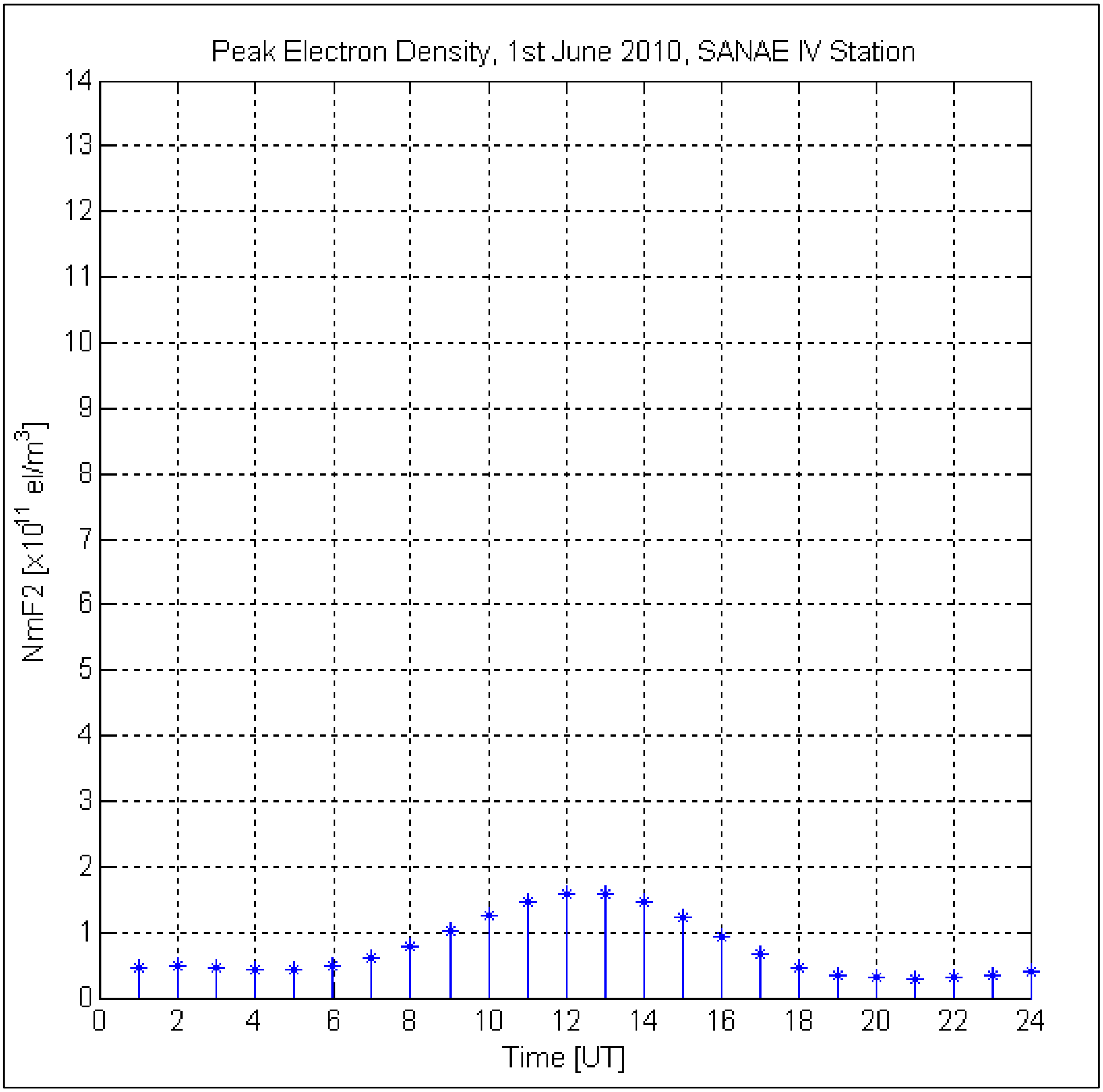

Figure 4.11: Peak electron density N_mF_2 vs. UT time derived from IRI model at SANAE IV on 1 June 2010.

Figure 4.11 presents the peak electron density with the profile peak at 12:00 UT, from which the LUF plots in Figure 4.12 were generated. By considering the chosen scales, Figure 4.12 presents a more acceptable data as it discloses the feasibility of the mission at SANAE IV during winter.

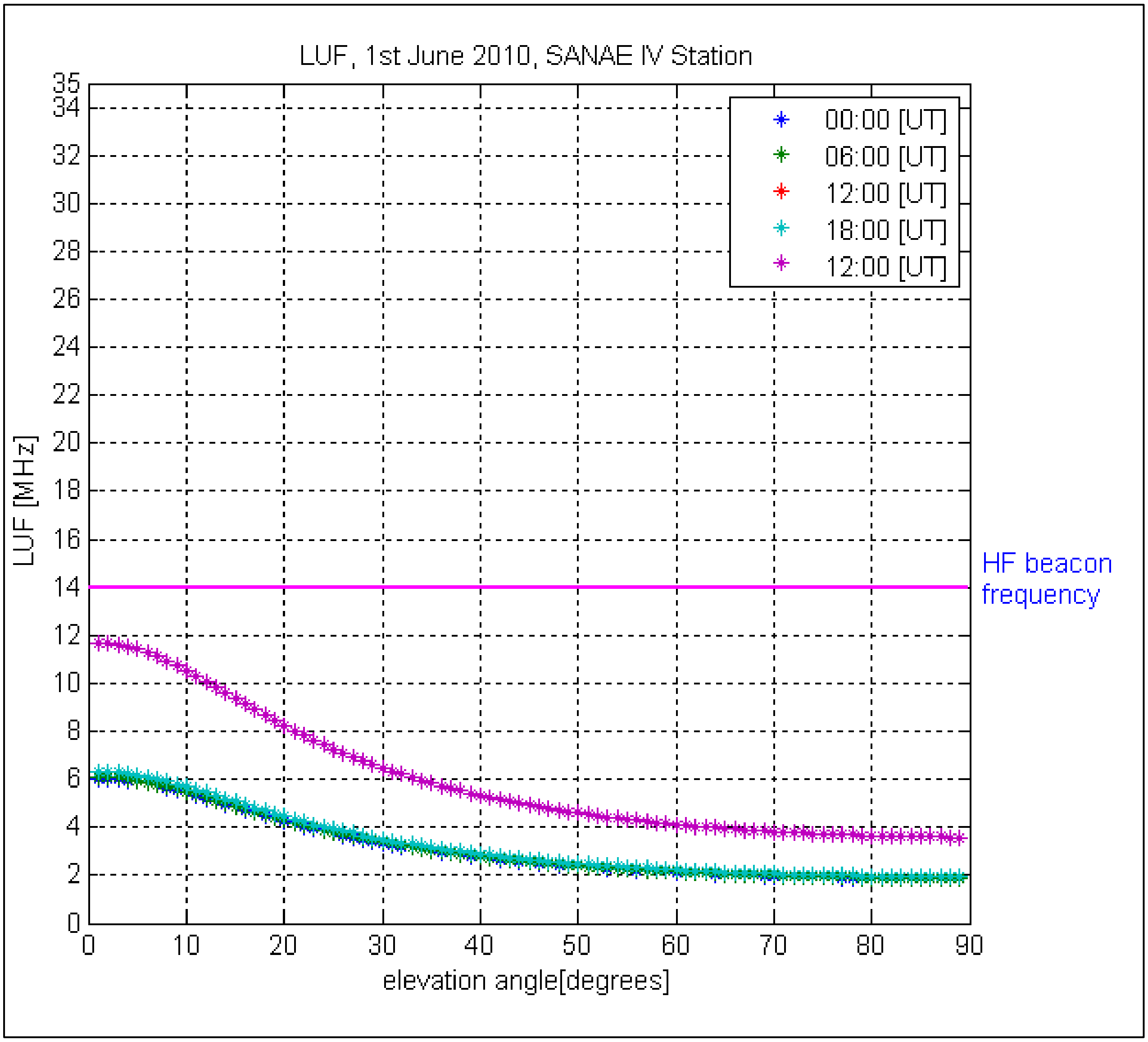

Figure 4.12: Calculated LUF profiles at SANAE IV from the derived N_mF_2 for 01 June 2010

Figure 4.13 presents the variation of N_mF_2 on the 1st August 2011. One can observe a rapid variation of the electron density in the ionosphere, with sudden increases in the peak electron density between 05:00 UT and 07:00 UT as well as sudden decreases between 15:00 UT and 17:00 UT, hence the increases in LUF in Figure 4.14.

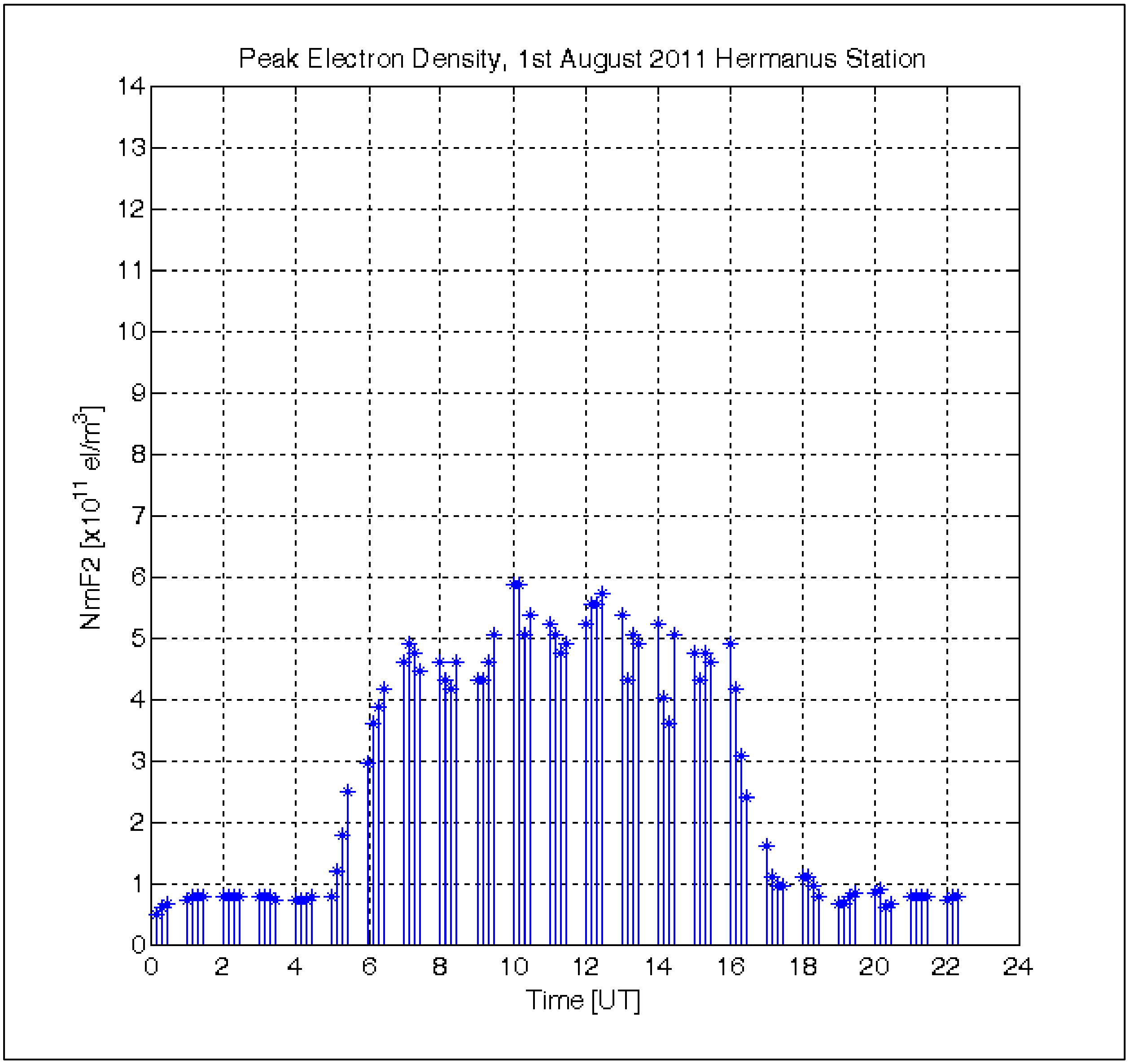

Figure 4.13: Peak electron density N_mF_2 vs. UT time measured at Hermanus on 1 August 2011

Because of this increase in the peak electron density in the ionosphere at midday on 1st August 2011 in Hermanus, the LUF value at this time of day rises above the beacon frequency for signals transmitted at low elevations (0°-25°), as shown in Figure 4.14. Above this elevation range, all signals at 14 MHz propagate through the ionosphere at any time of the day.

Days following the impact of a space weather storm on the ionosphere are mostly characterised by an increase in peak electron density in the ionosphere. An example of such an event resulted in an increase of N_mF_2 presented Figure 4.15, which reflects the summer profile of peak electron density vs. time of day at Hermanus on the day on which there was a space weather storm

(2011-11-30). The increase in N_mF_2 observed in Figure 4.15 becomes influential at midday. As a result, the range of elevations at which 14 MHz signals could penetrate the ionosphere is reduced, as depicted in Figure 4.16 (0° - 45°). Consequently, no signals could penetrate the ionosphere over Hermanus up to 35° elevation.

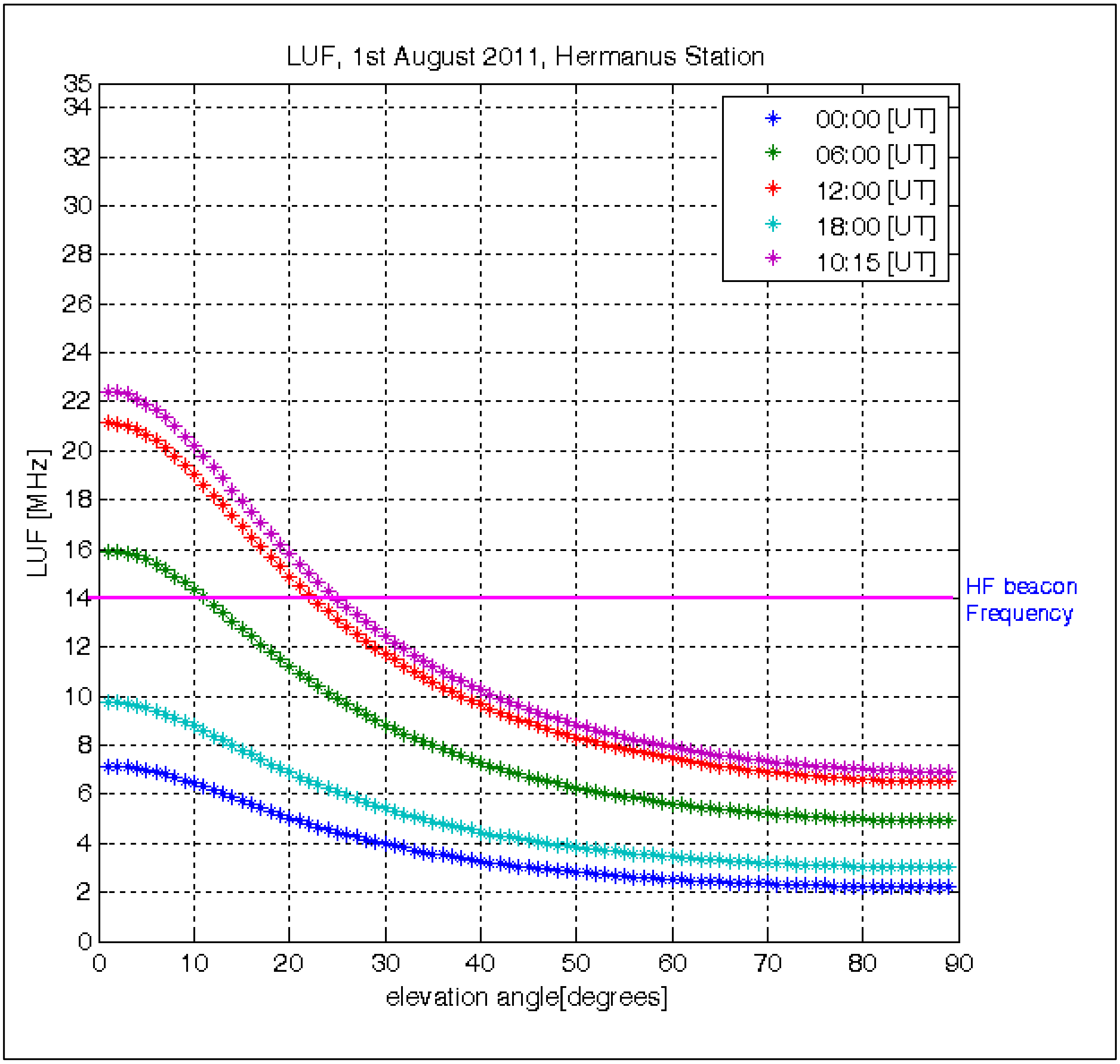

Figure 4.14: Calculated LUF vs. elevation angle from the 1 August 2011 peak electron density profile at Hermanus

Though the area of interest at Hermanus is above 30° for ionospheric c, it is observed from Figure 4.11 that one could only see the HF beacon any time of the day for all elevations above 45°. For low elevation this calibration may not be possible for a similar space weather conditions or worst. At SANAE IV, the HF beacon would be visible bout 30°, as the satellite would be appearing at low elevation due to the effect of the blind-spot.

Comparing the LUF at SANAE IV with that of Hermanus station, the magnitude of the N_mF_2 in 2011 is roughly 10 times higher than what was obtained from SANAE IV in 2010. Although one does not expect data from both sites to be parallel, however, the magnitude of the discrepancy is significant.

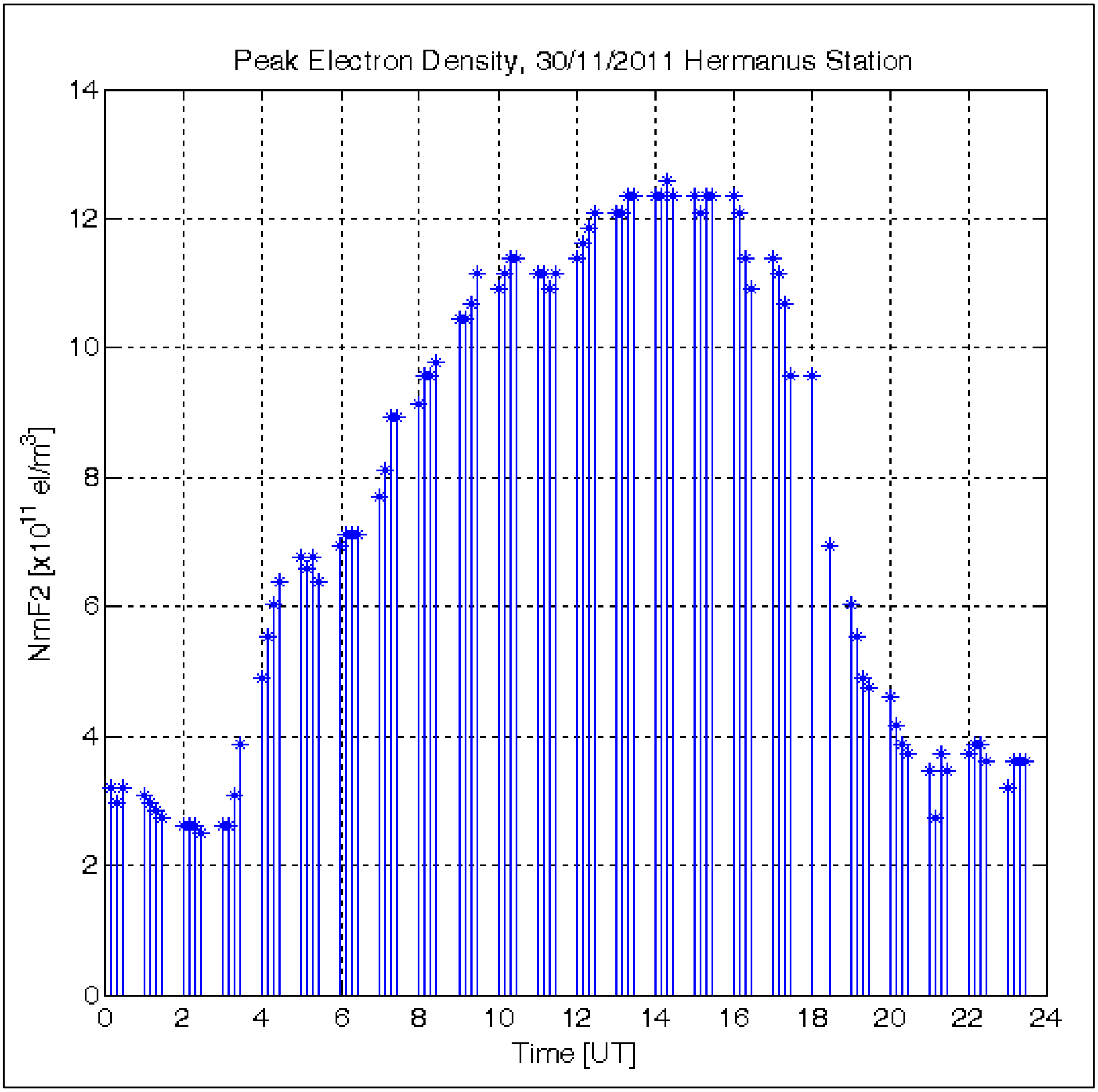

Figure 4.15: Electron density peak N_mF_2 measured at Hermanus during a space weather storm in summer

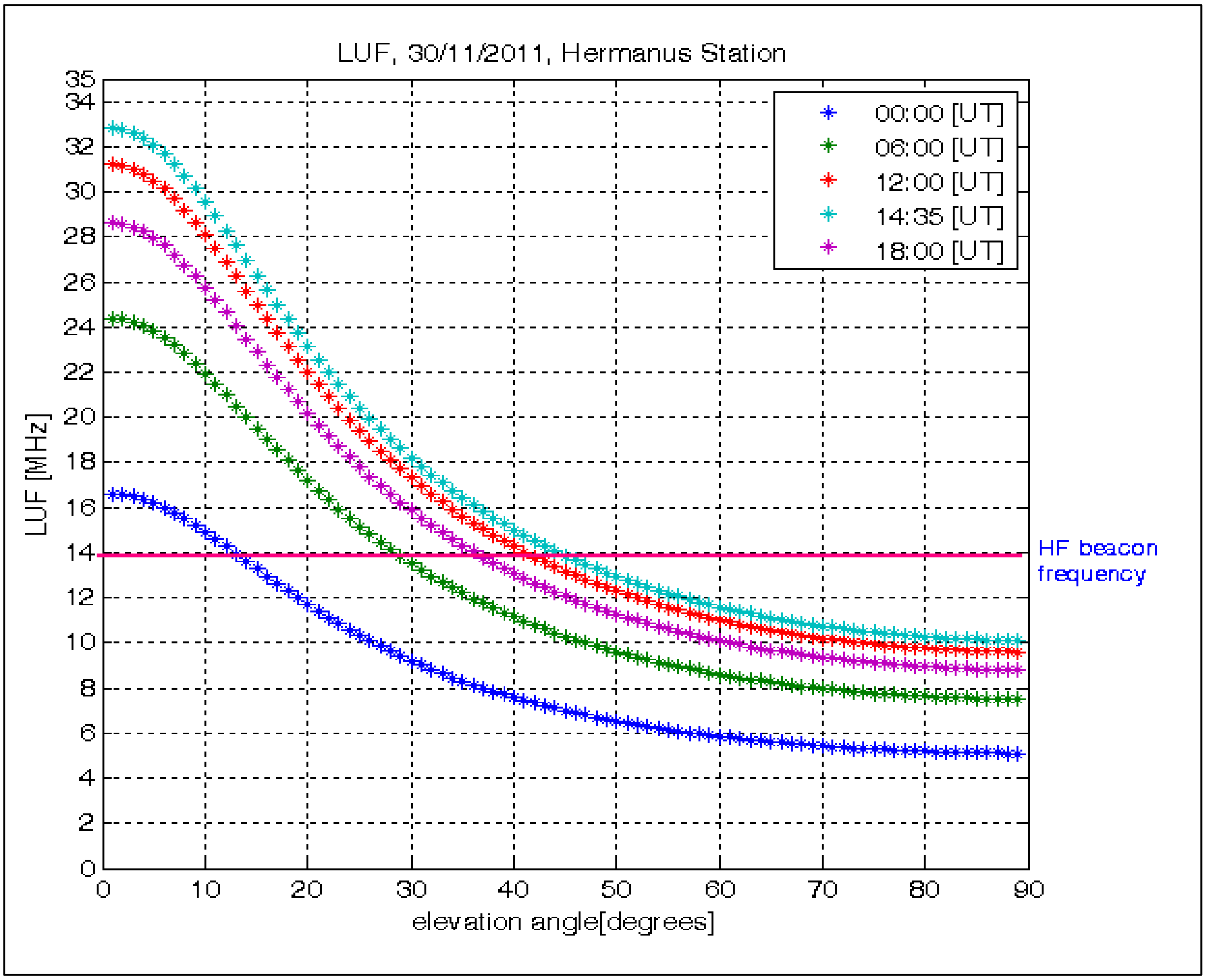

Figure 4.16: Calculated LUF from the summer profile at Hermanus for a day on which there was geomagnetic activity with intensity designated by K_p=4

Though the area of interest at Hermanus is above 30° for top to bottom ionospheric characterisation, it is obvious from Figure 4.16 that one could only see the HF beacon any time of the day for all elevations above 45°. For low elevation, top to bottom ionospheric characterisation may not be possible, for a similar space weather conditions.

Figure 4.17 presents the peak electron density vs. time. This was obtained from the ionosonde at Sondrestrom. The content of this graph reveals that diurnal N_mF_2 profile did fluctuate less as compared to what the plots obtained from the station at Hermanus presented. The discrepancy between the LUF measured at noon and that measured at midnight is not significant.

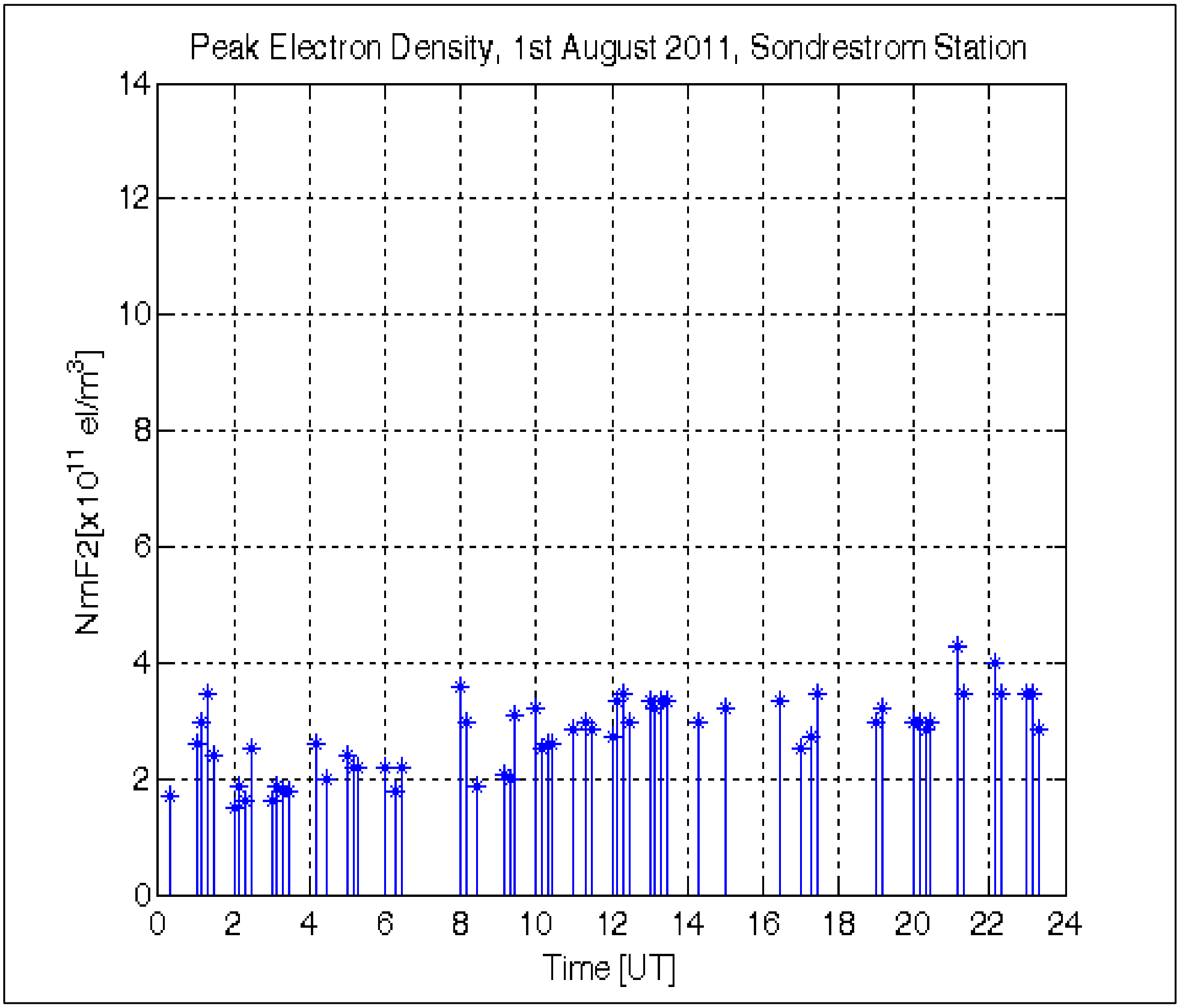

Figure 4.17: Peak electron density N_mF_2 vs. time as measured at Sondrestrom on 2011/08/01

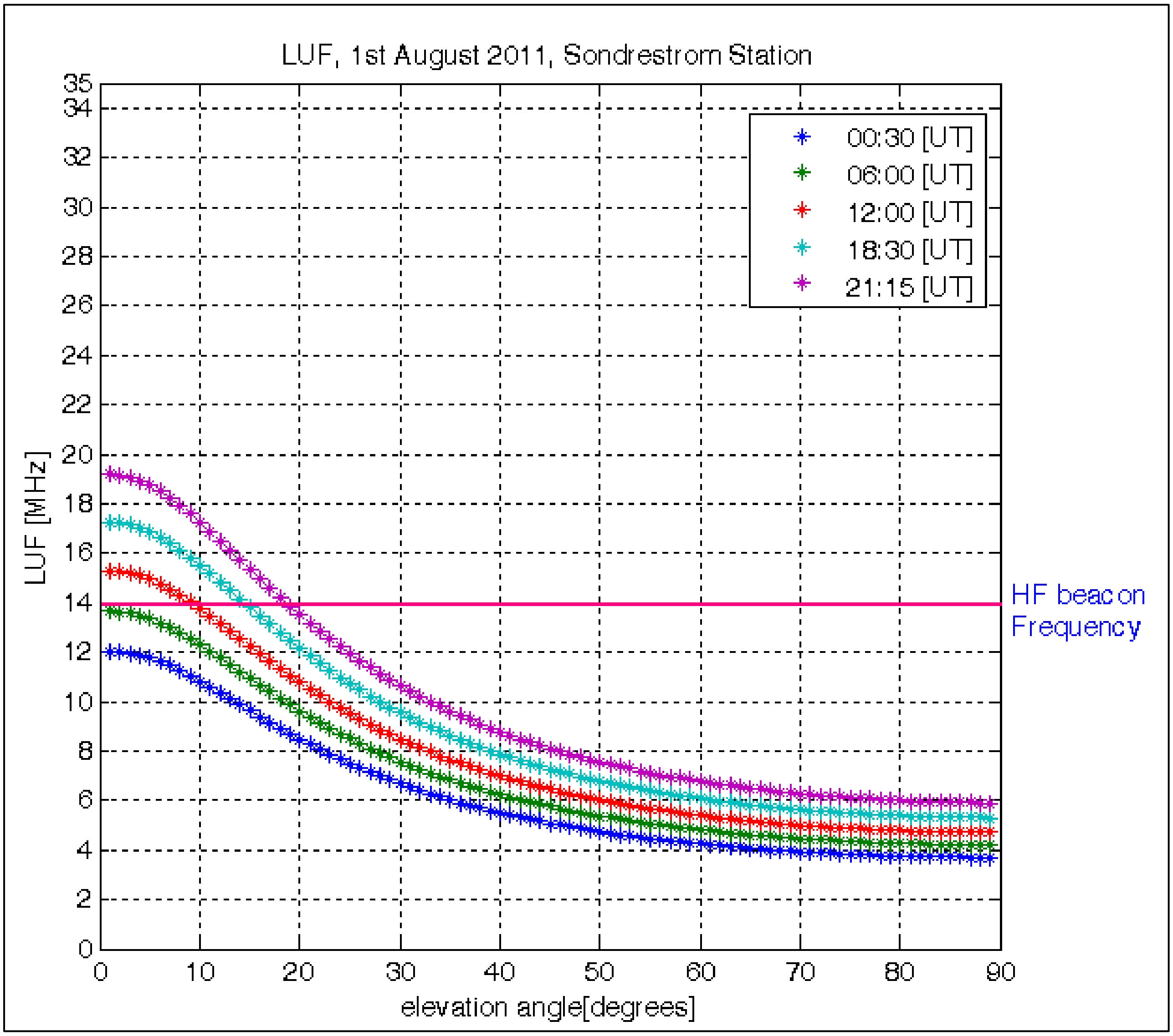

Figure 4.18: Calculated LUF for 1 August 2011 from the station at Sondrestrom

Figure 4.19 portrays less N_mF_2 variations at Sondrestrom on 22nd of February 2012, with a peak of 6×10^{11}el/m^3 occurring after 15:00 UT. Although the peak electron density in Figure 4.19 (summer) is higher than that in Figure 4.17 (winter), this is far less than what was measured from the station at Hermanus during summer (12.5×10^{11}el/m^3 around 15:00 UT). Considering times when peak electron density profiles were obtained, one observes that from midnight UT to 06:00 UT the LUF was reasonably low, and it gradually increased after 06:00. Consequently, the HF beacon signals originating from the satellite would have only been visible at Sondrestrom for all elevations, if the overpasses occurred during the following periods 00:00 to 06:00 UT on 22nd of February 2012.

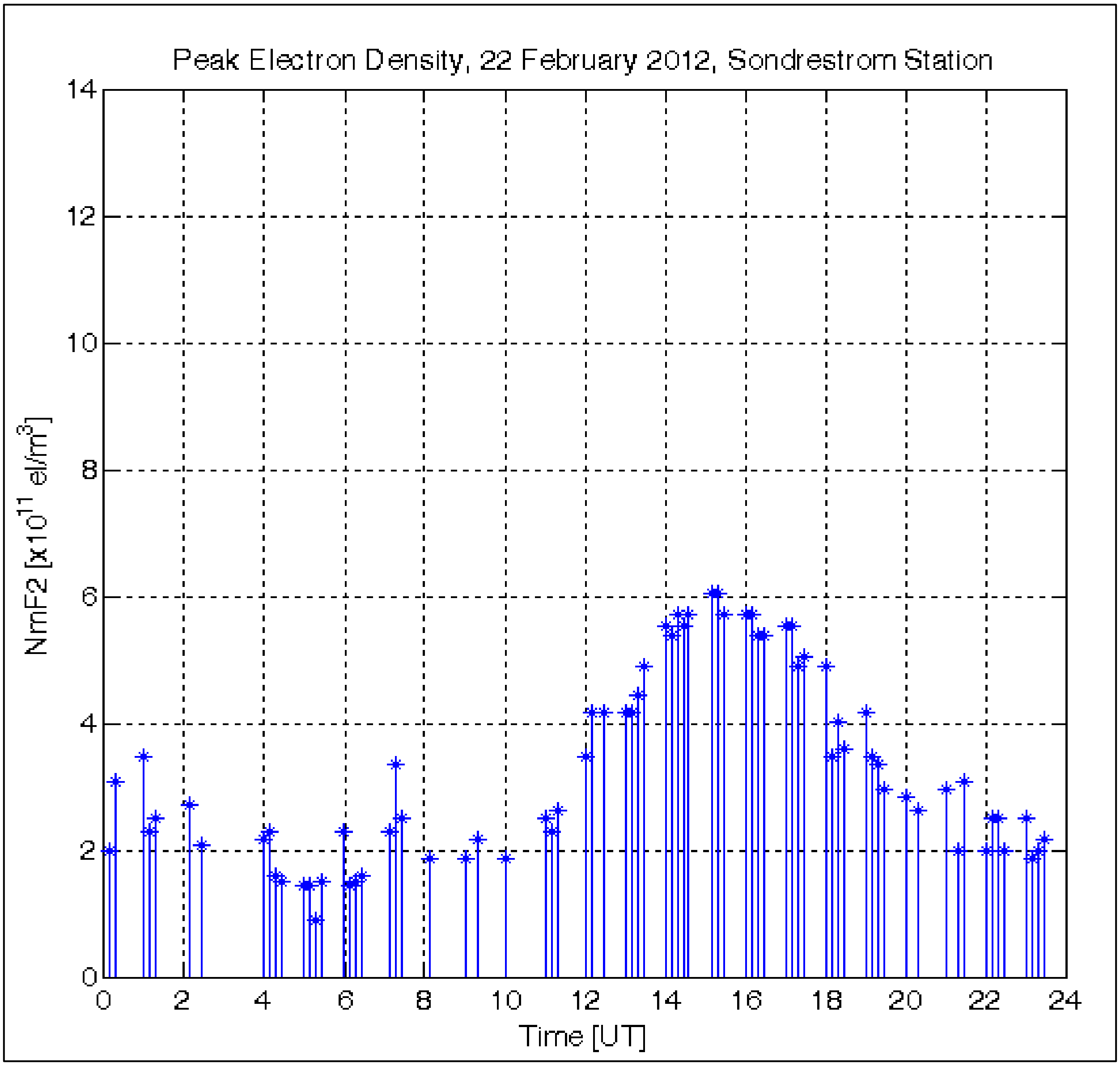

Figure 4.19: Peak electron density N_mF_2 vs. UT measured at Sondrestrom on 2012/02/22

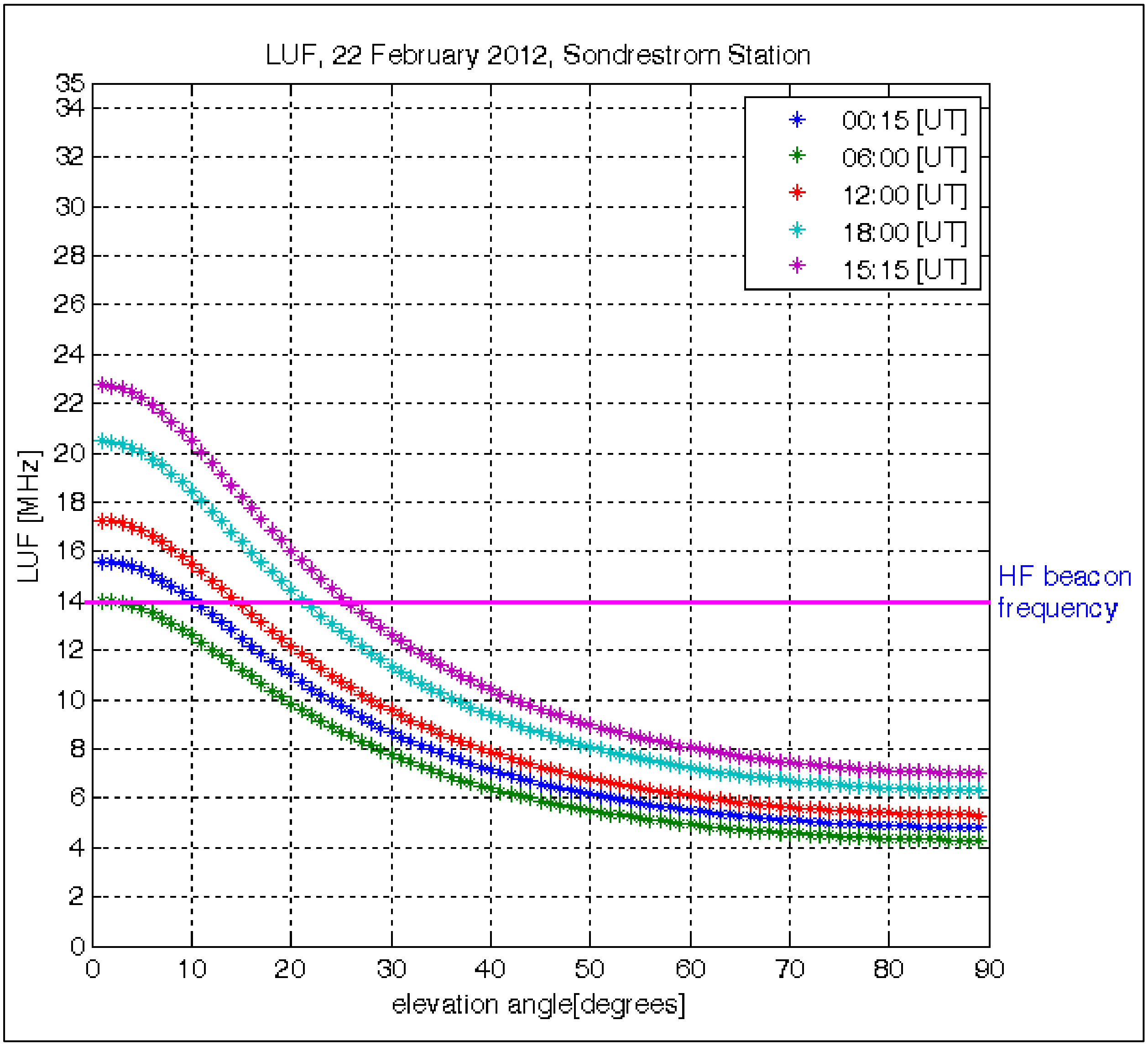

Figure 4.20: Calculated LUF for the station at Sondrestrom at selected hours on 2012/02/22

To validate the above LUF analyses, ray-tracing results obtained from SANSA SS for the station at SANAE IV was used. One hop was considered for these analyses, and the ray was traced from ground to space. Based on the simplified model of IRI2007, it was assumed that transmitter is at the origin (0,0). The elevation of incoming signals is determined using Equation 4.3[8]. From Figure 4.21(a) and (b), it is revealed that during midwinter in June 22, 2010, transionospheric propagations would not have been possible below 3.57° elevation at SANAE IV, at 00:00 UT (Figure 4.21(a)). Similarly, only signals with 20.55° apparent elevation and above would have traversed the ionosphere in midsummer, 22 December 2010 at 12:00 UT (Figure 4.21(b)).

---

[8] Only a range before a signal is refracted is considered as straight line.

$$\varepsilon = \tan^{-1}\left(\frac{\text{Height}}{\text{Range}}\right). \qquad 4.3$$

$$\varepsilon = \tan^{-1}\left(\frac{50}{600}\right) = 3.57^\circ \text{ in winter,}$$

$$\varepsilon = \tan^{-1}\left(\frac{225}{600}\right) = 20.55^\circ \text{ in summer.}$$

Where ε is the elevation angle, the range is the distance along the ground for spherical Earth model.

This ray tracing results confirm what was unfolded from the LUF analyses at SANAE IV for the same year, although from LUF analyses it appear that during winter all rays would have been received by the array for all elevations on 1st June 2011, this would only hold for flat Earth model. Since the spherical Earth was considered (Figure 2.12), only rays above 4° elevation would, practically, have been received.

These results can be applied to the ZACUBE-1 mission because the reciprocity of the ray tracing dictates that a 14 MHz signal that can traverse the medium (ionosphere) from one side of that medium to another (ground to space) would do the same in the opposite direction (space to ground) - given that the incident angle and the refraction index remain the same.

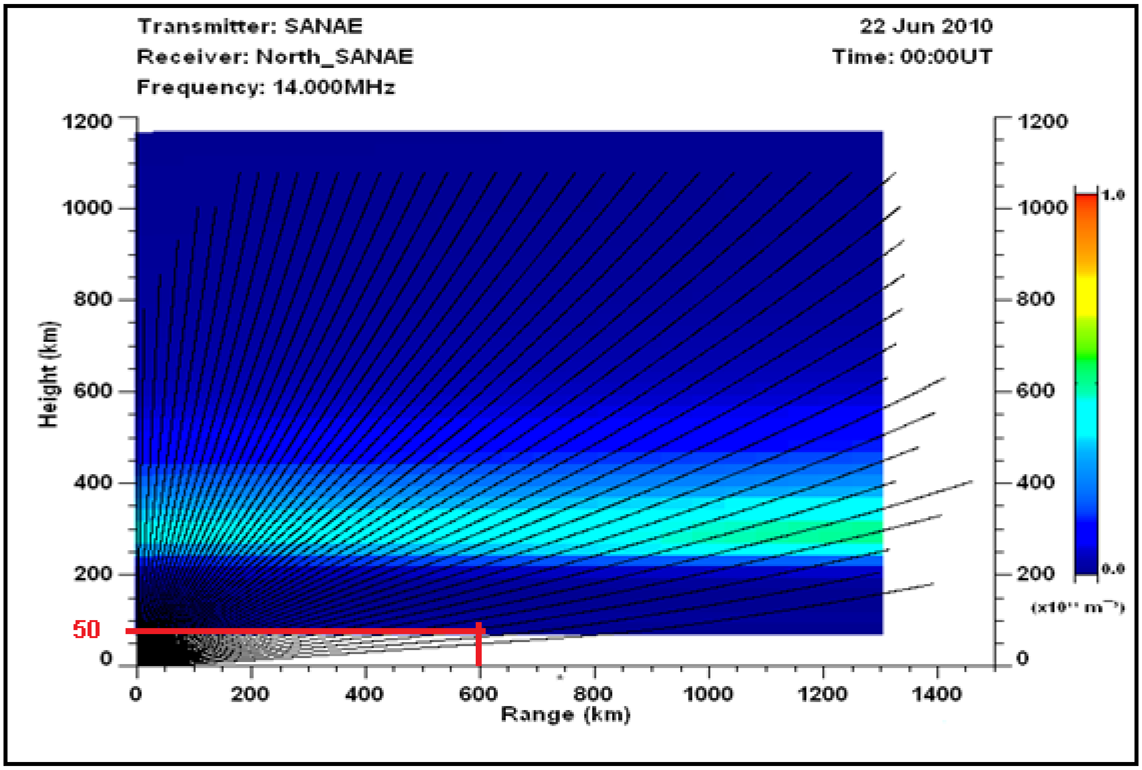

(a)

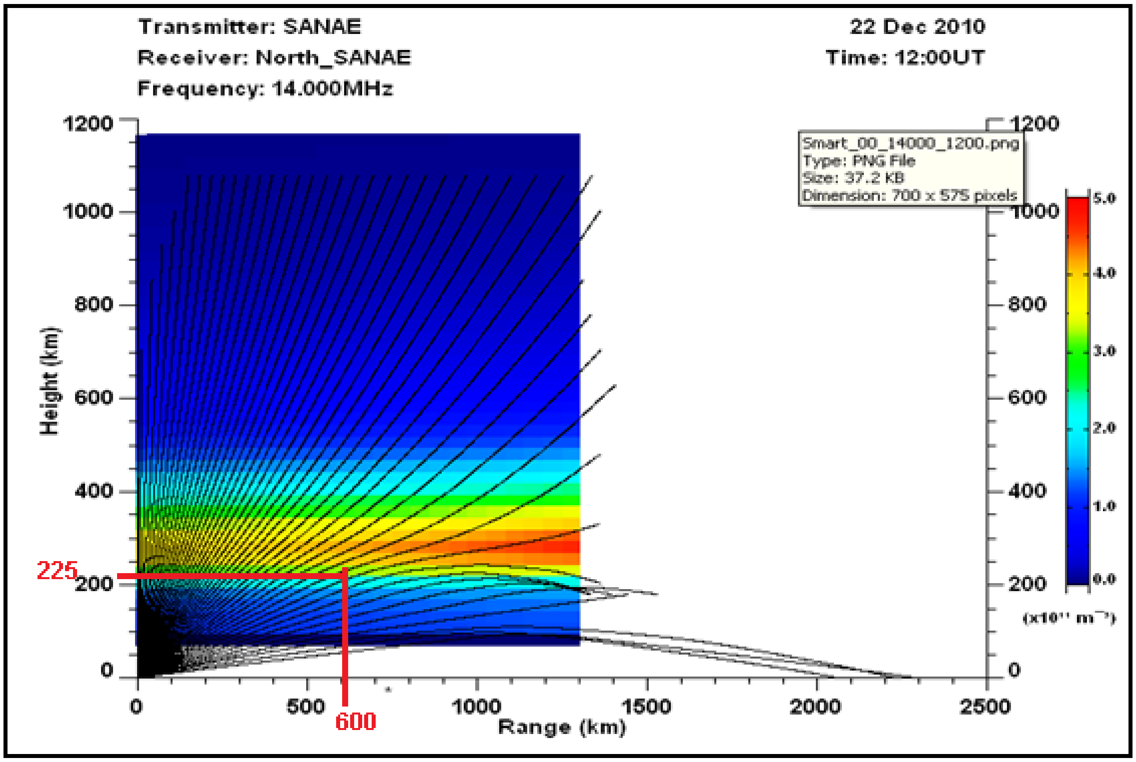

(b)

Figure 4.21: Ray tracing from SANAE IV using IRI2007: (a) midwinter, (b) midsummer (Cilliers *et al.*, 2011)

It thus follows that the satellite to ground propagation delay due to ionospheric refraction is given by:

$$t_{delay} = \frac{H}{c} = \frac{600 \times 10^3}{3 \times 10^8} = 2\,\text{ms}$$

For the case when the satellite is directly overhead the receiver,

where *c* is the speed of light, and the *H* the orbital altitude.

4.4 Antenna design and simulation

This section discusses the simulation of the SANAE IV SuperDARN antenna, the design of the satellite's HF antenna and the design and simulation of the HF antenna at CPUT.

4.4.1 SANAE IV SuperDARN antenna

The SuperDARN community developed the antenna model in electromagnetic simulation software named FEKO (FEKO, 2000). This model is used to investigate how different ground planes affect the antenna characteristics. Figure 4.22 gives the antenna's dimensions (Sterne, 2010). The radiation pattern of a single element is presented in Figure 4.23. Because of the low conductivity of the ice at SANAE IV, the ground plane does not reflects all the filed, thus, a conducting material was embedded a few maters in the ice underneath the antenna, to improve the ground's electrical properties. The model also shows reflector wires running horizontally at the back of the antenna elements; this ensures that the pattern is oriented in a desired direction (southward). The radiation pattern of Figure 4.24 shows the beam pattern of the TTFD. It presents a maximum gain of 9 dBi at 60° elevation (see Figure 4.25). In this section, theta denotes the antenna elevation, while phi denotes the azimuth angle.

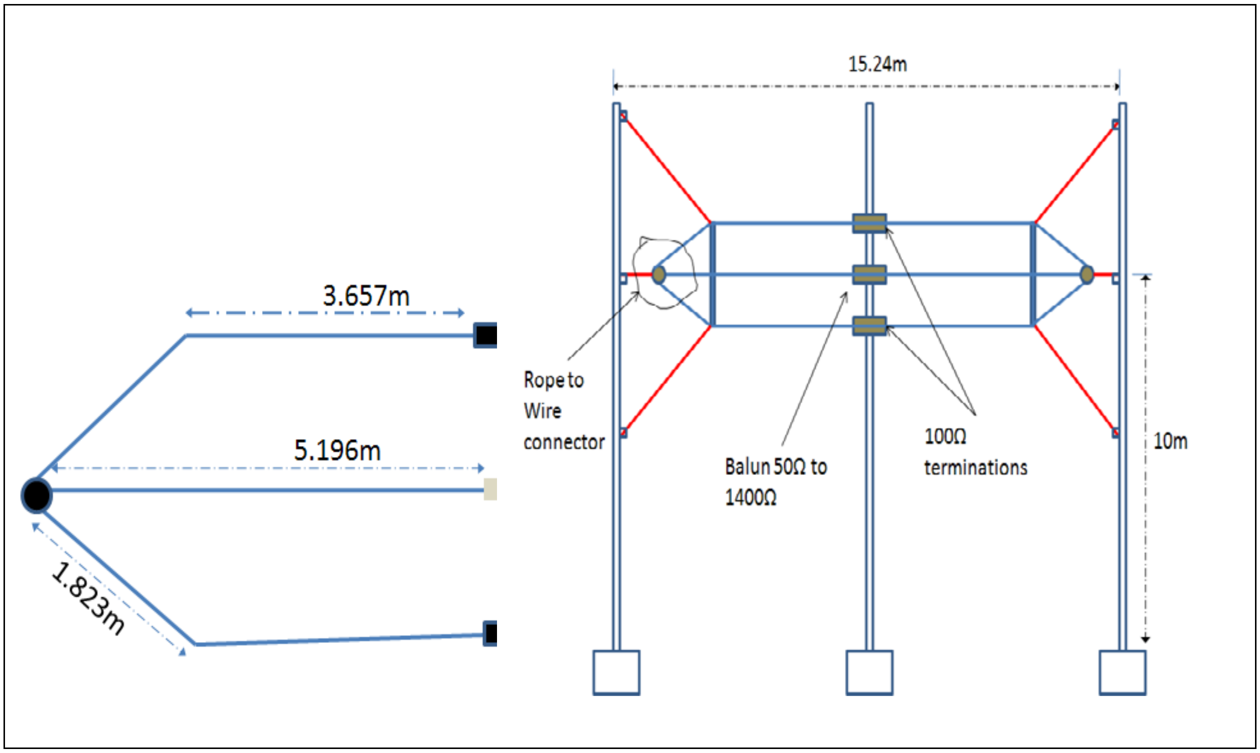

Figure 4.22: SANAE IV antenna structure representation with dimensions included

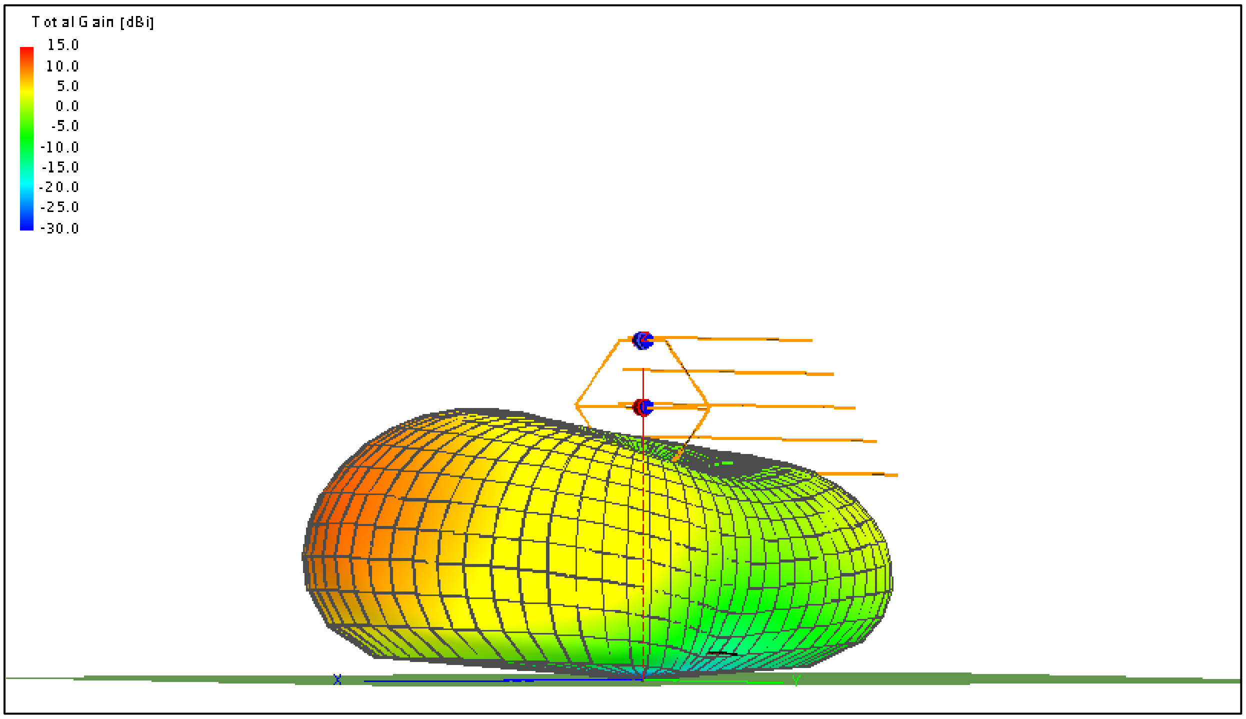

Figure 4.23: Post FEKO representation of the TTFD (single element)

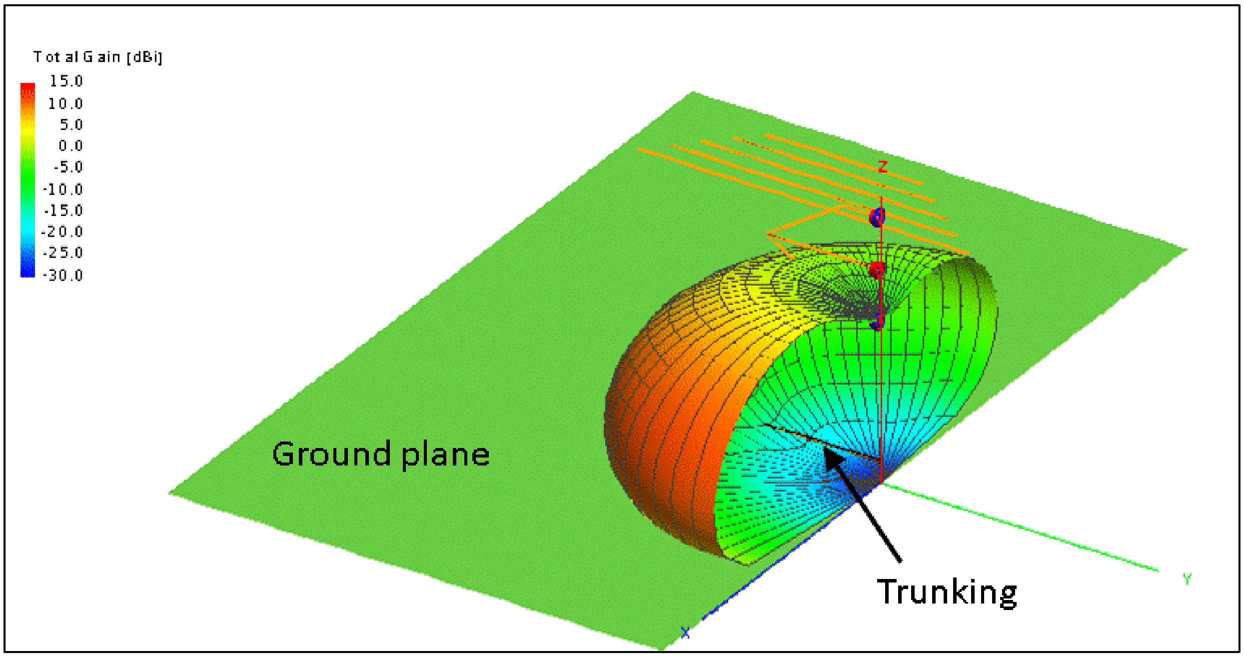

Figure 4.24: Simulated beam pattern (cut in the x-z plane) for the TTFD (single element)

.

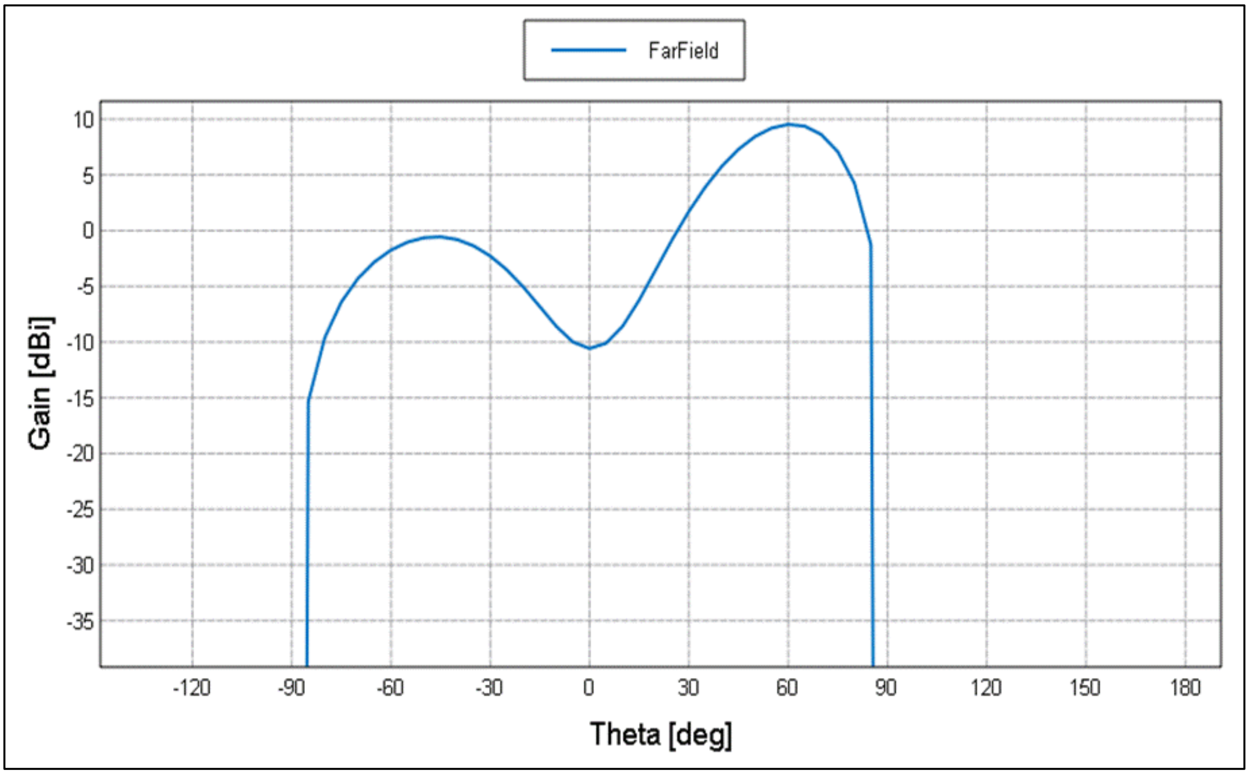

Figure 4.25: Simulated TTFD antenna gain (single element)

The next step involves simulating the combined array of 16 elements. In this simulation, the number of mesh points is decreased to improve the simulation speed of the computer, but at the cost of losing the beam shape resolution.

The antenna model in Figure 4.26(a) is the simulated antenna with no ground plane. The radiation pattern exhibits a significant back lobe, which is equal in magnitude to the main lobe. Thus, characterising such an antenna may be difficult as there may be ambiguities in measurements regarding the direction of the incoming signal.

The antenna gain given in Figure 4.26(b) is about 16 dBi. Using a ground with sandy clay parameters, the model in Figure 4.24 is simulated. It exhibits an increase in the overall gain achieved (21 dBi). The performance of the model in Figure 4.27 is compared with the one in Figure 4.25 where a ground with ice is assumed. It is evident that these two types of ground yield similar antenna characteristics. From these analyses, we conclude that an antenna array built and characterised at SANSA SS (sandy clay ground) will likely perform similarly at SANAE IV (ice ground).

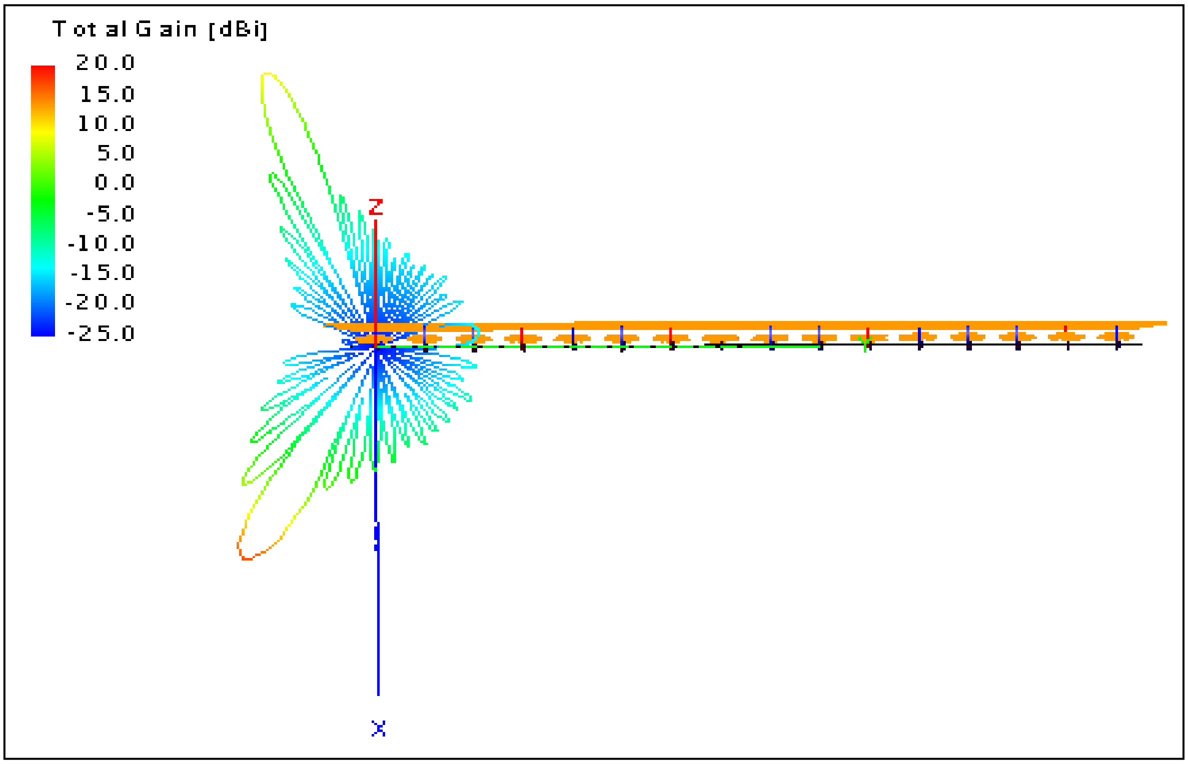

(a)

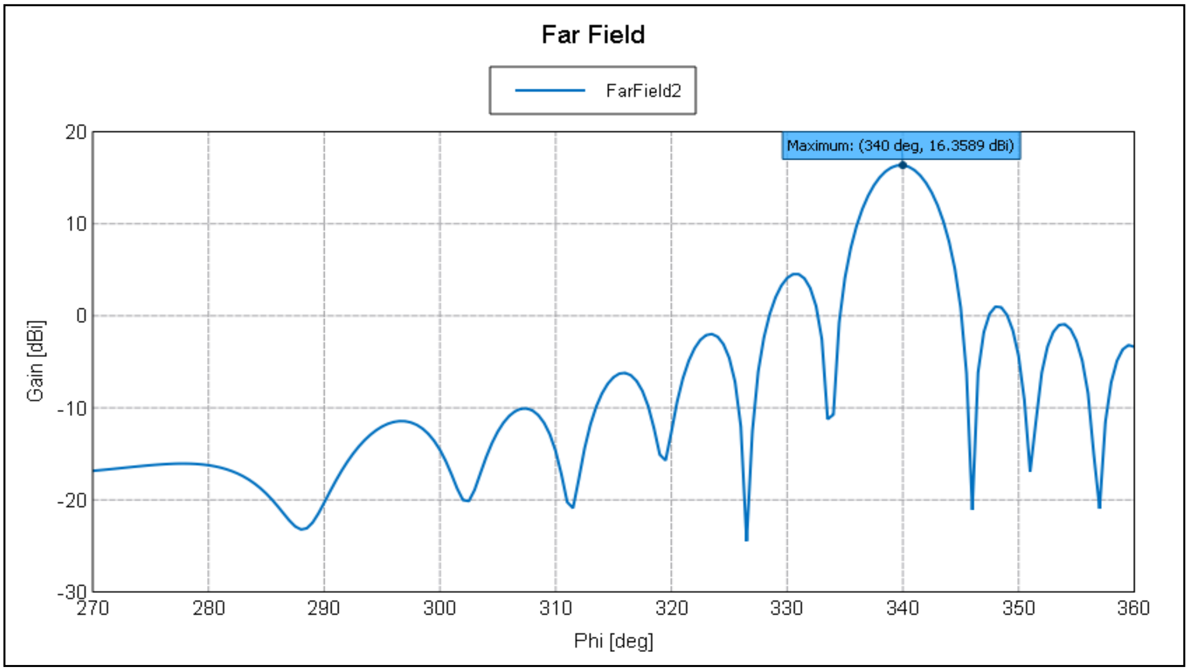

(b)

Figure 4.26: SANAE IV antenna array simulated without any ground plane: (a) antenna model, (b) antenna radiation pattern

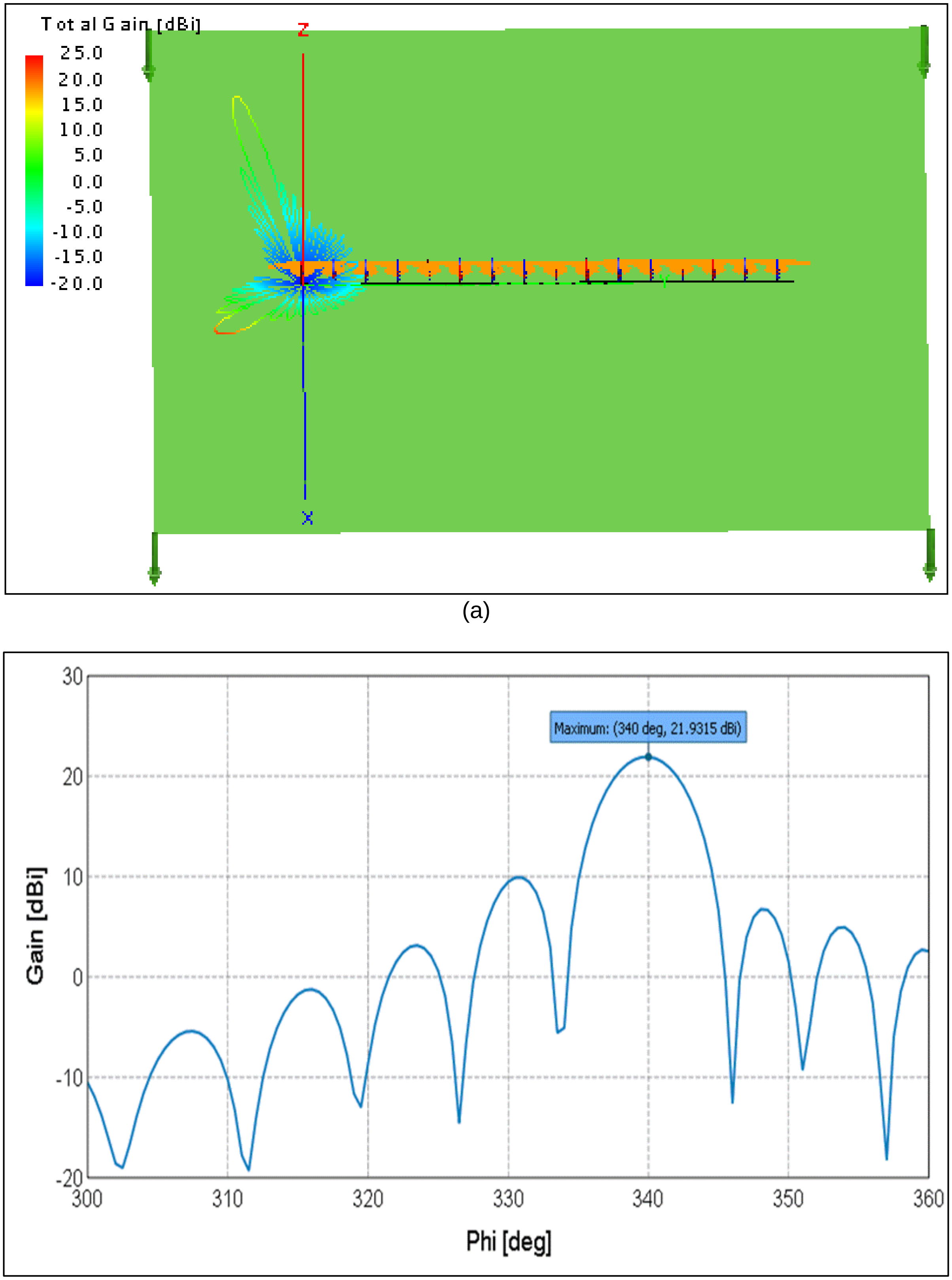

(a)

(b)

Figure 4.27: SANAE IV antenna array simulated with a ground plane having parameters of a sandy clay soil: (a) antenna model, (b) antenna radiation pattern

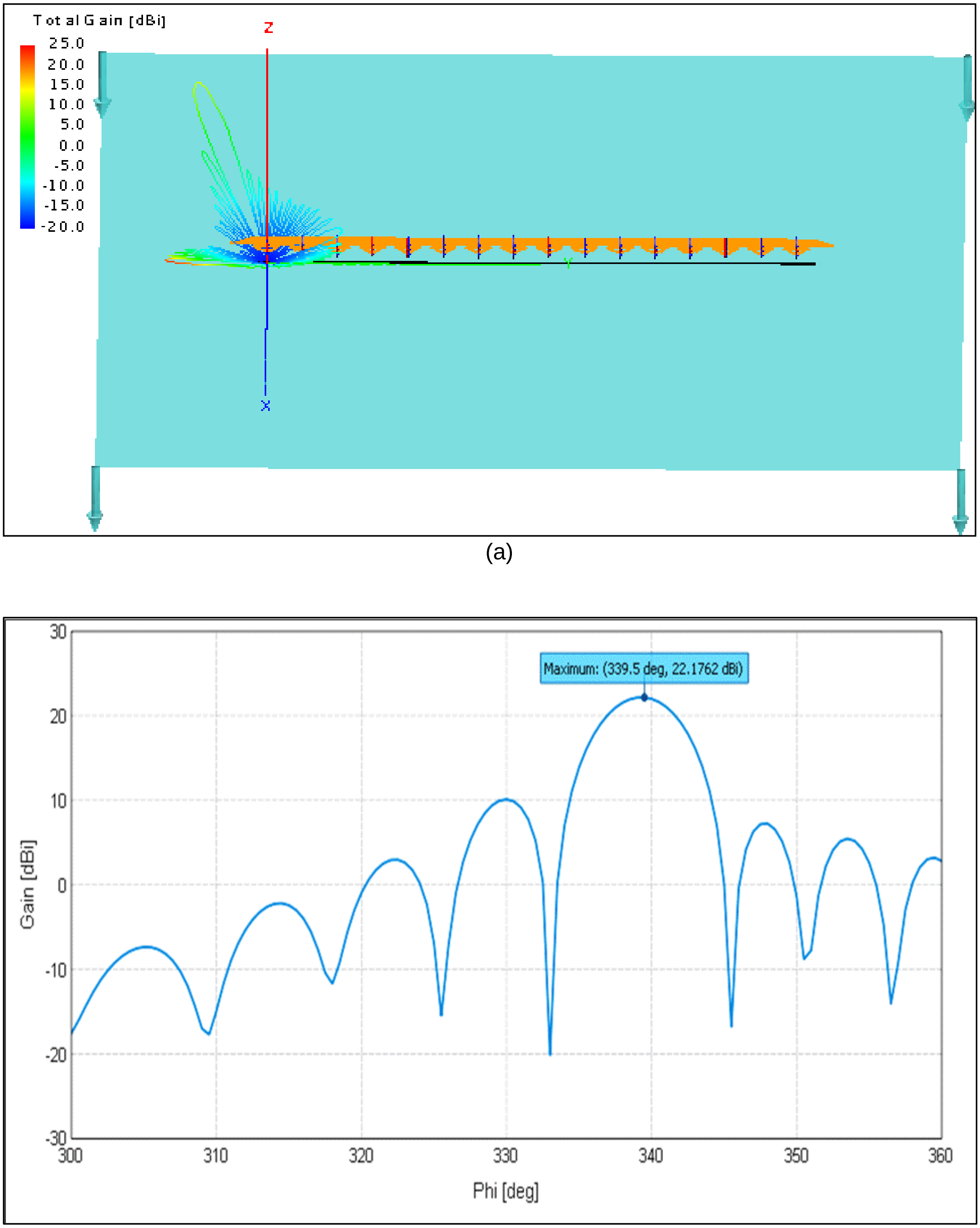

(a)

(b)

Figure 4.28: SANAE IV antenna array simulated with a ground plane having parameters of ice: (a) antenna model, (b) antenna radiation pattern

Having verified the radiation pattern of the modelled array, the reflection coefficient of the antenna was also analysed. Prior to this analysis, the reflection coefficients of other SuperDARN antennas arrays were considered.

At first, Sterne (2010:71-77) in his analyses describes an impedance improvement of Blackstone SuperDARN, after modification of the antenna-baluns. This modification led to a standing wave ratio (SWR) of about 1.3 at 14 MHz. He further describes a close correlation between Blackstone results and that at Wallops SuperDARN (Figure 4.29(a), the graph of -2 turns). The results at Hays SuperDARN for the same modified array solution balun illustrated in Figure 4.29(b) presents an SWR within acceptable range at 14 MHz.

Table 4.3, however, presents SWR measured at SANAE IV during January 2012. The second column are data from the network analyser, while the third column presents data from an SWR meter. It is observed that besides the faulty antenna (antenna element no 1), all other antenna elements have a SWR below 2, which is acceptable. Figure 4.30 presents the measured SWR of one SANAE IV antenna element over a frequency range between 8 MHz and 20 MHz with a much wider bandwidth.

Table 4.3: Standing Wave Ratio measurement from SANAE SuperDARN

Antenna element no	**SWR @ 12.5 MHz (NA)**	**SWR @ 12.5MHz (MFJ)**
1	3.29	3.2
2	1.39	1.5
3	1.39	1.5
4	1.44	1.5
5	1.5	1.6
6	1.4	1.5
7	1.37	1.5
8	1.34	1.4
9	1.32	1.4
10	1.38	1.4
11	1.32	1.4
12	1.34	1.4
13	1.36	1.4
14	1.37	1.4
15	1.38	1.4
16	1.4	1.4

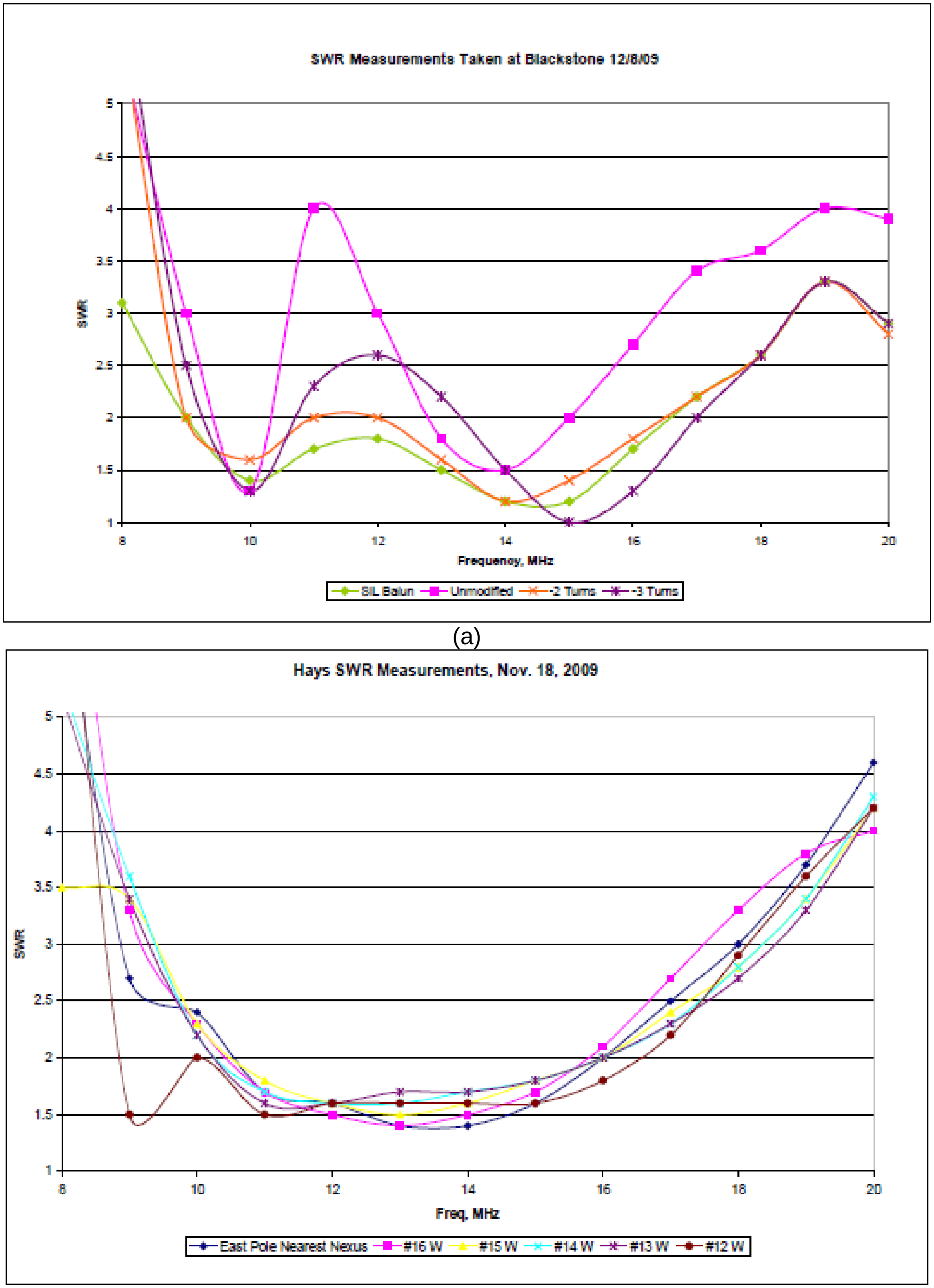

(a)

(b)

Figure 4.29: SuperDARN test measurements: (a) measured SWR of Blackston, (b) measured SWR of Hays (Adapted from Sterne, 2010:78)

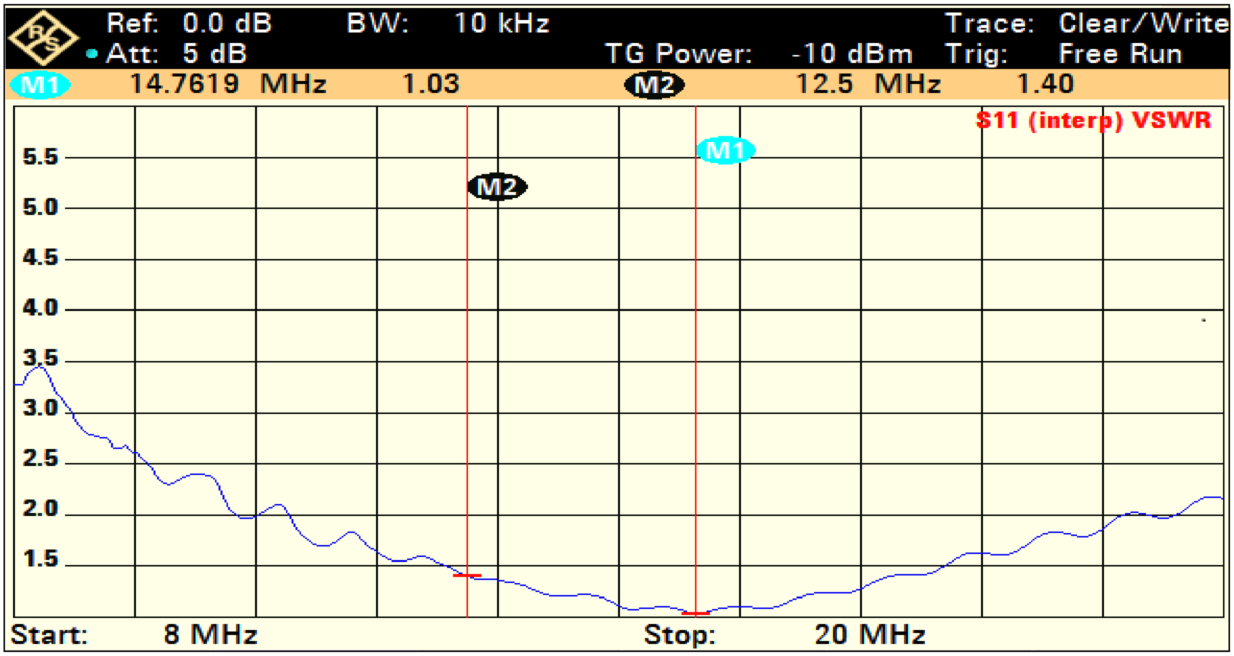

Figure 4.30: VSWR of SANAE IV SuperDARN

The SWR of the simulated array model was thus compared with the above data. To meet these results, the impedance of a solution balun was used. The array solution balun is an impedance transformer that transforms 50 Ω into 1250 Ω, and it has a power rating of 1 kW. This balun is the same as that used at SANAE IV. The simulation results of Figure 4.31(a) illustrates the reflection coefficient of each of the 16 antenna elements. Considering a reflection below -10 dB to be acceptable, one can observe a wide operating bandwidth. The SWR of one of the array elements is illustrated in Figure 4.31(b), and presents a more realistic result, close enough to those measured in Table 4.3 (at 12.5 MHz, SWR =1.825 MHz; at 14.47 MHz, SWR =1.4). It can be concluded that practical results and the simulated results are reasonably acceptable and comparable.

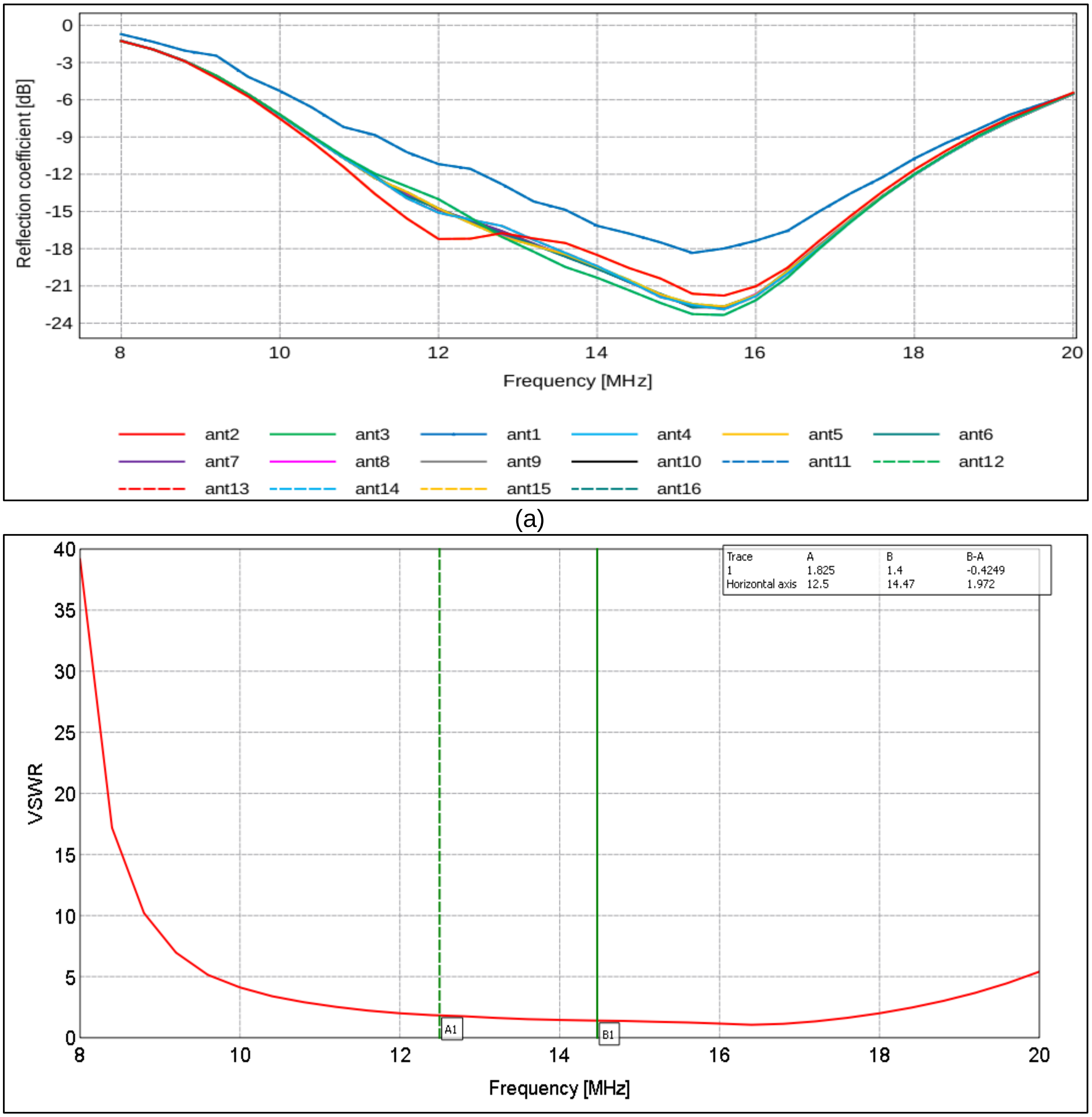

(a)

(b)

Figure 4.31: SANAE SuperDARN antenna response after including the solution balun impedance in the simulation: a) Reflection Coefficient (S_{11}), b) Standing wave ratio

4.4.2 HF antenna on the satellite

The next section discusses the HF antenna on the satellite. The choice of the antenna length and the deployable mechanism is also discussed.

4.4.2.1 Simulation

The basic monopole antenna is a quarter wavelength long at the operating frequency (≈ 5 m at 14 MHz). The method of images in electromagnetics (Balanis, 2005:205) requires the ground plane to be infinite for the above statement to be valid. According to Foged (2010) the ground plane can be assumed infinite (Figure 4.32(a)) when the distance between the antenna feed point and the edge of the plane is at least 2λ at the operating frequency. This assumption is not true for the case of a CubeSat Figure 4.32(b).

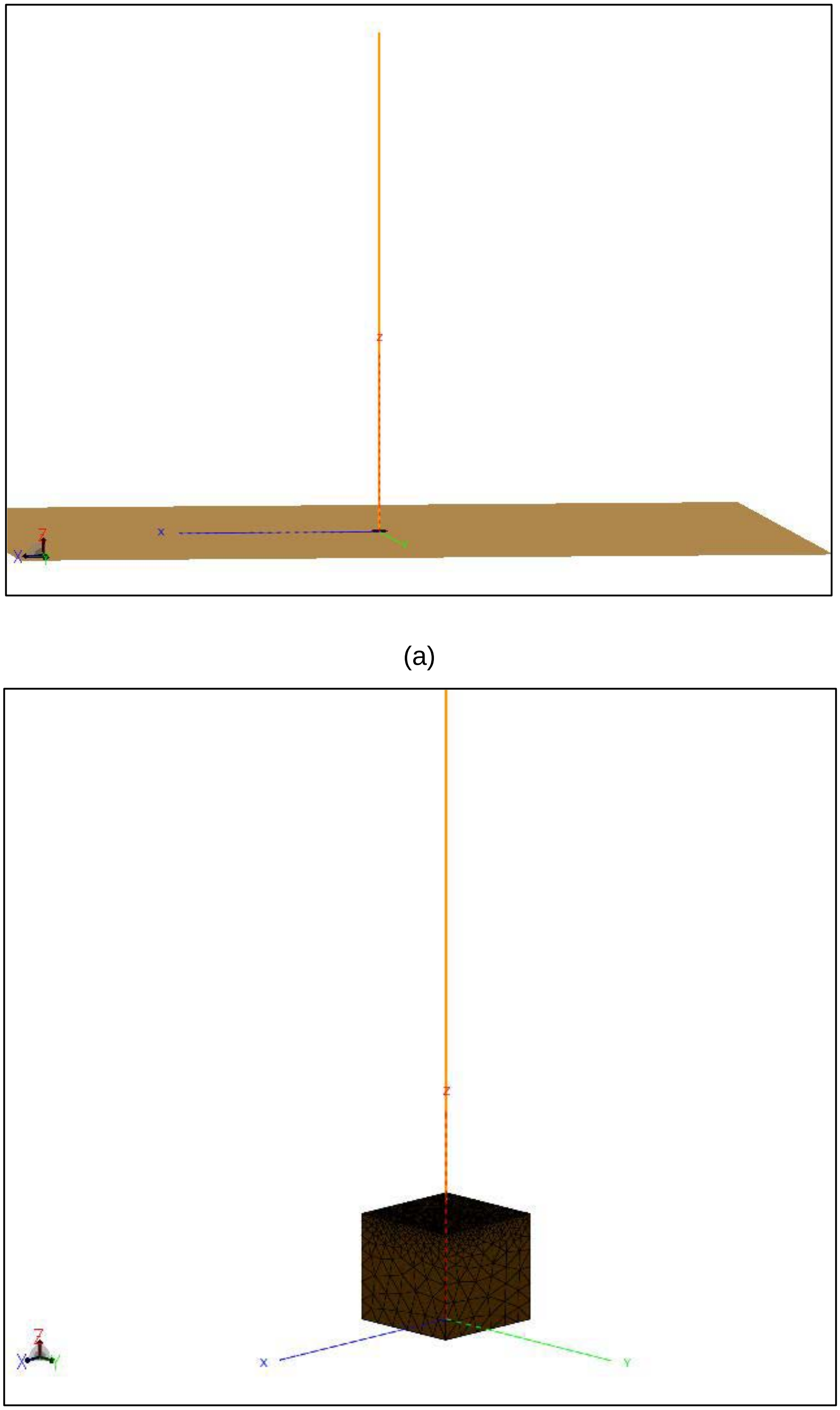

(a)

(b)

Figure 4.32: Comparison between antenna performances with two different ground planes: (a) with an infinite ground plane; and (b) using one CubeSat face as ground plane

It is expected that the antenna behaviour (radiation pattern and impedance) on the satellite differ from the ideal, infinite ground plane, scenario. This is illustrated in Figure 4.33.

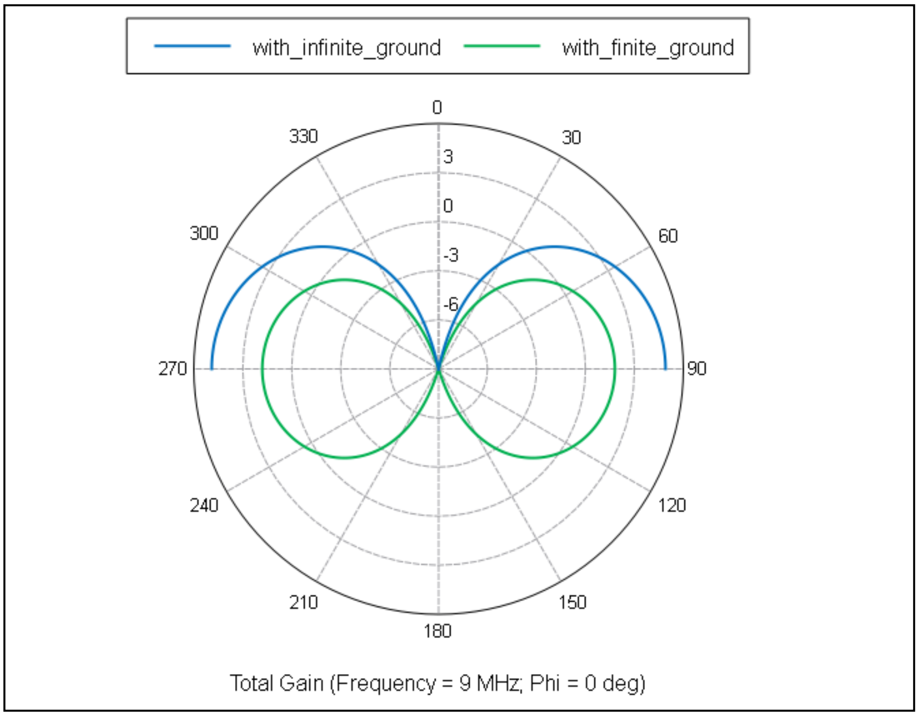

Figure 4.33: Satellite antenna's Radiation pattern: in blue is the radiation of a monopole with infinite ground plane, in green is that of the monopole on a CubeSat

From Figure 4.34, the impedance of the 5 m antenna on a finite ground plane is more reactive than resistive (see Figure 4.34(a) and Figure 4.34(b) respectively). This poses a challenge for the matching system because it results in narrow and sensitive matching requirements

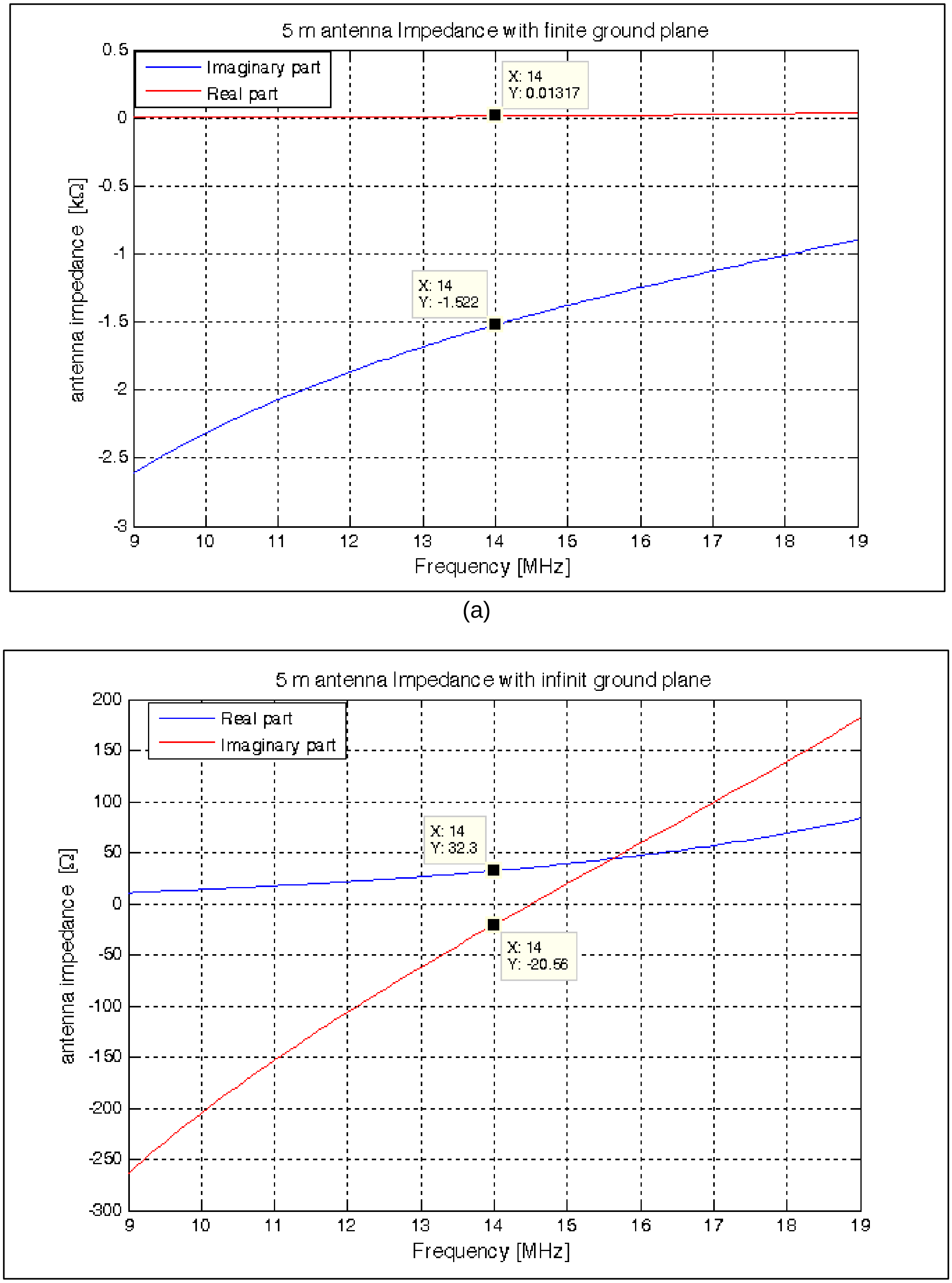

(a)

(b)

Figure 4.34: Satellite HF antenna's Impedance: (a) with a finite ground plane; and (b) with an infinite ground plane

From the above graphs, the respective ground planes lead to the following antenna impedances at 14 MHz.

- Finite ground plane Z=0.013 - j1522 kΩ
- Infinite ground plane Z=32.3 - 20.56 Ω

To reduce the antenna reactance, the antenna length was increased to 10 m. According to simulations in Figure 4.35(a), the antenna impedance Z at 14MHz is:

$$Z = 1.551 k\Omega - j0.082\,\mathrm{k}\Omega$$

Therefore, with an impedance transformer, one can match the antenna to the transmitter.

The unmatched reflection coefficient of the 10 m antenna is illustrated in Figure 4.35(b), and it is observed that a matching circuit is still required even with 10 m antenna (S_{11} = -0.544 dB at 14 MHz); however, the design of this matching network was not part of the research scope. Therefore, this is not covered in this document.

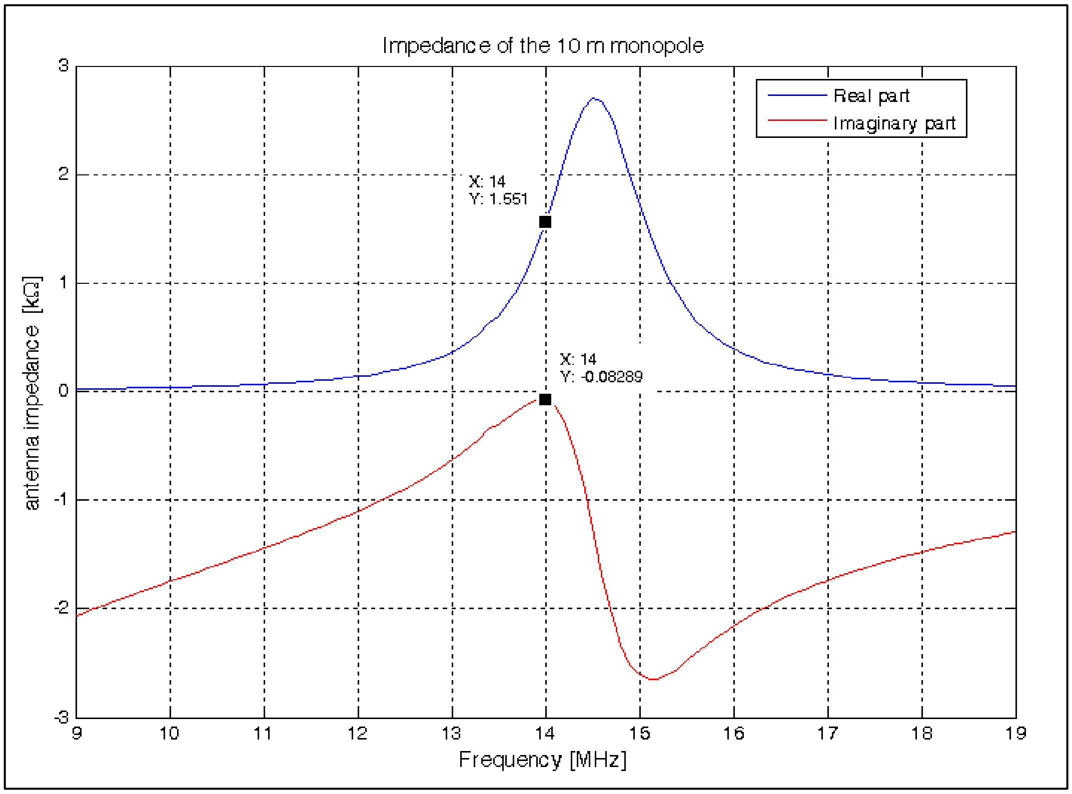

(a)

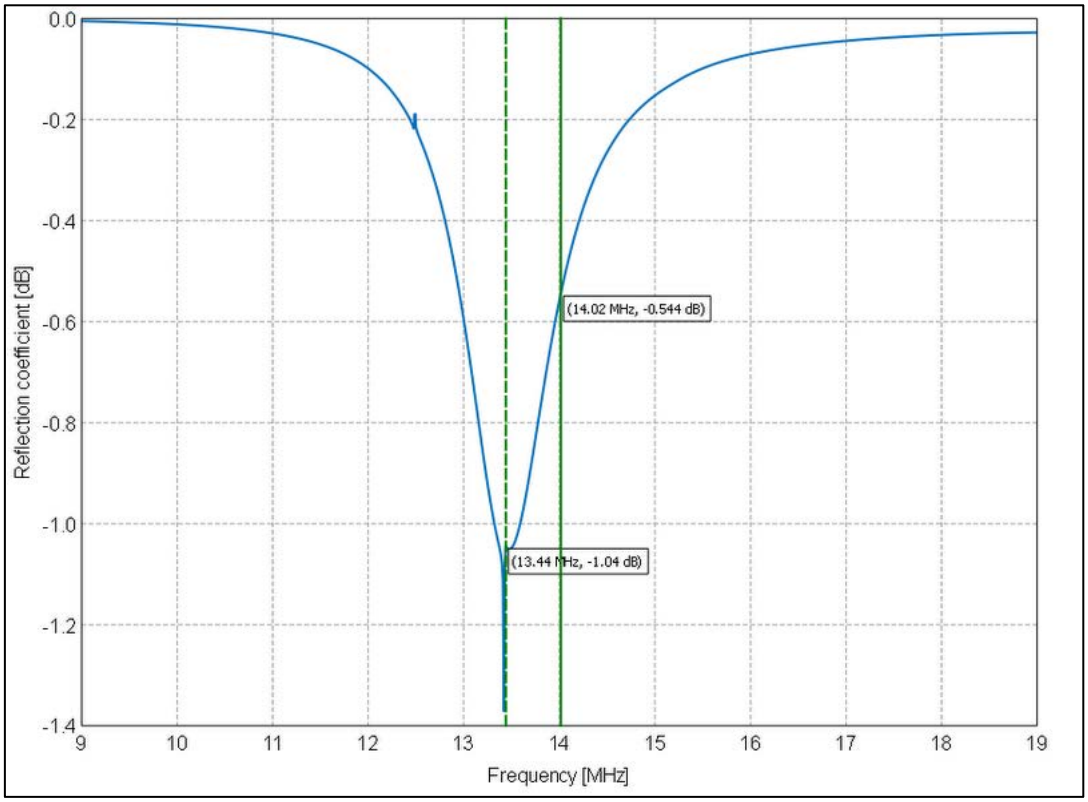

Figure 4.35: Impedance and reflection coefficient of the 10 m monopole on the satellite

Although the 10 m antenna seems to have resolved the problem of high reactive impedance, the other challenge that this system poses is the deployment mechanism of such a long antenna, since there is not enough space on the satellite to accommodate large systems. The following section discusses this antenna deployment mechanism.

4.4.2.2 HF antenna deployment mechanism

The HF antenna needs an aperture of half wavelength to radiate efficiently. This is about 10 m at 14 MHz. The antenna element is made of a flexible cable with a small tip mass attached to the open end and held by a little nylon wire (Figure 4.36 (a)). When the satellite passes over the GS at CPUT, a command is sent to the satellite enabling the deployment motor. The nylon wire burns, and the motor will deploy the 10 m antenna while the satellite is put in a Y-Thomson spin to keep the antenna extended.

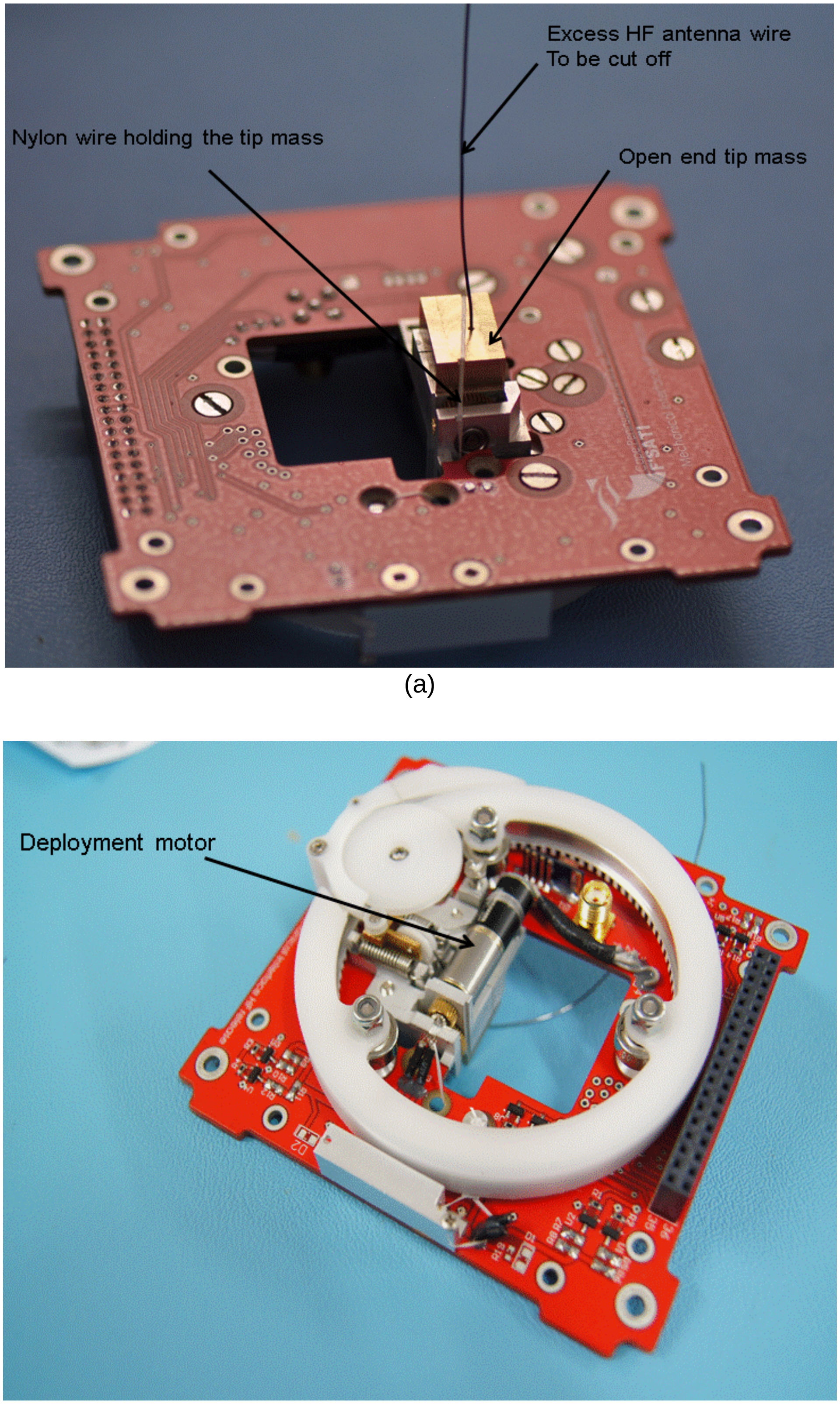

(a)

(b)

Figure 4.36: Satellite HF antenna deployment mechanism: a) prototype board, b) flight model

4.4.3 HF antenna at CPUT

This section discusses the design and simulation of the HF antenna at CPUT Bellville campus. The antenna was first simulated in FEKO, and from the obtained performance was the physical antenna built.

4.4.3.1 Simulation

The antenna modelling was done in FEKO (see Figure 4.37(a)). The parameters for a sandy clay ground were used in the modelling of the ground plane. The total height from the antenna to the ground is 21 m representing the height of the building on which it is located. The simulation was swept from 9 MHz to 19 MHz. The ground plane has considerable influence over the antenna performance and thus, overall beam pattern is affected resulting in the maximum gain of 3.8 dBi at 90° elevation angle (Figure 4.37(b) and Figure 4.38(a)) with side lobes at 5 dBi. The refection coefficient of Figure 4.38(b) shows a good match (-28 dB) at 14.1 MHz. Considering a reflection coefficient below -10 dB to be acceptable, a reflection bandwidth of 645 kHz is obtained.

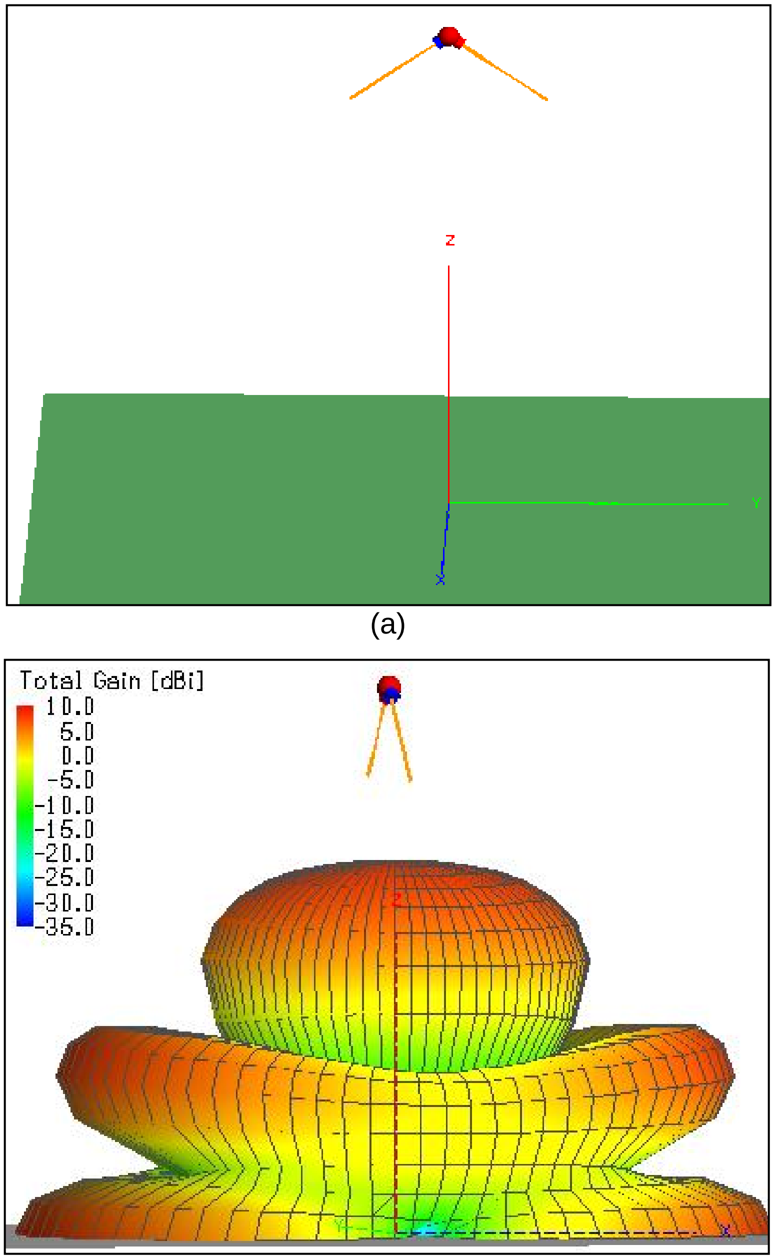

(a)

(b)

Figure 4.37: CPUT HF antenna simulation: (a) antenna configuration, (b) antenna radiation pattern.

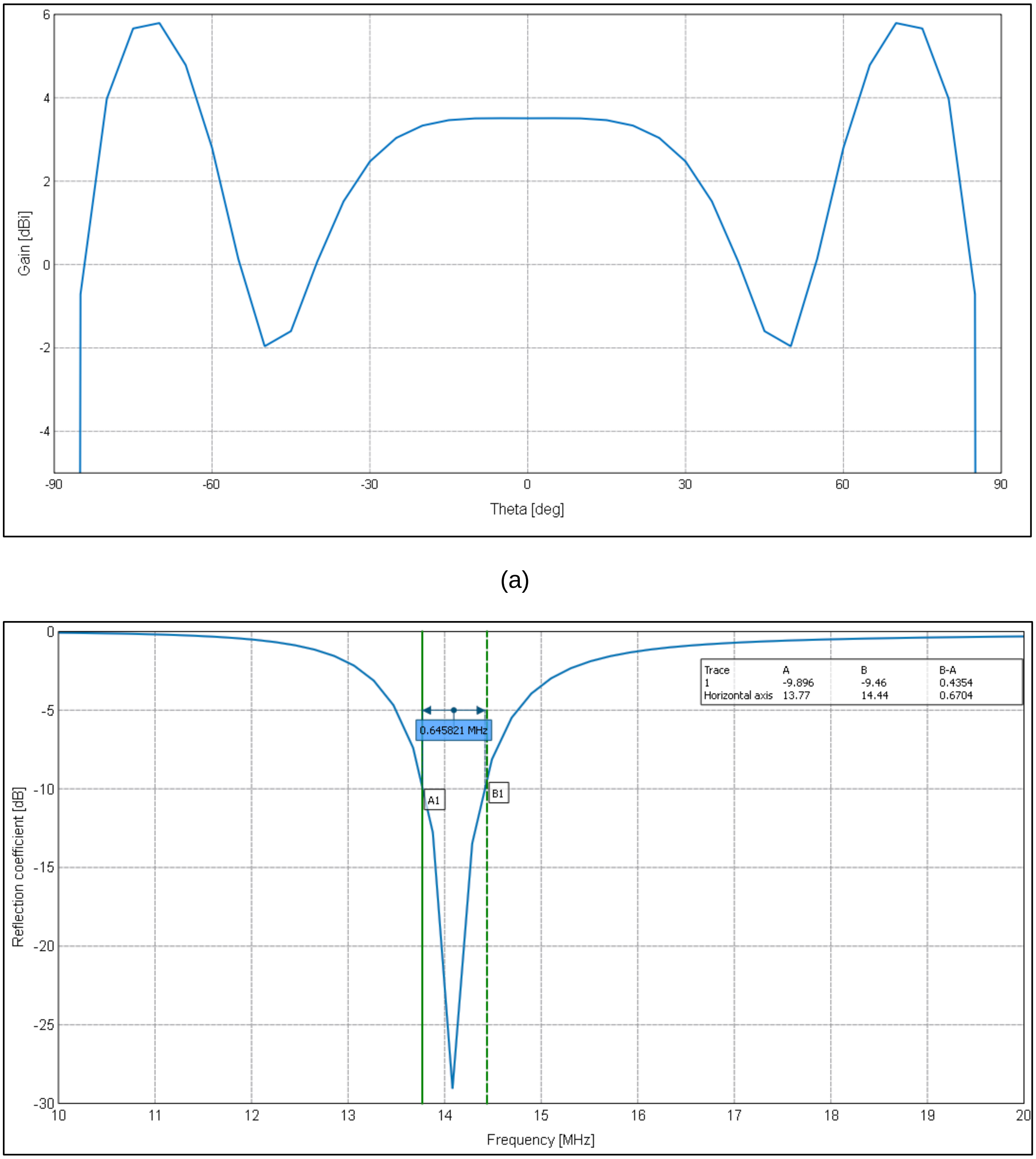

Trace	A	B	B-A
1	-9.896	-9.46	0.4354
Horizontal axis	13.77	14.44	0.6704

(a)

b)

Figure 4.38: CPUT antenna simulation results: (a) radiation pattern, (b) reflection coefficient

4.4.3.2 Physical implementation

Materials used for the construction the antenna are given in Figure 4.39. The antenna elements are made of a copper wire having 1.5 mm diameter.

Figure 4.39: Required materials used for construction of the antenna

Figure 4.40 shows the antenna's physical dimensions. Since the antenna is 20 m above the ground (building height =14 m and mast height = 6 m), these values where used to determine the required apex angle.

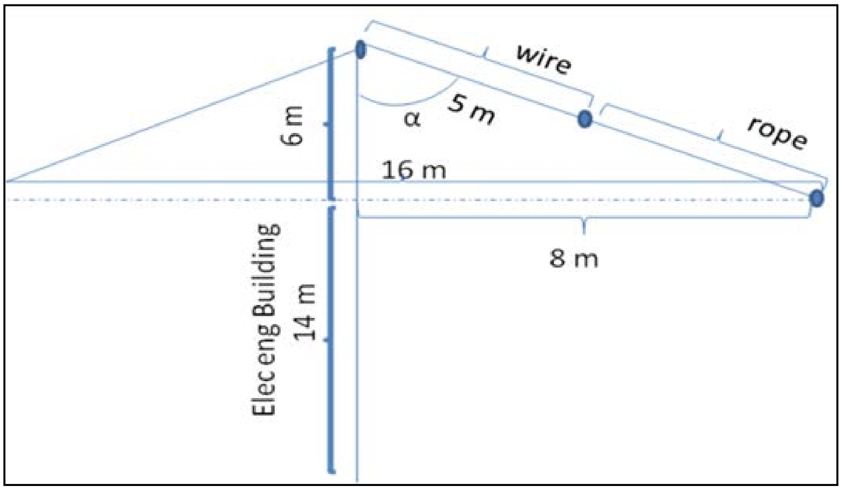

Figure 4.40: Physical implementation of the antenna

The apex angle is calculated from Equation 4.4:

$$\alpha = \tan^{-1}\left(\frac{8}{6}\right) = 53.13^{\circ}. \qquad 4.4$$

The apex angle is 2α=106.26°, which still meets the specifications (90° < 2α <160°) (Balanis, 2005). The motivation leading to this is because if the apex angle is less than 90°, there will be two parallel radiation patterns, which may lead to their cancellation. Therefore, for inverted V dipole antennas, apex angles should be greater than 90°. The antenna was mounted 3 m up on the VHF/UHF mast on a metallic pipe, which sticks out about 1.5m from the main mast. The arrangement is such to avoid the VHF/UHF mast to act as a screen to the radiation pattern of the HF antenna. The coaxial cable is connected to the feed point and runs down to the GS room, where it is connected to the receiver. The distance between the antenna and the receiver is about 10 m. Due to this long distance, there may be significant signal loss in the transmission line.

Using an antenna analyser, the SWR was measured to be 1.6 at 14 MHz, from which the reflection coefficient of the line was calculated (Equation 4.5):

$$SWR = \frac{1+\Gamma}{1-\Gamma}, \qquad 4.5$$

$$\Gamma = \frac{SWR-1}{SWR+1} = 0.23.$$

The reflection coefficient is 0.23, which means that 77% of the transmitter's power is radiated into space, and 23% is reflected. The elements' length was tuned to reduce the reflection coefficient. This resulted in an increase of the SWR. It was therefore concluded that the elements were shorter than the calculated lengths. The final VSWR = 1.4 provides a reflection coefficient of 0.17, therefore, 83% of the transmit power is radiated by the antenna. This is acceptable.

To test if the antenna was works properly, a communication link between the amateur radio operator at CPUT (ZS1GAM) and the amateur radio operator at SANSA SS (ZS1HMO) was successfully established. A few other amateur radios were received including the reception of some beacon signals around 15 LT, having significant signals strength.

4.5 HF beacon development

Table 3.5 presents the transmitter specifications. The block diagram in Figure 3.4 shows the bus architecture of ZACUBE-1. Each subsystem in this architecture is controlled by its individual microcontroller and is connected to the bi-directional data lines (I^2C bus) to acquire instructions from the on-board computer. A single controller, however, manages both the beacon payload and the camera, as they are prototyped on the same board due to size constraints. The beacon payload development is detailed in the following section.

4.5.1 RF and modulation

To generate the required RF signal, an RFID transceiver topology was opted for, owing to its low cost and its miniaturised size. This transceiver is a temperature controlled Texas Instrument (TI) chip (RI-R6C-001A). The system works according to the “reader talks first” principle. This means that the transponder keeps quiet until the reader sends a request to it; the reader being the microcontroller. Initially, the transceiver is off and turns on by “low” to “high” transitions on the “data in” line (see Figure 4.41) after a rising edge of the clock pulse (Figure 4.41 pin 15). In this state, the RF power is transmitted once the transceiver is configured. Configuring the transceiver entails the selection of the following:

- The mode of operation;
- The RF protocol;
- The modulation depth;
- The modulation scheme; and
- The data rate and bit parity.

The RF carrier will, thereafter, be generated and will be composed of one carrier amplitude modulation. All the above communication parameters are sent in one byte. This byte is the required protocol, and is thus selected as an encoder (see Figure 4.43 encircled in purple). Following this sequence, the transceiver is ready to receive any intelligence from the microcontroller, the length of which depends on the message that is transmitted. RF power is available at the transistor's drain TX_OUT (Figure 4.41, Figure 4.42, pin 2), and is matched to the 50 Ω load by an external matching network. For more information about the transceiver, refer to Appendix C.

The frequency of the carrier signal depends on the crystal oscillator that is used. The nominal crystal frequency is 13.56 MHz (Figure 4.43 encircled in red). However, crystal frequencies between 4 to 16 MHz may be used to generate the internal system clock. Output power may be varied by adjusting the supply voltage. The minimum acceptable voltage is 3 V, which will produce an RF power of 180 mW and a typical 5 V supply voltage will produce 200 mW.

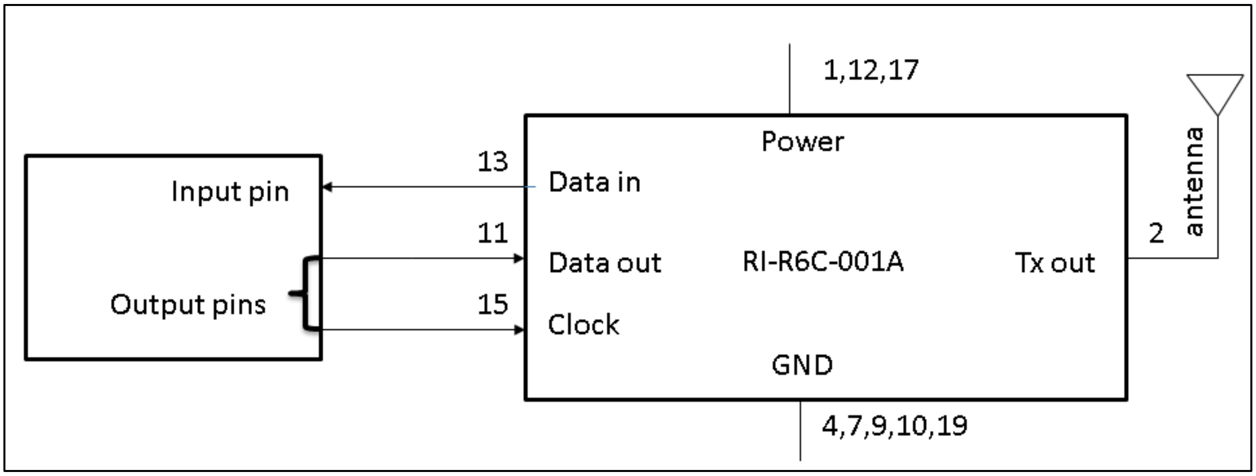

Figure 4.41: Simplified block diagram of the beacon transmitter

The internal structure of the transceiver is shown in Figure 4.43. There are three building blocks, namely the transmitter, receiver and digital section. As in the transmitter section, the receiver decoder demodulates RF signal into a data stream, which is read by the microcontroller on the D_out line (Figure 4.41). The digital section is responsible for modulating or demodulating the transmitted or received message, respectively (Figure 4.43 encircled in purple). Figure 4.42 shows the transceiver pin out and Table 4.4 defines acronyms that are used to describe the various pins.

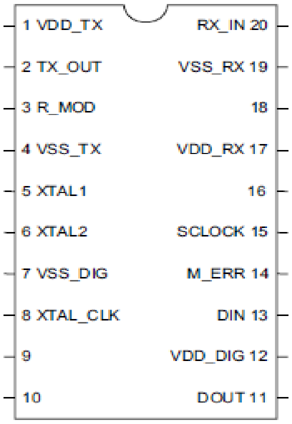

Figure 4.42: RI-R6C-001A transceiver pin out

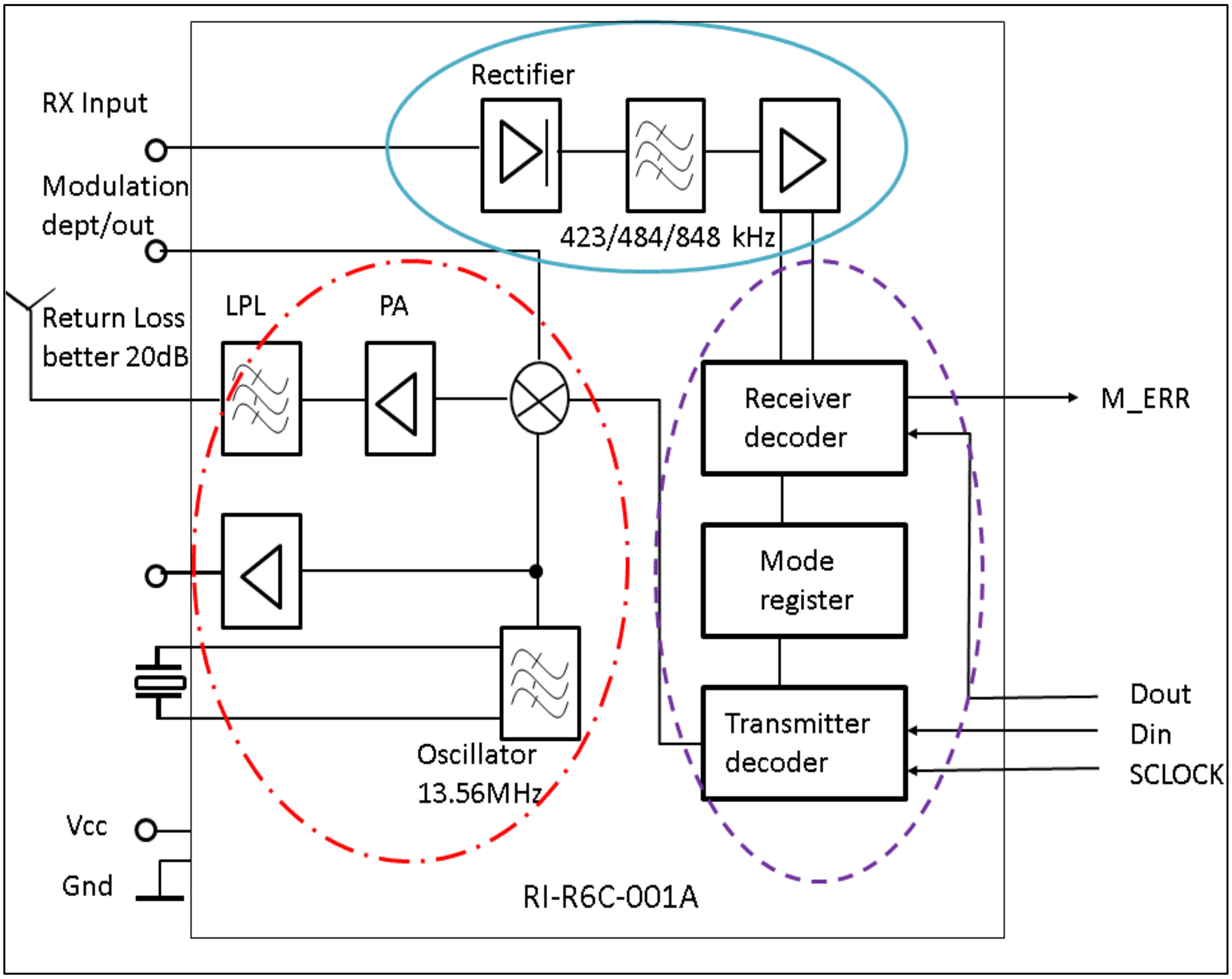

Figure 4.43 Simplified block diagram of the transceiver with its building blocks: the transmitter section is encircled in red; the receiver in blue; and the digital section in purple.

For simplicity purposes, the communication mode that was used was the direct mode. Other modes require long coding (for example, register mode), which are not efficient for the required application. The modulation technique that was adopted was Morse code. In the Morse code modulation technique, a constant amplitude and frequency is switched on and off and the information is carried in varying durations of groups in the "on" and the "off" periods. This technique can be regarded as a continuous wave, and is used by many radio amateurs, even when the carrier to noise ratio is less than 0 dB. Thus, owing to this advantage, signals coded in Morse are immune to noise, and can thus surpass even noisier channels.

Table 4.4: List of connections

Pin Number	Signal name	Description
1	VDD_TX	Transmitter power supply
2	TX_OUT	Output transistor drain connection
3	R_MOD	External resistor to set 10% modulation depth mode
4	VSS_TX	Transmitter section ground
5	XTAL1	Pin 1 of crystal resonator
6	XTAL2	Pin 2 of crystal resonator and external system clock
7	VSS_DIG	Digital section ground
8	XTAL_CLK	Buffered output for crystal oscillator
9	Not used	Grounded for normal operation
10	Not used	Grounded for normal operation
11	DOUT	Data output for serial link
12	VDD_DIG	Digital section power supply
13	DIN	Data input for serial link
14	M_ERR	Manchester error protocol flag
15	SCLOCK	Serial link clock
16	Not use	Leave open for normal operation
17	VDD_RX	Receiver section power
18	Not used	Leave open for normal operation
19	VSS_RX	Receiver section ground
20	RX_IN	Receiver input

4.5.2 Software development

The compiler used is the PICBASIC PRO compiler, and the code is written in the MPLAB IDE v8.02 platform, in PICBASIC PRO language. The microcontroller used for the prototype is a

PIC16F690. It is a microchip device, which has 256 bytes of memory with three I/O ports A, B, and C, including two I^2C pins on port B (see Appendix C (b)).

The programmer used is TOP2005+ universal programmer, with Topwin v5.99 software. Figure 4.44 shows the software development lifecycle that was adopted for the development of the software.

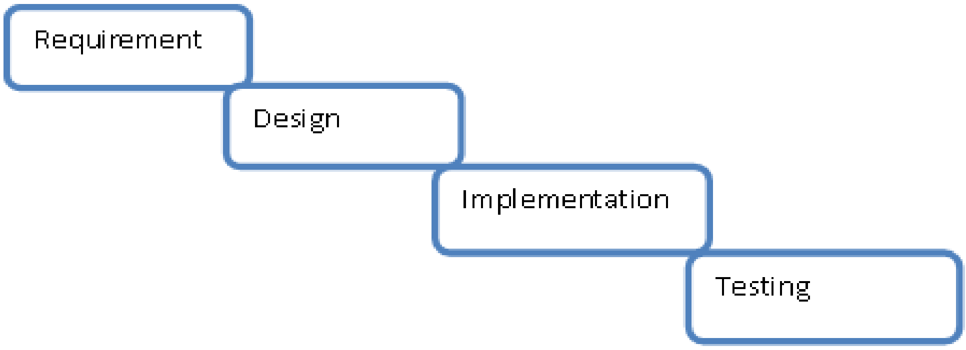

Figure 4.44: Software's lifecycle diagram

- **Requirements**

The software must acquire commands and perform relevant tasks, in accordance to the design's operational requirements. The software requirements are detailed in the design section below.

- **Design**

The On-board Computer (OBC) is scheduled to communicate with the microcontroller (for example, when passing over the polar regions). The software is, therefore, able to interpret the OBC requests and make them high-level priorities (by stopping any alternative task). It also manages communication between the OBC and the microcontroller and between the microcontroller, and the transceiver (BTX). The OBC sends the command over the I^2C to the microcontroller, which analyses and executes these commands. Initially, the microcontroller is in power saving mode (sleep or idle); the micro wakes up from this mode with an I^2C interrupt, which is followed by a ***turn on*** command. The OBC will send a ***turn off*** command after a period of about 12 minutes (once the satellite has passed the ground station).

- **Implementation**

The OBC (master) initiates communication by sending a ***start bit*** (S), then followed by a ***7-bit*** slave address (PIC micro), starting with the most significant bit first (MSB) and the ***read or not write bit*** (R/not W). The microcontroller in turn replies by sending an ***acknowledgment of***

receipt (ACK). The master then sends the data, which in this case will be either ***turn on*** or ***turn off*** commands. The slave replies by acknowledging receipt of this, and the communication stops with the master sending the ***stop bit*** (P) (see Figure 4.45).

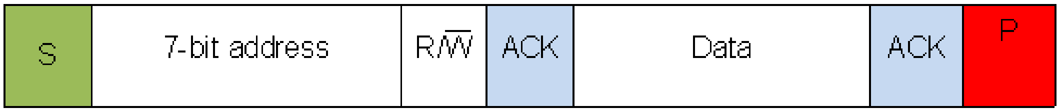

Figure 4.45: I^{2}C master-slave addressing

Following the receipt of the above OBC commands, the microcontroller initiates communication with the BTX by sending the start bit (S1): This is achieved by raising the clock signal (CLK), while keeping the data in line (DIN) low. DIN is then raised while CLK remains high. After a few millisecond, CLK is dropped, while DIN remains high. Figure 4.46(a) shows the communication sequence. Data is only latched in after each rising edge of the CLK (see Figure 4.46(b)). To stop the communication, the microcontroller sends ES1 to BTX. The piece of code that follows presents the configuration byte that prepares the BTX for communication. The communication protocol between the transceiver and the PIC is a modified I2C protocol (customised I2C).

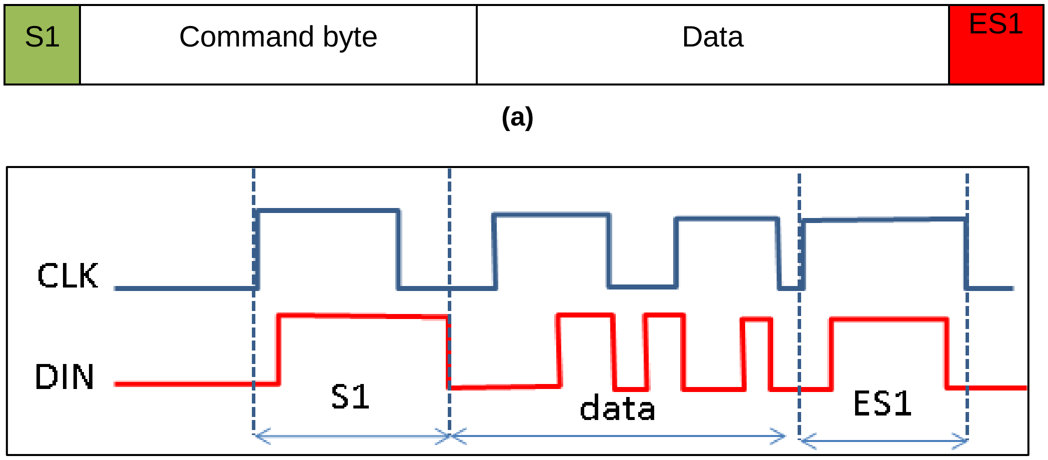

(a)

(b)

Figure 4.46: Microcontroller BTX communication: a) data structure, b) required signal transitions

```
 INCLUDE "HEADER.bas"
```

The header file contains the definition of the variable, pin configurations and a routine for testing the microcontroller’s functionality. The instruction sets below describe the S1 routine.
The clock line is represented by CLK, and the input data line by DIN.

```
'SET S1
'===================================================
'S1 (start bit)
SWITCH_ON:
CLK = 0
DIN = 0
PAUSE 0
CLK = 1
DIN = 0
PAUSE 0
CLK = 1
DIN = 1
PAUSE 0
CLK = 0
DIN = 1
PAUSE 0
CLK = 0
DIN = 0
PAUSE 0 'WAITING FOR 1mS
END
‘End of S1
```

Following the configuration byte is the command byte. The BTX register is configured with this command and the content of this byte is described in Appendix C (a). All the alphabetical characters are written in Morse code (dots and dashes) in the message algorithm, from which a look up table is generated. To transmit a character in the equivalent Morse code, the carrier signal is turned on and off, according to the equivalent Morse code sequence. The “on” time represent a dash or a dot depending on the length of the pulse. For example, the dashes are three times longer than the dots.

Taking an example of the following message; ZS1HMO 2011 ZACUBE1

The ZS1HMO represents the SANSA SS callsign, 2011 is the year that the software was written and ZACUBE1 represents the satellite’s name. Each of the above characters is first converted into their corresponding Morse code. The international Morse code chart is found in Appendix D (a). For example the character ‘A’ has as Morse code ●▬. Thus, to write ‘A’ the following steps are followed. Moreover, this constitutes the basic idea of the Morse code modulation that was used to program the above message.

```
‘Transmitting a character “A”
'==========================================
INCLUDE "config.bas"
INCLUDE "MORSE.BAS"
'==========================================
PAUSE 1000          ‘waiting for the transceiver to get ready
LOOP:
GOSUB SWITCH_ON     ‘writing a dot
PAUSE 10              ‘this produces the required pulse width
GOSUB SWITCH_OFF    ‘end of a dot
PAUSE 20              ‘this delay allows to differentiate between a dot and a dash
GOSUB SWITCH_ON       ‘beginning of a dash
PAUSE 30              ‘producing the required pulse width
GOSUB SWITCH_OFF    ‘end of a dash
END
'===========================================
```

In the file MESSAGE.bas, the entire message is written and is just included in the main code. A part of the code can be found in Appendix D (b).

To validate the code, a dual input oscilloscope is used with one channel connected to the clock line and the other channel to the data line. It is observed that the modulated signal has additional glitches on both the rising and falling edges. By connecting 1 kΩ resistors on each microcontroller input/output line and grounding all the active high lines of the transceiver chip, the magnitude of these glitches are reduced. The output of Figure 4.47 is visualised by the oscilloscope. This output is a representation of the encoded message in Morse code. The message on the oscilloscope screen is interpreted as “ZACUBE”, which is a portion of the “ZS1HMO 2011 ZACUBE1” message generated.

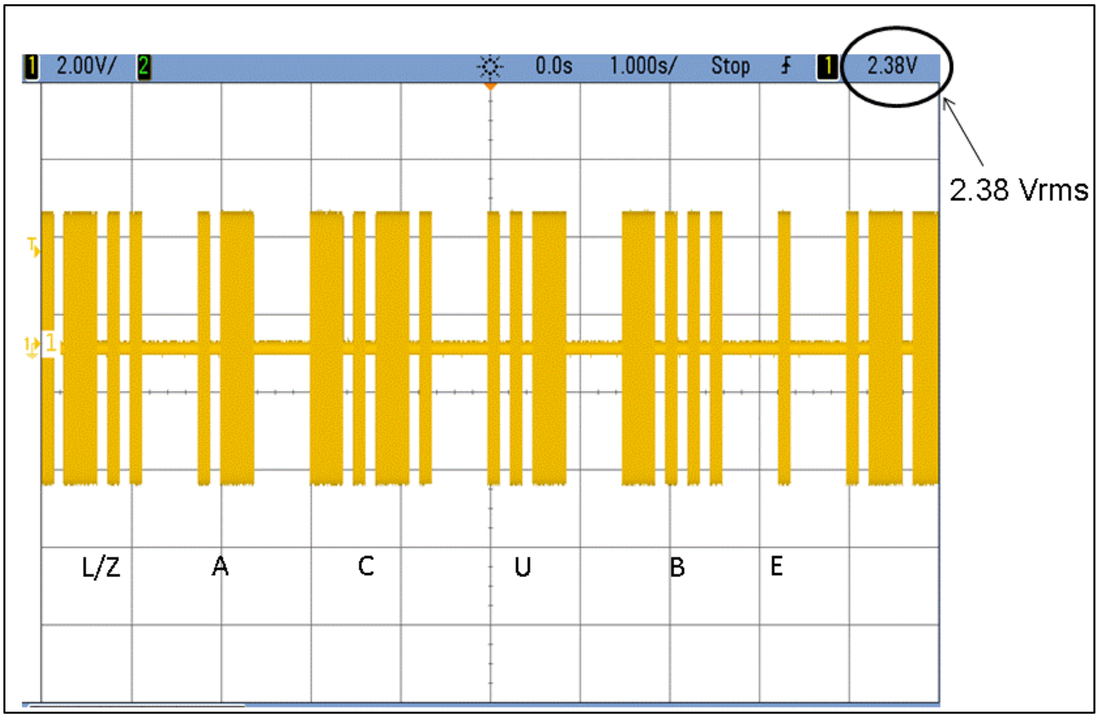

Figure 4.47: Transmitted Morse generated in the microcontroller

The printed circuit board (PCB) shown in Figure 4.48 was developed by using FR-4 board due to its low cost and its better dielectric constant compared to other materials such as FR-5, BT and Cyanate Esther, as mentioned in a survey (Ritchey,1999)(see Appendix C (c)). The schematic diagram and the assembly drawing are also found in Appendix C (c).

- **Testing and validation**

The flight model of the above prototype was developed in-house after the evaluation of the prototype. The operating frequency depends on the crystal oscillator that is used. In this case, 14.745 MHz was used due to its availability during the prototype development time. 14.099 MHz crystal oscillators are not standard off the shelf crystals. Thus, the crystal oscillator had to be customised for this frequency requirement.

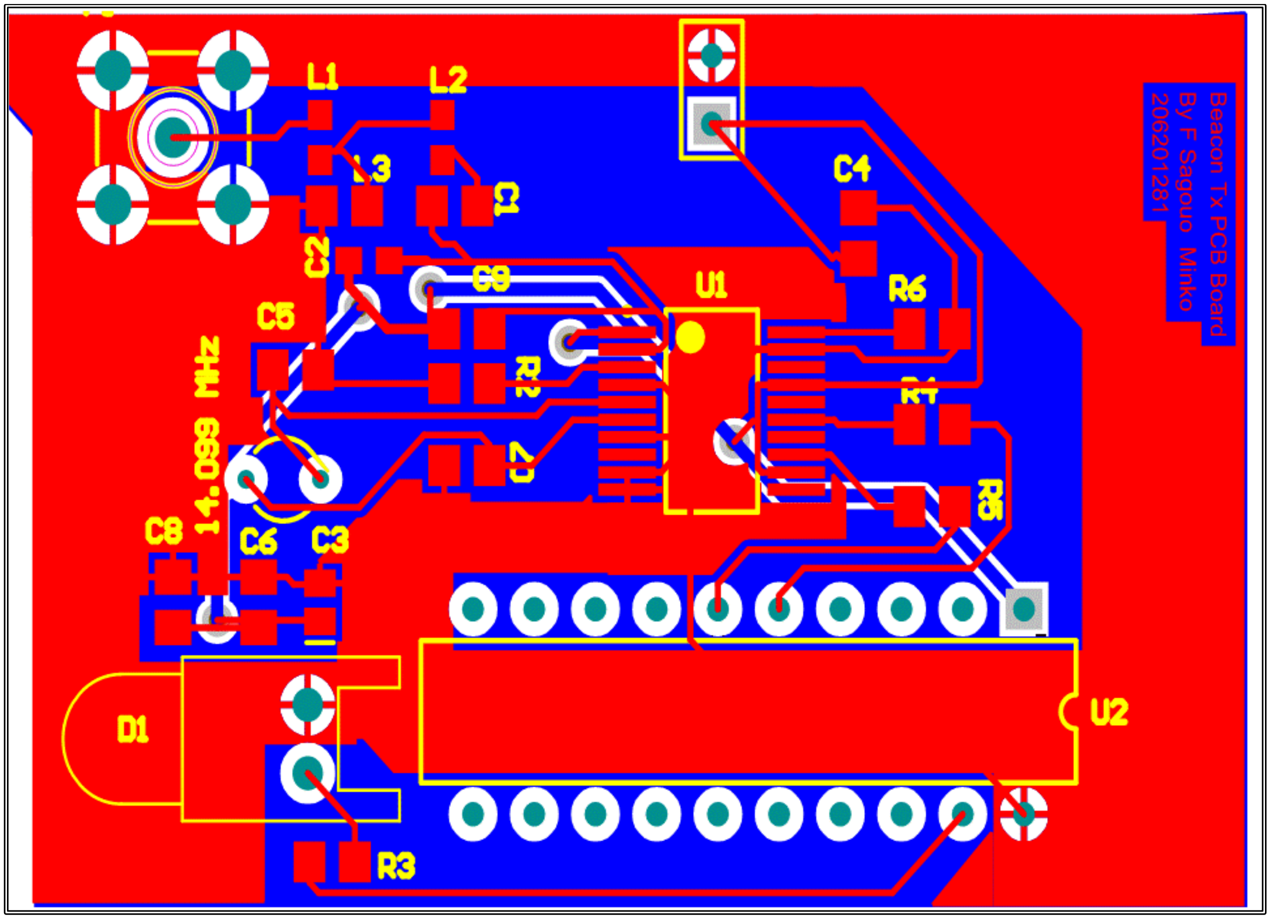

Figure 4.48: PCB prototype of the transmitter

Using a spectrum analyser, and a 15 dB attenuator, the transmit power is measured to be 5.905 dBm (see Figure 4.49) taking the noise floor at -70 dBm. The overall power was evaluated to be 20.9 dBm, and its Watts equivalent is:

$$P_{t(\mathrm{dB})} = 10\log_{10}\left(P_{t(\mathrm{mW})}\right), \tag{4.6}$$

$$P_{t(\mathrm{mW})} = 10^{\frac{P_{x(\mathrm{dB})}}{10}}, \tag{4.7}$$

thus,

$$P_{t(\mathrm{mW})} = 10^{\frac{20.905}{10}} = 123\,\mathrm{mW}. \tag{4.8}$$

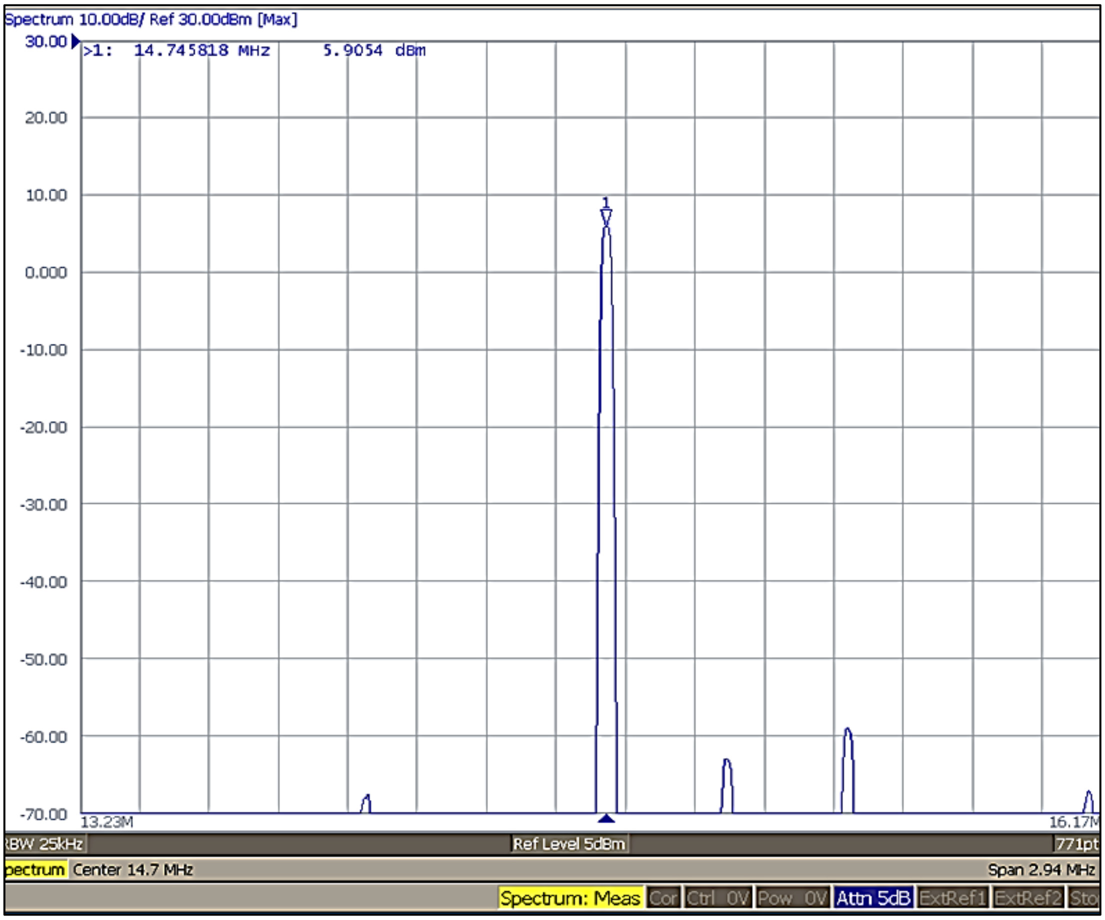

Figure 4.49: Measured output power of the transceiver using a spectrum analyser

To verify the correctness of the encoded data, the transmitter was moved 300 m away from the receiving antenna connected to a 5 m wire as antenna without any matching. In the GS, the radio receiver was interfaced with the computer through the audio channel. The Morse code demodulating software was installed on the computer. This software receives the audio signal spectrum, and has two detection levels; a cleared signal is received at the first level as a “1”, and the signal below the second level is considered as “0”. Since the carrier signal is switched on and off according to the transmit character, this is thus detected by the software, and is then converted to text, as shown in Figure 4.50.

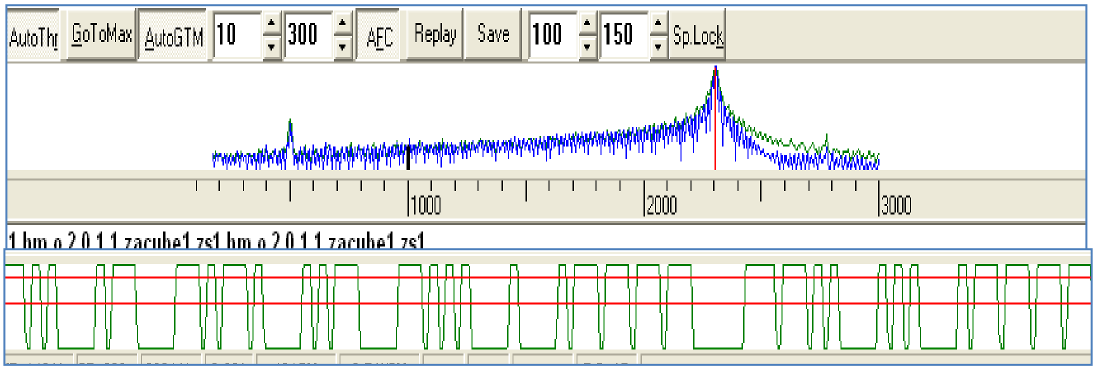

1 hm o 2 0 1 1 zacube1 zs1 hm o 2 0 1 1 zacube1 zs1

Figure 4.50: **Decoded Morse code signal written into a text file**

4.6 Summary

The first part of this chapter discussed the coverage of the ZACUBE-1 with respect to the orbital inclinations. A range of inclinations for which the satellite would be visible at SANAE IV was presented, including a range of expected elevations corresponding to visible overpasses.

A propagation analysis was conducted to evaluate the variation of the LUF with respect to seasons, location and time of the day. Using space weather data and mathematical models the LUF for expected satellite elevation angles were determined.

An analysis of the SANAE IV antenna performance was done using two ground planes. Using the conductivity and the relative permittivity of sandy soil and that of ice, two grounds were simulated. The results from SANAE IV antenna in free space was compared with those with ground planes. An analysis of the TTFD was also done to investigate the performance of a single array element located at SANSA SS.

Furthermore, the simulation of the satellite HF antenna was done to investigate whether the antenna performs as expected. A monopole of 5 m was first considered followed by a 10 m one due to drawbacks showed by the 5 m monopole antenna. Both antennas were simulated on a cuboid of 1000 cm^3, to evaluate their performance.

Finally, the chapter discussed the design of the CPUT HF antenna, as well as the development of the beacon transmitter. It also highlighted the techniques used to generate the Morse codes using the PICBASIC Pro programing language.

Chapter 5 Discussion of results

5.1 Orbit and coverage

From orbital analyses for the given orbital elements, the orbital period and the speed were found respectively to be 97 min and 6.628 km/s. Maximum overpass time of each orbit above the radar is 12 minutes. There are about 15 orbits per day globally, each of them converging over to the poles. With 15 orbits/day passing over SANAE IV, if one antenna element is characterised a day, it will take sixteen days to fully characterise the entire array. Only about 3 to 4 orbits/day maximum will cross over South Africa (about 2 overpasses if passes below 10° elevation are ignored). In Section 4.2 it was shown that, although the inclination affects the satellite coverage, other parameters should not be taken for granted in the coverage analyses. In Figure 4.1, for instance, it is shown that the altitude and the elevation angles also play an important role in the determination of the angle of coverage. In other words, with higher altitudes, such as in geostationary orbit, larger areas may be covered with narrow beam, low elevation antennas as compared to the coverage from the instruments on LEO satellites.

The coverage analyses of Chapter Two showed visually how various inclinations affect the satellite's footprint. It was observed that the satellite will not be visible at SANAE IV for up to almost 80° inclination. The same applies for most of the other southern hemisphere SuperDARN bases. Appendix A (b) presents one of the cases discussed above, at 65° inclination, and it is shown that the SANAE IV antenna radiation patterns are within the blind spot. Thus, the polar mission is impractical for all inclination below 80°; the mission becomes feasible if the inclination exceeds 80°. It was also concluded from the coverage analyses that near-polar orbiting satellites have overpasses at low elevation angles. Thus, there is a need for pointing antennas on the satellite so that the beam is oriented in the direction of the receiving antenna during the overpass.

It would be much easier and less complex if the satellite is launched in a polar orbit, since it was shown that at 90° inclination there is no blind spot. With this inclination, the designer is assured that for the 5110 overpasses obtained over a year, each of them will cut through the radar beam. In addition, the satellite will appear from all angles of azimuth, which will enable a three dimensional beam pattern plot. Consequently, 98° inclination is appropriate for polar missions, since there is less orbital tilt and the blind spot is minimised. With the total number of overpasses mentioned over a year, this data is sufficient to accurately characterise the array.

Considering the satellite lifetime, it was shown that the satellite’s maximum operational lifetime is expected to be about 3 years and orbital lifetime 25 years.

5.2 Propagation

It was shown in Section 4.3 that the LUF is proportional to the electron density in the ionosphere. Thus, it was observed that on summer days, the LUF value could rise above the beacon frequency for a certain range of elevation angles at certain locations. In correlation to the above observation, the LUF value increases during summer during the day, as compared to during winter during the day, as well as locations from which signals are received (Hermanus or SANAE IV). Although one found that the LUF value varies during various seasons, this variation took place during certain period of the day; consequently, transionospheric could still place during other hours once the refraction index drops below acceptable value. The reflection index can be such that no signal can propagate through the ionosphere during a space weather storm. Under such conditions, transionospheric propagation is not possible, only ground-to-ground communication is. Referring to Figure 4.16, which portrays the highest LUF for all the selected days, one can note that the LUF value approaches the transmission frequency for low elevation incidence. This was due to the magnetic storm of index k_p=4. Thus, with such ionospheric conditions signals will be reflected back to the satellite for a wide range of elevations. To verify this, ray tracing was done by using IRI2007 electron density profiles for year 2010 from SANAE IV. It was found that signals are reflected as they reach the F region for all elevations up to 20.55° during summer at midday and up to 3.76° during winter at midnight. At values above this range of elevations, all signals propagate through the ionosphere. The IRI2007 confirms results obtained using a simplified ionospheric model. The propagation delay that signals from ZACUBE-1 would experience was also computed. It was found that signals would be delayed by 2 ms from 600 km altitude for circular orbit. This delay would vary if the satellite were into an elliptical orbit due to apogee and perigee distances not being equal.

5.3 Hardware

A COTS transceiver integrated circuit (IC) was used for the payload design. The transceiver module outputs 123 mW when biased with 2.38 V, which is less than its total output capability of 200 mW. The operating frequency was 14.745 MHz for the prototype, since a 14.01 MHz crystal oscillator was not available at the time of development (note that a 14.01 MHz crystal oscillator was ordered for the flight model hardware). The prototype was tested by using the HF ground station at CPUT. We used a 5 m wire as the beacon transmitter antenna. It was noted that the

HF transmitter on the satellite was mismatched with the wire antenna leading to a significant power loss; this confirms the mismatch that was mentioned in Section 4.4.2. The HF transceiver on the satellite was not tested with a 10 m monopole as this antenna was still in the design process. The calculated link budget confirms that the mission is feasible from a communication perspective, despite a tight link margin. Thus, there is a need for a proper matching system on the satellite to guarantee maximum transfer between the satellite and the ground segment.

5.4 Ground support equipment

The antenna that was built at CPUT is for the detection of the CubeSat beacon as it passes over South Africa. The testing of the antenna was done by establishing a communication link with the amateur radio operators (a link between CPUT and Hermanus was successful). This test was conducted to verify whether the antenna is functional. The UHF and VHF antennas are also operational, and this set of antennas will be used for sending and receiving the CubeSat’s data.

The new infrastructure development work that was proposed for implementation at SANSA SS is still pending. This infrastructure is a set of additional antennas that should be developed to operate alongside the TTFD, in order to find the direction of the CubeSat as it orbits over South Africa. This antenna array is now under construction and is expected to be completed for the mission operation.

Chapter 6 Conclusion and Recommendations

6.1 Conclusion

The aim of the study was to develop an experiment to characterise the SuperDARN HF radar field-of-view. This experiment will serve as a tool to measure the satellite elevation angles, as well as to measure the beam pattern of the HF radar array at SANAE IV. A 1U CubeSat was selected as the satellite platform for the feasibility study in accordance with the set objectives. These objectives were shared between SANSA SS, where the concept originated, and F'SATI at CPUT where this concept was implemented. From the defined objectives, the requirements needed to meet the set goals, were identified, as well as the associated constraints.

It was found from the ionospheric propagation studies that, for signals to propagate through the ionosphere, the transmit frequency should be higher than the *LUF*, which is a function of the ionospheric critical frequency (f_oF_2) for a given electron density distribution *Ne*. It was also noted that the *Ne* varies according to the time of day, season, region, as well as solar activities. Figure 4.20 is an example of the above statement in which the *LUF* approaches 18 MHz during the day for low elevation signals, while at night the *LUF* remains less than the transmit frequency for all elevations during summer and winter. Comparing data pertaining to the summer of 2011-2012 to the data of in 2010, one can say that there is a significant increase in electron density in the ionosphere, which results in such an increase in LUF.

A satellite beacon payload was designed, and a prototype was built. Software to generate the required Morse code modulation was written. To test the transceiver and the encoded signal, an HF ground station was set up with the required Morse code interpreter software (Figure 4.50), and the transmitted call-sign of SANSA SS, the satellite name, and the date of data generation were displayed on a computer screen.

From a given orbital altitude and the mission objectives, the preliminary orbital parameters were determined via both mathematical and simulation methods. These parameters were used to propagate the orbits. These orbits were analysed from 60° to 98° inclination. SANAE IV and SANSA SS in Hermanus were identified as ground stations for these analyses, although other SuperDARN stations were also incorporated in the simulation. It was found that the satellite should be in polar orbit or in near polar orbit in order for it to be visible at SANAE IV. SANSA.SS is least affected by this inclination constraint, since it is covered even at 60° inclination with overpasses of up to 90°.

Since the satellite inclination is dictated by the launch sites, a survey was done to identify a potential launch candidate. Thus, Dnepr, Cosmos, Epsilon, PSLV, and Rockot were identified as launch candidates. Dnepr is the preferred launcher. This launcher will be deployed from Yasny Cosmodrom launch site in Russia. Yasny Cosmodrom is a high latitude launch site, suitable for launching polar mission satellites.

The overall analysis was completed with simulation of all antenna beam patterns. The simulation of the HF array showed that the ground reflector influences the radiation pattern and the gain of the array. The simulations also showed that the ground reflector found at SANAE IV improved the array performance. Thus, although the TTFD in Hermanus is a replica of the antenna at SANAE IV, the difference in the type of ground plays an important role. The reflection coefficient of the antenna on the satellite showed a significant mismatch, thus, there would be significant power loss if the antennas are not properly matched.

Phase measurement is an important aspect in the characterisation of the SuperDARN. Phase characterisation is only achievable if there are two or more receiving antennas. These antennas will receive incoming signals at different phases where the difference depends on the elevation angles.

The ZACUBE-1 mission was built as a fast track satellite mission. The goal for this mission was to get students involved in satellite mission design from concept to integration and during the launch campaign. This was successfully achieved, pending the launch in 2013.

The ZACUBE-1 mission payload does not require complex design and integration. The payload consists of a low cost RI-R6C-001A HF transceiver chip, which has a stable operation mode. The mission may also be used by a wide range of amateur radios for the characterisation of their antennas. This process is efficient, since the measurements can be repeated daily, as there will be a revisit time each day.

6.2 Recommendations

- The major challenge for this mission was the design of the a satellite antenna and its deployment mechanism. To reduce the complexity of this mission, more research on high efficiency small antennas can be conducted.

- The Global Positioning System (GPS) receiver is required on the satellite for its accurate position determination.
- Due to the mismatch observed, it is important that a matching system should be designed for the antenna on the satellite so that one is assured that maximum power is transmitted.
- For future missions, an analysis should be done on how sunspot numbers affect the f_oF_2 predicted values, especially after the solar maximum, since the sun would still be active. This implies higher electron density and higher LUFvalues in the F layer.
- The actual ZACUBE-1 data analyses should be a subject of academic research following launch.

References

Andre, R., & Dudok de Wit, T. (2003). Identification of the ionospheric footprint of magnetospheric boundariesusing SuperDARN coherent HF radars. *Planetary and Space Science,* (51):813-820.

Anil, K. M., & Varsha, A. (2007). Earth Ecoverage and Ground Tracks. In K. M. Anil, & A. Varsha, *Satellite Tecnhology: Principales and applications*. West Sussex: John Wiley & Sons.

Anil, K. M., & Varsha, A. (2007). Types of Satellite Orbits. In V. A. Anil K. Maini, *Satellite Technology, Principles and Applications*. West Sussex: John Wiley & Sons.

Anniina, J. (2000). *Sir Isaac Newton and Unification of physic and astronomy.* Astronomy 161, the Solar system: http://csep10.phys.utk.edu/astr161/lect/history/newton.html [September 8, 2011].

Antonio, F. *Keplerian Elements Tutorial.* amsat: http://www.amsat.org/amsat/keps/kepmodel.html#eccen [September 8, 2011].

Australian Goverment. (n.d.). *Introduction to HF Radion Propagation.* IPS Radio and Space Service.

Balanis, A. C. (2005). SMART ANTENNAS. in *Antenna Theory Analysis and Design*. NewJersey: John Wiley and sons.

Belehaki, A., Stanislawska, I., & Lilensten, J. (2009). An Overview of Ionosphere-Thermosphere Models.

Bilitza, D., & Reinisch, B. W. (2008). Intenational reference ionospher 2007: Improvements and new parameters. *Advances in Space Research 42*:599-609.

Bilitza, D. (2001). International Reference Ionosphere 2000. *RADIO SCIENCE, 36* (2), 261-275.

Boain, R. J. (2004). A-B-Cs of Sun-Synchronous Orbit Mission Design. *14th AAS/AIAA Space Flight Mechanics Conference:* 1. Maui: AAS/AIAA.

Bourdillo, A., Zolesi, B., & Cander, L. R. (2010). COST 296 action results for space weather ionospheric monitoring and modelling. *COSPAR* : 1173-1177.

Bourdillon, A. (2008). Ionospheric radiowavepropagation. Rennes, April 7-8. Rennes 1, France.

Bryson, G., Bristow, W., & Parris, T. (n.d.). *An Introduction to Radar and the Super Dual Auroral Radar Network.* Alaska.

Capderou, M. (2004). Kepler's laws. In M. Capderou, *Satellites Orbits and Missions*: 29-30. Paris: Springer.

Cape Peninsula University of Technology. (2010). History. CPUT: http://www.cput.ac.za/index.php?option=com_content&view=article&id=2&Itemid=391[October 20, 2011].

Chang, Y. K., Kang, S. J., Moon, B. Y., & Lee, B. H. (2006). LOW-COST RESPONSIVE EXPLOITATION OF SPACE BY HAUSAT-2 NANO SATELLITE. *4th Responsive Space Conference*,2-3. Los Angeles: AIAA-RS4.

Clyde-space.com. (2010). clyde space Web site: www.clyde-space.com [May 5, 2010].

Cohen, N., & Davies, K. (1990). Radio Wave Propagation. *Space Environment Laoboratory* , 2.

Cubesat. (2013). Past lauches. Cubesate.org. http://www.cubesat.org/index.php/missions/past-launches [January 28, 2013].

Eichmann, E. (2012). *store.amsat*: http://store.amsat.org/catalog/product_info.php?products_id=50 [November 09, 2012].

Eurockot. (2011). *Launch Vehicle*. Eurockot: http://www.eurockot.com/joomla/index.php?option=com_content&view=article&id=20040652&Itemid=54 [October 12, 2011].

Evans, B. G. (1999). Satellite engineering for communication satellites. In P. Harris, & J. J. Pocha, *Satellite Communication Systems*. London: Institute of Engineering and Technology.

Foged, L. (2010). Infinite ground plane antenna characterization from limited groundplane measurements. *Antennas and Propagation Society International Symposium:* 1. Toronto: IEEE.

Frederick, H. R., Robert, C., Richard, C., Murat. E., James, B. H., Arturo, M., Daniel, P. D. M., & John L. B. W. (2002). HF, VHF, and UHF Systems and Technology. *IEEE , 50* (3):888-899.

Gao, S., Brenchley, M., Unwin, M., Underwood, C. I., Clark, K., Maynard, K., Boland, L., & Sweeting, M. N. (2008). Atenna for Small Satellites. *Loughborough Antenna & Propagation.* Loughbohough: IEEE.

Gnevyshev, M. N. (1963). The corona and the 11 year solar cycle of solar activity. *Soviet Astronomy, 7* : 311.

Headquarters Department of the Army. (2004). *Communications-Electronics Fundamentals: Wave Propagation,Transmission Lines, and Antennas.* Washington, DC: Active Army, Army National Guard, and U.S. Army Reserve.

Heidt, H., Puig-Suari, J., Moore, A. S., Nakasuka, S., & Twiggs, R. J. (2000). CubeSat: A new Generation of Picosatellite for Education and Industry Low-Cost Space Experimentation. *14th Annual AIAA/USU Conference on Small Satellites. 5:*1-2. Logan, Utah: AIAA.

Hughes, J. M., Bristow, W. A., Greenwald, R. A., & Barnes, R. J. (2002). Determining characteristics of HF communications links using SuperDARN. *Annales Geophisicae*.

Ian, P. (1999). Radio Waves and the Ionosphere. Meadway, Staines, United Kingdom.

ISRO. (2011). *Polar Satellite Launch Vehicle*. ISRO: http://www.isro.org/launchvehicles/PSLV/pslv.aspx [October 14, 2011].

ITU. (2007). *P.372: Radio Noise*. Retrieved 01 28, 2013, from ITU.int: http://webs.uvigo.es/servicios/biblioteca/uit/rec/P/R-REC-P.372-9-200708-I!!PDF-E.pdf [January 28, 2013].

Jane, L. H., Hosken, W. R., & Pollock, H. C. (1999). Spacecraft Computer System. In R. J. Wertz, & J. W. Larson, *Space Mission Analysis and Design.* New York: Springler and Microcosm Press.

Kan, R. (2006). The idea of Space Weather – A historical perspective. *Advances in Space Research* , 1261-1264.

Keith, B. (2009). Sanae_newsletters/sanae-48-news-april2009*.* South African National Antarctic Program: http://www.sanap.org.za/sanap_sanae/sanae_newsletters/sanae-48-news-april2009.pdf [May Friday, 2011].

Klofas, B., Anderson, J., & Leveque, K. (2009). A Survey of CubeSat Communication Systems. *AMSAT* , 27-28.

Koskinen, H., Tanskanen, E., Pirjola, R., Pulkkinen, A., Dyer, C., Rodgers, D., Cannon, P; Mandeville, J-C., & Boscher, D. (2001). ESA Space Weather Study. *SPACE WEATHER EFFECTS CATALOGUE*.

Kosmotras. (2011). *Dnepr LV*. Kosmotras: http://www.kosmotras.ru/en/Launch2011/ [October 13, 2011].

Krasheninnikov, I. V., & Egorov, I. B. (2010). IRI-2001 model efficiency in ionospheric radiowave propagation forecasting. *ELSEVIER* , 268-275.

Lockhart, J. (n.d.). *THE BEFORE AND AFTER OF AN INFORMATION .* Cape Town: Cape Peninsula University of Technology,.

Loftus, P. C., & Teixeira, C. (2008). Launch Systems. In James, R. W., & Wiley, J. L., *Space Mission Analysis and Design.* Hawthorne; New York: Microcosm Press; Springer.

Louis, J., & Ippolito, J. (2008). *Satellite Communications Systems Engineering: Atmospheric Effects, Satellite Link Design and System Performance (Wireless Communications and Mobile Computing).* John Wiley and Sons.

Maral, G., Bousquet, M., & Sun, Z. (2009). *Satellite Communications Systems: Systems, Techniques and Technology.* UK: Willey

McKinnell, L. (2008, July 3). *Introducing Hermanus*. http://www.ips.gov.au/IPSHosted/INAG/web-69/2008/introducing_hermanus.pdf [September 27, 2011].

Michigan, U. O. (n.d.). *CubeSat Program*. www.personal.umich.edu: http://www-personal.umich.edu/~kgmerek/subsystems.html [April 27, 2011].

MixW. (n.d.). MixW. Ham Radio Software: http://mixw.net/index.php [November 09, 2012].

Montenbruck, O., & Eberhard, G. (2001). Introductory to Astrodynamics. In O. Dr. Montenbruck, & G. Dr. Eberhard, *Satellilte Orbites; Models, Methods and Application*. Berlin: Springer.

NLSA. (2011). Nova for windows. http://www.nlsa.com/nfw.html [SEPTEMBER, 2011].

Puig-Suari, J. (2001). Development of the Standard CubeSat Deployer and a CubeSat Class PicoSatellite. *Aerospace Conference. (1)*:347-353. Big Sky, Montana (USA): IEEE.

Pumkin. (n.d.). *3D CAD Design*. from Pumkin: http://www.cubesatkit.com/content/design.html [October 1, 2011].

Ravindran, R. (2009). Equations Governing Kepler's Laws of PlanetaryMotion. *RESONANCE* , 1-3.

Reinisch, B. W., & Huang, X. (2001). DEDUCING TOPSIDE PROFILES AND TOTAL ELECTRON CONTENT FROM BOTTOMSIDE IONOGRAMS. *Advances in Space Research.* (*27):*23-30. Massachusetts Lowell: Elsevier Science.

Riki, m. (2009). *CubeSat Design Specification Rev 12.* California Polytechnic State University.

Ritchey, W. L. (1999). *A SURVEY AND TUTORIAL OF DIELECTRIC MATERIALS USED IN THE.* California : Speeding Edge.

Rob, G. (2009, October 25). *Nano-Spacecraft Specialist Joins White Label Space*. from Space Fellowship: http://spacefellowship.com/news/art14826/nano-spacecraft-specialist-joins-white-label-space.html [October 11, 2011].

sansa. (n.d.). *South African Space Agency*. from South African Space Weather - Regional Warning Centre for Africa: http://www.spaceweather.co.za/intro.htm [June 29, 2011].

Schiffler, A. (1996). *Introduction to SuperDARN*. http://www.ferzkopp.net: http://www.ferzkopp.net/Personal/Thesis/node16.html [april 14, 2011].

Seybold, S. J. (2005). MODES OF PROPAGATION. In S. J. Seybold, *INTRODUCTION TO RF PROPAGATION*. New Jersey: John wiley & Sons.

Sterne, K. T. (2010). Testing the Re-designed SuperDARN HF Radar and Modeling of a Twin Terminated Folded Dipole Array. Blacksburg, Virginia.

Tanskanen, E. I., Pulkkinen, T. I., Viljanen, A., Mursula, K., Partamies, N., & Slavin, J. A. (2011). From space weather toward space climate time scale: Substorm analysis from 1993 to 2008. *American Geophysical Union* , 1.

Tech-Faq. (2011). *Satellite Launch Sites*. http://www.tech-faq.com/satellite-launch-sites.html [October 13, 2011].

The University of Waikato. (2011). Earth's magnetic field. Science learning: http://www.sciencelearn.org.nz/Contexts/Dating-the-Past/Sci-Media/Images/Earth-s-magnetic-field [September 24, 2011].

Toorian, A., Blundell, E., Puig Suari, J., & Twiggs, R. (2005). CUBESATS AS RESPONSIVE SATELLITES. *3rd Responsive Space Conference:* 4. Los Angeles: AIAA.

Van Helden, A. (2005). Johannes Kepler. the Gaileo Project: http://galileo.rice.edu/sci/kepler.html [September 8, 2011].

Visser, F. D. (n.d.). *Why Satellite Systems in South Africa?* Cape Peninsula University of Technology: http://active.cput.ac.za/fsati/public/index.asp?pageid=955 [May 2011].

www.dwd.de. (n.d.). satellite based remote sensing. www.dwd.de: http://www.dwd.de/bvbw/appmanager/bvbw/dwdwwwDesktop%3Bjsessionid=HPlyNB8DBZqXrMT2vTTzN9Rwwy9jt4pgRfJXJ0PzTzdlGLpGXR2F!-1071012350!677929436?_nfpb=true&portletMasterPortlet_i1gsbDocumentPath=Navigation%252FForschung%252FAnalyse__Modellierung%252FFU__DA__f [April 29, 2011].

Yates, S. (2009). Homemade HF Antenna Balun. www.dxzone.com: http://www.dxzone.com/cgi-bin/dir/jump2.cgi?ID=11596 [May 18, 201].

Zoller, N. J. (2011). *Satellite Regulations*. International Telecommunication Union: http://www.itu.int/net/newsroom/wrc/2012/features/satellite_regulations.aspx [June 22, 2012].

Appendices

Appendix A: Satellite field-of-view for Southern Hemisphere

a. FOV of satellite at 98^o inclination

- This FOV presents the visibility of the satellite as seen from the southern hemisphere using the global map.

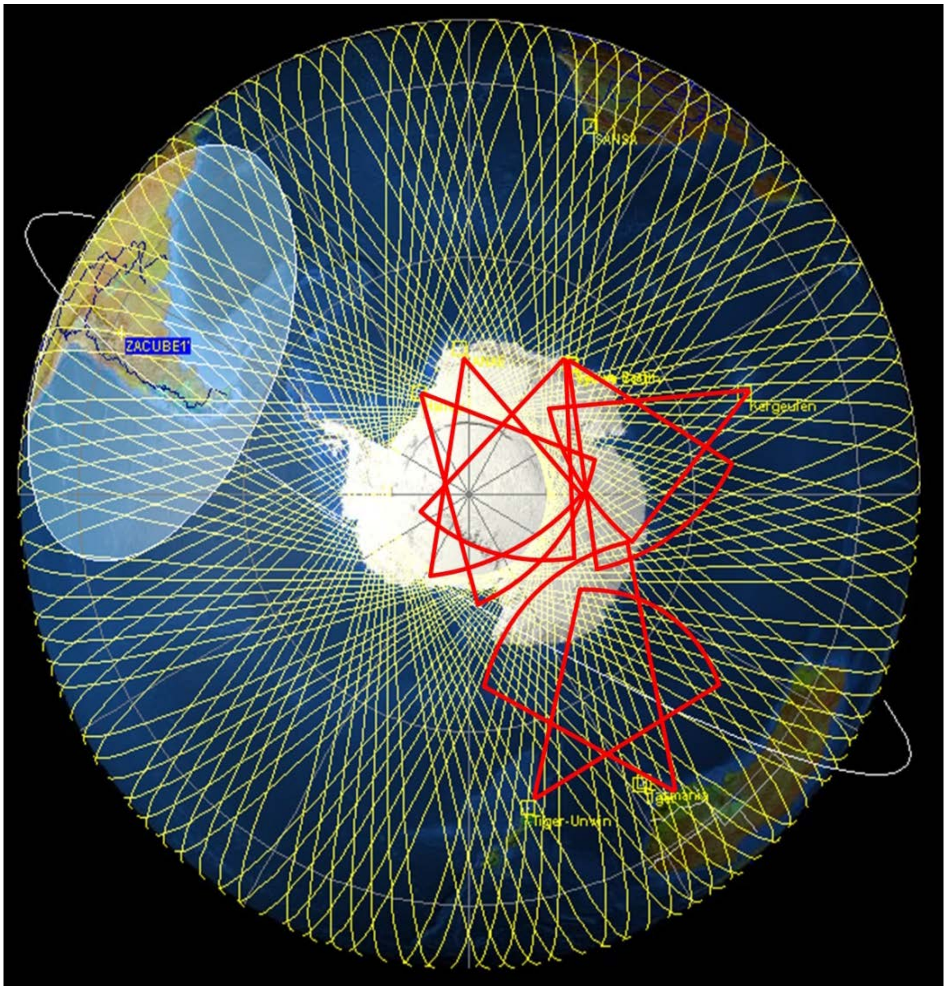

- This FOV presents the visibility of the satellite as seen from the southern hemisphere using the radar map.

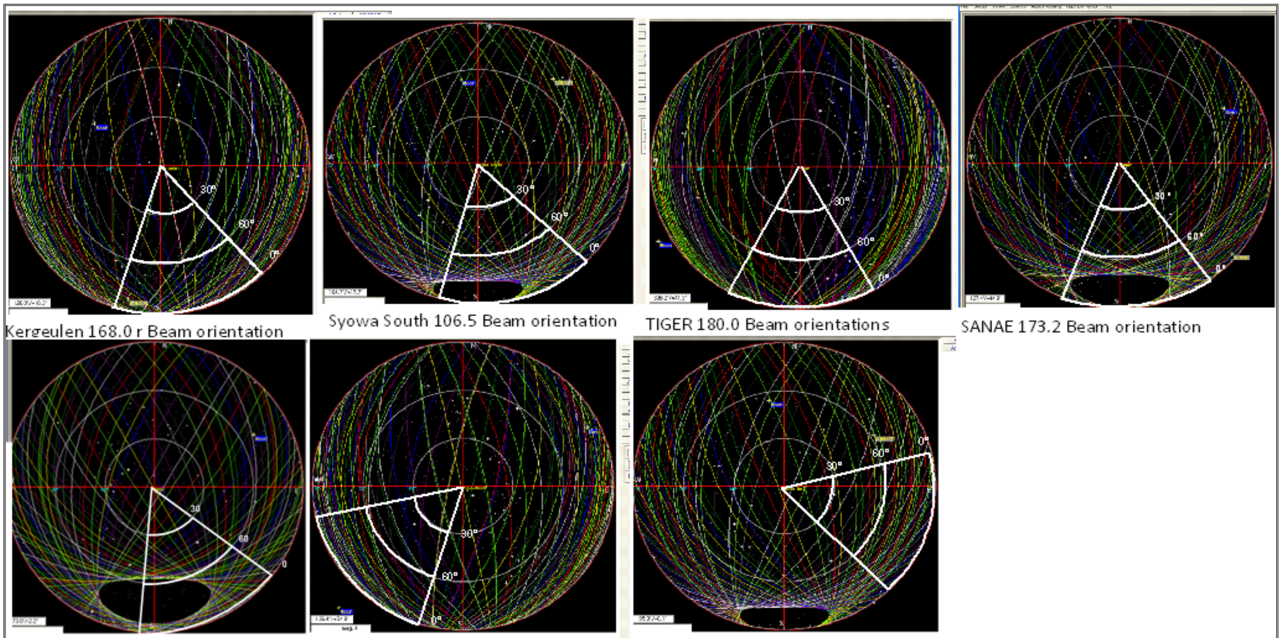

Kergeulen 168.0 r Beam orientation

Syowa South 106.5 Beam orientation

TIGER 180.0 Beam orientations

SANAE 173.2 Beam orientation

HALLEY 165.0 Beam orientation

TIGER-Unwin 227.9 Beam orientation

Syowa East 106.5 Beam orientation

b. FOV of satellite at 65^o inclination the global map

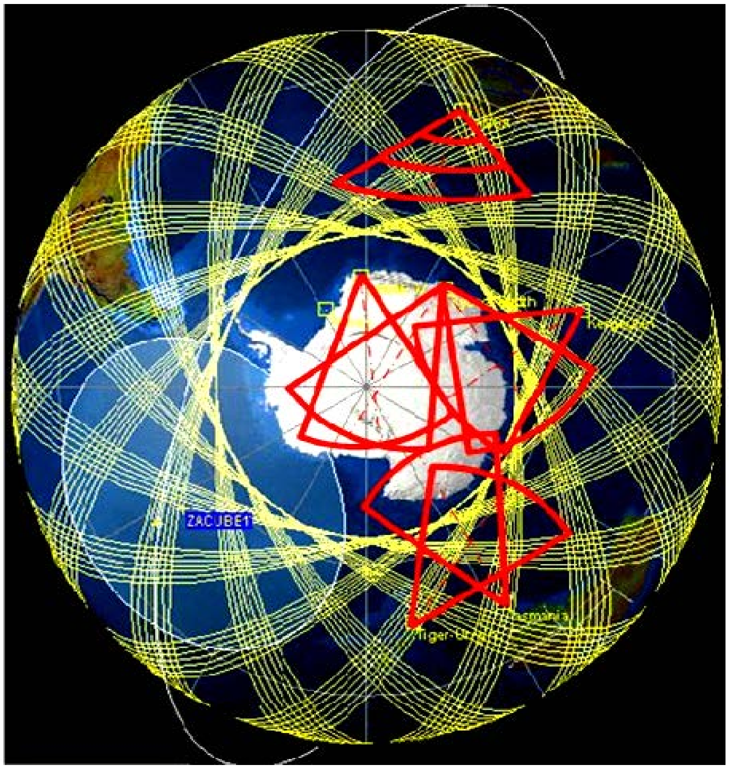

c. FOV of satellite at 65°(a), 70°(b), 80°(c), and 90°(d) inclination from the radar map

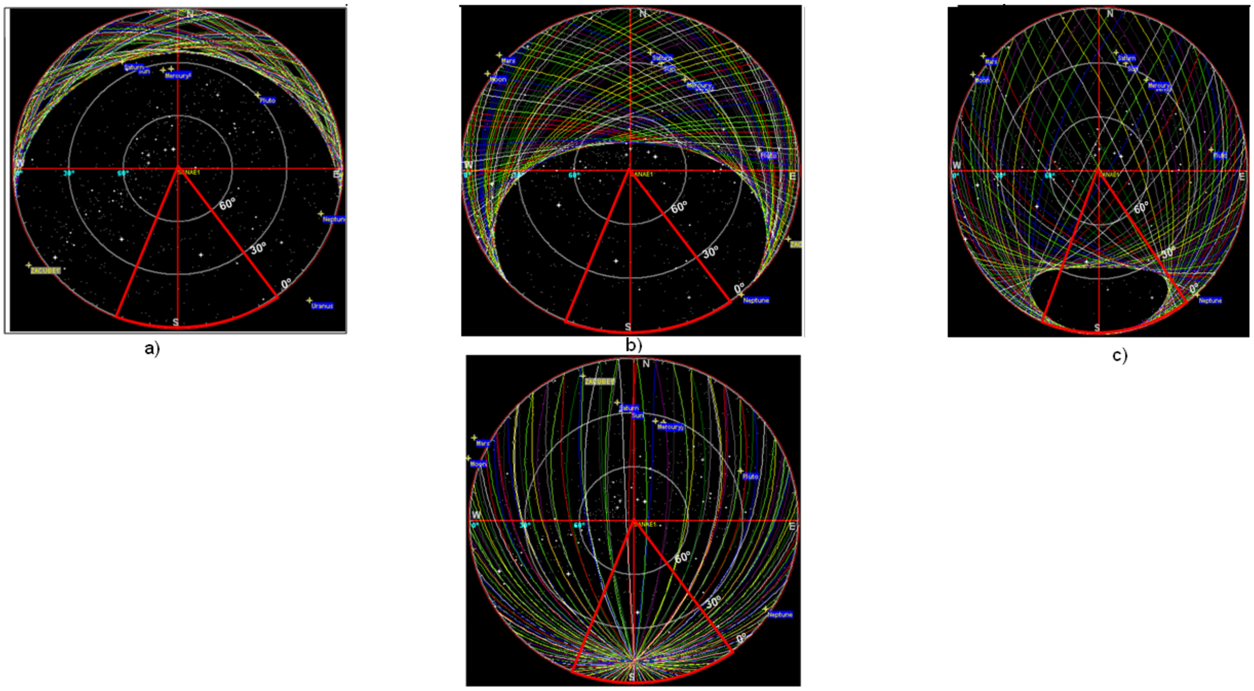

a)

b)

c)

d)

Appendix B: Antenna simulation results

a. *Antenna beam pattern and reflection coefficient*

Antenna beam pattern

Description and brief discussion

The Twin Terminated Folded Dipole in SANSA Space Science

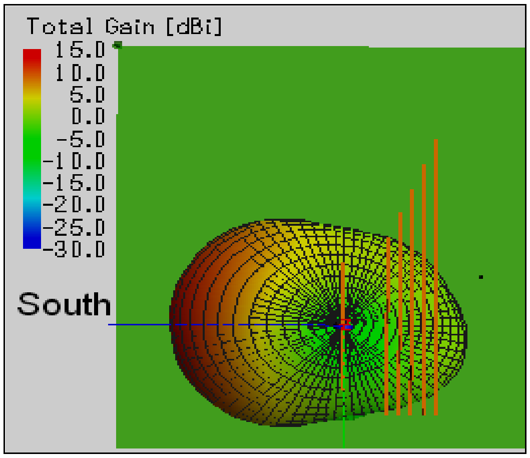

(a)

All simulation results presented here were done in FEKO. The TTFD at SANSA Space Science radiates towards the south in the direction of SANAE-IV. The reflectors at the back of the array enhance the directivity. The green surface represents the ground plane introduced using sandy clay soil parameters.

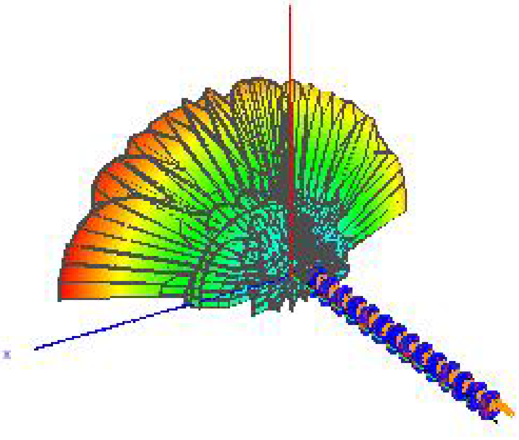

(b)

In this model no ground plane was used.

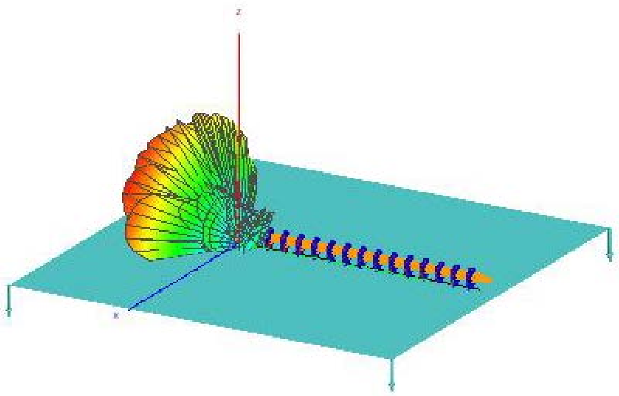

(d)

In this model the ground plane used was ice.

The ground is sandy clay

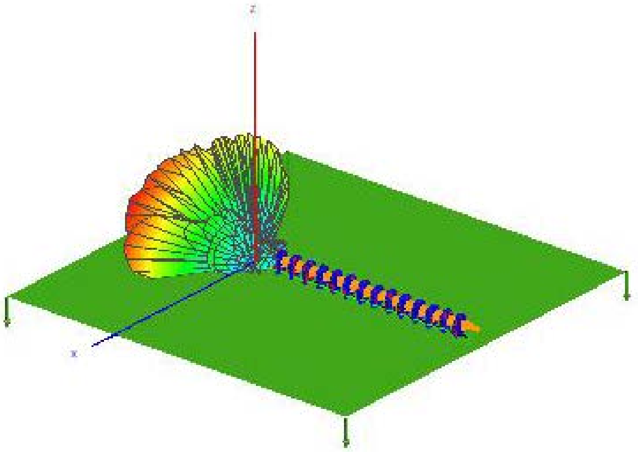

(e)

Parameters of the sandy clay soil were used in defining this ground plane.

The inverted-V radiation and the reflection coefficient

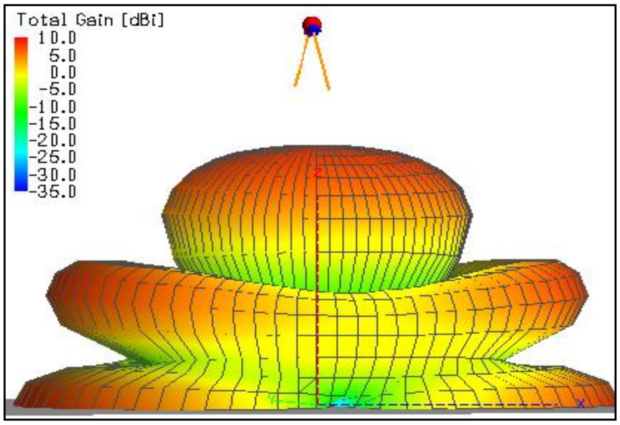

(f)

This pattern represents the beam pattern of the HF antenna at CPUT,

Appendix C: Datasheets

a. RI-R6R-001A RFID transceiver (TI, 2005)

- Photograph of the RFID transceiver.

- RFID transceiver's block diagram

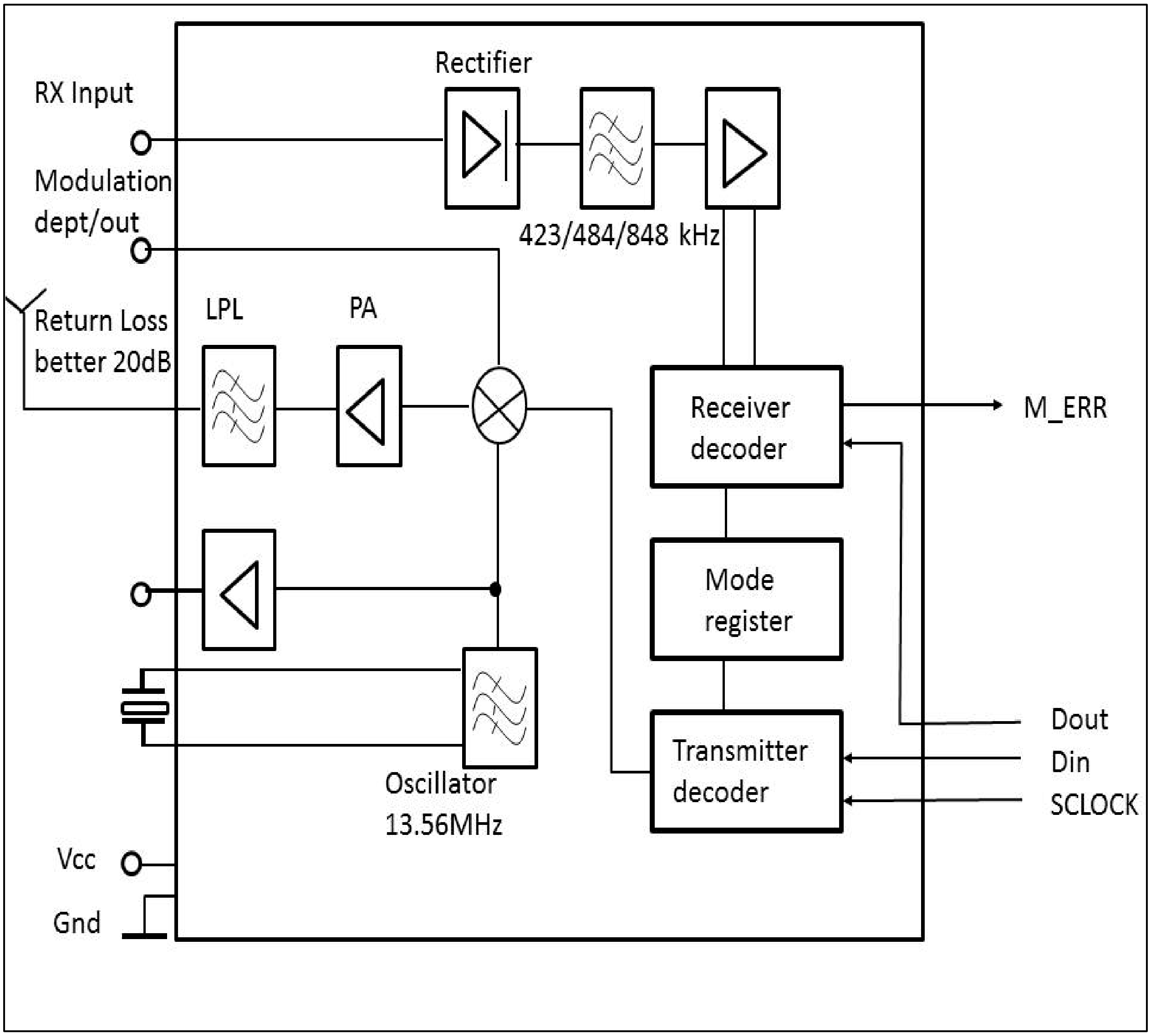

- Transceiver pin out diagram and pin out description table

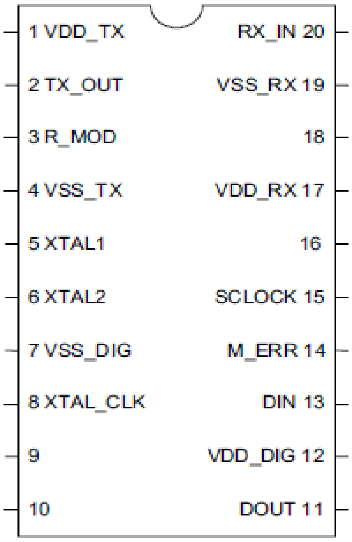

PIN NUMBER	SIGNAL NAME	DESCRIPTION
1	VDD_TX	Transmitter power supply
2	TX_OUT	Output transistor drain connection
3	R_MOD	External resistor to set 10% modulation depth mode
4	VSS_TX	Transmitter section ground
5	XTAL1	Pin 1 of Xtal resonator
6	XTAL2	Pin 2 of Xtal resonator and external system clock input
7	VSS_DIG	Digital section ground
8	XTAL_CLK	Buffered output of Xtal oscillator
9	not used	Grounded for normal operation
10	not used	Grounded for normal operation
11	DOUT	Data output for serial link
12	VDD_DIG	Digital section power supply
13	DIN	Data input for serial link
14	M_ERR	Manchester Protocol error flag
15	SCLOCK	Serial link clock
16	not used	Leave open for normal operation
17	VDD_RX	Receiver section power supply
18	not used	Leave open for normal operation
19	VSS_RX	Receiver section ground
20	RX_IN	Receiver input

- Transceiver’s specification table

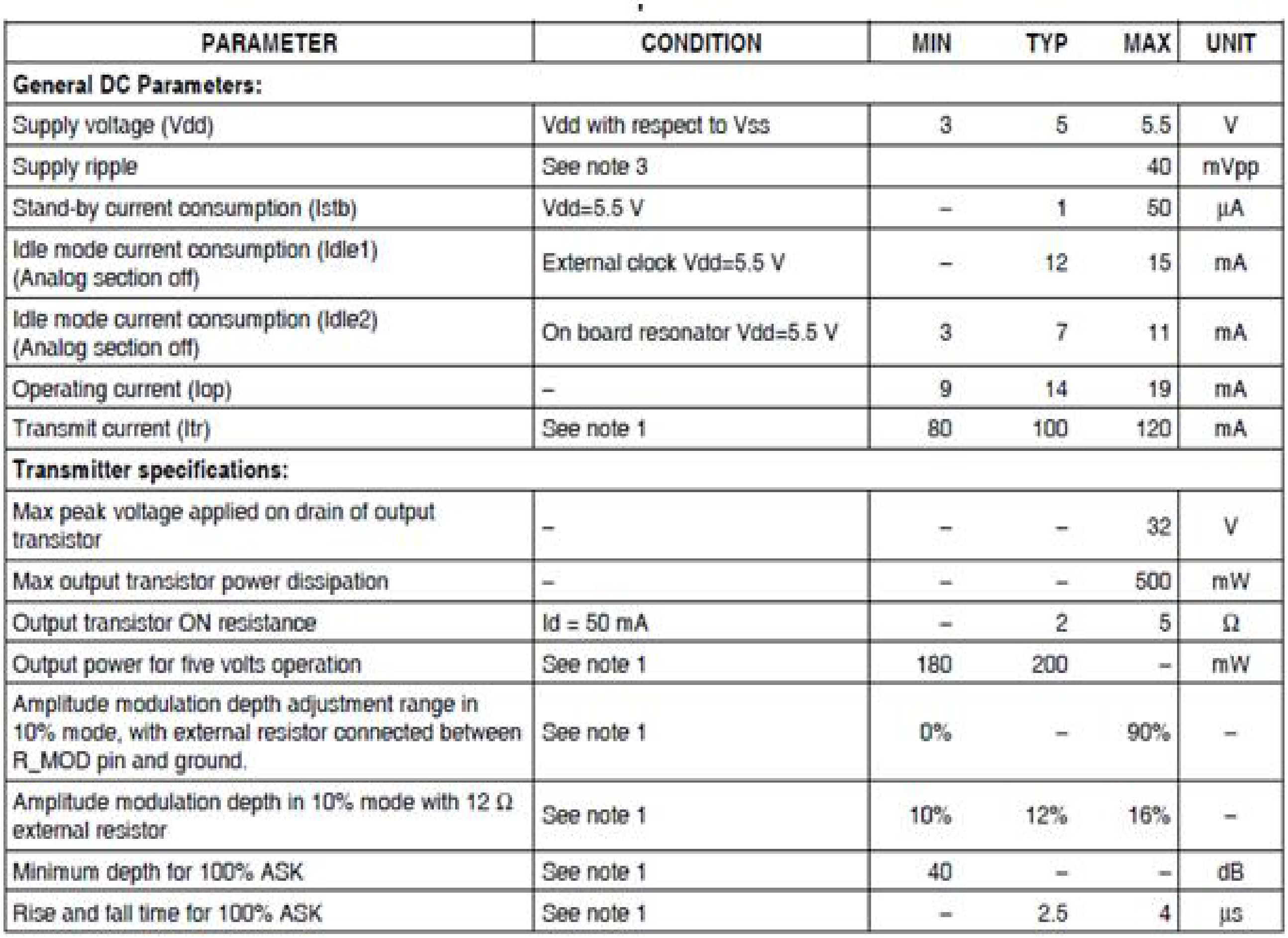

PARAMETER	CONDITION	MIN	TYP	MAX	UNIT
General DC Parameters:					
Supply voltage (Vdd)	Vdd with respect to Vss	3	5	5.5	V
Supply ripple	See note 3			40	mVpp
Stand-by current consumption (Istb)	Vdd=5.5 V	–	1	50	µA
Idle mode current consumption (Idle1) (Analog section off)	External clock Vdd=5.5 V	–	12	15	mA
Idle mode current consumption (Idle2) (Analog section off)	On board resonator Vdd=5.5 V	3	7	11	mA
Operating current (Iop)	–	9	14	19	mA
Transmit current (Itr)	See note 1	80	100	120	mA
Transmitter specifications:					
Max peak voltage applied on drain of output transistor	–	–	–	32	V
Max output transistor power dissipation	–	–	–	500	mW
Output transistor ON resistance	Id = 50 mA	–	2	5	Ω
Output power for five volts operation	See note 1	180	200	–	mW
Amplitude modulation depth adjustment range in 10% mode, with external resistor connected between R_MOD pin and ground.	See note 1	0%	–	90%	–
Amplitude modulation depth in 10% mode with 12 Ω external resistor	See note 1	10%	12%	16%	–
Minimum depth for 100% ASK	See note 1	40	–	–	dB
Rise and fall time for 100% ASK	See note 1	–	2.5	4	µs

- Communication timing description

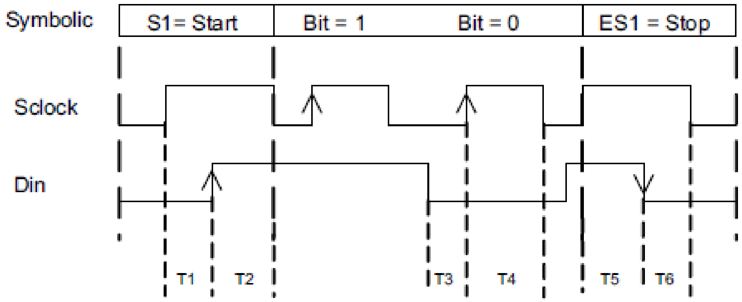

Minimum timings

T1: 300ns	T4: 600ns
T2: 300ns	T5: 300ns
T3: 66ns	T6: 300ns

- Configuration byte description

	Size/length	
Start (S1)	1 Bit	
	Command byte	Bit #7 = L, Normal Mode
		Bit #6 = L, Tag-it protocol
		Bit #5 = L, "
		Bit #4 = H, "
		Bit #3 = H, 100% modulation
		Bit #2 = L, FM demodulator
		Bit #1 = H, this field is not applicable, it is set to default
		Bit #0 = H, even parity
	Data to the tag: Binary data are converted into the Tag-it RF-protocol	
Stop (ES1)	1 Bit	

Modulation%	Resistor Value (Ω)	Comment
10	12	Minimum modulation depth
20	18	Recommended modulation depth
30	25	Maximum modulation depth

b. Pic Microntroller specifications

Pic16F690 Microcontroller

PIC16F690 Pin Diagram (PDIP, SOIC, SSOP)

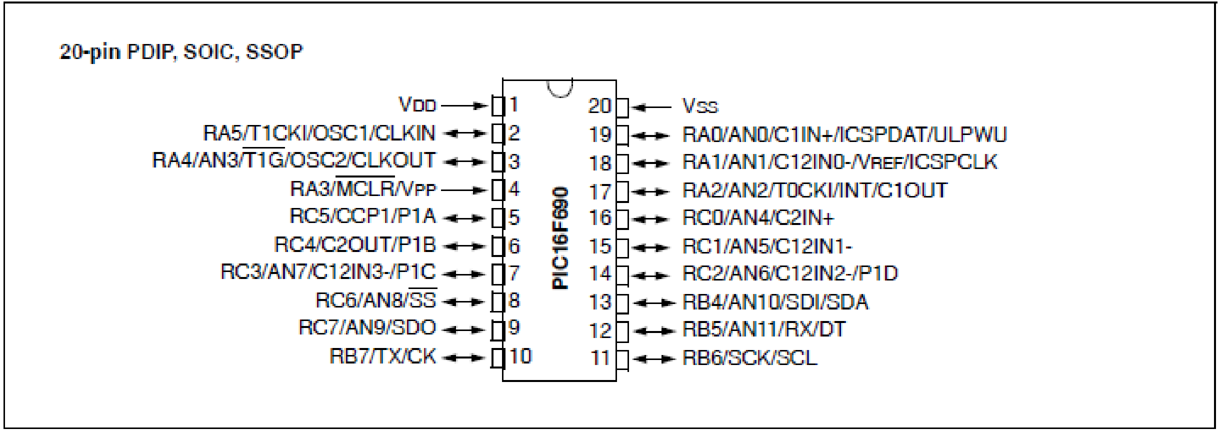

- Microcontroller's block diagram

FIGURE 1-5: PIC16F690 BLOCK DIAGRAM

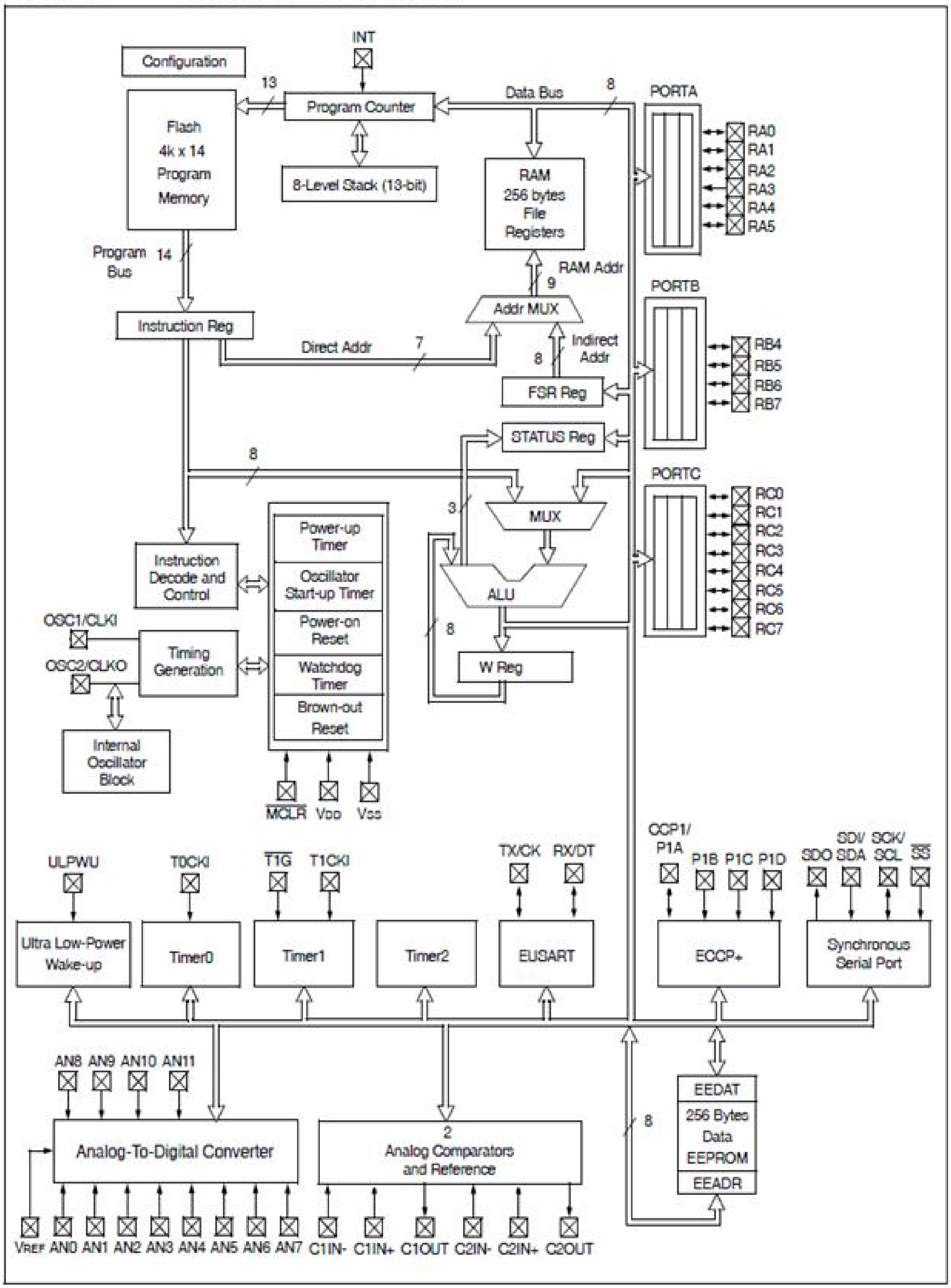

- Microcontroller pin out description

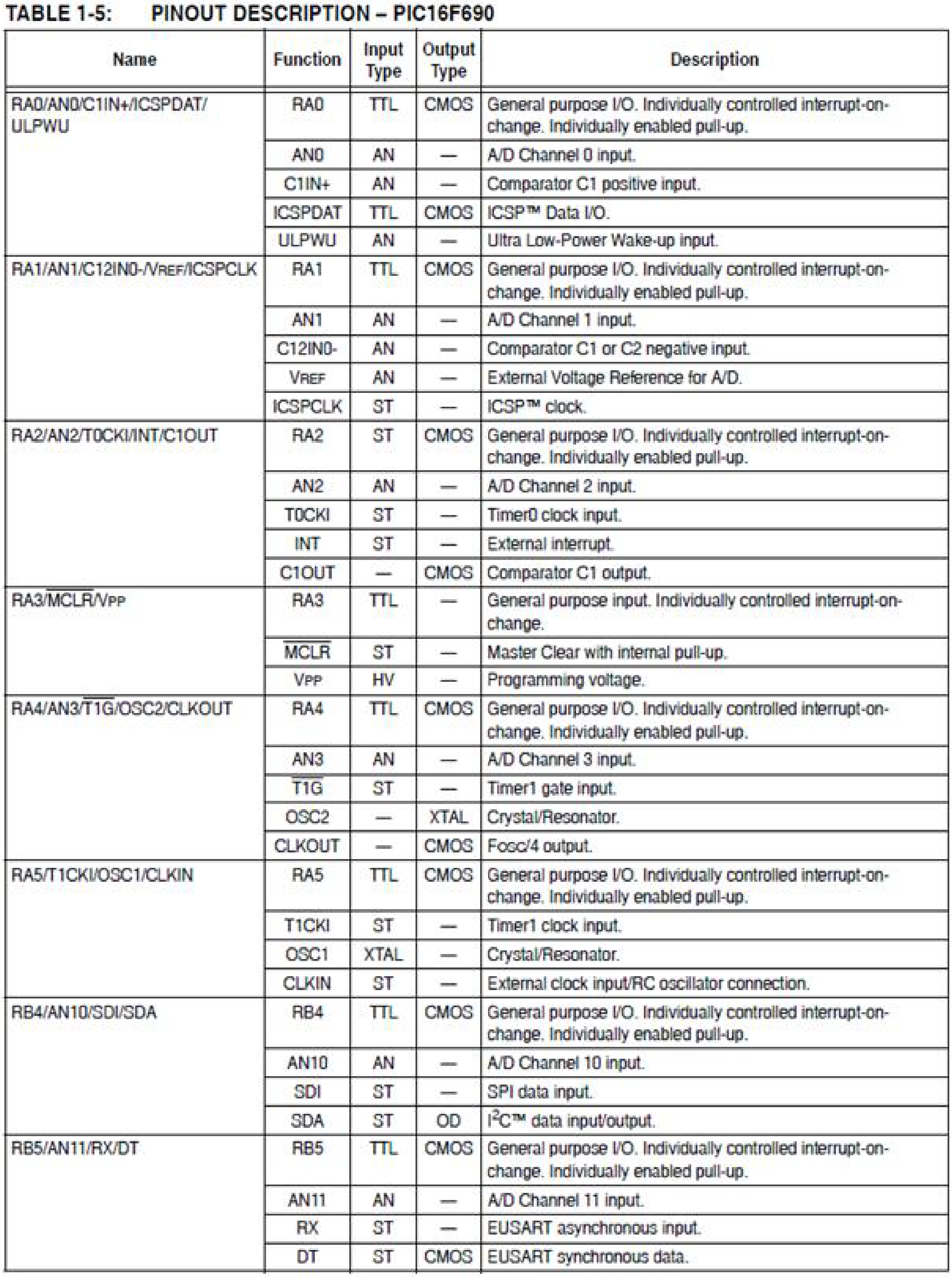

TABLE 1-5: PINOUT DESCRIPTION – PIC16F690

Name	Function	Input Type	Output Type	Description
RA0/AN0/C1IN+/ICSPDAT/ULPWU	RA0	TTL	CMOS	General purpose I/O. Individually controlled interrupt-on-change. Individually enabled pull-up.
	AN0	AN	—	A/D Channel 0 input.
	C1IN+	AN	—	Comparator C1 positive input.
	ICSPDAT	TTL	CMOS	ICSP™ Data I/O.
	ULPWU	AN	—	Ultra Low-Power Wake-up input.
RA1/AN1/C12IN0-/VREF/ICSPCLK	RA1	TTL	CMOS	General purpose I/O. Individually controlled interrupt-on-change. Individually enabled pull-up.
	AN1	AN	—	A/D Channel 1 input.
	C12IN0-	AN	—	Comparator C1 or C2 negative input.
	VREF	AN	—	External Voltage Reference for A/D.
	ICSPCLK	ST	—	ICSP™ clock.
RA2/AN2/T0CKI/INT/C1OUT	RA2	ST	CMOS	General purpose I/O. Individually controlled interrupt-on-change. Individually enabled pull-up.
	AN2	AN	—	A/D Channel 2 input.
	T0CKI	ST	—	Timer0 clock input.
	INT	ST	—	External interrupt.
	C1OUT	—	CMOS	Comparator C1 output.
RA3/$\overline{MCLR}$/VPP	RA3	TTL	—	General purpose input. Individually controlled interrupt-on-change.
	$\overline{MCLR}$	ST	—	Master Clear with internal pull-up.
	VPP	HV	—	Programming voltage.
RA4/AN3/$\overline{T1G}$/OSC2/CLKOUT	RA4	TTL	CMOS	General purpose I/O. Individually controlled interrupt-on-change. Individually enabled pull-up.
	AN3	AN	—	A/D Channel 3 input.
	$\overline{T1G}$	ST	—	Timer1 gate input.
	OSC2	—	XTAL	Crystal/Resonator.
	CLKOUT	—	CMOS	Fosc/4 output.
RA5/T1CKI/OSC1/CLKIN	RA5	TTL	CMOS	General purpose I/O. Individually controlled interrupt-on-change. Individually enabled pull-up.
	T1CKI	ST	—	Timer1 clock input.
	OSC1	XTAL	—	Crystal/Resonator.
	CLKIN	ST	—	External clock input/RC oscillator connection.
RB4/AN10/SDI/SDA	RB4	TTL	CMOS	General purpose I/O. Individually controlled interrupt-on-change. Individually enabled pull-up.
	AN10	AN	—	A/D Channel 10 input.
	SDI	ST	—	SPI data input.
	SDA	ST	OD	I^2C™ data input/output.
RB5/AN11/RX/DT	RB5	TTL	CMOS	General purpose I/O. Individually controlled interrupt-on-change. Individually enabled pull-up.
	AN11	AN	—	A/D Channel 11 input.
	RX	ST	—	EUSART asynchronous input.
	DT	ST	CMOS	EUSART synchronous data.

c. *Transceiver schematic diagram, PCB layout and component list*

- Schematic diagram

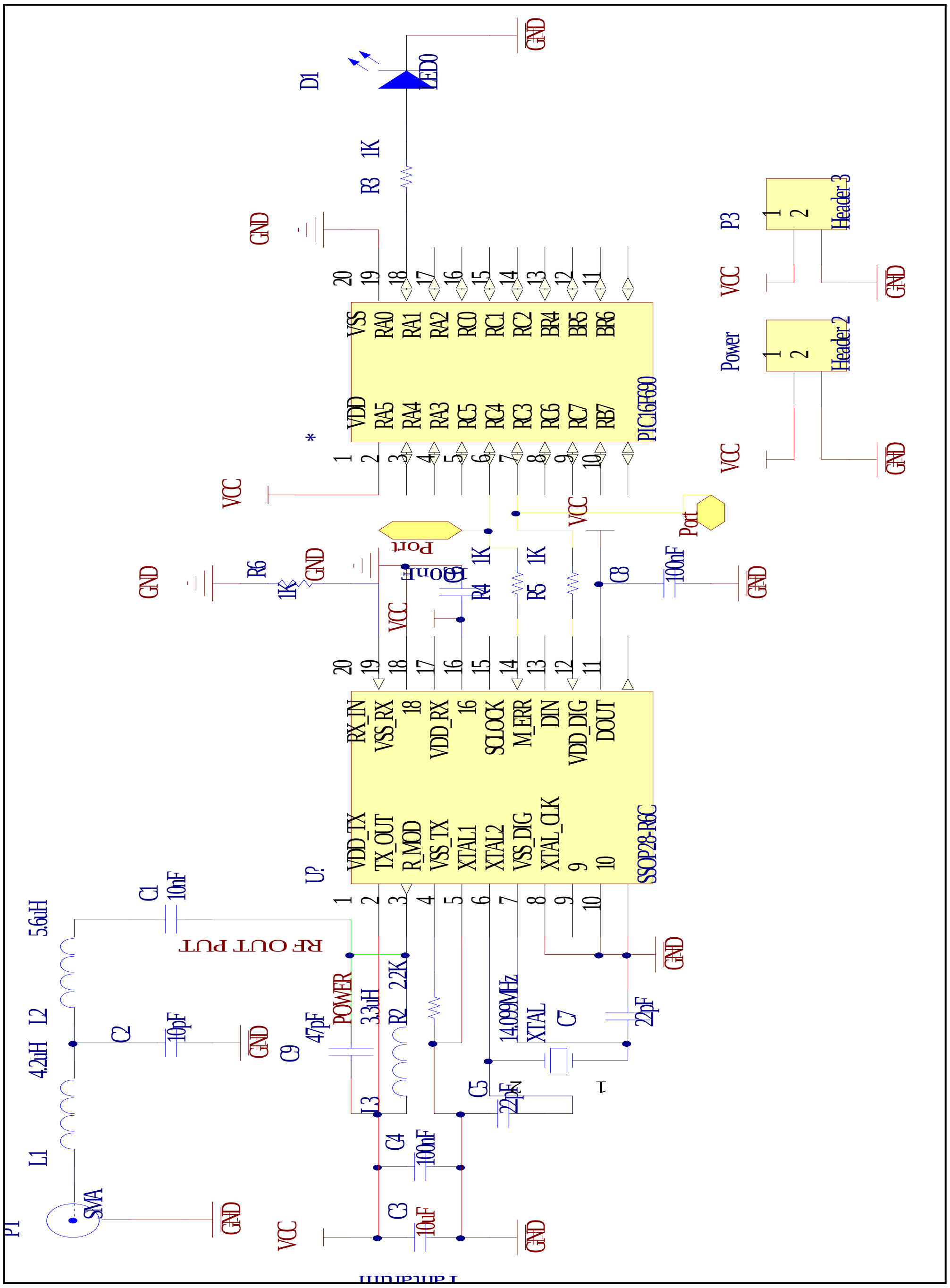

- PCB layout

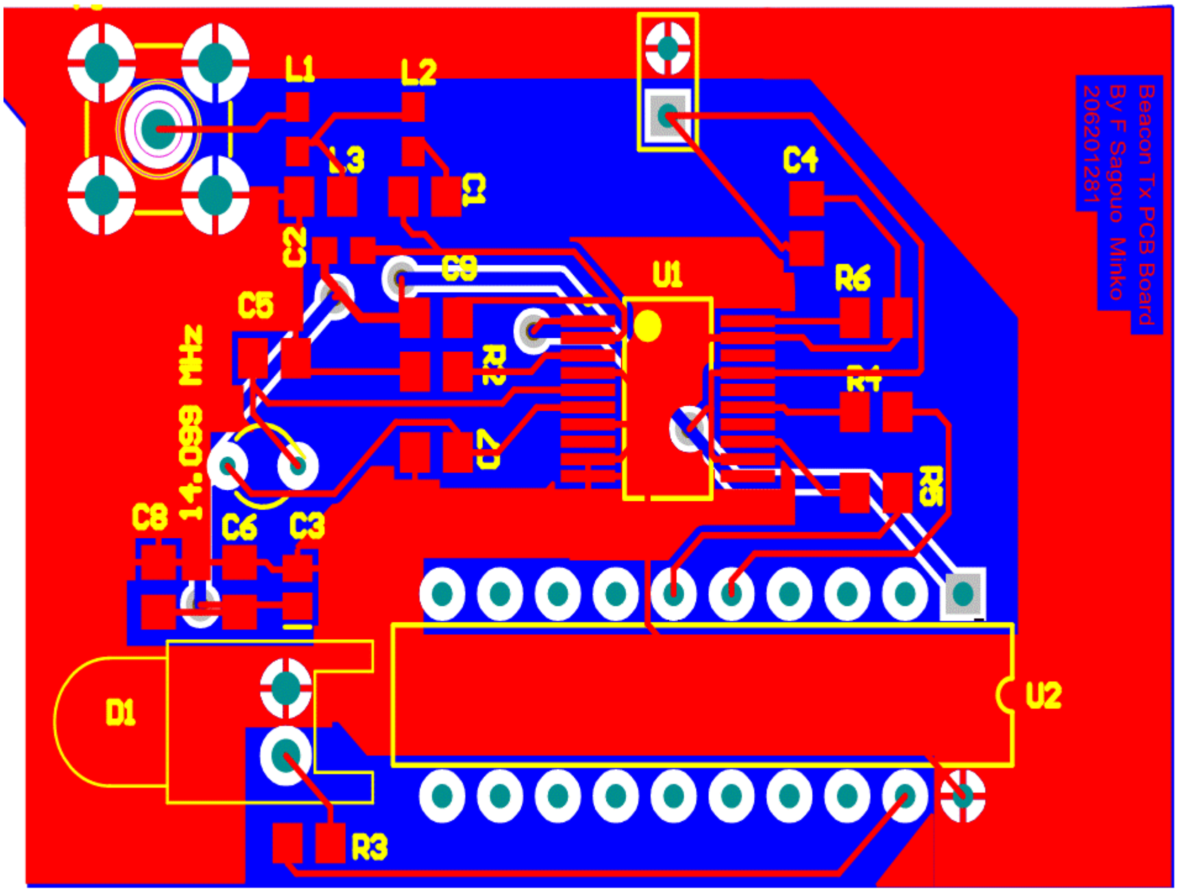

- Assembly drawing

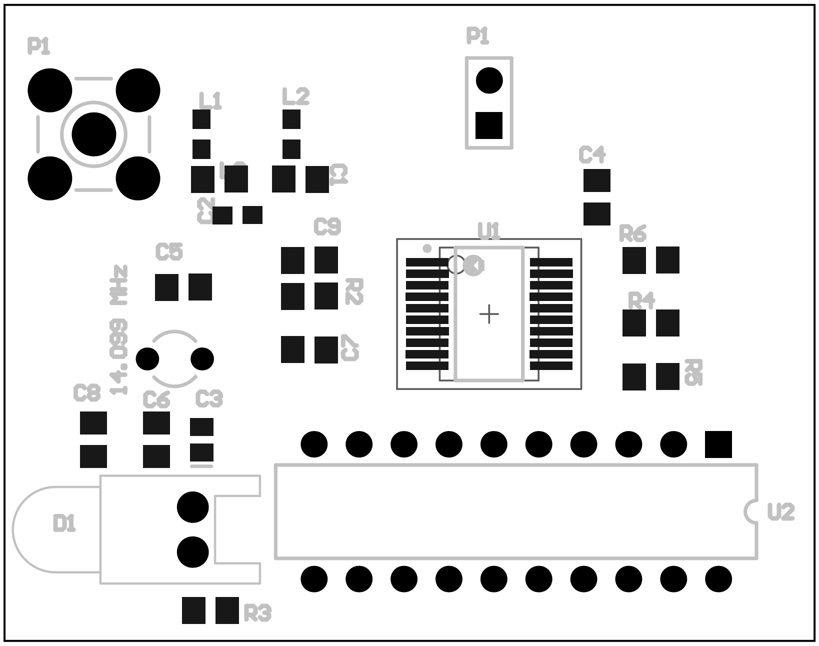

- Component list

Component	Value	Component	Value
C1	10nF	L1	4.2µH
C2*	56pF	L2	5.6µH
C3	10µF Tantalum	L3	3.3µH
C4	100nF	–	–
C5*	22pF	R1	2.2kΩ
C6	100nF	R2	18Ω
C7*	22pF	–	–
C8	100nF	–	–
C9*	47pF	–	–

Note: For devices marked with * , Class I (COG, NPO) ceramic type capacitors should be used.

Recommended inductance parameters:
Q factor: 20 to 40
Self resonant frequency: > 27MHz

- PCB material specifications

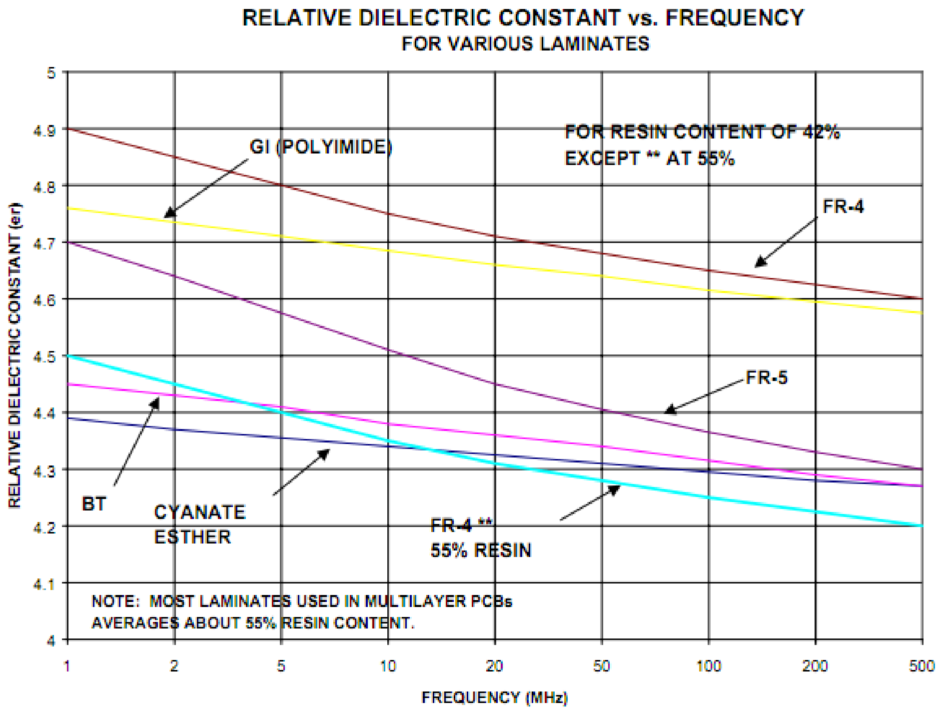

DIELECTRIC CONSTANT FOR FR-4 TYPE MATERIALS AS A FUNCTION OF GLASS TO RESIN RATIO

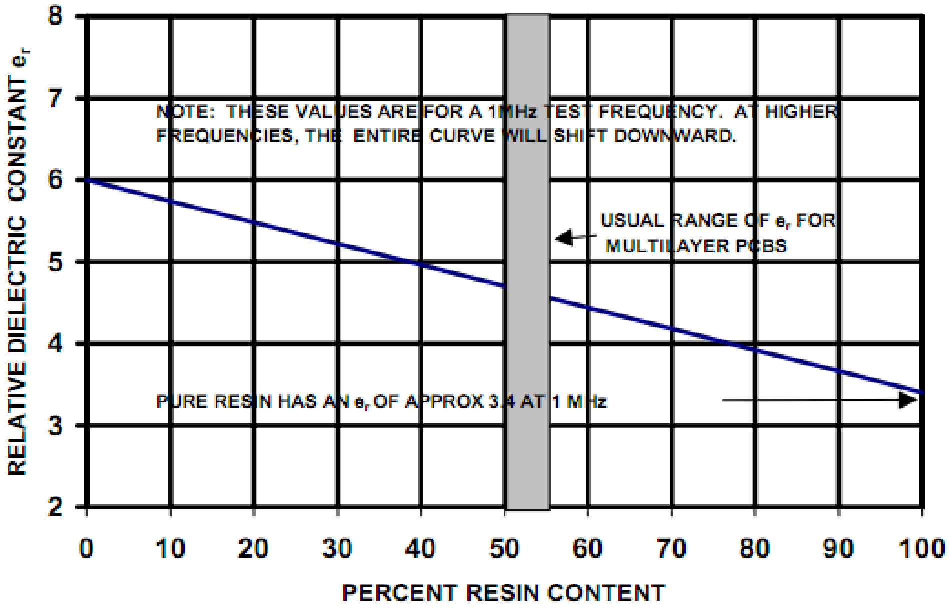

Material	Tg	e_r*	Tan (f)	DBV (V/mil)	WA, %
Standard FR-4 Epoxy Glass	125C	4.1	0.02	1100	0.14
Multifunctional FR-4	145C	4.1	0.022	1050	0.13
Tetra Functional FR-4	150C	4.1	0.022	1050	0.13
Nelco N4000-6	170C	4	0.012	1300	0.10
GETEK	180C	3.9	0.008	1100	0.12
BT Epoxy Glass	185C	4.1	0.023	1350	0.20
Cyanate Ester	245C	3.8	0.005	800	0.70
Polyimide Glass	285C	4.1	0.015	1200	0.43
Teflon	N/A	2.2	0.0002	450	0.01
		* Measured with a TDR using velocity method. Resin content 55%			

Appendix D: Pic-microcontroller code

a. *International Morse code Table*

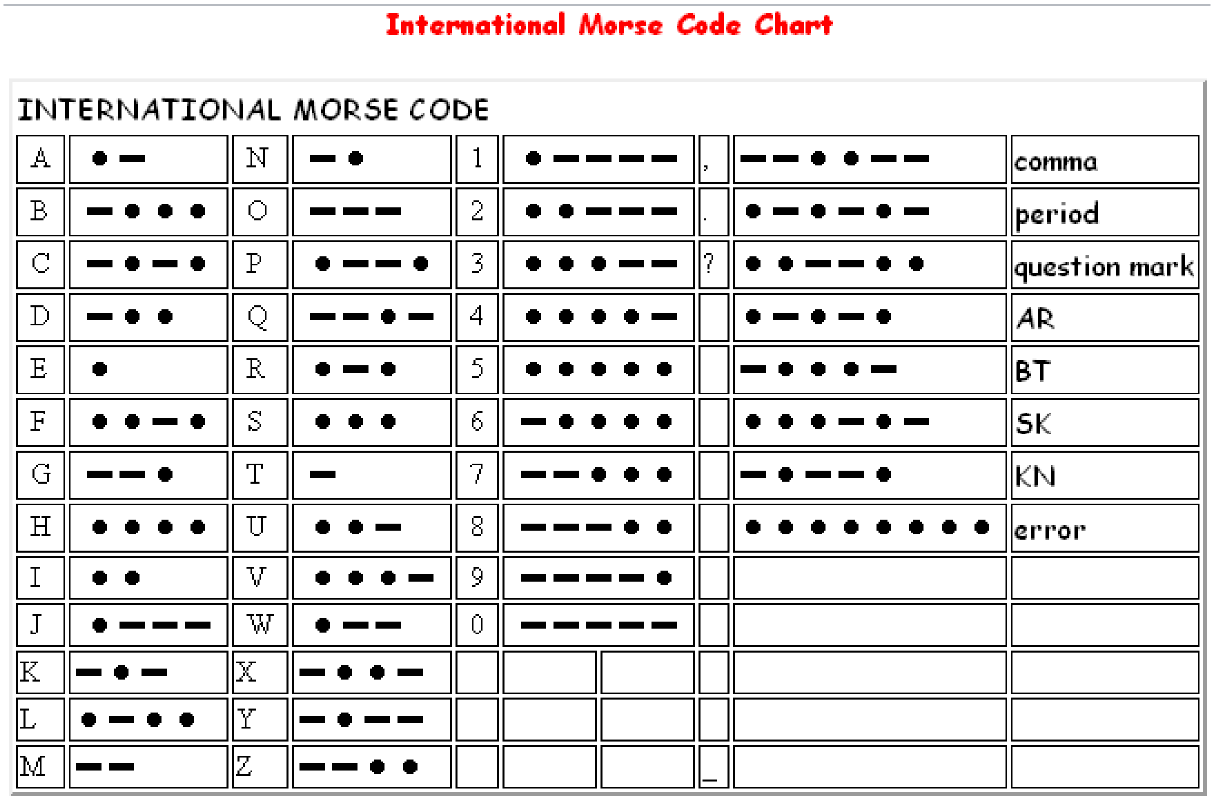

International Morse Code Chart

INTERNATIONAL MORSE CODE

A	● ▬	N	▬ ●	1	● ▬ ▬ ▬ ▬	,	▬ ▬ ● ● ▬ ▬	comma
B	▬ ● ● ●	O	▬ ▬ ▬	2	● ● ▬ ▬ ▬	.	● ▬ ● ▬ ● ▬	period
C	▬ ● ▬ ●	P	● ▬ ▬ ●	3	● ● ● ▬ ▬	?	● ● ▬ ▬ ● ●	question mark
D	▬ ● ●	Q	▬ ▬ ● ▬	4	● ● ● ● ▬		● ▬ ● ▬ ●	AR
E	●	R	● ▬ ●	5	● ● ● ● ●		▬ ● ● ● ▬	BT
F	● ● ▬ ●	S	● ● ●	6	▬ ● ● ● ●		● ● ● ▬ ● ▬	SK
G	▬ ▬ ●	T	▬	7	▬ ▬ ● ● ●		▬ ● ▬ ▬ ●	KN
H	● ● ● ●	U	● ● ▬	8	▬ ▬ ▬ ● ●		● ● ● ● ● ● ● ●	error
I	● ●	V	● ● ● ▬	9	▬ ▬ ▬ ▬ ●			
J	● ▬ ▬ ▬	W	● ▬ ▬	0	▬ ▬ ▬ ▬ ▬			
K	▬ ● ▬	X	▬ ● ● ▬					
L	● ▬ ● ●	Y	▬ ● ▬ ▬					
M	▬ ▬	Z	▬ ▬ ● ●			_		

b. *The code*

```
'BEACON TRANSMITTER FINAL EDITTED CODE
'LAGUAGE USED BASICPROF
'COMPILER PICBASIC PRO
'WRITTEN BY SAGOUO MINKO F
'20/06/2011
'*************************************
'*************************************
'defining variables
CLK VAR PORTC.5
DIN VAR PORTC.4
CB VAR BYTE
CNT VAR BYTE
TEMP VAR BYTE

'configuring the microntroller
TRISB = %00000000
TRISA = %00000000
TRISC = %00000000

'*** Main Loop ******
'testing the microcontroller's healt stat by blinking the LED
    FOR CNT = 0 TO 7
        PORTA.0 = 1
        PAUSE 50
        PORTA.0 = 0
        PAUSE 50
    NEXT CNT
PAUSE 0 'GIVE TIME TO SETTLE
```

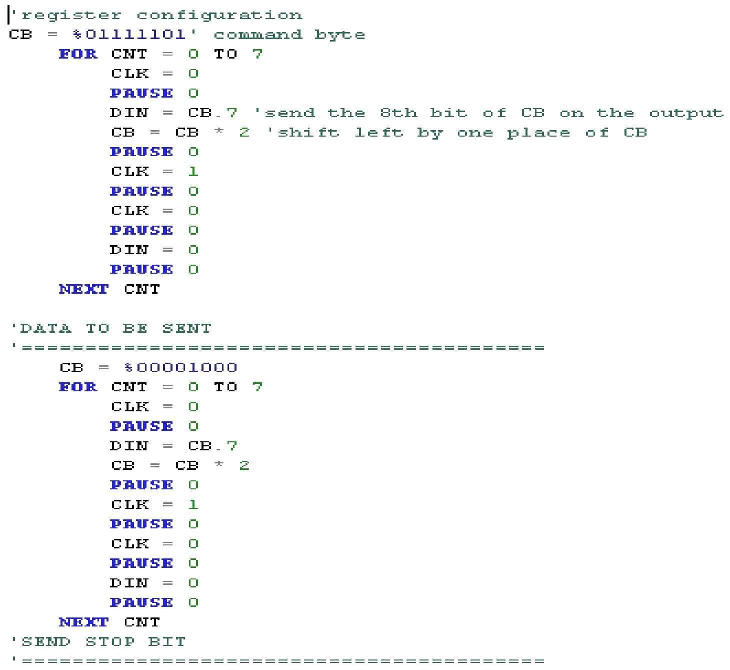

```
'register configuration
CB = %01111101' command byte
    FOR CNT = 0 TO 7
        CLK = 0
        PAUSE 0
        DIN = CB.7 'send the 8th bit of CB on the output
        CB = CB * 2 'shift left by one place of CB
        PAUSE 0
        CLK = 1
        PAUSE 0
        CLK = 0
        PAUSE 0
        DIN = 0
        PAUSE 0
    NEXT CNT

'DATA TO BE SENT
'=========================================
    CB = %00001000
    FOR CNT = 0 TO 7
        CLK = 0
        PAUSE 0
        DIN = CB.7
        CB = CB * 2
        PAUSE 0
        CLK = 1
        PAUSE 0
        CLK = 0
        PAUSE 0
        DIN = 0
        PAUSE 0
    NEXT CNT
'SEND STOP BIT
'=========================================
```

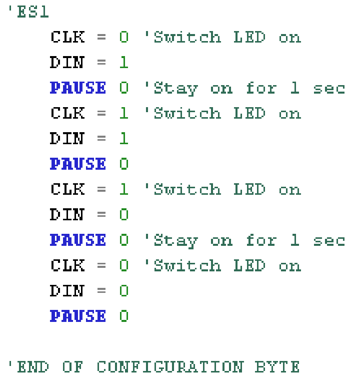

```
'ES1
    CLK = 0 'Switch LED on
    DIN = 1
    PAUSE 0 'Stay on for 1 sec
    CLK = 1 'Switch LED on
    DIN = 1
    PAUSE 0
    CLK = 1 'Switch LED on
    DIN = 0
    PAUSE 0 'Stay on for 1 sec
    CLK = 0 'Switch LED on
    DIN = 0
    PAUSE 0

'END OF CONFIGURATION BYTE
```

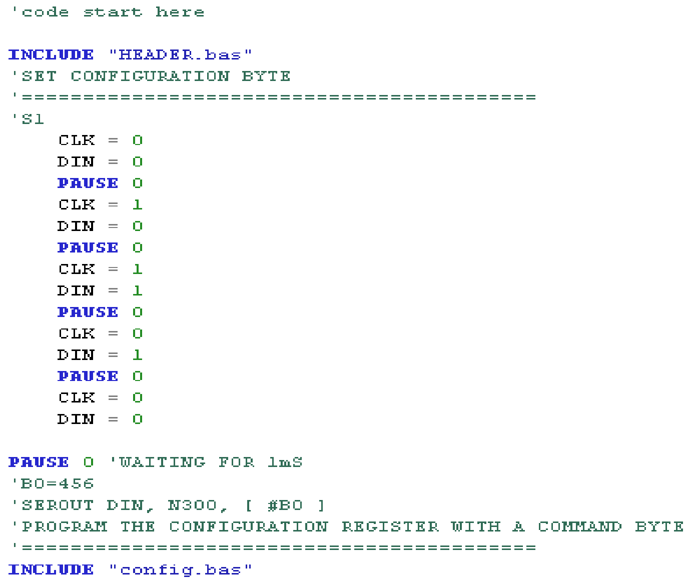

```
'code start here

INCLUDE "HEADER.bas"
'SET CONFIGURATION BYTE
'=========================================
'S1
    CLK = 0
    DIN = 0
    PAUSE 0
    CLK = 1
    DIN = 0
    PAUSE 0
    CLK = 1
    DIN = 1
    PAUSE 0
    CLK = 0
    DIN = 1
    PAUSE 0
    CLK = 0
    DIN = 0

PAUSE 0 'WAITING FOR 1mS
'B0=456
'SEROUT DIN, N300, [ #B0 ]
'PROGRAM THE CONFIGURATION REGISTER WITH A COMMAND BYTE
'=========================================
INCLUDE "config.bas"
```

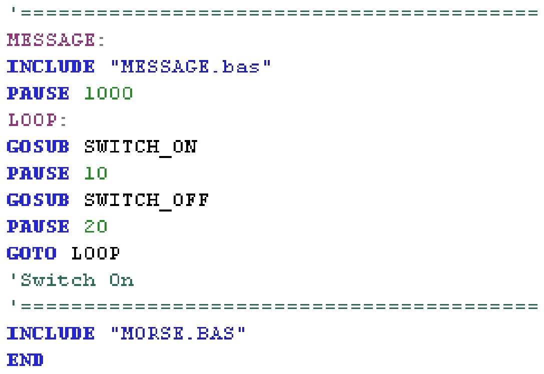

```
'=========================================
MESSAGE:
INCLUDE "MESSAGE.bas"
PAUSE 1000
LOOP:
GOSUB SWITCH_ON
PAUSE 10
GOSUB SWITCH_OFF
PAUSE 20
GOTO LOOP
'Switch On
'=========================================
INCLUDE "MORSE.BAS"
END
```